FRM II
Forschungs-Neutronenquelle
Heinz Maier-Leibnitz

MLZ
Heinz Maier-Leibnitz Zentrum

Annual Report 2013

JÜLICH
FORSCHUNGSZENTRUM

Helmholtz-Zentrum
Geesthacht
Zentrum für Material- und Küstenforschung

Technische Universität München

Bayerisches Staatsministerium für
Bildung und Kultus, Wissenschaft und Kunst

SPONSORED BY THE

Federal Ministry
of Education
and Research

The Heinz Maier-Leibnitz Zentrum (MLZ) is a leading centre for cutting-edge research with neutrons and positrons. Operating as a user facility, this cooperation involving the Technische Universität München (TUM), Forschungszentrum Jülich and Helmholtz-Zentrum Geesthacht (HZG) offers a unique suite of high-performance neutron scattering instruments. FRM II, the Jülich Centre for Neutron Science (JCNS), the German Engineering Materials Science Centre (GEMS) at HZG, and the Max-Planck-Society are responsible for the instrument operation and contribute significantly for the funding and user operation. Additional support is provided by nine German university groups. The neutron source is operated by the TUM, Forschungs-Neutronenquelle Heinz Maier-Leibnitz (FRM II). The MLZ is funded by the German Federal Ministry of Education and Research (BMBF), together with the Bayerisches Staatsministerium für Bildung und Kultus, Wissenschaft und Kunst (StMBW), and the partners of the cooperation.

Annual Report 2013

Heinz Maier-Leibnitz Zentrum (MLZ)

Content

Directors' Report

View of the FRM II reactor building
and the art work.

1

MLZ a new brand for neutron research in Germany

The three capital letters MLZ (Heinz Maier-Leibnitz Zentrum) stand for competence in research using neutrons and positrons in Germany and represent the scientific cooperation, which began on January 1st 2011, between the Technische Universität München and two Helmholtz Centres, namely the Forschungszentrum Jülich, and the Helmholtz Centre in Geesthacht. It is embedded in a network of partners consisting of several university groups as well as institutes from the Max Planck Society to provide a user service for scientists from Germany and abroad.

The inauguration of the MLZ was celebrated on February 21st 2013, accompanied by the launch of our new website that addresses the general public and, in particular, our scientific users. In addition to background information on neutron research in general and the MLZ in particular, this web portal presents all the MLZ-instruments in detail, as well as the service groups supporting our users.

To strengthen the focus of MLZ on research, six science groups representing relevant fields at the MLZ were established. They cover materials science, soft matter, quantum phenomena, structure research, astro- & particle physics and neutron methods. A primary goal of the groups is to deepen the scientific exchange both within the groups and with external research institutions and universities from the greater Munich area. One of the aims of MLZ is to address disciplines more distant from its core activities. This was achieved, for example, with the 1st International Conference on Neutron Imaging and Neutron Methods in Archaeology and Cultural Heritage Research (NINMACH) held at MLZ in September 2013.

MLZ offers a wide spectrum of neutron scattering instrumentation at one of the best neutron sources in the world. In order to extend our instrumentation even further through the new Neutron Guide Hall East, its linking to the reactor building was realised in 2013. The new guide hall will host the instruments SAPHiR, MEPHISTO, TOPAS, POWTEX, TRISP, EDM and the positron beam facility NEPOMUC, thereby expanding the use of ultra-cold, cold and thermal neutrons as well as positrons at the MLZ.

The MLZ, as an important element of the European scientific infrastructure, is heavily involved in international collaboration, with a special focus on Europe. All partners participate in the Integrated Infrastructure Initiative NMI3, a European project of 18 partner organisations in 10 countries, including 13 facilities. It supports transnational (with respect to the location of the respective facilities) users with access and promotes technical development for neutron instrumentation ranging from detectors to sample environments and method development. NMI3 includes a dissemination work package that is located at the MLZ. On the occasion of the International Conference on Neutron Scattering ICNS 2013 in Edinburgh, this initiative resulted in the launching of a world-wide promotion of neutron research and the establishment of the web site neutronsources.org hosted at the MLZ.

None of the scientific achievements and fascinating technological and methodological developments presented in this report would have been possible without the reliable and extensive supply of neutrons from our source. In 2013, the FRM II provided a full 240 days of operation and thus delivered neutrons for research, industry and medicine at maximum capacity. However, in 2014 the neutron source will be operated for only around 120 days, since an extensive maintenance break after ten years of operation is under way. We celebrated this anniversary on 12th March 2014. Ten years of FRM II in operation marks not only a moment in time to look back, but is also an occasion for gratitude and to look forward to a bright future for FRM II with its novel structure for scientific exploitation under the umbrella of MLZ.

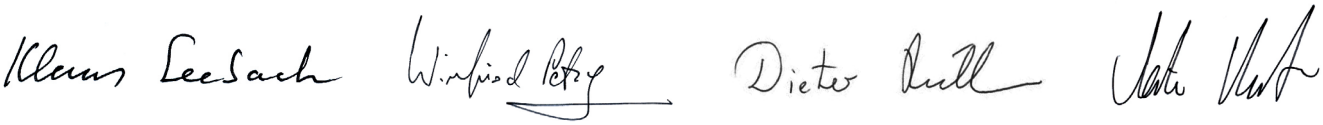

Klaus Seebach | Winfried Petry | Dieter Richter | Anton Kastenmüller

The year in pictures

February 21st
Prof. Dr. Dieter Richter (left) and Prof. Dr. Winfried Petry inaugurate the Heinz Maier-Leibnitz Zentrum.

February 27th
Participants at the 24th Seminar „Activation Analysis and Gamma Spectroscopy“ (SAAGAS) during a coffee break.

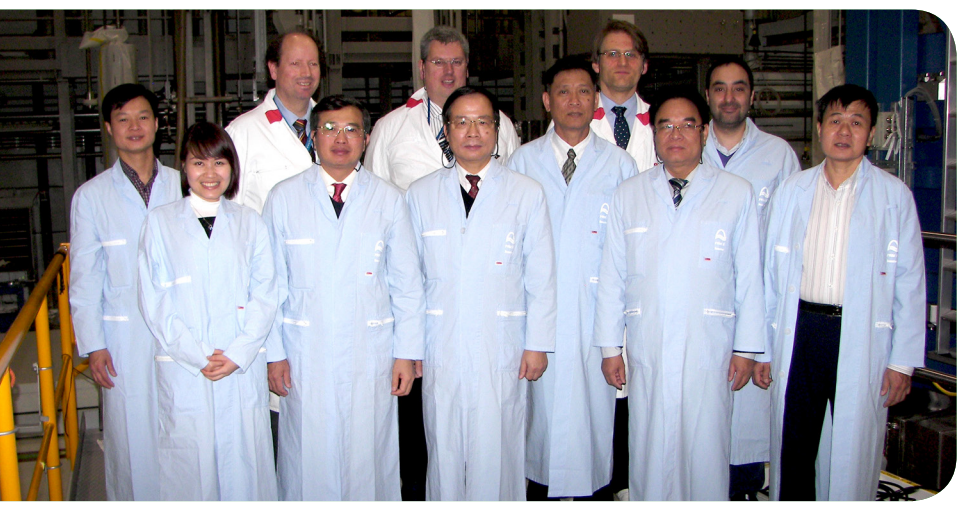

April 3rd
A Vietnamese delegation, including the deputy Minister for Science and Technology of Vietnam, visits the FRM II facilities for education and training purposes.

April 19th
Students at the Think Big Day, visiting large scale facilities in physics at the FRM II, shown around by Prof. Dr. Winfried Petry.

June 20th
Josef-Andreas Weber (l.) as well as PD Dr. Christoph Hugenschmidt (not in the picture) received the Ehrennadel from Prof. Dr. Dr. h.c. mult. Wolfgang A. Herrmann, President of Technische Universität München, for their engagement in education with the TUMKolleg Gauting.

September 9th
The 1st International Conference on Neutron Imaging and Neutron Methods in Archaeology and Cultural Heritage Research hosted by the MLZ attracted almost 100 international scientists.

The year in pictures

September 17th
The MLZ was part of the “Highlights der Physik” exhibition in Wuppertal presenting videos, brochures, Lego robots and a ball toss stand with “neutron balls”.

September 18th
PD Dr. Christoph Hugenschmidt kicks off the social part of the SLOPOS conference by tapping a barrel of beer.

September 25th
If you want to get to know your colleagues, go paddle in a boat, go hiking or try archery. This was the motto of the 2013 FRM II summer excursion to the Altmühltal.

October 9th
The company Varta Storage, a partner in the Lithium battery project EEBatt of Technische Universität München, visits one of the EEBatt-partners, FRM II, shown around by Dr. Ralph Gilles (6th from right) and Dr. Michael Hofmann (4th from right).

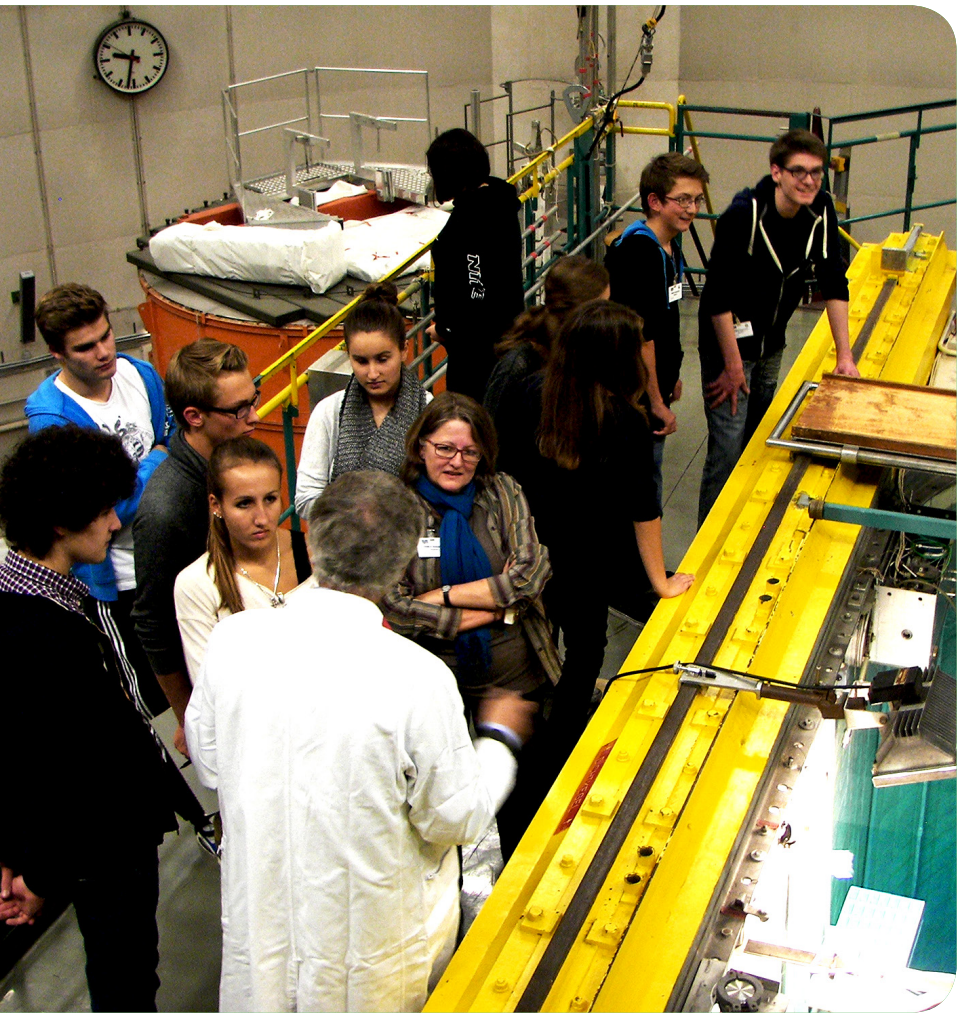

October 9th
Students of the P-Seminar "Garching schlüpft aus dem Atom-Ei" at Gymnasium Garching visiting the Atomic Egg accompanied by Prof. Dr. Klaus Böning.

October 19th
The neutron ball toss as well as two neutron scattering instruments made of Lego models attracted not only a lot of young visitors at the open day of the Campus Garching in the Physics Department.

Instruments & Methods

Sample to be examined
at the new radiography and tomography station ANTARES.

2

News from the instruments

M. Zamponi[1], J. Park[2], W. Häußler[2], R. Georgii[2], S. Mühlbauer[2], J.-F. Moulin[3], H. Frielinghaus[1], C. Hugenschmidt[2], M. Schulz[2], P. Fierlinger[4], P. Link[2]

[1]Jülich Centre for Neutron Science (JCNS) at MLZ, Forschungszentrum Jülich GmbH, Garching ,Germany

[2]Heinz Maier-Leibnitz Zentrum (MLZ), Technische Universität München, Garching, Germany

[3]German Engineering Materials Science Centre (GEMS) at MLZ, Helmholtz-Zentrum Geesthacht GmbH, Garching, Germany

[4]Exzellenzcluster „Origin and Structure of the Universe“, Technische Universität München, Garching, Germany

Extending the instrument capabilities for the user is an ongoing major concern of the instrument teams. Improved resolution or focusing of the beam optics for small samples enhance the instruments' equipment. Underlining the unique role of neutron scattering for the study of the magnetic properties of matter, emphasis is laid on using polarized neutrons on more and more instruments using small-angle scattering, namely KWS-1, REFSANS to imaging and spectroscopy. ANTARES, NEPOMUC and SANS-1 had their first successful year of user operation, NEPOMUC and ANTARES in the wake of a complete renewal last year. While the construction work for the Neutron Guide Hall East goes on, the world record magnetic shielding of the EDM experiment allows for first measurements.

SPHERES - Improvement of small angle resolution

The resolution for small scattering angles at the neutron backscattering spectrometer SPHERES has been improved by reducing the azimuth angle range of the analyzers.

Since the small angle detectors must be placed outside the incoming neutron beam, the small angle analyzer rings cannot be aligned to exact backscattering geometry (contrary to the large angle analyzers). This causes a variation in the analyzer Bragg angle along the ring which results in a broadened resolution function. By partially covering the analyzer rings with cadmium (fig. 1 top), the resolution can be improved with little loss of the peak intensity (fig. 1 bottom). The measured resolution function agrees well with the simulations, which demonstrates the dominance of the geometric effect.

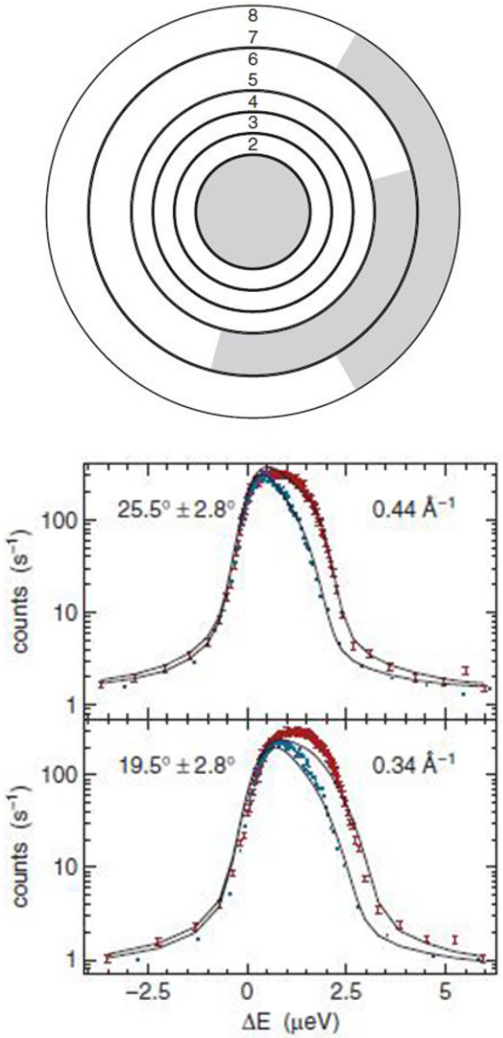

Figure 1: Improving the resolution at SPHERES. Top: Small angle analyzer rings, the shaded area indicates the removable cadmium cover. Bottom: Resolution spectra for two small angle detectors, red: resolution without cadmium cover, blue: with cadmium cover. Lines simulation results.

PUMA multi-analyzer and polarized neutrons on thermal TAS

The new multi-analyzer system is now ready for

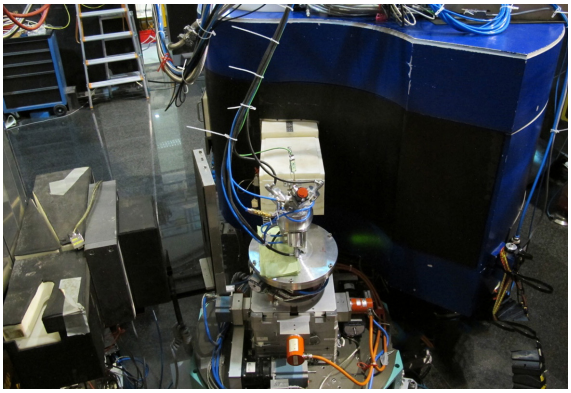

Figure 2: Measurement of phonon soft modes using the PUMA multi-analyzer system.

use. It can simultaneously accept a scattering angle range of 16 degrees, so that flexible Q-ω pathways can be realized without repositioning the instrument. The multi-analyzer and -detector system allows not only Q-ω space mapping measurements, but also time-resolved kinetic measurements of collective excitations that vary during processes such as chemical reactions, demixing, phase transitions, or the switching of ferroelectrics.

Last July, in collaboration with instrument scientists on POLI, we carried out the first technical test for a polarized neutron scattering experiment at PUMA. By putting two ^{3}He spin filters after a monochromator and before an analyzer, we obtained the maximum flipping ratio of 30 at k_i = 2.662 Å^{-1} and 10 at k_i = 4.1 Å^{-1}. This neutron polarization option will later be combined with our multi-analyzer system which will provide the unique opportunity to simultaneously measure both spin flip and non-spin flip components of neutrons scattered off a sample.

We adopted the new instrument control software NICOS 2 which makes the operation of PUMA simpler and more user-friendly. Moreover, the same software is now being used in other three axes spectrometers at MLZ (PANDA and MIRA), so that users will benefit from a consistent mode of operation for these instruments.

RESEDA – from MIEZE to LNRSE

At RESEDA in 2013, a complete new secondary spectrometer arm was installed, which is modularly built. The basis of this arm is constructed from commercially available profiles (ITEM). It is movable on air pads and a friction wheel provides positioning. The arm is connected to the sample environment by a turntable with encoder, in order to control the movement and position. On this basis, several instrumental options can be realized. First, the standard NRSE setup as used at RESEDA until today can be mounted (fig. 3, upper part), being identical to the primary spectrometer arm and consisting of a µ-metal shielding and two NRSE coils. In addition, for SANS and MIEZE-SANS experiments, a setup of an evacuated flight-tube with variable length and an area detector fits onto the new basis. Finally, a completely new NRSE-MIEZE setup with solenoids providing magnetic fields along the neutron beam direction has been constructed. With this longitudinal NRSE (LNRSE) setup (fig. 3, lower part), quasi-elastic scattering experiments with higher time resolution can be performed.

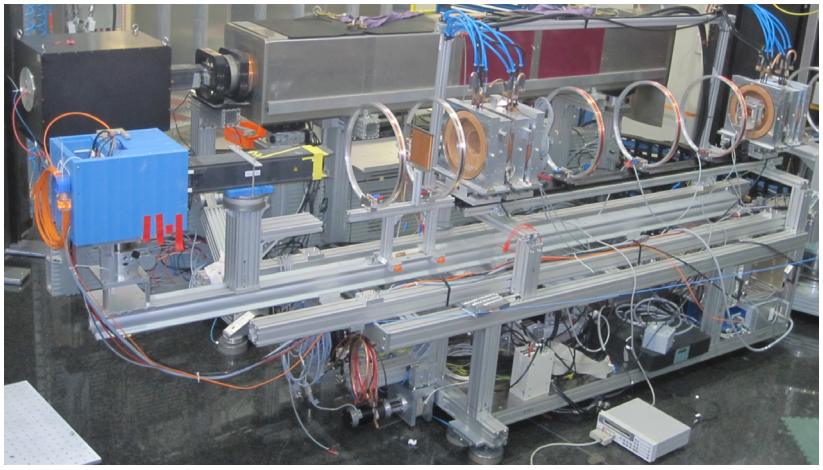

Figure 3: Instrumental setups at RESEDA: The standard NRSE setup (upper part) consists of a µ- metal shielding containing the NRSE coils. The longitudinal coils of the completely new LNRSE setup built from copper are clearly visible (lower part).

TAS mode on MIRA with focusing optics – high flux on small samples

Recently, MIRA has successfully put into operation a system of elliptical focusing guides that can enhance intensity in inelastic measurements by a factor 10 and more. The system consists of two four-sided focusing guide elements mounted

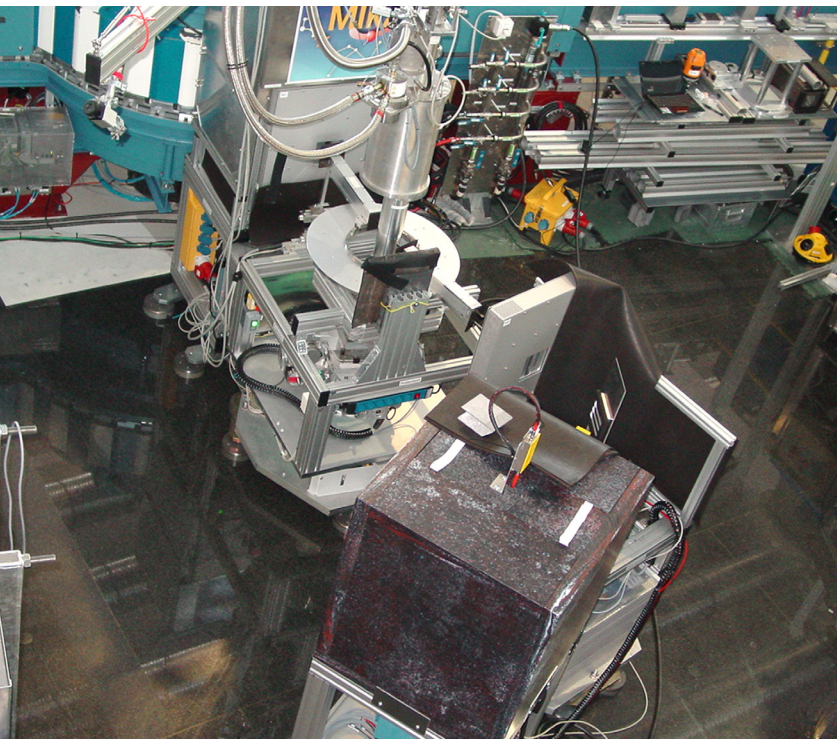

Figure 4: MIRA in TAS mode with a cryostat and the elliptic mirror system installed.

on rails positioned before and after the sample, with the second guide fixed to the sample scattering angle (fig. 4). The guide elements have a length of 50 cm and a focal length of 8 cm, the size of the focal spot being 7 x 3.5 mm². Due to highly reproducible mounting, they can easily be removed and replaced for measurements with and without focusing.

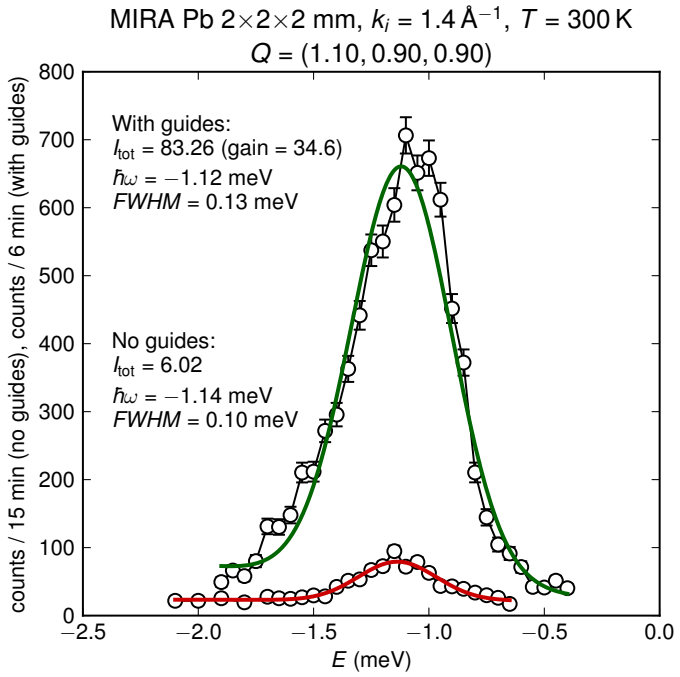

Figure 5: The intensity of a TA phonon in a 2 x 2 x 2 mm³ lead sample without guides (red) and with the guides installed (green). A gain of more than 30 in the integrated intensity has been achieved.

In figure 5, an energy scan over a TA phonon in lead is shown for a small cube of 2 x 2 x 2 mm³ proportions using the guides in comparison with a measurement without the guides installed. With the guides in place, the integrated intensity is bigger by a factor 30, while the background increases only by a factor 2. Of course, due to the deterioration in the resolution, it can be hard to measure in the vicinity of strong elastic features. Depending on the application, the guides can be very valuable for reducing counting times with small samples, especially in extreme environments.

SANS-1 – first year in full user operation

2013 has been the first year of full user service for the small-angle neutron scattering instrument SANS-1 at MLZ. A total number of 42 user experiments have been successfully performed with a strong focus on materials research and magnetism. Typical applications in materials research included the extensive investigation of high temperature CoRe alloys (fig. 6, panels (A) and (B) shows typical data) for new generation turbine blades and in-situ research of different types of batteries and battery materials. In magnetism, a broad variety of scientific problems have been tackled, ranging from Skyrmion lattices in helimagnetic compounds, through superconducting vortex lattices (fig. 6, panel (C) shows typical data) and magnetic precipitates to photonic crystals. To cater for the specific needs for this range of experiments, a pool of different sample environments including high temperature furnaces, combinations of different magnets and cryostats have been successfully integrated into the instruments' hard- and software.

During this first year of user operation, the hardware and software of SANS-1 was continuously improved to guarantee the highest possible performance, stability and reliability: A new in-

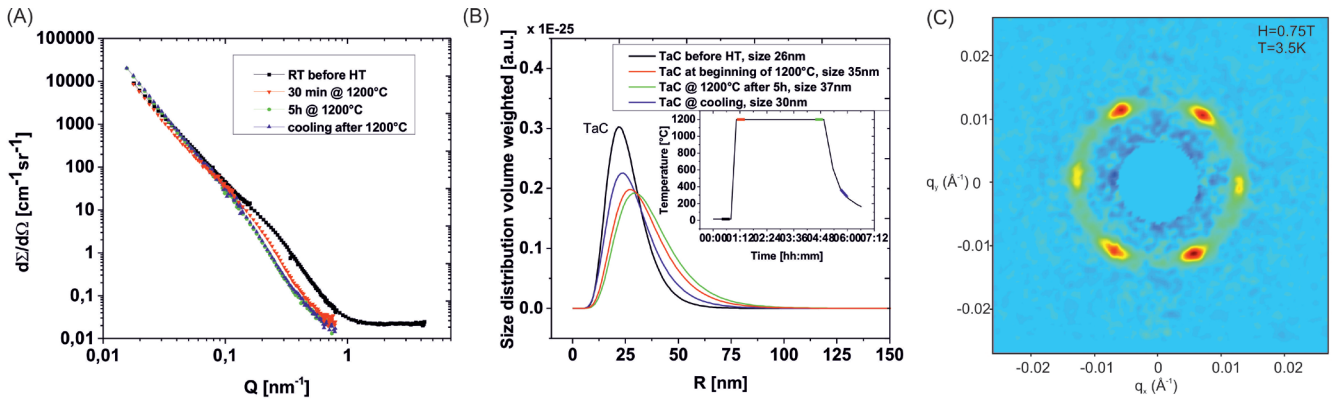

Figure 6: Panel (A): Typical SANS data of CoRe alloys while heating up to 1200 °C. Panel (B): Size distribution of the strengthening phase of TaC while heating up to 1200 °C and during a heating cycle derived from SANS. Panel (C): Vortex lattice of a doped FeAs based superconductor in a magnetic field of 0.75 T and at a temperature of 3.5 K. The figure represents a sum over a rocking scan with respect to a vertical axis. The background has been obtained at zero magnetic field and is subtracted. The direct beam is masked.

terchangeable nose system with sapphire windows, installed at the sample position end of the collimator ensures lowest possible residual background scattering and a flexible adaption for different sample environments. The use of a new firmware for the readout electronics of the 1 m² position sensitive detector has increased the maximal useable count-rate by a factor two to ≈ 1 MHz. An extension of the instrument platform to the sample area provides enough space to set up complicated sample environments as well as the preparation of successive experiments with minimal loss of beam-time.

In situ polarized GISANS at REFSANS

Within the DFG Transregio TRR80, a dedicated UHV sputtering chamber has been designed for operation at REFSANS. Several conventional specular reflectometry experiments performed so far have established the concept of the in situ NR characterization of metallic thin films. Recently a more challenging experiment has been performed: a polarizing supermirror was installed upstream of the chamber and the collimation switched to a pinhole geometry, allowing GISANS measurements for the characterization of the evolution of lateral correlations in the sample. Figure 7 shows the evolution of the polarized signal with the thickness of an iron layer grown on an asymmetric Al_2O_3 grating aligned parallel to the beam. Following the imminent installation of a dedicated broad band polarizer and flipper in the collimation chamber, such measurements will become accessible to routine operation even for the largest samples. This opens new perspectives for the characterization of hybrid materials, e.g. embedded magnetic particles in an organic matrix. Moreover, the polarized incident beam will be used together with polarization analysis to suppress the incoherent background inherently affecting measurements on soft-matter samples.

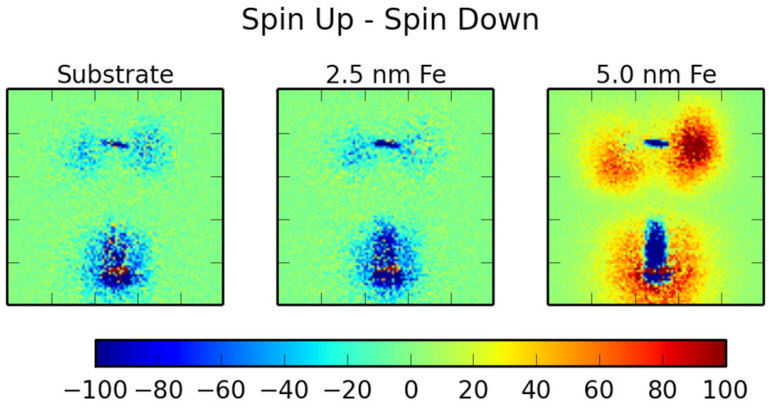

Figure 7: Polarized GISANS data at REFSANS: evolution of the polarized signal with the thickness of an iron layer grown on an asymmetric Al_2O_3 grating aligned parallel to the beam.

KWS-1 upgrade for polarized neutrons

The instrument strategy of KWS-1 is aimed at the

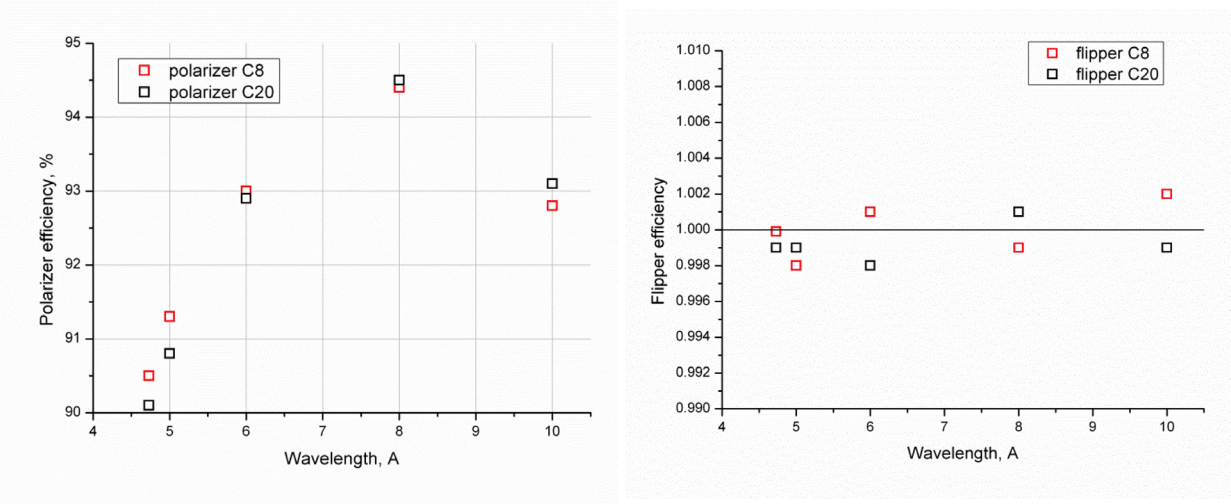

Figure 8: (Left) The polarization performance of the three-cavity polarizer with V-shaped super-mirrors as a function of wavelength. (Right) The performance of the RF spin-flipper as a function of wavelength (spin-flip probability > 99.8 %).

analysis of magnetic structures as one important option, and during the last upgrade the polarizer and flipping option was successfully installed. The three-cavity polarizer from Swiss Neutronics with V-shaped super-mirrors performed well with respect to polarization with values of up to 94 % (fig. 8 left, fig. 9). The radio frequency spin-flipper worked perfectly with a spin-flip probability better than 99.8 % (fig. 8 right). Thus, from point of view of polarization preparation, the instrument is ready for scientific measurements. The measurement software is currently being upgraded to automatically change the polarization during the measurement.

In parallel, KWS-1 obtained the same performance-boosting options as KWS-2, which are (1) a double disc chopper for high Q-resolution measurements of up to 1 %, and (2) MgF_2 parabolic lenses for high intensity and low-Q measurements. The commissioning and software-implementation is ongoing. From KWS-2 we know and extrapolate that the Q-resolution can be increased down to 1 or 2 %, and that intensity gains of 11 are possible.

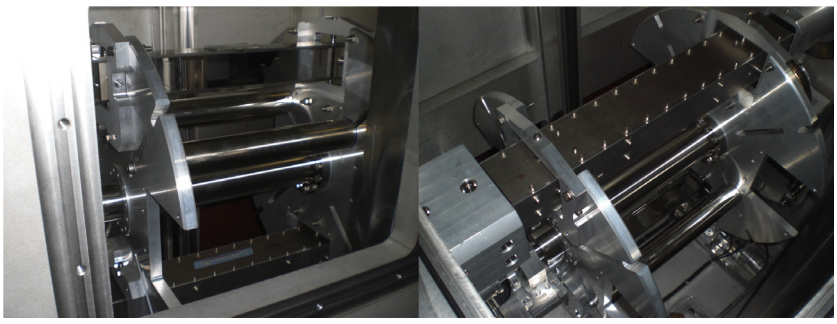

Figure 9: The revolver polarizer changer between (left) a plain neutron guide segment and (right) the polarizer. The two remaining positions have been left for further options.

Upgrade of the instruments for positron beam experiments at NEPOMUC

After the successful replacement of the beam-tube, the new positron source NEPOMUC upgrade enables the continuation of a large variety of studies using the high-intensity positron beam as well as the development of new experiments. These experiments range from high-sensitivity and elemental selective investigations in surface physics, through defect spectroscopy in thin films and solids to fundamental studies in atomic and plasma physics. At NEPOMUC the upgrade in the intensity of the monoenergetic positron beam was determined to $>10^9$ moderated positrons per second.

1. Characteristics of the Positron Beam

The positron beam parameters such as shape and intensity can be determined at the first accessible place outside the reactor shielding. For this purpose, a beam monitor and an Al target, which are mounted on an UHV-manipulator, can be moved onto the axis of the beam line (fig 10). The beam monitor consists of a micro-channel plate (MCP) detector with a phosphorus screen and a mirror. The image of the beam is recorded

by a CCD-camera through an UHV-window. The detection of annihilation quanta emitted from positrons hitting the Al target enables the positron beam intensity to be determined. The intensity of the monoenergetic positron beam was determined to $1.14(7) \cdot 10^9$ moderated positrons per second at an energy of 540 eV, the beam diameter being <10 mm. The positron beam is transported in a magnetic guide field of typically 7 mT, and the kinetic energy of the primary (re-moderated) positron beam was recently set to 1 keV (20 eV).

2. Positron Beam Experiments

A new switching and remoderation device has been installed in order to allow toggling from the high-intensity primary beam to a brightness enhanced remoderated positron beam. At the positron beam facility NEPOMUC four different instruments are permanently installed, and one beam port is open for positron experiments provided by external users.

Surfaces

The upgraded surface spectrometer at NEPOMUC allows for comprehensive surface analysis with STM, XPS and Auger spectroscopy, as well as sample preparation under UHV conditions. In particular, Positron annihilation induced Auger Electron Spectroscopy (PAES) for element selective surface studies has excellent advantages over conventional AES such as suppressed secondary electron background in the range of Auger-transition energies and exceptional surface sensitivity. Time dependent PAES allows the observation of the segregation process in-situ. For future studies X-ray induced Photoelectron Spectra (XPS) will provide additional information about oxidation states due to the chemical specificity of XPS. The Scanning Tunneling Microscope (STM) is used as a complementary method to investigate the electron density with atomic resolution of the same sample. Hence, the combination of PAES, XPS and STM allow the characterization of both the elemental composition and the topology of the surface.

Defects and thin films

Coincident Doppler broadening spectroscopy (CDBS) with the high intensity positron beam at NEPOMUC has been successfully applied in a large variety of physical systems such as thin metallic and oxide films, embedded layers, severely plastically deformed materials and irradiated alloys. CDBS enables element specific defect studies in the near surface region and in the bulk of the specimen up to a few micrometer according to a positron energy of up to 30 keV. The sample defects can be mapped by scanning the beam in two dimensions with a lateral resolution of <300 µm. Recently, a new sample heater has been installed that makes in-situ (C)DBS possible at temperatures up to 1300 K. In order to bias the specimen at high voltages up to 30 kV, the light of a 250 W halogen lamp, which is positioned in one of the foci of an elliptic reflector, is focused onto the specimen.

The Pulsed Low-Energy Positron System (PLEPS) is operated in collaboration with the Universität der Bundeswehr (UniBW) München for depth dependent positron lifetime measurements. At NEPOMUC lifetime spectra can be recorded within a few minutes, and the high peak-to-background ratio of 10^4 allows the extraction of at least three lifetime components reliably. Recently, the time window was extended to 40 ns in order to detect Positronium annihilation in nanopores with greater accuracy.

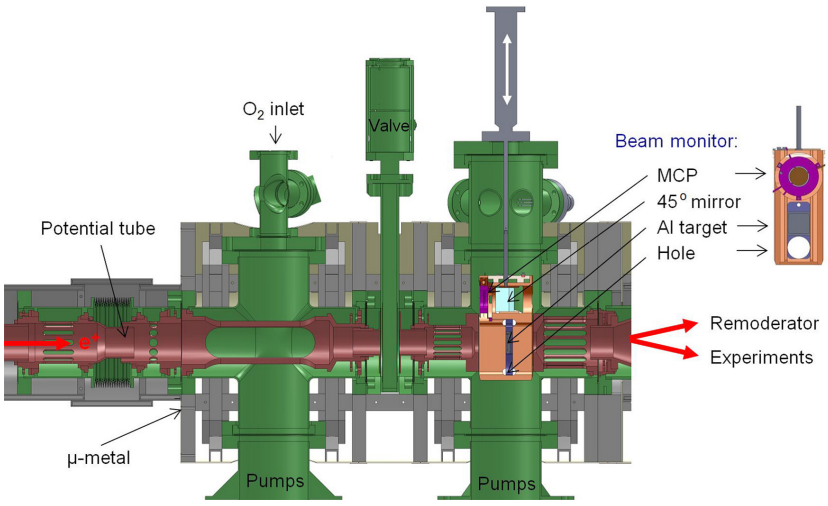

Figure 10: Characterization of the primary positron beam: Movable beam monitor (MCP detector with phosphorus screen and 45° mirror) and Al target for intensity measurements.

First measurements with the newly built interface including pulsing units and an additional remoderator for brightness enhancement was put into operation. This device is required to connect the Scanning Positron Microscope (SPM) to the NEPOMUC beam line.

Fundamental studies

Additional experimental setups can easily be connected to the positron beam line at the open beam port. Currently, the production and the in-flight decay of cold Positronium are being investigated. Due to limitations of space in the present location, it has been necessary to extend the positron beam facility to the new Neutron Guide Hall East close to the reactor building. It is also planned to move the new spectrometer for the measurement of the Angular Correlation of Annihilation Radiation (ACAR) to the Neutron Guide Hall East in order to allow for depth dependent non-destructive studies of the electronic structure in thin films, at interfaces and at surfaces. Another long-term experiment at an additional beam port will be the implementation of a stellarator setup for the creation and study of electron positron plasmas.

ANTARES – introducing polarized and monochromatic neutron imaging

The new ANTARES beam line is now operational! User experiments are running, including studies of plants, batteries and archeological objects. Furthermore, several new features are now available and were tested successfully during the last reactor cycle in 2013. A polarized neutron imaging experiment with polarizing V-cavities has been carried out using a newly designed cryostat manipulator and a compact normal conducting 0.5 Tesla magnet. In this study, a series of metallic samples close to quantum criticality were investigated to identify residual traces of ferromagnetism at the lowest temperatures. Figure 11 shows the setup used for the experiment. Additionally, an ASTRIUM neutron velocity selector was installed and tested for the first time. The selector now allows for wavelength-dependent neutron imaging down to a wavelength of 2.95 Å with a wavelength resolution of $\Delta\lambda / \lambda = 10$ %. The selector was also used in an experiment with polarized neutrons. Figure 12 shows a series of spin rotation groups for differ-

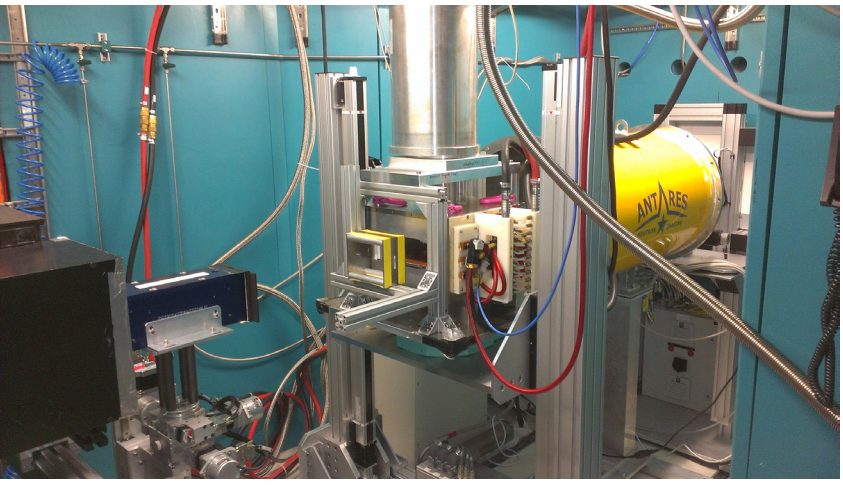

Figure 11: Experimental setup for polarized neutron imaging on ANTARES.

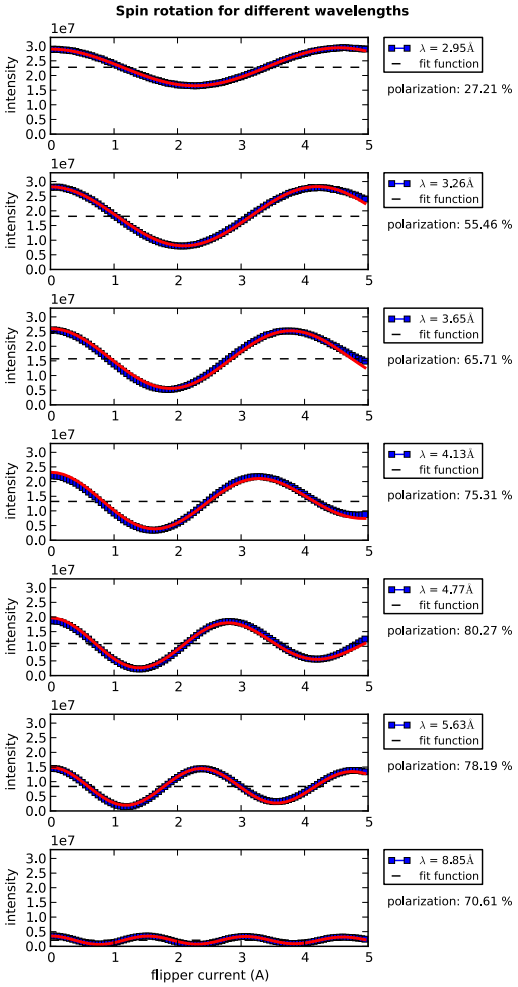

Figure 12: Series of spin rotation groups for different wavelengths measured using a Mezei-type flipper coil and the velocity selector of ANTARES.

ent wavelengths measured using a Mezei-type flipper coil. The observed rotation of the neutron polarization is in very good agreement with the predicted values.

The Neutron Electric Dipole Moment measurement at the FRM II

The asymmetry of matter and antimatter in the universe remains one of the major unresolved questions in particle physics and cosmology. It turns out that in basically every approach to explain this broken symmetry in the universe, a time-reversal-symmetry violating electric dipole moment of the neutron should also be observed. These processes that drive the primordial asymmetry would then be diluted residual effects that cause this asymmetric property of the neutron.

Within the next generation of experiments at roughly one dozen institutions worldwide, an improvement in sensitivity by two orders of magnitude from the previous limits, $2.9.10^{-26}$ ecm, to few 10^{-28} ecm, is planned. Our approach is currently the only one being installed and commissioned worldwide and has evolved into an international collaboration, see nedm.ph.tum.de.

The concept of the measurement is a spin-clock comparison measurement of ultra-cold neutrons trapped in two chambers at room-temperature with at least one co-habiting polarized species present in the same chambers at the same time in the presence of a small magnetic field.

A next generation measurement will have to deal with a variety of new systematic effects, almost all dependent on the quality of the magnetic environment for the measurement. In particular, so-called geometric phases due to any kind of magnetic field gradients are crucial. The temporal stability of the magnetic field on a level of Femto-Tesla over few 100 s is measured with the co-habiting magnetometer gas, initially ^{199}Hg vapor in our approach. To properly determine the spatial distribution of the magnetic field, an additional array of Cs magnetometers is deployed to characterize the magnetic field on a level of 10^{-4} relative homogeneity online. Such a homogeneous field is difficult to achieve in an ultra-low field NMR experiment at Micro-tesla magnetic fields, as this is a superposition of a generated field with residual fields stemming from magnetic shielding material surrounding the actual measurement.

In 2013, the outer magnetic environment of the neutron EDM experiment was installed at the EDM beam position in the east hall of the FRM II, providing one of the world's best magnetically shielded environments with unprecedented gradients of 0.1 nT/m over a typical length scale of 1 m. This environment is a combination of a non-magnetic concrete pit in the east hall, an external field stabilization oil system with 24 correction coils of 9 x 6 x 6 m dimension and a passive magnetic shield. A typical field map of the inner volume of the experiment is shown in figure 13, measured with SQUID magnetometers from PTB Berlin.

In parallel with the development of the fields, another development in 2013 was the measurement of the free precession decay of SEOP polarized ^{3}He and ^{129}Xe in the shielded environment with T2*-times exceeding 10000 s. SEOP polarization by groups at TUM, PTB Berlin, JCNS and FRM II (HELIOS) were all used for these tests. While the performance of the ^{199}Hg co-magnetometry system could at this point provide a precision that would limit a false effect to 10^{-27} ecm, the implementation of the Cs magnetometer array and the final inner magnetic environment is ongoing. Tests of the UCN relevant components, ultimately with spin-precession measurements, are being scheduled at the ILL Grenoble for 2014.

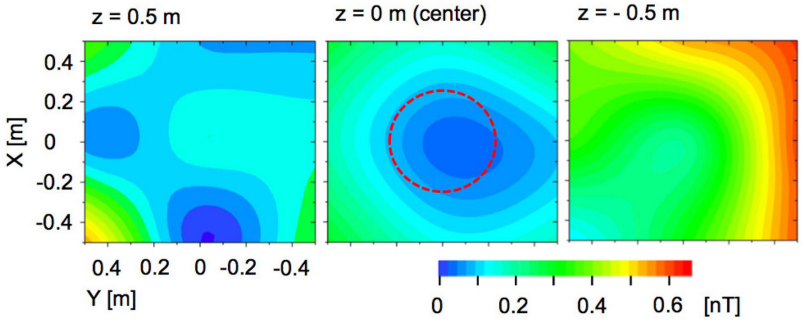

Figure 13: Horizontal cuts through the magnetic residual field in the EDM experiment region. The red dotted circle denotes the size of the actual measurement chambers.

Service groups supporting the instruments

P. Link[1], S. Masalovich[1], K. Zeitelhack[1], J. Peters[1], N. Arend[2], J. Krüger[1], H. Wenninger[1], J. Wuttke[2], J. Pulz[1], H. Reithmeier[1], J. Neuhaus[1]

[1]Heinz Maier-Leibnitz Zentrum (MLZ), Technische Universität München, Garching, Germany

[2]Jülich Centre for Neutron Science at MLZ, Forschungszentrum Jülich GmbH, Garching, Germany

The service groups at MLZ support the instrument teams and the scientific users in various fields. The Neutron Optics group is responsible for the neutron guide system and is active in various areas of instrument development and experimental support. The Detector group offers broad support in terms of the maintenance and service of detectors, electronic components and also detector development. The Sample Environment group ensures that the appropriate equipment such as magnets, cryostats and furnaces are available for the successful outcome of an experiment. The Project group coordinates projects and tasks for the commissioning and development of the instrument suite in respect of electronics, detectors, mechanical engineering, and control software. The Instrument Control group guarantees the smooth operation of the instruments and assists with data flow control and data storage. The Scientific Computing group supports by developing and maintaining data analysis software. The IT Services build and maintain the IT network and operate central services for data storage and communication. The Infrastructure group deals with coordination, planning and construction projects.

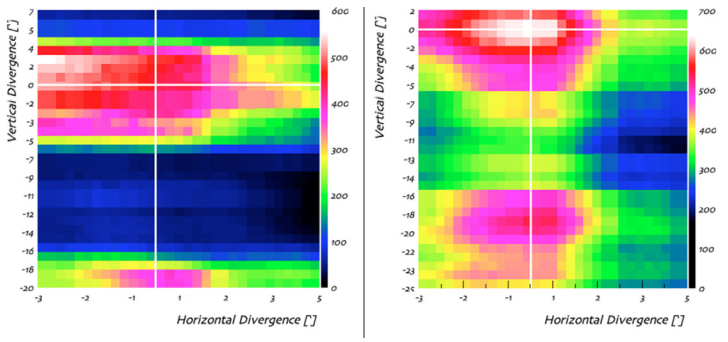

Figure 1: Intensity matrix measured before the mirror (11m away from the last guide) of KWS-3 before and after upgrade of the S-guide system. By x- and y-movement of the He-3 monitor (5 x 5 mm²) we were able to measure horizontal and vertical divergence of the beam leaving the guide system.

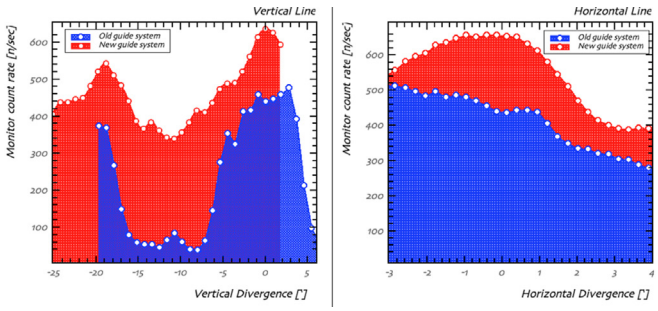

Figure 2: Slices, corresponding to white lines in figure 1.

Neutron guides for new and improved instruments

In preparation for the relocation of the instrument Mephisto to the Neutron Guide Hall East, the Neutron Optics Group completed the production of the required neutron guides. The 40 m guide, which is planned to be installed at beam tube SR4b, consists of 20 elements with a section of 50 mm × 106 mm bend on a radius of 3000 m. The m = 2.5 supermirror coating (total area ~ 13.2 m²) has a state of the art reflectivity at m = 2.5 of 90 ± 2 %. The guide, which is now ready for installation, will be set up inside an external vacuum housing.

In addition to this long-planned production, a number of replacement guide elements were built in-house over the course of the year. For example, the instrument KWS-3 situated on guide NL3a-u-S was given an incident neutron flux boost of a factor 4 to 5 after the replacement of the complex 3-fold beam splitter NL3a. A preceding endoscopic visual inspection had shown that parts of the beam splitter were damaged. Calculation of the fluence into the substrate showed the failure to be most likely due to irradiation of the thin borofloat substrate glass-plate bend on the extremely small r = 30 m radius. Therefore the replacement beam-splitter was built using

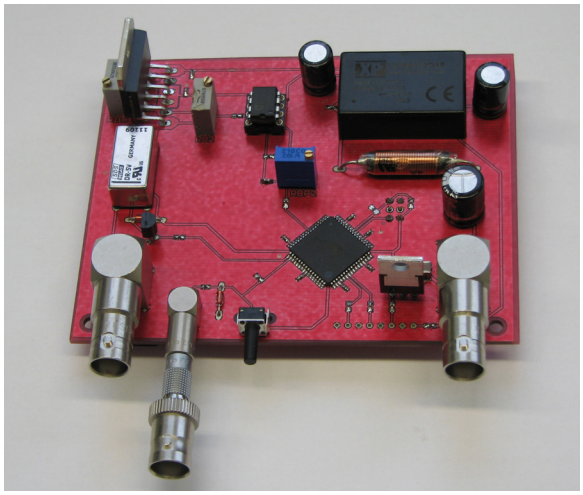

Figure 3: The electronic circuit of the AFP ^{3}He spin-flipper built at the Neutron Optics group.

Boron free float glass. Analysis of the KWS-3 incident beam after installation of the new beam splitter shows not only the tremendous gain in intensity, but also improved illumination uniformity (see fig. 1, 2).

Our efforts to improve the reliability of the neutron guide system were continued with the replacement of 20 m of the NL6-S guide by elements with increased side plate thickness for better mechanical stability. The guide element replacement has been used to upgrade the neutron transport properties of the guide by changing the originally ^{58}Ni coated guide to a supermirror m = 2 coated one, which has resulted in a substantial flux gain of almost a factor 2 at the instruments Mira-2 and DNS.

HELIOS – polarized ^{3}He gas for neutron polarization analysis

In 2013, HELIOS provided cells with a polarized ^{3}He gas for the instruments POLI, SANS-1, MIRA, RESEDA and MEPHISTO. At the instrument PUMA a first feasibility test of neutron polarization analysis using polarized ^{3}He cells was successfully performed. ^{3}He gas polarized at HELIOS was also implemented for the test and adjustment of the magnetic field homogeneity at the instrument EDM in the Neutron Guide Hall East and the long precession time was first demonstrated.

With the aim of extending the capabilities of the cells with polarized ^{3}He gas, a new adiabatic fast passage (AFP) spin-flipper for ^{3}He cells was developed and built. This radio-frequency device with its compact electronic circuit (see fig. 3) can be integrated into a ^{3}He neutron spin filter setup and thus offer a neutron spin flip with a very high efficiency. The measured flipping efficiency of the very first ^{3}He spin-flipper built on site was shown to be F = 0.99991.

Improving neutron detection

The backbone of the data acquisition hardware for single neutron detectors at all TUM instruments is formed by a DAQ-board in cPCI/ PCI standard for all kinds of counting or time resolved applications. A new generation of DAQ board based on a mother board plus m-module architecture has been developed. This makes it possible to adapt the design easily to each individual instrument and will now successively replace its predecessor.

The new detector system of SAPHiR

In 2013 the detector group embarked on a new large scale detector project. The design of the detector system for the new SAPHiR instrument, which provides extreme pressure and temperature environments for Time-of-Flight neutron diffraction, will combine the use of two different detector technologies. The rear detector bank of SAPHiR will consist of four scintillation detector modules with wavelength-shifting fibres developed by the Forschungszentrum Jülich detector group. The forward and the two 90° detector banks will be built by curved arrays of 640 horizontally mounted position sensitive ^{3}He tubes developed by the TUM detector group. The tubes are of 8 mm diameter and 40 cm active length. They are filled with 20 bar ^{3}He gas, which was chosen as the optimum fill pressure resulting from test measurements studying tubes with a fill pressure up to 30 bar. The localisation of the neutrons is undertaken by the method of charge division along the wire. The pulse processing front end electronics is placed directly behind

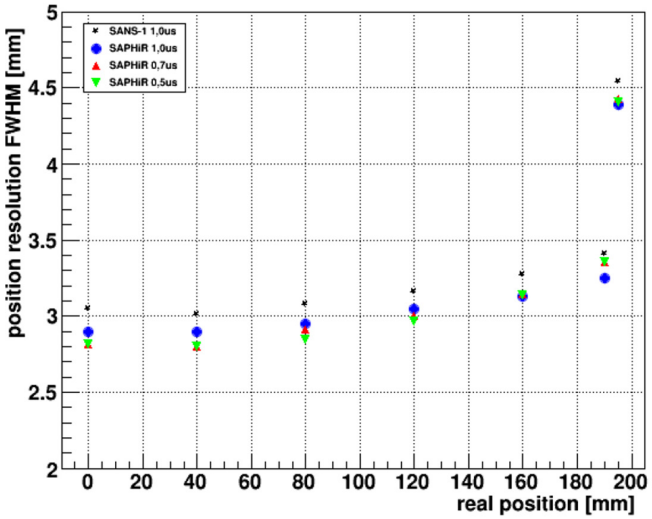

Figure 4: Position resolution (FWHM) as function of the position along the tube axis achieved with the prototype readout system for shaping times of τ = 0.5, 0.7 and 1.0 µs.

the detector and connected via bus signals to data acquisition modules providing position, amplitude and time stamp in list mode.

In test measurements performed at TREFF, a first version of the commercial readout system was studied with prototype ^{3}He tubes to determine the optimal parameters of the front end electronics. Figure 4 shows the achieved position resolution as a function of the position along the tube axis for shaping times of τ = 0.5, 0.7 and 1.0 µs. In December 2013 all 640 ^{3}He-tubes were evaluated in a dedicated measurement campaign to establish efficiency, position resolution and homogeneity. Figure 5 shows a photograph of 16 ^{3}He-tubes mounted in a module placed on the precision X-Y linear stage of the detector test bench at TREFF.

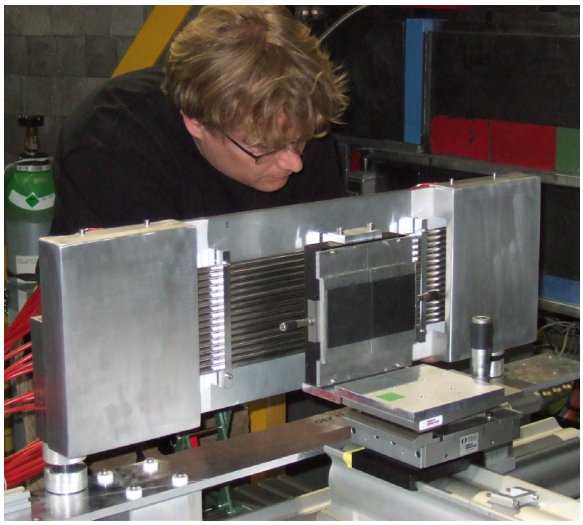

Figure 5: A module with 16 position sensitive ^{3}He-tubes destined to be used at SAPHiR during a test with collimated neutron beam at TREFF. Currently, the qualification of all tubes and the corresponding readout electronic modules recently arrived as well as the mechanical design of the detector is in progress.

New sample environment provided

The 5 Tesla SANS-Magnet, manufactured by Oxford Instruments, was set into operation at the Small Angle Neutron Scattering Instrument SANS-1 (fig. 6). First user experiments have been performed successfully. Both operational field modes, symmetric and asymmetric, allow for experiments using non-polarized and polarized neutrons. Some further work has to be done to integrate the system into the MLZ Instrument control software TACO/TANGO. The 80 mm room temperature bore (RTB) provides a broad range of different experimental applications such as low temperature, high temperature or pressure cells etc.

To allow for temperatures down to 3 K, a new dedicated top loading refrigerator (CCR) has been developed based on the FRM II type CCR. Different sample sticks are available. An assembly robotics helps to avoid damage to the CCR and magnet when assembling the experimental setup. Furthermore, our long tailed Closed Cycle Cryostat developed for the 7,5 T magnet has been modified to fit into the SANS Magnet RTB.

The design of the spherical high temperature furnace dedicated for the instrument POWTEX has been completed. The sophisticated laser heating system minimises undesirable background scattering and shadowing. All parts and components have been manufactured. The assembly of the parts and tests began at the end of 2013 .

Coordinating efforts for instrument development by the Project group

The Project group at MLZ, established at the end of 2012, is responsible for coordinating projects

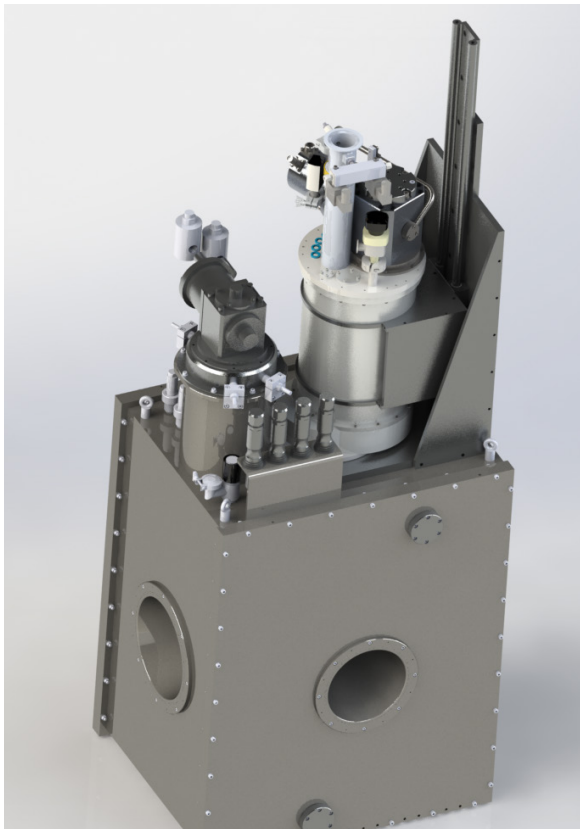

Figure 6: SANS Magnet with dedicated CCR and mounting/lifting device.

and tasks for the commissioning and development of the instrument suite in the fields of electronics, detectors, mechanical engineering, and control software. The establishment of the group was a matter of urgency as important resources in terms of electronics and engineering are based outside the MLZ. The main collaborators since then have been the Central Institutes for Engineering and Electronics (ZEA-1 and ZEA-2) of the Forschungszentrum Jülich GmbH in Jülich, the instrument control group of the FRM II and JCNS IT.

The Project group is the first contact for instrument scientists and MLZ management in the event of larger scale projects at the instruments being planned. In the first step the Project group prepares a conceptual design in close collaboration with the instrument team. This comprises targeted improvements compared to the current state, a specification sheet, and a rough plan with timelines, manpower, and cost. A proposal for a project team and a project coordinator is also included. This concept is presented by the project office to the MLZ directorate for approval. The directorate comes to a decision based on the financial resources available and priority as compared to other projects. The progress of the project is tracked via regular reports from the project coordinator and the project office. In this way, the group is working toward the standardization of both hardware and software components deployed across MLZ.

In April 2013 it was decided that the MLZ partners, TUM/FRM II, HZG and JCNS, should join forces in developing common instrument control software. Aside from synergy effects, this will provide scientific users with a common user experience across instruments at MLZ. NICOS (Network Integrated Control System), the control software project developed at FRM II more than a decade ago, was chosen and is now contributed to by software developers from TUM, ZEA-2, and JCNS.

Recently, the most noticeable and extensive projects have been

- Electronics of the ANTARES neutron imaging facility
- POLI/HEIDI hot neutron diffractometers
- Working towards the goal of making the instrument control software NICOS the MLZ-wide standard, especially at the JCNS instruments
- Upgrades for KWS-1 SANS diffractometer
- Computer software/hardware standardization, new administration and maintenance concept
- Development of a concept for an EMC-compliant layout of the new Neutron Guide Hall (East) and its instruments

The first FRM II instrument supported by the project group was the neutron imaging facility ANTARES. In cooperation with the instrument team and local support groups, ZEA-2 implemented the instrument electronics. NICOS became the instrument control software, with the hardware

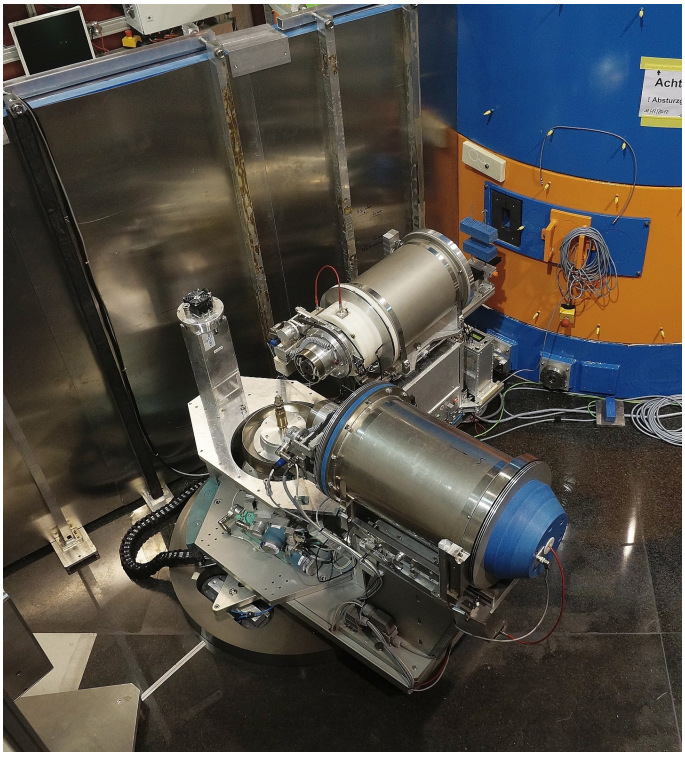

Figure 7: The recently commissioned instrument POLI in the Experimental Hall. Until the end of 2013 POLI shared a beam port with the diffractometer HEiDi. Therefore, not only did essential components such as the monochromator have to be newly designed and controlled, but the entire safety concept had to be implemented.

access layer being TANGO, following the newly developed facility-wide software interface definition.

The hot neutron diffractometers POLI and HEiDi previously shared a common beam port. The project of separating the two instruments required the development and implementation of new neutron optical components (e.g. monochromator), motor and shutter control, an independent safety concept for POLI. The project was completed by the end of 2013 and POLI delivered the first neutrons in February 2014 (see fig. 7).

The JCNS Small Angle Neutron Scattering diffractometer KWS-1 received upgrades for polarization capability including a revolver system to switch between measurement modes. Furthermore, a lens system to improve neutron flux and resolution by beam focusing and a chopper system for Time-Of-Flight-resolved measurements have been installed.

From 2013, the instrument control computers at JCNS instruments are being replaced with common, more fail-safe hardware including an extensive spare part pool. With the Linux Enterprise Operating System CentOS 6 a new standard was defined. In addition, the software administration and maintenance approach was changed to a centralized repository providing all necessary and requested software packages for the instruments.

In response to electromagnetic interference problems with detector systems in the Neutron Guide Hall West, a project was launched to prevent similar issues in the new guide hall currently under construction. Two external experts will be entrusted with the development of specifications and guidelines for the building infrastructure layout and instrument installation.

Common instrument control software at MLZ

The main activities of the instrument control group during the last year cover the ongoing development of the instrument control software NICOS, the introduction of a professional development environment and workflow as well as the extension of embedded system based solutions (TACO box).

NICOS

Following the decision to establish the NICOS instrument control suite as standard for all instruments at the MLZ, the development was intensified in 2013. With over 1200 individual reviewed patches, fixing several bugs, and providing dozens of requested new features from instrument scientists and sample environment groups, the NICOS development proceeded at a fast pace. In order to maintain a stable release of NICOS only critical bug fixes are installed during reactor operation. This led to quarterly releases of new versions in 2013, resulting in no loss of beamtime due to a malfunction of NICOS. Now the support for TANGO (successor of TACO) devices, mainly used at ANTARES, is included. A major revamping of the graphical user interface (GUI) was completed as well as support for

special Beckhoff PLC devices being added. The rewriting of the data storing and metadata management paves the way for compliance with anticipated EU-wide standards such as ICAT.

ANTARES instrument goes online with NICOS
When ANTARES (fig. 8) was rebuilt, it was the first instrument converted to and is now fully working with NICOS. Moreover, we supported the ANTARES team with the setting up of its magnet and providing additional support software to ensure it could also be used reliably at other instruments or institutes (such as PSI).

Professional development environment and workflow
NICOS has been developed in an agile, continuous deployment scheme since 2013. The source code is managed in a source code management system (SCM) called “Git”. Each code change has to pass our new code review tool (the more eyes the better) called “Gerrit” and is interconnected to our tool for agile bug and ticket tracking, called “Redmine”. Finally, an integrated test suite (“Jenkins”) has to be passed. Using this environment makes for far more agile and structured code writing and testing, which leads to high stability and improved quality of the code.

Embedded system based solutions (TACO-Box)
Based on the flexibility needed at and by the instruments, performing experiments in frequently changing configurations, it is crucial to have highly modular, robust and easily integrateable special function ‘blocks’. A typical example is the sample environment, which can be used on many different instruments. In recent years, the TACO-Box concept was developed and in the last year refined to a new level of integration. We created and are now deploying auto detection capabilities into the NICOS platform, so that a freshly attached mobile environment is almost instantly detected by the control software and all required internal control connections designed to be able to use this equipment.

Based on the very positive experience of using this concept, we now also use the famous Raspberry Pi embedded computers as a control platform, where applicable. These embedded devices have more than enough computing power to handle the communication between the control electronics of such modular blocks and the instrument control software via our standardized TACO/TANGO interface. Also, it is easy to integrate those small devices within the control racks housing the electronics, keeping everything grouped together to facilitate movement from instrument to instrument.

Closer cooperation
with the sample environment groups
To provide stable solutions for our sample environments with software and hardware working together properly, the groups responsible needed closer cooperation. There is now a weekly collaboration meeting, not only between the FRM II instrument control group and the FRM II Sample Environment group but also with our partners from the Project group.

New organizational software at FRM II

Founded in the summer of 2012, the Organization Software group is one of three IT Service groups at the FRM II. Currently the group has two members.

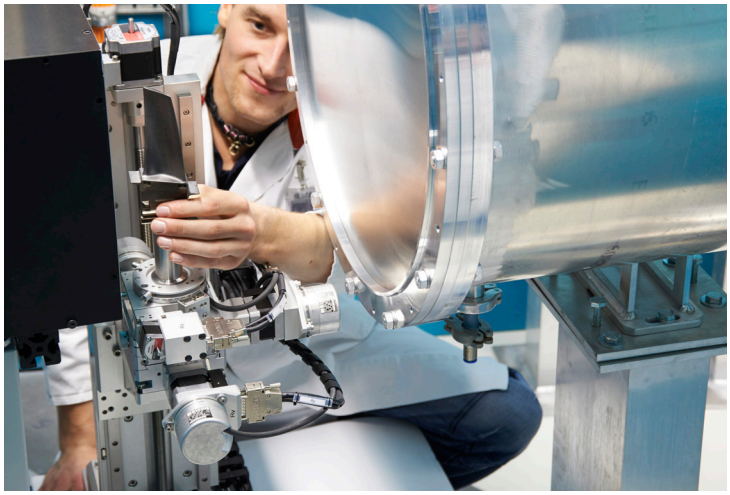

Figure 8: Instrument ANTARES is equipped with NICOS instrument control software.

Although it is formally new, as a part of the IT Services it has for many years been providing applications for staff and users of the FRM II.

One of the software products is the "Organization Software", which was developed during 2013. The aims of the program are to support a uniform, user-friendly interface to login, obtain information about user rights and run several organizations' programs at the same time.

The most important part of the "Organization Software" is the DORIS-application (Dokumentations-, Rückverfolgungs- und Informationssystem). This comprehensive software solution provides services for the operational division of the FRM II, which includes the tracking of recurring checks and the life cycle of the technical equipment. Beginning with DORIS1 in 2003 the system was later modernized to DORIS2. In 2013, DORIS2 was separated into two parts, namely quality management (QS) with master data and recurring checks (WKP) – DORIS3, respectively.

DORIS3 is a completely new system. It is better adapted to the current workflow used at the FRM II and has a more advanced database system. Furthermore, DORIS3 provides search and scheduling facilities and enables the fast creation of reports.

Among other things, the Organization Software group has developed and currently supports the following software:

- the reactor cycles ("Zyklen")
- the archive database ("Archiv-Datenbank")
- the personal database for radiation protection ("Strahlenschutz-Personal-Datenbank")
- the software for the FRMII identification office (Ausweisbüro)
- for the sentry and technical services (Warte and TD)
- digital user office

Further developments of data analysis software

The Scientific Computing Group at MLZ supports instrument scientists and users by developing and maintaining data analysis software.

BornAgain

The first large project of the Scientific Computing Group is the development of BornAgain, a software to simulate and fit grazing-incidence small-angle scattering (GISAS) using the distorted-wave Born approximation. By developing BornAgain, we are responding to user needs at the MLZ reflectometers MARIA and REFSANS as well as supporting in-house research in magnetism and soft matter and serving the GISAS community at large. The software is not limited to neutrons (GISANS) but also supports X-ray scattering (GISAXS).

The first major version of BornAgain almost fully reproduces the functionality of the hitherto standard program IsGisaxs (R. Lazzari), supports parallel multiprocessor computing, and provides unprecedented flexibility in the composition of the sample model. It has been successfully applied to experimental data; first publications are in preparation. Figure 12 shows a GISAXS image of a complex nanoparticle assembly and the result of a BornAgain simulation. The excellent match was achieved using a meso-crystal ensemble statistics model (E. Josten, A. Glavic; to be published), fitted to the experimental image using twelve free parameters.

The next major version of BornAgain will come with full support for polarized neutrons. Prior to the implementation, considerable theoretical developments were necessary. A graphical user interface (GUI) is also under development.

Other Highlights

Whenever possible, our software is composed of standard open-source components. Where such components do not yet exist, we contribute back to the open-source community by publishing our own solutions as separate modules. Specifically, we implemented an efficient high precision com-

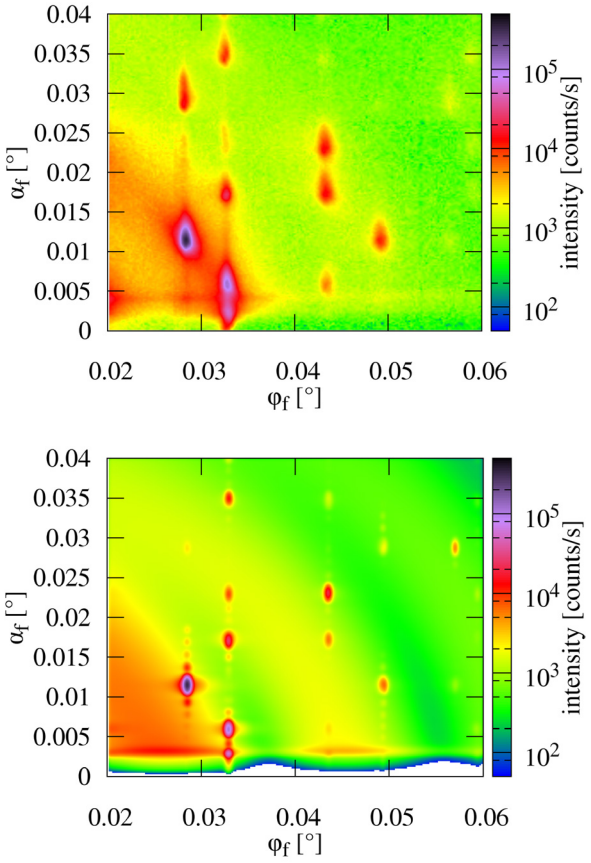

Figure 9: GISAXS data form nanoparticle assembly (top, E. Josten, A. Glavic;to be published) and BornAgain simulation after a 12-parameter fit.

putation of the Fourier transform of the stretched exponential, often used to fit soft matter spectra, and we packaged a C library providing complex error functions, Dawson's integral and Voigt's convolution of a Gaussian and a Lorentzian, which is currently under review for inclusion in Debian.

We are involved in discussions on data analysis methodology, and we contribute to simulation-based instrument improvements. A theoretical study of generalized Darwin-Hamilton equations improves our understanding of neutron deflection by mosaic crystals and will help in future neutron optical optimizations.

Future Directions

Next on our agenda is support for the time-of-flight spectrometers at MLZ: TOFTOF, DNS and TOPAS (in construction). We are currently investigating to what extent we meet requests by adapting existing software from other facilities.

We are in close contact with computing groups at other neutron facilities, in particular the ILL, ISIS, and the ESS. We will coordinate future projects to avoid duplication of work. In all likelihood, we will assume leadership for the consolidation and curation of reflectometry software, as a natural extension of our current involvement with GISAS. In exchange, for some other classes of neutron instruments, we will rely on software maintained by other facilities.

Challenges for extending IT-Services

Due to the increase in office and laboratory space, we had to extend our network infrastructure into the premises of the „Max-Planck-Institut für Plasmaphysik" (IPP). Thanks to our very good cooperation with the „Leibniz-Rechenzentrum" (LRZ) and the „Rechenzentrum Garching" (RZG) of the „Max-Planck-Gesellschaft & IPP", we were able to integrate the rented rooms seamlessly into our infrastructure and provide the same connectivity as on site.

In order to begin realizing the long-standing plan of providing single sign-on (SSO) capabilities to the users of our central services, we renewed our authentication backend cluster. All four machines involved have undergone a major hardware, operating system and software update and are now additionally equipped with the Heimdal implementation of Kerberos 5.

The first services were reconfigured to make use of the new authentication mechanism that is provided alongside all previous available mechanisms.

Given the increasing number of employees, collaborators and projects over the last years, the necessity for a central groupware system evolved. Besides well-known groupware functionality such as email, calendar, tasks and notes the system has to provide synchronization capabilities for different client systems and has to fit into our server and authentication infrastructure. We tested and evaluated several systems and finally decided to use Horde Groupware which is

a browser based collaboration and communication system.

In an effort to reduce the number of physical server machines and consequential charges and to make efficient use of today's server resources, we have converted and migrated about 75 % of our Microsoft® Windows® Server installations into virtual machines. The hypervisor of choice is VMware® vSphere® 5.1 that, besides many other features, offers reliability, performance, easy management and high availability. Together with this infrastructural change, we prepared a major update for our Terminal Server farm and scheduled the final migration for early 2014.

For easier updates and software installations on client computers, we started to operate a Microsoft® System Centre Configuration Manager (SCCM). A lot of effort was put into the preparation of packages for standard software. These are used to preload new computers, for automated roll-out or are self-installed by our users. Using this method of software distribution, nowadays we install about 80 % of all programs on client computers in a standardized way. In the overall process of standardization and to reduce the time needed for (re)installing computers, we severely reduced the number of desktop- and mobile computer system flavours. Due to this endeavour, we are now able to use pre-configured operating system images to set up about 95% of our client computers. In order to make use of these centrally hosted and continuously updated images, we extended our already existing PXE boot service. With the imminent end of extended support for Microsoft® Windows® XP and Microsoft® Office 2003 on 8th April 2014, we aim to get rid of almost all remaining machines by the end of April 2014.

Infrastructure group paves the way to expanding MLZ instrumentation

As a current major project of the Scientific Infrastructure group, the structural connection of the new Neutron Guide Hall East has to be emphasized. We would like to highlight here the execution of construction work for the new building connecting the Experimental Hall and Neutron Guide Hall East, which is presently close to being finished. Some of this construction work is shown in figures 13 to 16.

Throughout this project, the task of the Scientific Infrastructure group was to carry out and coordinate the planning, and to supervise the executive construction companies during the execution of the construction work, ensuring in particular compliance of all construction work with the operational guidelines and with the legal requirements of the Atomic Energy Act.

As an ongoing task the coordination of the build-up of instruments in the new Neutron Guide Hall East has continued. The placement of the instruments according to the neutron and positron beams has been finalised and further details on the usage of the ever limited space in the hall re under discussion. A detailed 3D model of the instruments and beams is maintained by our group. It will be extended to the Experimental Hall as well as to the Guide Hall West in order to facilitate more detailed planning for the Neutron Optics group.

In order to prepare for the transmission of neutrons to the new Neutron Guide Hall East, the shutter of SR5 has to be replaced. Working in close collaboration with the engineering group of FZJ (ZEA-2), the design of the new shutter has been completed, which will allow three as opposed to two neutron beams to be extracted from beam tube SR5. The shielding on the adjacent guide tunnel has been constructed to bridge the shutter to the exit of the Experimental Hall.

Together with the exchange of the beam plug of the through-going beam tube SR6 for the future use of the ultra-cold neutron source, the concept of waste disposal of heavy components of the shutter of SR5 is under way. The necessary expertise has been built up in our group to support and manage radioactive waste disposal of the scientific instrumentation at the FRM II.

Figure 13: Preparation of the construction zone between the Experimental Hall and the new Neutron Guide Hall East with wall elements already deinstalled.

Figure 14: Removal and reconstruction of concrete base for provision of a new entrance from the Neutron Guide Hall East to the new building connecting the Experimental Hall and Neutron Guide Hall East.

Figure 15: Built-up of wall elements.

Figure 16: View into the new building connecting the Experimental Hall and Neutron Guide Hall East after concreting work. The new entrance from the Neutron Guide Hall East to the new connecting building can be seen after the access door had been installed (compare to fig. 14).

Lens for the in-situ polarizer at the instrument MARIA.

Scientific Highlights

3

Topological unwinding of a Skyrmion lattice by magnetic monopoles

P. Milde[1], D. Köhler[1], J. Seidel[2], L. M. Eng[1], A. Bauer[3], A. Chacon[3], J . Kindervater[3], S. Mühlbauer[4], C. Pfleiderer[3], S. Buhrandt[5], C. Schütte[5], A. Rosch[5]

[1]Institut für Angewandte Photophysik, Technische Universität Dresden, Dresden, Germany

[2]School of Materials Science and Engineering, University of New South Wales, Sydney, Australia

[3]Physik-Department E21, Technische Universität München, Garching, Germany

[4]Heinz Maier-Leibnitz Zentrum (MLZ), Technische Universität München, Garching, Germany

[5]Institut für Theoretische Physik, Universität zu Köln, Köln, Germany

Skyrmion lattices in chiral magnets can be regarded as macroscopic lattices formed by topological entities with particle-like properties where the particle-like character of the Skyrmions is reflected in the integer winding number of their magnetization. Due to their topology, Skyrmions cannot be destroyed or created by smooth deformation of a trivial spin texture. We use magnetic force microscopy in combination with numerical simulations and small angle neutron scattering to study the topological unwinding of Skyrmion lines in a bulk crystal of $Fe_{1-x}Co_xSi$ (x = 0.5). Our study shows that the Skyrmion lines decay by means of point defects which act in a way similar to the slider of a zipper. We show that these point defects can be regarded as quantized magnetic monopoles of emergent magnetic flux [1].

Skyrmions: Topological protection & particle-like properties

Two objects or configurations are topologically different (they belong to a different homotopy group) if there exists no continuous transformation of one configuration into the other without cutting or gluing [2]. The same applies to Skyrmions: The concept goes back to Tony Skyrme, who succeeded in describing the constituents of the nucleus – protons and neutrons - as particle-like excitations with non-trivial topology that emerge in the presence of non-linear excitations [3]. Recently, Skyrmionic matter has also been observed in a completely different context: Materials exhibiting helical magnetic structures such as MnSi [4], $Fe_{1-x}Co_xSi$ [5] or Cu_2OSeO_3 [6] show peculiar spin textures with non-trivial topology, characterized by an integer winding number of -1. These Skyrmion lines can be seen as magnetic whirls – akin to vortices in type II superconductors – with particle-like properties, oriented parallel to a small external magnetic field (fig. 1 A). Due to their topology, these magnetic Skyrmions cannot be destroyed or created by a smooth deformation of a trivial spin texture - such as a ferromagnet. A similar idea applies to magnetic domain walls, which are examples of planar topological defects in two dimensions.

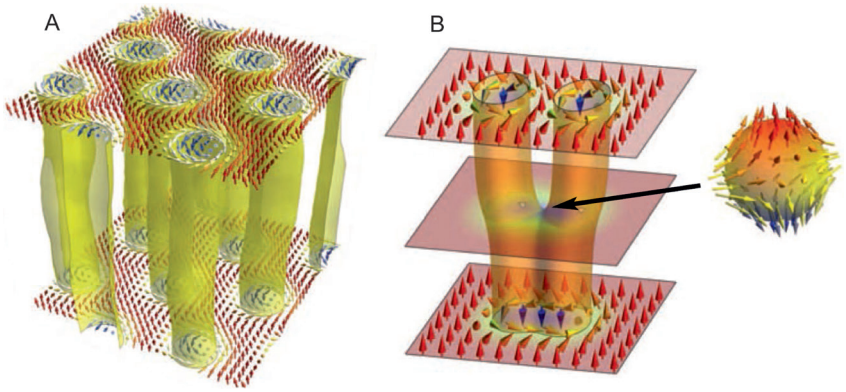

Figure 1: Panel (A): Typical spin configuration of the Skyrmion lattice of $Fe_{1-x}Co_xSi$ for x=0.5 obtained by Monte Carlo simulations. Panel (B): Schematic depiction of the merging of two Skyrmion lines. At the merging point the magnetization vanishes (arrow). The point defect can be seen as emergent magnetic antimonopole, acting like a zipper merging two Skyrmion lines [1].

Skyrmion lattices – regular crystalline arrangements of Skyrmion lines found in chiral magnets provide an excellent showcase for the investigation of topological stability and phase conversion. We combine magnetic force microscopy (MFM) with numerical Monte Carlo (MC) calculations and small-angle neutron scattering (SANS) [1] to investigate the topological stability and decay of Skyrmions in the B20 helimagnet $Fe_{1-x}Co_xSi$ (x = 0.5) [1].

Skyrmion decay in $Fe_{1-x}Co_xSi$ (x = 0.5)

With a typical length scale of ≈ 90 nm, the Skyrmion lattice of $Fe_{1-x}Co_xSi$ (x = 0.5) is large compared to the resolution of MFM; however the bulk information is still accessible using SANS. Moreover, the possibility of undercooling the Skyrmion lat-

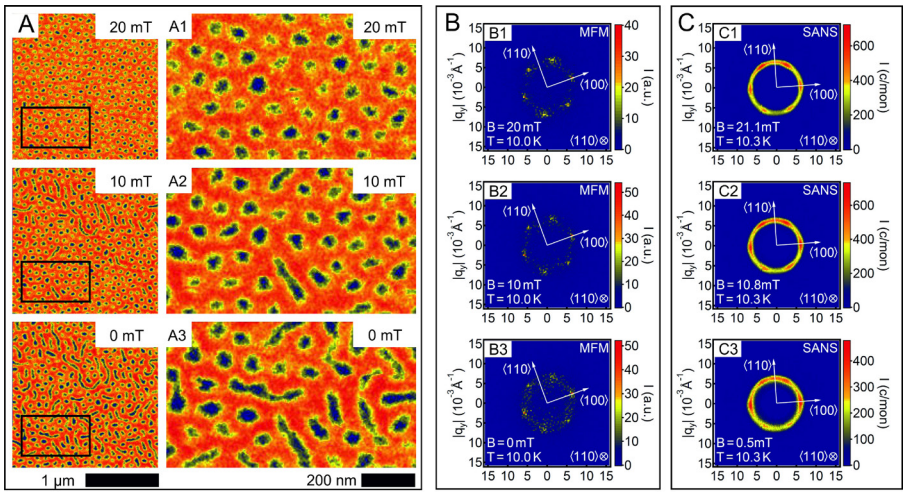

Figure 2: Panel (A): Typical MFM data of $Fe_{1-x}Co_xSi$ for x = 0.5 for different magnetic fields. The data is recorded after cooling in a magnetic field of 20 mT to a temperature of 10 K (A1), followed by a magnetic field ramp to 10 mT (A2) and 0 mT (A3). The magnetic field is aligned perpendicular to the surface of the sample. Panels (B1) to (B3) show the Fourier transform of the real space MFM data. Panels (C1) to (C3) show corresponding SANS data for the same sample following a similar temperature and magnetic field protocol [1].

tice phase of $Fe_{1-x}Co_xSi$ (x = 0.5) from T_c = 45 K to a metastable state at low temperature allows one to study the generic mechanism of the topological unwinding without the dominating influence of thermal fluctuations close to T_c.

Typical MFM data for different magnetic fields is shown in figure 2(A). Data is recorded after cooling from T_c in a magnetic field of 20 mT to a temperature of 10 K (A1), followed by a magnetic field ramp to 10 mT (A2) and finally 0 mT (A3). The magnetic field is aligned perpendicular to the surface of the sample. It is clearly visible that individual skyrmions (as indicated by the blue spots) form a well-ordered Skyrmion lattice at 20 mT. Decreasing the field in this metastable state leads to a coalescence of Skyrmions which finally form elongated structures. Panels (B) of figure 2 show the corresponding Fourier transforms of the real space MFM data, confirmed by typical SANS patterns obtained on the same sample following an identical magnetic field and temperature protocol (panel (C)). The agreement with bulk sensitive SANS data, obtained on SANS-1 at MLZ clearly proves that the surface sensitive MFM captures the essential features of the topological unwinding of Skyrmions in $Fe_{1-x}Co_xSi$ (x = 0.5) in this bulk sample.

With the help of classical MC simulations on a 42 x 42 x 30 spin system, the mechanism behind the coalescence of Skyrmion lines could be examined in closer detail. Typical MC data is shown in figure 1 panels A and B. As the field is reduced, transverse fluctuations of the Skyrmion lines grow until individual Skyrmion lines touch and merge. Due to the topological charge or winding number of the Skyrmions, the point of coalescence necessarily carries a quantized emergent magnetic charge which can be interpreted as “emergent magnetic monopole” [1]. Two different processes can be identified: (i) The Skyrmion lines merge at the surface of the sample, an emergent (anti)monopole enters the sample through the surface. (ii) The point of coalescence can be located in the bulk of the sample, corresponding to monopole/ antimonopole pairs moving towards the surface. However, there is a finite linear potential (string tension) holding the monopole and antimonopole pair together. During phase conversion, the string potential vanishes and eventually becomes negative.

As interesting open question remains as to whether deconfined emergent monopoles exist as independent entities in chiral magnets. A promising candidate may be the unconventional non-Fermi liquid properties of MnSi under high pressure [7,8].

[1] P. Milde et al., Science 340, 6136, (2013).
[2] N. Manton et al., Topological Solitons, Cambridge Univ. Press, Cambridge (2004).
[3] T. Skyrme, Nucl. Phys. 31, 556 (1962).
[4] S. Mühlbauer et al., Science 323, 915 (2009).
[5] W. Münzer et al., Phys. Rev. B 81, 041203(R) (2010).
[6] S. Seki et al., Science 336, 198 (2012).
[7] C. Pfleiderer et al., Nature 414, 427 (2001).
[8] R. Ritz et al., Nature 497, 231 (2013).

Novel magnetic orders and spin-glass-like phase in $Na_3Co(CO_3)_2Cl$

Z. Fu[1], Y. Zheng[2], Y. Xiao[3], S. Bedanta[4], A. Senyshyn[5], G. Simeoni[5], Y. Su[1], U. Rücker[3], P. Kögerler[6], Th. Brückel[3]

[1]Jülich Centre for Neutron Science (JCNS) at MLZ, Forschungszentrum Jülich GmbH, Garching, Germany

[2]Frontier Institute of Science and Technology, Xi'an Jiaotong University, Xi'an, China

[3]JCNS-2, PGI-4: Streumethoden, Forschungszentrum Jülich GmbH, Jülich, Germany

[4]School of Physical Sciences, National Institute of Education and Research, Orissa, India

[5]Heinz Maier-Leibnitz Zentrum (MLZ), Technische Universität München, Garching, Germany

[6]Institut für Anorganische Chemie, RWTH Aachen University, Aachen, Germany

Pyrochlore magnets have been attracting intensive attention in the study of geometrical spin frustration and still hold surprises for exotic magnetic ground states. Neutron scattering technique is essential for a deep understanding of the complicated magnetic behaviour of frustrated magnets. Our research on pyrochlore antiferromagnet $Na_3Co(CO_3)_2Cl$ reveals a unique coexistence of novel magnetic orders and a spin-glass-like phase. Neutron powder diffraction on SPODI identifies a chemically-ordered cubic structure of the sample. Polarized neutron scattering on DNS confirms an all-in-all-out type of long-range magnetic order below 1.5 K. Inelastic neutron scattering on TOFTOF shows spin-wave-like excitations at 3.7 K, indicative of an unconventional spin glass transition at 4.5 K.

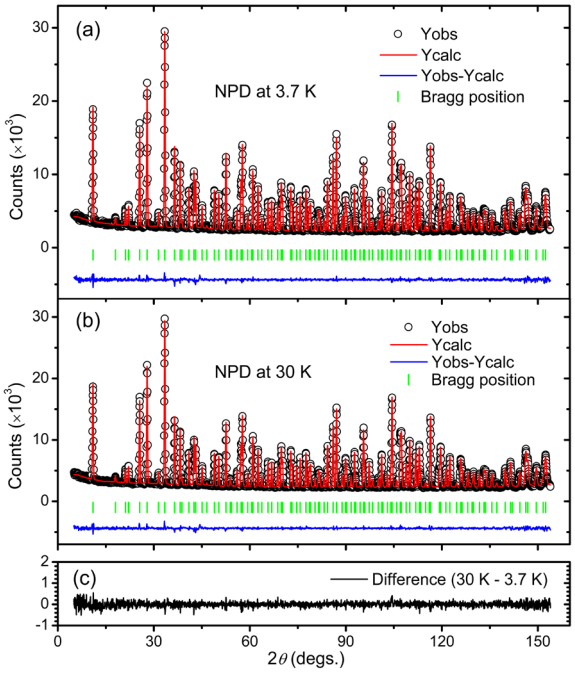

Figure 1: NPD patterns obtained at (a) 3.7 K and (b) 30 K with the Rietveld refinement. (c) Difference pattern between the data for 3.7 and 30 K.

Frustrated pyrochlore magnets have been attracting intensive attention owing to the new intriguing phases discovered, e.g., magnetic monopoles and Higgs transition in spin ice systems. [1,2] In antiferromagnetic pyrochlores, the high ground-state degeneracy can be lifted by perturbations from further-neighbour interactions, resulting in interesting magnetic behaviour. The formation of a spin-glass phase generally requires both chemical disorder and frustrated interactions. However spin-glass-like behaviour has been observed in a few examples of pyrochlore magnets which are chemically ordered. The origin of this spin-glass-like behaviour has not yet been understood.

A new spin-frustrated antiferromagnetic pyrochlore $Na_3Co(CO_3)_2Cl$ was discovered. The temperature dependence of AC susceptibility shows that $Na_3Co(CO_3)_2Cl$ undergoes a spin-glass-like phase transition at 4.5 K and exhibits collective magnetic behaviour at 17 K. The specific heat measured down to 60 mK reveals a long-range magnetic phase transition at 1.5 K. [3]

Neutron powder diffraction at SPODI

In order to identify the average crystal structure and possible atomic disorder in $Na_3Co(CO_3)_2Cl$, we performed neutron powder diffraction (NPD) on SPODI. The experimental NPD patterns for 3.7 and 30 K are shown in figure 1, together with the Rietveld refinement with the space group F d -3. Satisfactory refinement was obtained without introducing any magnetic contribution. No clear evidence for atomic disorders has been found within the resolution of SPODI.

Polarized neutron scattering at DNS

Diffuse neutron scattering with polarization analy-

sis was performed on DNS to detect short-range spin correlations and long-range magnetic order in $Na_3Co(CO_3)_2Cl$. The nuclear coherent, spin-incoherent and paramagnetic scattering contributions were separated unambiguously using the xyz-polarization method. Figure 2 shows the differential magnetic cross section $d\sigma_{mag}/d\Omega$ measured on DNS at various temperatures. At 50 mK, long-range magnetic order is evidenced by clear magnetic Bragg peaks superposed on the magnetic diffuse scattering. Symmetry analysis based on the representation theory shows an all-in-all-out spin configuration for the Co^{2+} spins (see the inset of figure 2).

An analytical simulation of short-range spin correlations in $Na_3Co(CO_3)_2Cl$ was carried out by attempting a least-square fit to the measured magnetic scattering cross section with the following Fourier transform of spin-pair correlation functions,

$$\frac{d\sigma_{mag}}{d\Omega} = \frac{2}{3}S(S+1)\left(\frac{\gamma e^2}{mc^2}\right)^2 f^2(Q) + \left(\frac{\gamma e^2}{mc^2}\right)^2 f^2(Q) \times \sum_{n=1}^{N} c_n \left[B_n \frac{\sin Qr_n}{Qr_n} + (2A_n - B_n)\left(\frac{\sin Qr_n}{Q^3 r_n^3} - \frac{\cos Qr_n}{Q^2 r_n^2}\right)\right].$$

The best fit was achieved when introducing dominating antiferromagnetic nearest-neighbour interactions and weak ferromagnetic next-nearest-neighbour interactions. The fitting results of the short-range spin correlations and the magnetic reflections are plotted as the blue line in figure 2.

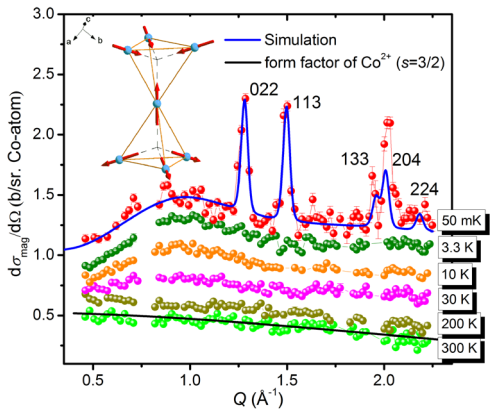

Figure 2: Temperature evolution of the differential magnetic cross section measured on DNS. Inset: Schematic representation of the all-in-all-out spin configuration of Co spins in $Na_3Co(CO_3)_2Cl$.

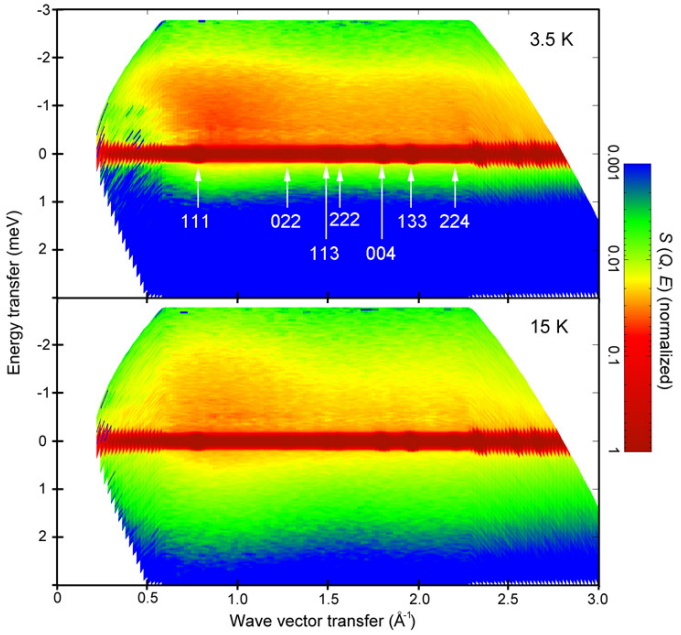

Figure 3: Contour plot of the dynamic structure factor S(Q, ω) of $Na_3Co(CO_3)_2Cl$ at 3.5 and 15 K.

Time-of-flight inelastic neutron scattering at TOFTOF

The spin dynamics of $Na_3Co(CO_3)_2Cl$ is explored by means of inelastic neutron scattering on TOFTOF. Figure 3 shows the contour plot of the dynamic structure factor $S(Q, \omega)$ at 3.5 and 15 K. The scattering intensity indicates a modulation due to the magnetic form factor and thus should be of magnetic origin. Spin-wave-like excitations can be seen centering at around 0.9 $Å^{-1}$ at 3.5 K, indicating that the transition at 4.5 K is not a conventional spin glass transition.

In conclusion, by means of extensive experimental investigations, we have revealed a novel coexistence of a long-range magnetic order, an intermediate partially-ordered magnetic phase, and a spin-glass-like phase, in one antiferromagnetic pyrochlore, $Na_3Co(CO_3)_2Cl$.

[1] D. J. P. Morris et al., Science 326, 41 (2009).
[2] L.-J. Chang et al., Nat. Commun. 3, 992 (2009).
[3] Z. Fu et al., Phys. Rev. B 87, 214406 (2013).

Change in interface magnetism of an exchange coupled system due to Au spacer

A. Paul[1], N. Paul[2], P. Böni[1]

[1]Physik-Department E21, Technische Universität München, Garching, Germany

[2]Heinz Maier-Leibnitz Zentrum (MLZ), Technische Universität München, Garching, Germany

We report on the effect of nonmagnetic spacer layers on the interface magnetism and the exchange bias in an archetypical $[Co/CoO]_{16}$ system [1]. The separation of the magnetic bilayers by Au layers with various thicknesses *d*Au ≥ 25 nm leads to a threefold increase in the exchange bias field (*H*eb). Reflectometry with polarized neutrons at the TREFF reflectometer does not reveal any appreciable change in the domain population. This result is in agreement with the observation that the granular microstructure within the [Co/CoO] bilayers is independent of *d*Au. A considerable proportion of the increase in Heb can be attributed to the loss of magnetization at each of the Co-Au interfaces with increasing *d*Au. We propose that the interfacial magnetism of ferro- and antiferromagnetic layers can be significantly altered by means of metallic spacer layers, thereby affecting the exchange bias significantly [2]. This study shows that the magnetism in magnetic multilayers can be engineered by nonmagnetic spacer layers without involving the microstructure of the individual layers.

Au spacer in exchange coupled system

The exchange bias phenomenon can be described as a form of unidirectional magnetic anisotropy that arises due to the interfacial exchange coupling between a ferromagnet (FM) and an antiferromagnet (AF) and can effectively delay the superparamagnetic limit [1,2]. It may be noted that exchange bias systems are often coated with a Au film, in order to protect them against further oxidation. Moreover, Au is often used as metallic leads for spin-valve structures. Thus, the Au/FM (or AF) interfaces and their effect on exchange bias cannot be ignored. The aim of this study was, therefore, to systematically investigate the magnetization of exchange coupled bilayers of Co/CoO that are separated by nonmagnetic Au spacer layers.

Specular and off-specular neutron scattering

We have investigated multilayers of the composition SiO_2/[Co(11.0nm)/CoO(5.0nm)/Au(25,30,50 nm)]N=16 and compared them with SiO_2/[Co(11.0nm)/CoO(7.0nm)]N=20/Au(50nm). The structural evolution of the ferromagnetic grains as seen by transmission electron microscopy (XTEM) measurements is interrupted by growing Au layers of appropriate thickness. Depth sensitive vector magnetometry was carried out using polarized neutron scattering at the TREFF reflectometer at MLZ. In our experiment four different cross sections can be distinguished, namely, non spin-flip (NSF) (R++ and R--) and spin-flip (SF) channels (R+- and R-+) measuring the respective longitudinal and transverse component of magnetization with respect to the guiding field. The specimens are field cooled in H = 4.0 kOe to 10 K inside a cryostat at the instrument. Detailed examination of the chemical species has been effectively done by x-ray absorption spectroscopy (XAS) at the Siam Photon Source (electron energy of 1.2 GeV), Synchrotron Light Research Institute, Thailand.

Reduced magnetic moment

The bias field H_{eb} and coercivity H_C versus the spacer layer thickness was seen to increase with increasing spacer layer thickness. Polarized neutron reflectivity data show an improvement in the fit quality by considering a 13 % reduction in the moment for the entire Co layer (11.0 nm) for the 50 nm Au spaced specimen as compared to

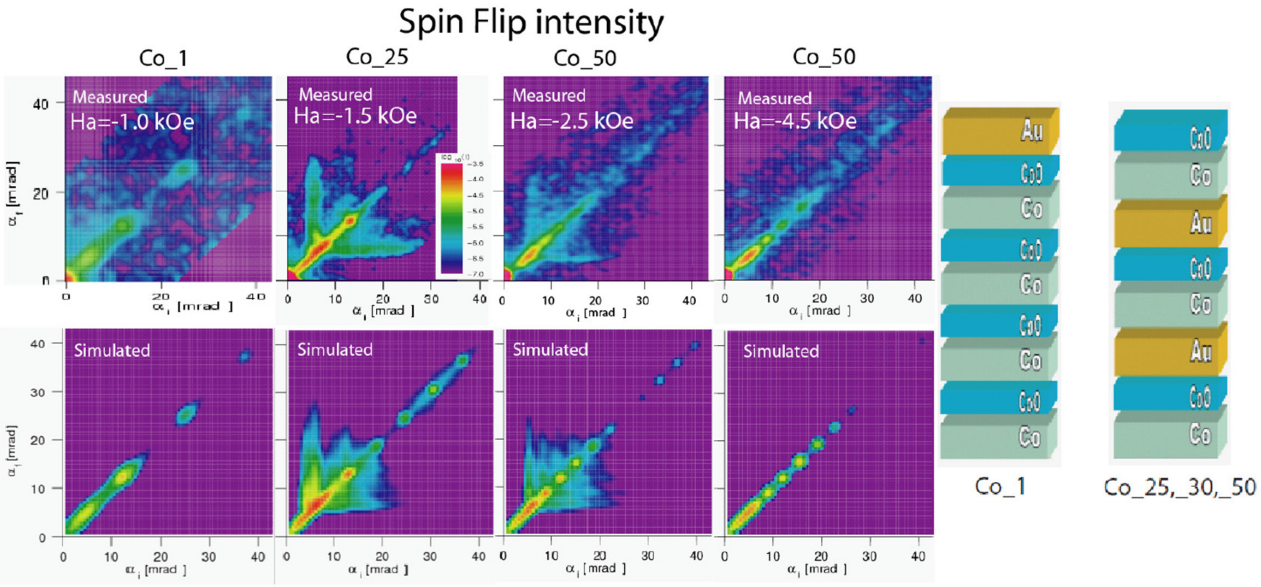

Figure 1: The spin flip intensity maps from various multilayers of Co/CoO with different thickness of Au layers separating the bilayers at different applied fields. The DWBA simulations for the respective cases give an estimate of their domain correlations.

the non-spaced one [2]. The SF intensities are shown in figure 1 at a field that is close to the first switching fields along the decreasing branch of the respective hysteresis loops. These intensities eventually disappear at saturation, demonstrating their magnetic origin. The specular and the off-specular intensity is simulated within the distorted wave Born approximation (DWBA). It should be noted that we did not observe any appreciable change in the domain size with spacer layer thickness, at least not for the separated multilayers for support of non-evolving grains within the multilayers with spacers. Using XAS, we found ≈ 4 % increase in the Co_3O_4 proportion within the AF layers. This can increase the number of uncompensated spins within the AF and also increased un-oxidized proportions of Co (Co_xO_y). Since the absolute thickness of such an unoxidized layer is very small (below 10 monolayers), with increased possibility of Au in its neighborhood, the unoxidized Co magnetic moments can turn out of plane. Thus, one can argue that the observed increase in the bias field can be attributed to the canting of the Co moments – out of plane – at the Co-Au interface (effective reduction in the FM layer thickness) and/or increased proportion of uncompensated moments within the CoO layers.

Conclusion

The Au layer in Co/Co/Au multilayers has been seen to decouple the structural and magnetic properties of the magnetic bilayers, thus inhibiting the evolution of domains across the heterostructures. This is evident from the XTEM and off-specular polarized neutron scattering. In spite of the decoupling, an increment in the H_{eb} with spacer thickness was seen. This was due to reduced magnetic moment of the Co layer as inferred from the magnetometry and polarized neutron reflectivity measurements. The XAS measurements could account for the relative proportions of the FM and AF species within these systems. Finally, the out-of-plane orientation tendencies of the Co moments at the Co-Au interfaces with varying AF-FM proportions could effectively explain the in-plane decrease of the magnetic moment with increased Au spacer thickness.

[1] A. Paul et al., Phys. Rev. B 86, 094420 (2012).
[2] A. Paul et al., Phys. Rev. B 87, 014431 (2013).

Neutron spin resonances in superconducting $NaFe_{1-x}Co_xAs$

C. Zhang[1,2], H. F Li[3], Y. Su[3], T. Das[4], R. Yu[1], G. Tan[2], Y. Song[1,2], A. Schneidewind[3], E. Faulhaber[5], O. Sobolev[6], J. A. Fernandez-Baca[2,7], Th. Brückel[3], A. V. Balatsky[4], Q. Si[1], T. Egami[2,7], P. Dai[1,2]

[1]Department of Physics and Astronomy, Rice University, Houston, USA

[2]Department of Physics and Astronomy, University of Tennessee, Knoxville, USA

[3]Jülich Centre for Neutron Science (JCNS) at MLZ, Forschungszentrum Jülich GmbH, Garching, Germany

[4]Theoretical Division, Los Alamos National Laboratory, Los Alamos, USA

[5]Heinz Maier-Leibnitz Zentrum (MLZ), Technische Universität München, Garching, Germany

[6]Institut fur Physikalische Chemie, Georg-August-Universitat Göttingen, Göttingen, Germany

[7]Oak Ridge National Laboratory, Oak Ridge, Tennessee, USA

The presence of spin resonance in neutron spectroscopy is a hallmark of unconventional superconductivity. It is generally believed that the neutron spin resonance is directly related to the superconducting gap and electron pairing symmetry. We have investigated the spin resonance phenomenon in $NaFe_{1-x}Co_xAs$ superconductors comprehensively at the high-flux triple-axis spectrometers PANDA and PUMA. In the slightly overdoped regime, we observed a very sharp spin resonance, which cannot be reproduced within an S^{++}-wave pairing symmetry, therefore giving compelling evidence on the S^{+-}-wave scenario. On the contrary, double spin resonances were observed unexpectedly in the underdoped region. We strongly argued that they are likely to be related to an anisotropic superconducting gap, thus highlighting the important role of orbitals in understanding the pairing mechanism of the multi-orbital electrons in iron based superconductors.

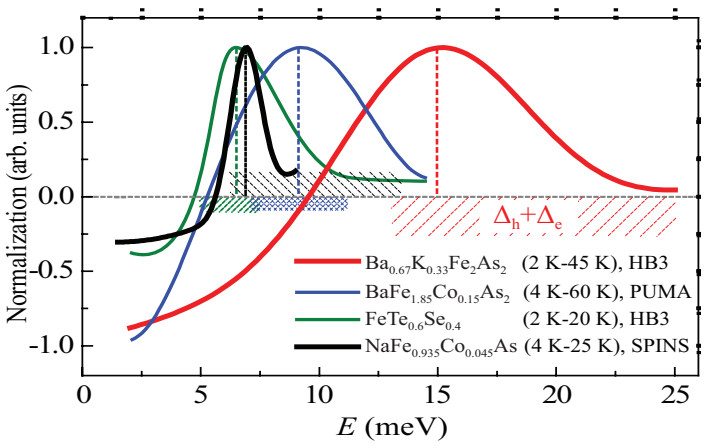

Figure 1: The schematics of neutron spin resonances for different iron superconductors. The dashed regions show the range of 2Δ as determined from different ARPES and other experiments. In all cases, the resonance can be either below or above the 2Δ.

Sharp spin resonance

In iron based superconductors, theories based on the S^{+-}-wave pairing symmetry predict the presence of a sharp neutron spin resonance at an energy below the sum of the hole and electron superconducting (SC) gap energies (i.e. $E \leq 2\Delta$) below T_C. On the other hand, a broad spin excitation enhancement is expected from the S^{++}-wave pairing symmetry at an energy above 2Δ below T_C. While the resonance has been observed in a number of iron based superconductors at an energy below 2Δ consistent with the S^{+-}-wave pairing symmetry, the mode has also be interpreted as arising from the S^{++}-wave pairing symmetry with $E \geq 2\Delta$ due to its broad energy width (see fig. 1) and the large uncertainty in determining the SC gap. Via comprehensive inelastic neutron scattering experiments carried out at PUMA and PANDA, we observed a sharp spin resonance at the wavevector (0.5,0.5,0.5) at E = 7 meV in the slightly overdoped NaFe0.935Co0.045As superconductor (T_C = 18 K) [1] (see fig. 2(d)), which is several times sharper than resonances usually observed in other iron based superconductors. By comparing to the calculated spin excitation spectra within both S^{+-}- and S^{++}-wave pairing symmetries, we conclude that such sharp resonance can only be reproduced in the former scenario, thus giving compelling evidence on the S^{+-}-wave pairing symmetry for iron based superconductors.

Double spin resonances

In contrast to the single resonance for the overdoped $NaFe_{0.935}Co_{0.045}As$, surprisingly, we observed double spin resonances at the

same commensurate wavevector for the underdoped $NaFe_{0.985}Co_{0.015}As$ superconductor (T_C = 15 K) [2] (see fig. 2(c)). The resonances in $NaFe_{0.985}Co_{0.015}As$ peak at 3.25 meV and 6 meV, respectively, and both track down T_C. This is fundamentally different from the c-axis dispersion of the resonances in the electron-doped $BaFe_2As_2$ and hole-doped copper oxide superconductor $YBa_2Cu_3O_{6.85}$. The doping evolution of the spin resonance coincides with that of the SC gap anisotropy in ARPES experiments. Our experimental discoveries, together with our theoretical analysis, thus strongly suggests that the orbital selectivity plays an important role in understanding the SC pairing of the multi-orbital electrons in the iron pnictides.

In iron pnictides, the Fermi surface is composed of multiple orbitals. In electron doped $NaFe_{1-x}Co_xAs$, the dominant orbital character of the electron pockets would be either d_{xy} or $d_{xz/yz}$, depending on the direction in the Brillouin zone (see fig. 2(a) and 2(b)). Recent theories and experiments find that the effective strength of electron correlations can be very different between the d_{xy} and $d_{xz/yz}$ orbitals. This may induce orbital selective SC pairing strengths, which naturally give anisotropic SC gaps along the electron pockets. The neutron resonance in the SC state is a bound state at energies just below the particle-hole excitation energy $E_r \leq \Delta_h + \Delta_e$. The anisotropic SC gap in the electron pocket is large. As in the underdoped $NaFe_{0.985}Co_{0.015}As$, there are two characteristic gaps $\Delta_{e1} \neq \Delta_{e2}$ (respectively associated with d_{xy} and $d_{xz/yz}$ orbitals). Two resonance peaks are expected as a result of this separation of energy scales (see fig. 2(e)). As the electron doping is increased to the overdoped regime, the orbital selectivity of the correlations is reduced, giving rise to a smaller SC gap anisotropy with $\Delta_{e1} \approx \Delta_{e2}$. Therefore, only one resonance peak will present (see fig. 2(f)).

Because the multiplicity of electron orbitals is a distinct feature of the iron-based superconductors and is likely to make a major contribution to their superconducting pairing, our results further suggest that resonance, superconducting gap and T_C in underdoped region of $NaFe_{1-x}Co_xAs$ cannot be simply scaled by a universal relationship.

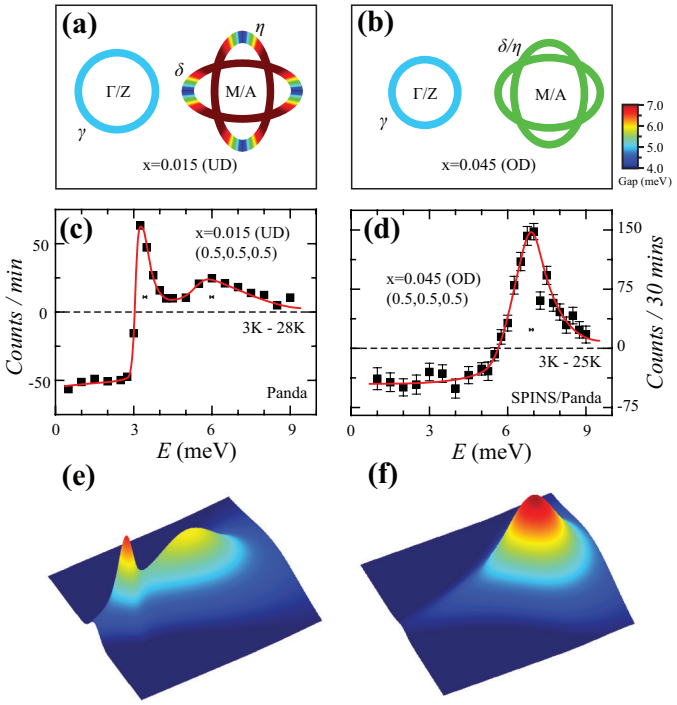

Figure 2: (a-b) Schematics of Fermi surfaces and superconducting gaps in underdoped and overdoped samples near the Γ and M points. (c-d) Double resonances and single resonance are obtained by taking temperature difference below and above T_c in underdoped $NaFe_{0.985}Co_{0.015}As$ (T_C = 5 K) and overdoped $NaFe_{0.935}Co_{0.045}As$ (T_C = 18 K) at the wave vector (0.5,0.5,0.5). (e-f) Schematic view of double resonances and single resonance in the [H,H] and E plane.

Experiments at PANDA and PUMA

All essential inelastic neutron scattering results were obtained at the high-flux triple-axis spectrometers PANDA and PUMA at MLZ. Measurements were mainly carried out by using a focusing PG monochromator and analyzer with a fixed final neutron energy of E_f = 14.7 and 5 meV, respectively. About 5 g of single crystals of overdoped $NaFe_{0.935}Co_{0.045}As$ and underdoped $NaFe_{0.985}Co_{0.015}As$ were prepared by the self-flux method.

[1] C. Zhang et al., Phys. Rev. B 88, 064504 (2013).

[2] C. Zhang et al., Phys. Rev. Lett. 111, 207002 (2013).

Enhanced low-energy magnetic excitations in the superconductor $Fe_{0.98-z}Cu_zTe_{0.5}Se_{0.5}$

J. Wen[1,2,3], S. Li[1], Z. Xu[4], C. Zhang[4], M. Matsuda[5], O. Sobolev[6], J. T. Park[6], A. D. Christianson[5], E. Bourret-Courchesne[7], Q. Li[4], G. Gu[4], D.-H. Lee[2,3], J. M. Tranquada[4], G. Xu[4], R. J. Birgeneau[2,3,8]

[1]National Laboratory of Solid State Microstructures and Department of Physics, Nanjing University, Nanjing, China

[2]Department of Physics, University of California, Berkeley, California, USA

[3]Materials Science Division, Lawrence Berkeley National Laboratory, Berkeley, California, USA

[4]Condensed Matter Physics and Materials Science Department, Brookhaven National Laboratory, Upton, New York, USA

[5]Quantum Condensed Matter Physics, Oak Ridge National Laboratory, Oak Ridge, Tennesse, USA

[6]Heinz Maier-Leibnitz Zentrum (MLZ), Technische Universität München, Garching, Germany

[7]Life Sciences Division, Lawrence Berkeley National Laboratory, Berkeley, California, USA

[8]Department of Materials Science and Enginnering, University of California, Berkeley, California, USA

We use Cu to replace Fe in $Fe_{0.98}Te_{0.5}Se_{0.5}$, an Fe-based superconductor with a superconducting temperature (T_c) of ~ 15 K, and perform inelastic neutron scattering measurements on the samples. We find that the low-energy magnetic excitations are strengthened, contrary to expectation, but consistent with the idea that the main effect of Cu doping is to localize conduction states, thereby suppressing the itinerancy and enhancing the low-energy magnetic excitations.

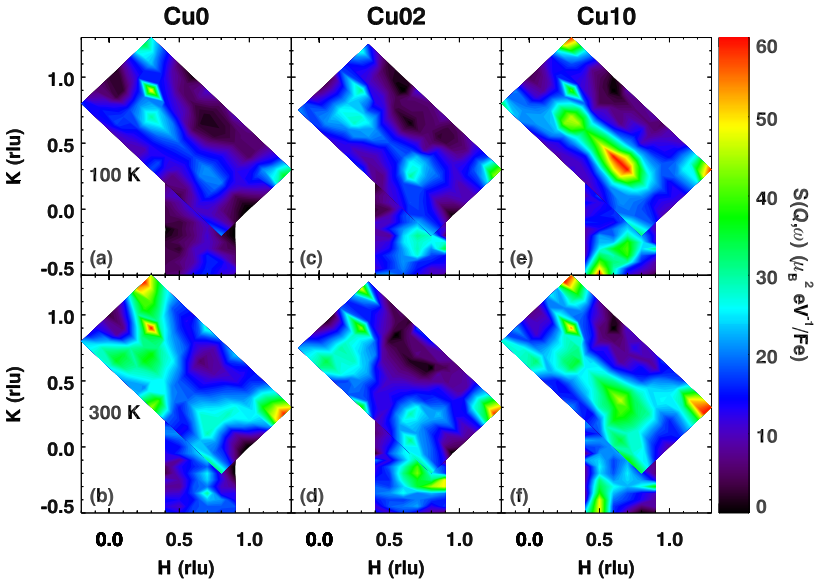

Figure 1: Contour plots of the magnetic scattering at 6 meV at 100 K (upper panels) and 300 K (bottom) for Cu0 (left column), Cu02 (middle), and Cu10 sample (right).

Roles of 3d transition metal substitution

Understanding how superconductivity emerges from their non-superconducting parent compounds has been one of the central topics in condensed matter physics. For example, in $BaFe_2As_2$ (Ba122), initially, it is believed that substituting Fe with 3*d* transition metals such as Co and Ni that act as effective electron dopants renders the superconductivity. [1] Such approaches typically describe the doping effects based on a rigid-band-shift model. [2] However, such a model has faced serious challenges from both the experimental and theoretical perspectives, [3] each of which indicates the inadequacy of a rigid-band description. Furthermore, there is a dichotomy between Co/Ni and Cu substitution effects in terms of the emergence of superconductivity. [1] In this work, we explore the effects of transition metal substitution by carrying out inelastic neutron scattering measurements on thermal neutron three-axes spectrometers including PUMA at MLZ on a different Fe-based superconductor system, namely $Fe_{1+y}Te_{1-x}Se_x$.

Cu-induced localizations

We use Cu to substitute for Fe in $Fe_{0.98}Te_{0.5}Se_{0.5}$, and measure how the low-energy magnetic excitations evolve as a function of Cu concentration. We studied three samples of $Fe_{0.98-z}Cu_zTe_{0.5}Se_{0.5}$ with nominal z = 0, 0.02, and 0.1, which we labeled as Cu0, Cu02, and Cu10. Without Cu substitution, the sample has the highest T_c of ~ 15 K among the $Fe_{1+y}Te_{1-x}Se_x$ system. The T_c is suppressed rapidly by the Cu doping—with 0.02-Cu substitution, it is reduced to 8 K; with 10% Cu

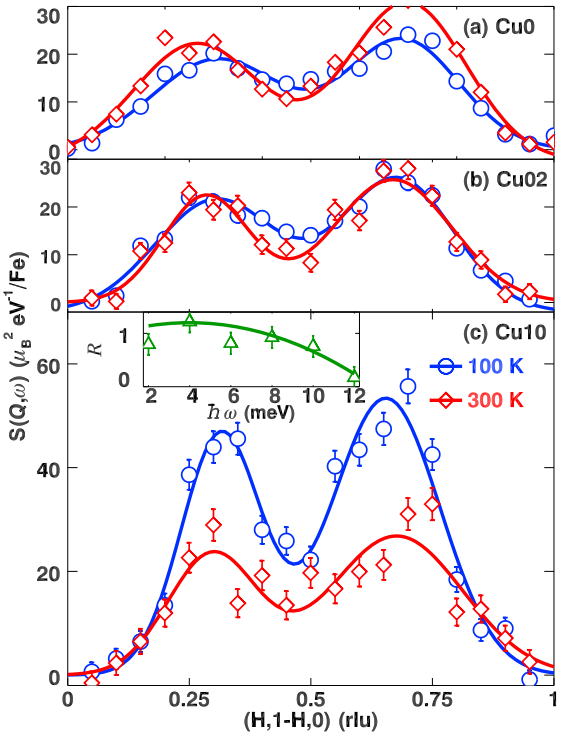

Figure 2: Constant-energy scans of 6 meV through (0.5, 0.5) along the [1-10] direction at 100 K and 300 K. In the inset of (c) we plot the ratio of enhancement of 100 K over 300 K.

doping, the sample is no longer superconducting, and behaves like an insulator.

The low-energy (≤12 meV) magnetic excitations respond to the Cu doping by showing enhanced spectral weight and increased dynamical spin-spin correlation lengths. The key results are summarized in figure 1. From the 100 K data in figure 1 (the upper panels), it is clear that the spectral weight is greatly enhanced in the Cu10 sample compared to that of the Cu0 and Cu02 samples. By analyzing the data, it is found that the dynamical spin-spin correlation length also becomes larger with Cu substitution. For each sample, as the temperature increases from 100 to 300 K, the magnetic excitations become broader, especially along the [110] direction. However the temperature dependence of the Cu10 sample differs from that of the other two in an important way. As shown in figure 2, while the scattering intensity for all three samples is comparable at 300 K, only in the case of Cu10 does it grow substantially on cooling to 100 K.

We have studied the energy dependence of the enhancement on the integrated intensities for the [1-10] scan for the Cu10 sample at 100 K compared to that at 300 K, and the results are shown in the inset of figure 2(c). At low energies, for example, from 2–10 meV, the integrated intensities are almost doubled.

Combining these results, we conclude that in the Cu10 sample, the magnetic scattering is significantly strengthened. The results are in contrast to the expectation that using weakly non-magnetic Cu to replace magnetic Fe^{2+} suppresses the magnetic correlations. The behavior that we observe can naturally be explained by assuming that the main effect of Cu doping is to localize conduction states, thereby suppressing the itinerancy. As a result, either the local moments are enhanced, or the spin fluctuation rate is reduced, and the spectral weight is transferred to low energies. Either case will give rise to an enhancement of the low-energy magnetic scattering. Our results demonstrate that Cu substitution in the $Fe_{1+y}Te_{1-x}Se_x$ system cannot be described by a rigid-band-shift model.

[1] P. C. Canfield et al., Phys. Rev. B 80, 060501(R) (2009).
[2] M. Neupane et al., Phys. Rev. B 83, 094522 (2011).
[3] G. Levy et al., Phys. Rev. Lett. 109, 077001 (2012).

Correlation between supercoiling & conformational motions of the bacterial flagellar filament

A. M. Stadler[1], T. Unruh[2], K. Namba[3], F. Samatey[4], G. Zaccai[5]

[1]Jülich Centre for Neutron Science (JCNS) and Institute for Complex Systems (ICS), Forschungszentrum Jülich GmbH, Jülich, Germany

[2]Lehrstuhl für Kristallografie und Strukturphysik, Friedrich-Alexander-Universität Erlangen-Nürnberg, Erlangen, Germany

[3]Osaka University, Osaka, Japan

[4]Institute of Science and Technology, Okinawa, Japan

[5]Institut Laue-Langevin and CNRS, Grenoble, France

The bacterial flagellar filament is a very large macromolecular assembly of a single protein flagellin. We investigated the correlation between supercoiling and protein dynamics in the flagellar filament using incoherent neutron scattering. Our results strongly support the theory that supercoiling of the protofilaments in the flagellar filament is determined by the strength of molecular forces in and between the flagellin subunits.

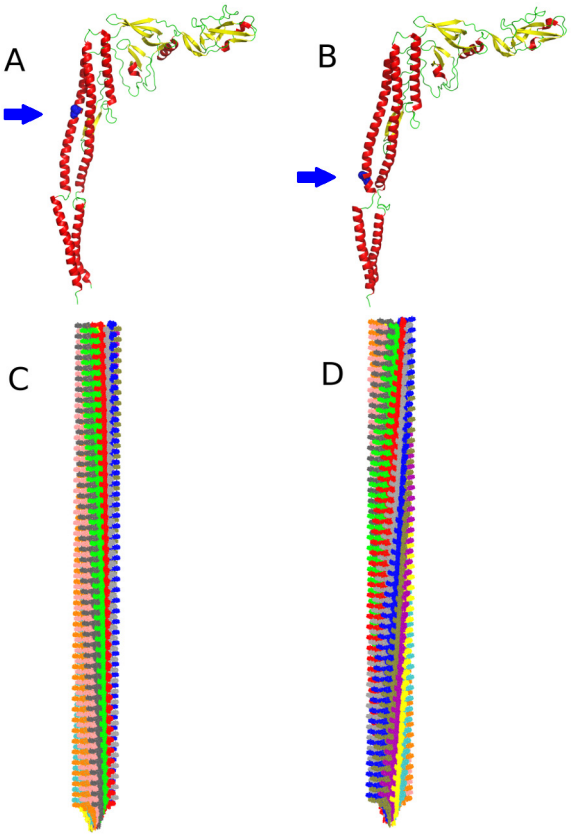

Figure 1: Structure of flagellin. The L-type (A) and R-type (B) conformations. The point mutations are highlighted by blue arrows and blue solid spheres. Models of the straight filament in the L-type (C) and R-type (D) conformations.

Bacterial flagellar filament

Bacteria swim in an aqueous medium by using their flagella, which act as true nanomachines [1]. The bacterial filament serves as a propeller and reaches lengths of up to 15 µm, but the diameter does not exceed 25 nm. The filament has a helical tubular structure made by polymerization of >20,000 copies of a single protein called flagellin. The filament can be described as a tubular structure made of 11 protofilaments and can exist in 10 different supercoiled conformations, as well as two different straight forms [2]. The extreme forms are the L- and R-type straight filaments, which consist of protofilaments with left- and right-handed helical symmetry, respectively (see fig. 1). The supercoiled filament has a composition of two protofilaments in the R-type state and nine protofilaments in the L-type state [2]. Flagellin can be trapped either in the L-type or R-type state by single point mutations. The structures of both mutants of flagellin are shown in figure 1 A and B with both point mutations highlighted by blue arrows and blue solid spheres. The aim of the present work was to study the correlation between supercoiling of the filaments and protein dynamics on different time-scales, using incoherent neutron scattering [3].

Incoherent neutron scattering experiments

Neutron scattering of the L- and R-type conformations and of the wild-type resting conformation of the bacterial flagellar filament was measured on the cold neutron time-of-flight spectrometer TOFTOF at the MLZ in Garching, and on the thermal high-resolution neutron backscattering spectrometer IN13 at the ILL in Grenoble. The wild-type filament served as a reference and control. Motions in the picosecond timescale were investigated on TOFTOF.

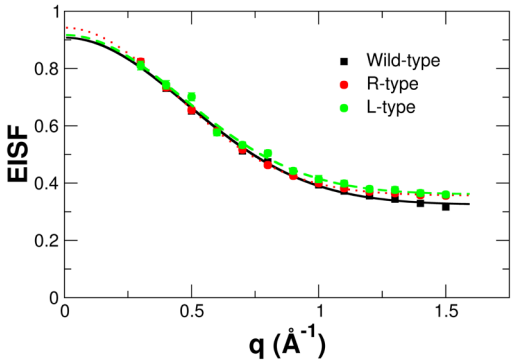

Figure 2: EISFs of the different samples measured on TOFTOF. The lines are fits to the data using the Gaussian approximation.

The Elastic Incoherent Structure Factor (EISF) was extracted from the measured spectra and interpreted within the Gaussian approximation to determine the mean square displacements (MSDs) and the fraction of protons participating in the motions (see fig. 2). Slower dynamics in the 0.1 ns time-range were measured with IN13. MSDs were calculated from the IN13 data using the Gaussian approximation and an extension of the Gaussian approximation to account for motional heterogeneity (q^4-extension), (see fig. 3). The temperature dependence of the MSDs gave valuable information on stabilizing forces within the proteins.

Molecular dynamics of the bacterial flagellar filament

Amplitudes of motion and the fraction of hydrogen atoms participating in the fast dynamics on the picosecond timescale were found to be similar, irrespective of the filament conformation. Nevertheless, compared to other biological systems, the large protein assembly of the flagellar filament shows quite a high flexibility on the picosecond timescale [3]. MSDs on the 0.1 ns timescale demonstrate that the L-type state is more flexible than the R-type, whereas the wild-type state shows intermediate flexibility. Protein stiffness was found to be smaller in the L-type than in the R-type state. Our results on protein dynamics agree with a structural comparison between the L-type and R-type filaments using electron cryomicroscopy [4]. The latter study showed that a cluster of hydrophobic residues, which is responsible for determining the protofilament conformation, is stably formed in the R-type but not in the L-type.

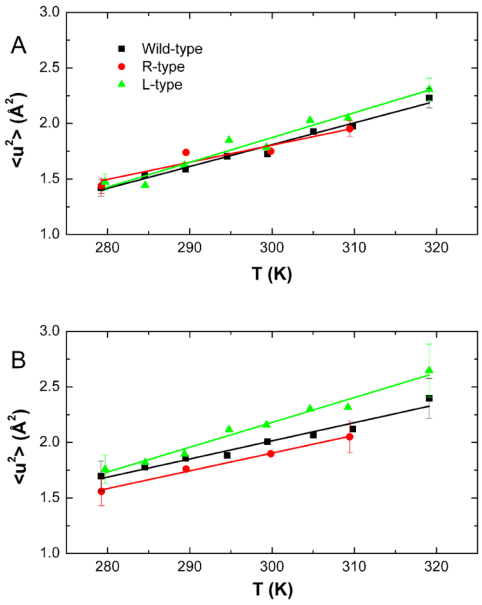

Figure 3: MSDs of the filaments on the 0.1 ns timescale by using the Gaussian approximation (A) and the Gaussian approximation with the q^4 extension (B).

Regulating the packing interaction

Our results provide strong support for the observation that local interactions within and between subunits are weaker in the L-type filament than in the R-type. Molecular forces in and between the flagellin subunits seem to regulate the packing interactions and the supramolecular assembly of the filaments.

[1] K. Namba et al., Q. Rev. Biophys. 30, 1 (1997).
[2] I. Yamashita et al., Nat. Struct. Biol. 5, 125 (1998).
[3] A. M. Stadler et al., Biophys. J. 105, 2157 (2013).
[4] S. Maki-Yonekura et al., Nat. Struct. Mol. Biol. 17, 417 (2010).

SANS kinetic study of pH degradable polymer micelles intended for controlled drug delivery

S. K. Filippov[1], J. M. Franklin[2], P. V. Konarev[2], P. Chytil[1], T. Etrych[1], A. Bogomolova[1], M. Dyakonova[3], C. M. Papadakis[3], A. Radulescu[4], K. Ulbrich[1], P. Stepanek[1], D. I. Svergun[2]

[1]Institute of Macromolecular Chemistry, AS CR, Prague, Czech Republic

[2]European Molecular Biology Laboratory, EMBL c/o DESY, Hamburg, Germany

[3]Physik-Department, Technische Universität München, Garching, Germany

[4]Jülich Centre for Neutron Science (JCNS) at MLZ, Forschungszentrum Jülich GmbH, Garching, Germany

We report on kinetic studies of therapeutically highly potent polymer-drug conjugates consisting of amphiphilic N-(2-hydroxypropyl) methacrylamide (HPMA) based copolymers bearing the anticancer drug doxorubicin (Dox). We performed time-dependent SANS measurements (KWS-2 beamline) after sharp changing pH levels to characterize the drug release and changes in particle size and shape. For most conjugates, nanoparticle growth or decay was observed within a time range of several hours. We concluded that the spacer structure determined the fate of a cholesterol derivative after the pH jump [1].

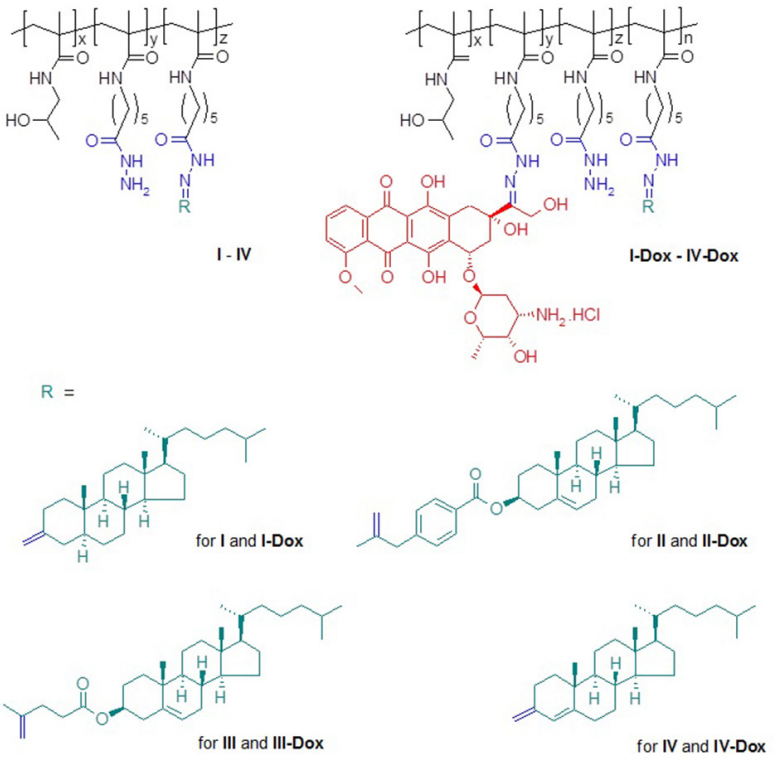

Figure 1: Schematic structures of the hydrophobic moieties. Left part- polymers without Dox, Right part – polymers with Dox.

Hydrolytically degradable polymer micelles intended for controlled drug delivery

Polymer therapeutics is one of the most challenging and promising trends in biomedical technology. Polymer drug carriers based on *N*-(2-hydroxypropyl)methacrylamide (HPMA) copolymers have been developed for the treatment of tumors, with special focus on site-specific delivery and controlled release of anti-cancer agents into tumor tissues or cells. Such interest requires a knowledge of the detailed interior structure of the polymeric nanoparticles and structure evolution during drug delivery. Amphiphilic HPMA-based polymer drug carriers with anticancer drug doxorubicin (Dox) show promising results, exhibiting enhanced tumor accumulation and excellent antitumor activity in the treatment of solid tumors [2].

In the present work, the overall properties and internal structure of the new copolymers were investigated as a function of time using SANS/SAXS after a sudden change in pH from 7.2 to 5. Subsequently, the mechanisms of the nanoparticle transformations were analyzed. In contrast to our previous studies [3], fewer hydrophobic pH-responsive HPMA copolymers (fig. 1) were synthesized and used for the experiments. All copolymers had almost the same content of cholesterol derivatives.

SANS kinetic study of hydrolytically degradable polymer micelles

The release of Doxorubicin (Dox), an anti-cancer drug, from amphiphilic N-(2-hydroxypropyl) methacrylamide (HPMA) based copolymers was characterized using time-dependent SANS (KWS-2 beamline) and SAXS measurements after a pH jump simulating the particle transport

from blood (pH=7.4) to a tumor environment (pH=5.0). To the best of our knowledge, we were able, for the first time, to monitor the change in properties of a drug delivery carrier with time in conditions mimicking the tumor microenvironment using the SANS/SAXS methods. For most conjugates, nanoparticle growth or decay was observed within a time range of several hours (fig. 2). It was established that the growth/decay rate and the steady-state size of nanoparticles depend on the spacer structure. We concluded that the spacer structure determines the fate of a cholesterol derivative after a pH jump. The elution of Dox from a nanoparticle was traced over time. Fitting results for 5α-cholestan-3-one and Lev-chol spacers implied that cholesterol moieties were continuously escaping from the nanoparticle core and concentrated in the hydrophilic shell (fig. 3). In contrast, the cholest-4-en-3-one spacer seemed to be stable in conditions mimicking tumor cells due to its conjugated double bonds, thus preventing cholesterol escaping. Dox moiety release was only observed for the cholest-4-en-3-one spacer with change in pH (fig. 3). Such findings justify the model proposed in our previous paper. Conversely, micelles composed of Opb-spacers grew more compact with time due to their higher hydrophobicity.

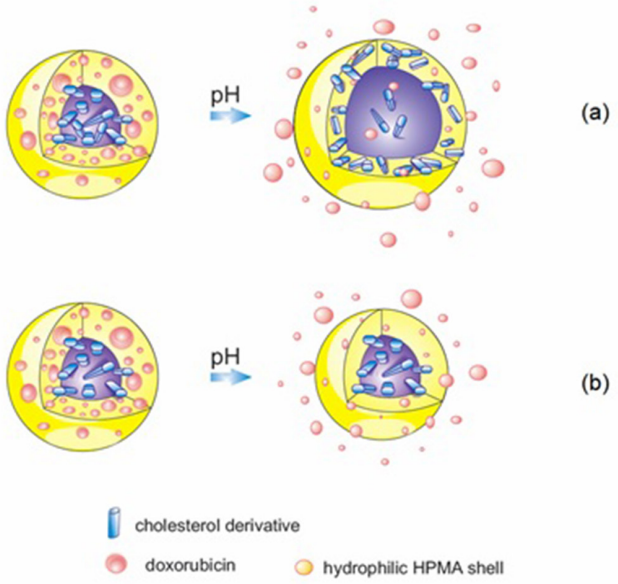

Figure 3: Hypothetical model of the structural evolution of nanoparticles composed of conjugates I-Dox and III-Dox (a), and IV-Dox (b) after a pH jump from 7.2 to 5.0.

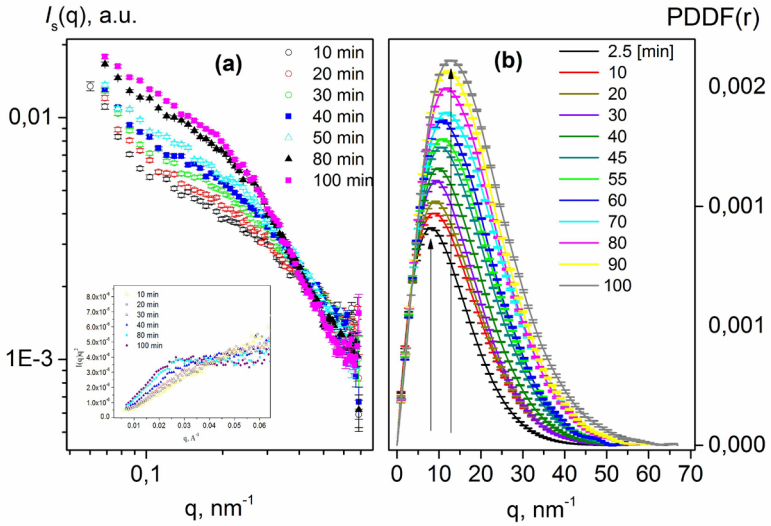

Figure 2: Time evolution of SANS curves (a, inset: Kratky plot) and PDDFs (b) for HPMA conjugate.

Acknowledgements

M.D. thanks the MaMaSelf (Master in Materials Science Exploiting Large Scale Facilities) master program for financial support. The MLZ is also acknowledged for beam time allocation. The authors acknowledge financial support from the European Commission under the Seventh Framework Program by means of the grant agreement for the Integrated Infrastructure Initiative N. 262348 European Soft Matter Infrastructure (ESMI). The authors also acknowledge financial support Nr. CZ09-DE06/2013-2014 from the ASCR - DAAD Programme PPP 2013-2014 and from the German Bundesministerium für Bildung und Forschung grant BioSCAT, Contract no: 05K12YE1.

[1] S. Filippov et al., Biomacromolecules 14, 4061 (2013).
[2] P. Chytil et al., Macromol. Chem. Phys. 213, 858 (2012).
[3] S. Filippov et al., Biomacromolecules 13, 2594 (2012).

Structure of metallo-supramolecular micellar gels

C. Mugemana[1], A. Joset[2], P. Guillet[3], M.-S. Appavou[4], N. De Souza[5], C.-A. Fustin[1], B. Leyh[2], J.-F. Gohy[1]

[1]Institute of Condensed Matter and Nanosciences (IMCN), Bio- and Soft Matter division (BSMA), Université catholique de Louvain, Louvain-la-Neuve, Belgium

[2]Department of Chemistry, Molecular Dynamics Laboratory, University of Liège, Sart-Tilman, Belgium

[3]Equipe Chimie Bioorganique et Systèmes Amphiphiles, Université d'Avignon et des Pays de Vaucluse, Avignon, France

[4]Jülich Centre for Neutron Science (JCNS) at MLZ, Forschungszentrum Jülich GmbH, Garching, Germany

[5]Bragg Institute, Australian Nuclear Science and Technology Organisation, Kirrawee, Australia

SANS analysis of metallo-supramolecular micellar gels from polystyrene-*block*-poly(*tert*-butylacrylate) PS-*b*-PtBA-diblock copolymers is presented. The solubilization of the PS-*b*-PtBA-tpy diblock copolymer in ethanol-d_6 gives micelles formed by a polystyrene core and surrounded by P*t*BA coronal chains bearing terpyridine at the chain end. Adding metal ions to generate a micellar network gives rise to a micellar gel whenever the metal-ligand complexes are stable enough to strengthen the network. A significant neutron scattering signal is thus generated due to the contrast between the non deuterated copolymer micelles and deuterated ethanol.

Synthesis and self-assembly of PS-*b*-PtBA-terpy diblock copolymer

A PS_{70}-*b*-$PtBA_{180}$-tpy copolymer was synthesized by nitroxide-mediated radical polymerization. This copolymer was dissolved in deuterated ethanol, a selective solvent for the PtBA block, and a non-solvent of the PS block. The characteristic features of the resulting micellar solutions in the dilute regime were first investigated using dynamic light scattering at a concentration of 0.05 g L^{-1}. DLS analysis showed well-defined objects with a hydrodynamic radius of 25.8 nm (PDI as determined by DLS: 0.06).

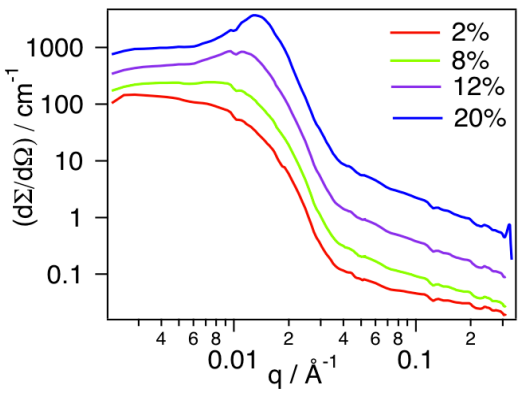

Figure 1: SANS intensities dΣ/dΩ (*q*) versus *q* for the PS_{70}-*b*-$PtBA_{180}$-tpy block copolymer dissolved in deuterated ethanol for several copolymer concentrations.

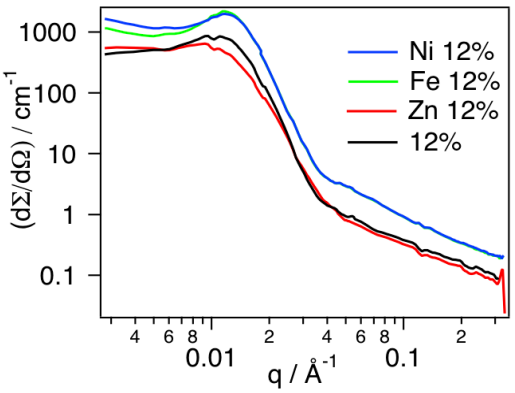

Figure 2: SANS intensities dΣ/dΩ (*q*) versus *q* for the gels prepared from the PS_{70}-*b*-$PtBA_{180}$-tpy block copolymer in deuterated ethanol 12% *w/v* copolymer concentration.

Neutron scattering intensities of micellar solutions loaded with metal ions

Figure 1 shows the scattered intensities obtained by SANS on micellar solutions in deuterated ethanol at 2, 8, 12 and 20% *w/v* concentrations. At the lowest concentration investigated (2% *w/v*), the macroscopic scattering cross section, dΣ/dΩ (*q*), decreases monotonically, suggesting that only isolated micelles are observed in this concentration regime, and thus giving access to the form factor of the micelles. In contrast, by increasing further the concentration to 8, 12 and 20% *w/v*, the scattering profiles revealed more and more clearly a structure factor peak arising from mutual interferences between the neutron waves scattered by different micelles.

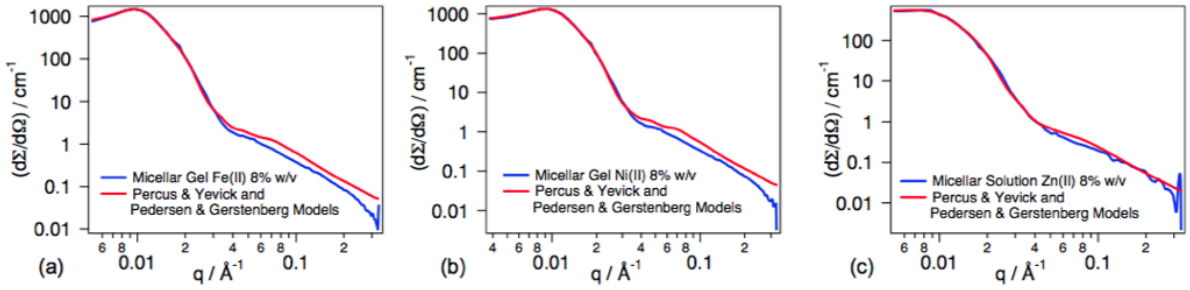

Figure 3: Experimental and calculated SANS intensities of the micellar solutions, from the PS_{70}-*b*-$PtBA_{180}$-tpy at a concentration of 8% *w/v*, with Fe(II) (a), Ni(II) (b) and Zn(II) (c) ions.

The impact of the addition of metal ions on the structure and spatial organization of the micelles was further investigated by adding of 0.5 eq. (with respect to the concentration of terpyridine ligands) of each metal ion, *i.e.* Fe(II), Ni(II) and Zn(II), to the micellar solutions. The resulting scattering cross sections are plotted in figure 2 for the micellar solutions at a concentration of 12% *w/v*. In the case of the micellar solutions dosed with Fe(II) and Ni(II) ions, an increase in the intensity of the structure factor peak in the low *q* regime was observed compared to the micellar solution with no metal ion. Such an increase is most likely to result from the formation of a network of micelles connected via metal-terpyridine complexes, since Ni(II) and Fe(II) ions preferentially form *bis*-terpyridine complexes. In the case of Zn(II), no structure factor peak was observed since Zn(II) forms, rather, *mono*-terpyridine complexes, which do not lead to a network of micelles, in agreement with previous results from rheology experiments [1].

Pedersen-Gerstenberg and Percus-Yevick models

The internal structure of the micelles, from diluted to concentrated solutions, were studied using the Pedersen-Gerstenberg model [2]. The impact of the metal ions on the formation of a micellar network was further investigated. To this end, the micellar solutions were exposed to three metal ions, *i.e.* Ni(II), Fe(II) and Zn(II). These transition metals form complexes with terpyridine ligands exhibiting various binding strengths. The neutron scattering data of the micellar gels were analyzed using the models of Percus-Yevick for the structure factor and of Pedersen-Gerstenberg for the form factor. The experimental and the fitted neutron scattered intensities of the gels obtained upon addition of metal ions to the PS_{70}-*b*-$PtBA_{180}$-tpy micellar solutions are shown in figure 3.

The addition of 0.5 eq. of Ni(II) or Fe(II) to the 8% *w/v* micellar solution leads to the formation of a network since these ions form stable complexes with terpyridine ligands. An increase in the copolymer volume fraction is observed, corresponding to a contraction of the system which becomes a gel. Volume fractions similar to those obtained for the 12% *w/v* micellar solution without metal ion are reached. Interestingly, the hard sphere interaction distance, σ, is not affected, indicating that the network is consistent with micelles interconnected via metal-terpyridine complexes, without, however, interpenetration of the coronal chains that may lead to coronal chain entanglements.

Conclusion

SANS appears to be a powerful tool for investigating such complex systems based on supramolecular micellar gels by providing an insight into the inner structure and the spatial organization of the micelles.

[1] P. Guillet et al., Soft Matter 5, 3409 (2009).

[2] C. Mugemana et al., Macromol. Chem. Phys. 214, 1699 (2013).

Interfacial smoothening of polymer multilayers with molecules

A. Paul[1], N. Paul[2] , P. Müller-Buschbaum[3] , P. Böni[1]

[1]Physik-Department E21, Technische Universität München, Garching, Germany
[2]Heinz Maier-Leibnitz Zentrum (MLZ), Technische Universität München, Garching, Germany
[3]Physik-Department E13, Technische Universität München, Garching, Germany

The development of polymer-based structures is hindered due to the difficulties in realizing well-defined modulated structures without interpenetration of charged polymers. Two types of polyelectrolyte multilayer structures, with and without embedded layers of the biomolecule, glutamic acid, are compared using infrared spectroscopy as well as X-ray and neutron scattering techniques. Using specular and off-specular neutron scattering at the TREFF reflectometer, we gain insight into the in- and out-of-plane arrangement of the structure [1]. A reduced roughness in a multilayer with the glutamic acid is associated with a drastic decrease in chain mobility responsible for interpenetration. In contrast, the multilayer without the biomolecule forms an island-like structure. Thus, biomolecules can interrupt the propagation of island-like structures at such interfaces which can be effectively used to achieve well-defined supramolecular layer structures from charged polymers.

Polyelectrolyte and Glutamic acid

Polymers are lighter, flexible and cheaper compared to their inorganic counterparts. However, there is an inherent difficulty in realizing well-defined modulated structures without interpenetration of charged polymers [2]. In this study, we modify the polyelectrolyte interfaces during growth by introducing glutamic acid (GA) within the polyelectrolyte interface assembly. We demonstrate that the new growth protocol reduces the polymer interpenetration normally observed, thereby decreasing the interface roughness. This modified polyelectrolyte multilayer system (containing GA) is compared to the conventionally prepared polyelectrolyte multilayer system using primarily scattering techniques

Specular and off-specular neutron scattering

Polyelectrolyte films were deposited on Si substrates using the layer-by-layer (LbL) protocol. The sample labeled ML was formed by alternating depositions of the protonated bilayer $(PSS/PAH)_2$ and deuterated bilayer (dPSS/PAH) for 3 cycles/repeat units to get $PEI/((PSS/PAH)_2/(dPSS/PAH))_3$. The sample labeled ML+GA was formed by alternating depositions of the protonated bilayer $(PSS/PAH)_2$ and deuterated bilayer (dPSS/PAH/ GA) for 3 cycles/repeat units to get $PEI/((PSS/PAH)_2/(dPSS/PAH/GA))_3$. The NR experiments were performed on the reflectometer TREFF at the MLZ. A home-built sample cell especially designed for NR experiments at the solidliquid interface was used. Using attenuated total reflection Fourier transform infrared (ATR-FTIR) spectroscopy, an enhanced sensitivity to the chemical identification of molecular species at the solid-liquid interface was shown [1].

Reduced chain mobility

In order to identify the presence of GA layers in the ML+GA structure, we deposited the layers *in situ* on a silicon crystal placed in the ATR liquid cell, recorded its spectrum and subtracted it by the spectrum of the pure ML film. The corresponding difference spectrum resembled the spectrum of GA, thus chemically verifying the occupancy of GA within ML+GA.

In figure 1a, the NR spectra can be seen along with their SLD profiles in the inset. For both samples (a) Kiessig fringes due to a finite thickness of the multilayer and (b) Bragg peaks due to a regular arrangement of deuterated polymer layers of

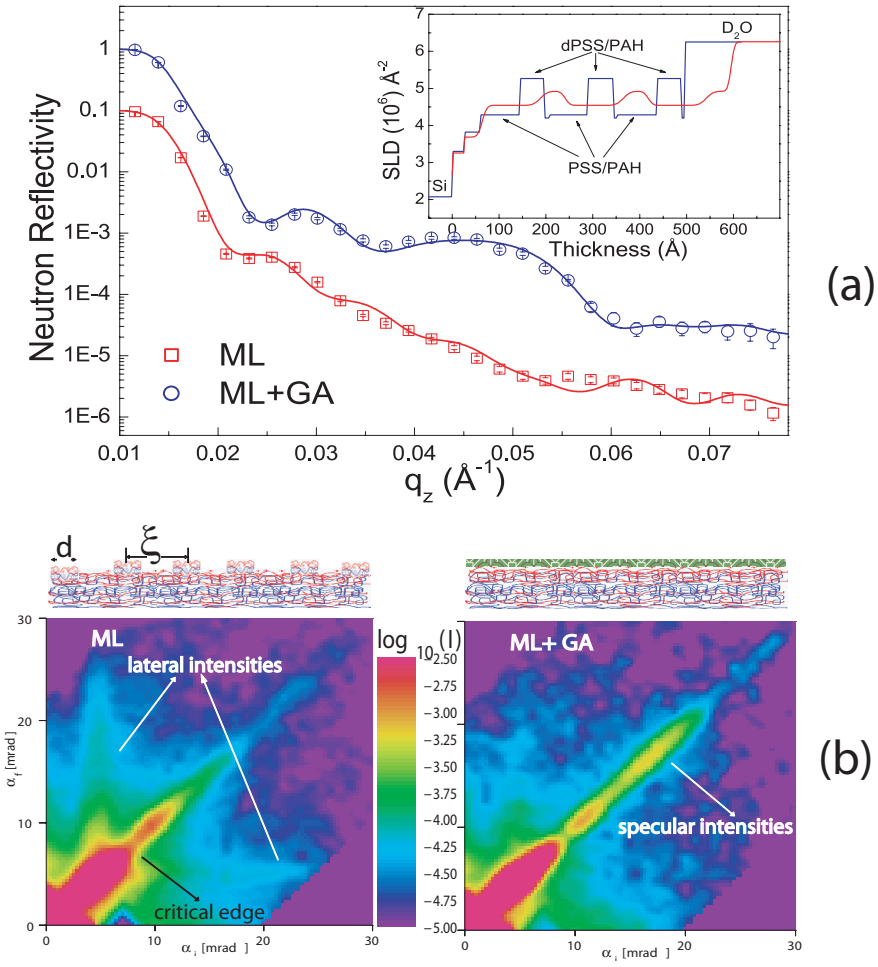

Figure 1: (a) NR data and fits for ML (squares) and ML + GA (circles). The inset shows the variation in the scattering length density with thickness. (b) Off-specular and specular neutron reflectivity data from the samples (bottom left) ML and (bottom right) ML + GA. Here α_i and α_f are the incident and exit angles, respectively and momentum transfer vector $q_z \sim (\alpha_i + \alpha_f)$. The correlation length ξ of island-like structures is shown schematically in ML against their absence in ML + GA.

dPSS within the structures was expected. However, a smearing out of both oscillations is observed for the sample without GA. This is due to contrast loss between protonated and deutered blocks and is interpreted as strong intermixing between them. On the other hand, NR oscillations are well pronounced in the case of ML+ GA which suggests not only better SLD contrast between the D_2O solvent and the deposited film but also a reduced intermixing within the structure. In figure 1b, we show the 2D intensity maps (off-specular and specular scattering signals) for the PEM with and without GA. No features of conformal roughness (Bragg-sheets) are observed in either case. However, most interestingly, Yoneda scattering (non-conformal roughness) running out of the critical edge as lateral intensities is distinct in ML. ML+GA does not show any such off-specular intensities away from the specular intensities along q_z.

Conclusion

A GA modified PEM system leads to a reduction in interfacial roughness by almost 0.14 the thickness of a bilayer as compared to the conventional PEM system. In ML+GA, we observe quasi-Bragg reflections in the NR pattern showing a well-defined and distinct layer separation. In ML, lateral structures related to polyelectrolyte complexes are detected. These are, however, not present in ML+GA, indicating a close relation between the polyelectrolyte complexes and interfacial roughening. These lateral structures gave rise to Yoneda wings in the off-specular pattern. Model simulations within the DWBA describe the features satisfactorily. In ML+GA we encounter reduced chain mobility and interpenetration due to selective interactions of GA with PAH [3].

[1] N. Paul et al., Soft Matter 9, 10117 (2013).
[2] M. Tarabia et al., J. Appl. Phys. 83, 725 (1998).
[3] N. Paul et al., J. Phys. Chem. B 116, 4492 (2012).

Neutron reflectivity characterization of the diffuse layer at a metal-polymer interface

N. S. Yadavalli[1], J.-F. Moulin[2], D. Korolkov[3], M. Krutyeva[4], S. Santer[1]

[1]Department of Experimental Physics, Institute for Physics and Astronomy, University of Potsdam, Potsdam, Germany

[2]German Engineering Materials Science Centre (GEMS) at MLZ, Helmholtz-Zentrum Geesthacht, Garching, Germany

[3]Bruker AXS GmbH, Germany

[4]Jülich Centre for Neutron Science (JCNS-1) & Institute for Complex Systems (ICS-1), Forschungszentrum Jülich GmbH, Jülich, Germany

In microfabrication processes, ultra-thin metallized polymers are commonly prepared using physical vapor deposition of a metal film on the polymer surface. During the deposition process, it is often expected that the metal layer will defuse into the polymer surface, thereby creating a bonding/sandwich layer near the metal/polymer interface. In this work, we demonstrate the presence of a diffused metal layer and its thickness using neutron reflectometry [1] and also discuss the electrical conductivity and mechanical properties of these metallized polymers [2, 3].

The azobenzene containing photosensitive polymer PAZO (pol{1-[4-(3-carboxy-4-hydroxyphenylazo)benzenesulfonamido]-1,2-ethanediyl,sodiumsalt}) with molecular weight of M_n = 1.4×10^4 g/mol (ca. 40 repeat units) is dissolved in a solvent mixture of 95 % methoxyethanol and 5 % ethyleneglycol. A micrometer thick polymer film is prepared by spin coating the PAZO solution with 250 mg/ml concentration onto a glass substrate (5x7 cm^2) followed by the physical vapor deposition of 10 nm thin gold film on top. The samples are then used to obtain neutron reflectivity curves at the time of flight reflectometer REFSANS Instrument operated at the MLZ in Garching near Munich.

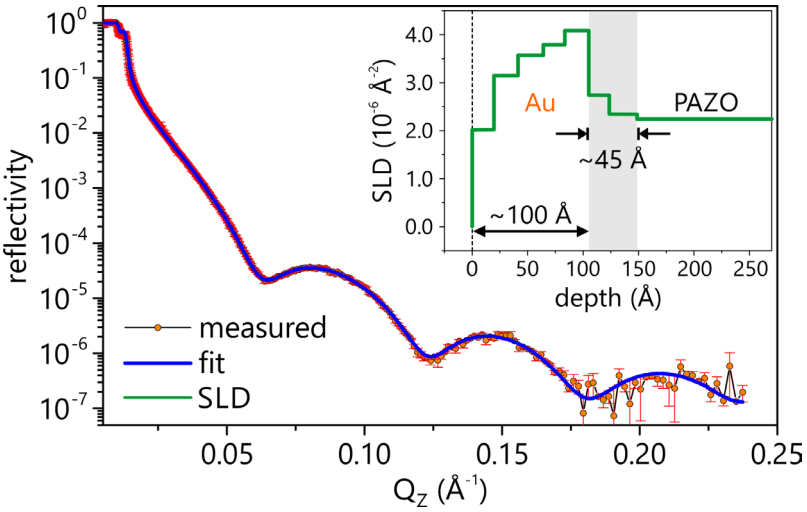

Figure 1: Neutron reflectivity analysis of bonding layer at metal/polymer interface. The final scattering length density profile is shown in the inset [1].

Neutron Reflectometry

Due to the unique possibility it offers, we chose neutron reflectometry to study the diffused metal layer near the metal/polymer interface. The instrument was operated using an incident wavelength spectrum ranging from 2 to 10 Å with a Δλ/λ resolution of 3 %. The opening of the beam defining slits were selected so as to keep the total ΔQ/Q = 6 % and the reflectivity was measured using three consecutive overlapping measurements at incident angles 0.3°, 0.6° and 1.4° over the q range extending to 0.2 Å^{-1}.

We performed neutron reflectivity measurements on a pure glass substrate, PAZO/glass and Au/PAZO/glass samples. To model the neutron reflectivty data, we used a matrix formalism in terms of dynamical scattering theory. The parameters of our samples were optimized using the Levenberg-Marquardt least square fitting procedure. For the pure glass sample, the parameters obtained are as follows: scattering length density (SLD) 3.565×10^{-6} ± 1.014×10^{-9} Å^{-2} and roughness σ = 8.003 ± 0.024 Å.

Since the PAZO/Glass and Au/PAZO/Glass samples were prepared on the same glass substrate, we used the values obtained in further simulations. For the PAZO/Glass sample, we found that the air/polymer interface has a square-root gradient profile and is characterized by the follow-

ing parameters: SLD of PAZO film at z = 0 ρ_{PAZO} (z = 0) = 1.135×10^{-6} ± 4.49×10^{-9} Å^{-2}, gradient thickness 125.9 ± 1×0.5 Å, mean SLD and absorption SLD of PAZO = 2.245×10^{-6} ± 2.557×10^{-9} Å^{-2}, ρ_{PAZO}^{abs} = 4.479×10^{-9} ± 2.732×10^{-11} Å^{-2}.

On depositing a 10 nm gold layer on the polymer surface, one would expect it to form a interdiffusion layer composed of two compounds, a polymer and Au and an averaged profile which would be a superposition of two profiles. In order to confirm this, the first 200 Å of the scattering length density profile including the Au layer and the interface between the gold layer and the PAZO film is split into 10 slices. The parameters of every slice were optimized independently for each slice with physical constrains on the slice thickness and SLD. The former could have values in the range from zero to 25 Å, defined by the maximum experimental scattering vector Q_{max}, and the latter was limited from the upper side by 5×10^{-6} Å^{-2}, which is larger than the calculated value of the scattering length density of gold 4.5×10^{-6} Å^{-2}. The result in figure 1 shows perfect agreement between the measured and fitted curves and clearly indicates an approximately 45 Å thin diffused Au layer with gradient into the PAZO surface from the SLD profile (inset).

Mechanical and electrical properties

To study the mechanical properties of ultra-thin metal films, we utilized the unique photosensitive properties of the PAZO material. Azo-modified photosensitive polymer film is a suitable candidate, offering the possibility of reshaping bulk polymers and thin films by light-irradiation while in the glassy state. Azo-benzene molecules undergo photo-isomerisation transitions from the trans to the cis configuration and mass transports during irradiation with light interference patterns resulting in the formation of surface relief grating (SRG). The metal film deposited on a photosensitive polymer creates a spontaneous bonding layer (fig. 2a) and gives the advantage of making it possible to translate the optomechanical strain induced in a photosensitive polymer to the metal film on top leading to crack formation

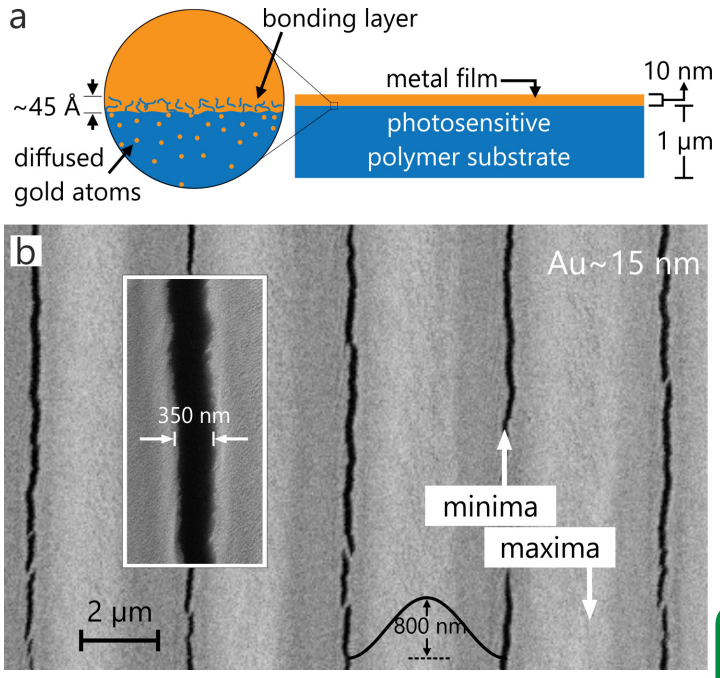

Figure 2: a) Scheme of metallized polymer sample with interfacial layer [1]. b) SEM image of around 15 nm thick gold film ruptured during SRG formation [2].

under very localized stresses (fig. 2b). More details are provided in our recent reports [1, 2]. We also observed that when thin metal films are ruptured, up to 80 % of metal film width and 500 nm depth into the polymer has no significant influence on the film's electrical conductivity, making the ultra-thin metallized polymers advantageous for applications in deformable electronics [3].

[1] N. S. Yadavalli et al., submitted.

[2] N. S. Yadavalli et al., ACS Appl. Mater. Interfaces 5, 7743 (2013).

[3] F. Linde et al., Appl. Phys. Lett. 103, 253101 (2013).

The effect of organic matter on mineral scaling of membranes for desalination of wastewater

V. Pipich[1], Y. Dahdal[2], H. Rapaport[3], R. Kasher[2], Y. Oren[2], D. Schwahn[4]

[1]Jülich Centre for Neutron Science (JCNS) at MLZ, Forschungszentrum Jülich GmbH, Garching, Germany

[2]Zuckerberg Institute for Water Research, Jacob Blaustein Institutes for Desert Research, Ben-Gurion University of the Negev, Beer-Sheva, Israel

[3]Department of Biotechnology Engineering, Ben-Gurion University of the Negev, Beer-Sheva, Israel

[4]Heinz Maier-Leibnitz Zentrum (MLZ) and Physik-Department E13, Technische Universität München, Garching, Germany

A consequence of high demand for potable water in arid areas such as the Mediterranean is the increasing number of desalination plants using membrane-based reverse osmosis (RO) and nanofiltration (NF) technologies. A serious problem is membrane biofouling and scaling. Small-angle neutron scattering reveals the strong influence of organic molecules on mineralization. This leads to the conclusion that scaling could be minimized if organic molecules were not present [1].

Figure 1: Ashkelon Seawater Desalination Plant (Israel) using Reverse Osmosis (RO) Technique. Produces 330,000 m^3 potable water per day for 0.57 $/$m^3$. The two young ladies are former students of the Zuckerberg Institute for Water Research.

Potable water in arid areas

In 2000, Israel initiated a “desalination master plan” with the aim of producing potable water at the rate of approximately 650 million m^3 per annum from seawater by the year 2020 [2]. At present time, a decision was made by Israel, Jordan, and the Palestinian National Authority to divert 200 million m^3 per annum of water from the Red Sea to the Dead Sea. A seawater desalination plant is planned near the Jordanian city of Aqaba to convert 40 % of this water to potable water to be shared between Jordan and the city of Eilat (Israel) [3]. Desalination plants are large factories, as demonstrated in figure 1 which shows part of the RO membrane units of the Ashkelon seawater desalination plant. In October 2013, the largest desalination plant in Sorek, south of Tel Aviv, became operational with a capacity of 624,000 m^3 per day catering for about 10 % of the country’s drinking water consumption [2]. Despite this extensive activity, water supply in many countries, especially those that are far from the sea, is a serious problem. In these cases, recycling of impaired water such as municipal wastewater, upgraded to the level of unlimited application, is a reasonable solution. Another, no less important aspect of recycling is environmental protection. Membrane-based technologies are extensively used today in this respect.

Small-Angle Neutron Scattering as a tool for exploring biofouling and scaling

A serious problem of RO/NF desalination is biofouling and scaling of the membranes, which limits the efficiency of desalination and membrane lifetime. In particular, scaling by calcium phosphate is a severe problem as no reliable antiscalants (special agents for preventing scale

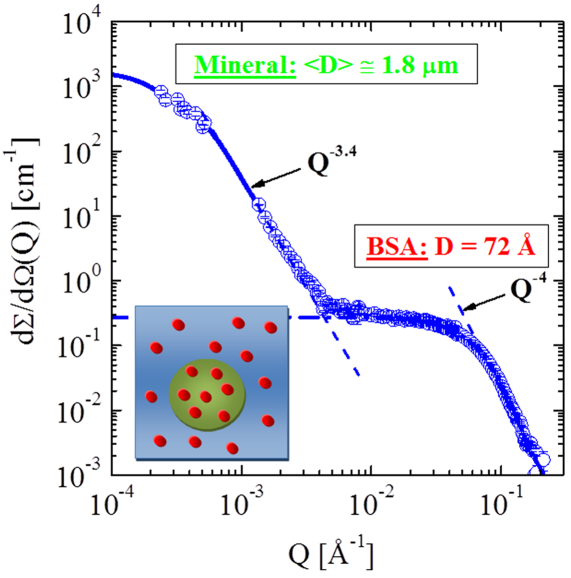

Figure 2: Scattering after adding 5 mg/mL BSA in SSE-D_2O solution. Particles of 1.8 µm diameter are formed and reside in parallel to BSA monomers [1].

formation) are currently known. Small-angle neutron scattering (SANS) may contribute valuable information to the mechanisms associated with these problems as neutrons distinguish between organic and inorganic phases and quantitatively analyze particles of size between nm and µm.

Protein induces mineralization

Mineralization has been explored in the presence of the two proteins bovin serum albumin (BSA) and lysozyme in a simulated secondary effluent (SSE). The SSE models the mineral fraction of an RO concentrate from the Shafdan Wastewater Treatment Plant (Israel) [4]. The two proteins are important examples of extracellular polymeric substances (EPS) forming biofilms and limiting the desalination efficiency of secondary wastewater effluents, particularly of RO membranes. Both proteins initiate a complex process of mineralization in SSE.

Scattering experiments of SSE-H_2O and SSE-D_2O solutions performed 4 days after preparation provided evidence of amorphous calcium phosphate (ACP) particles of 180 ± 16 Å diameter and of $8 \cdot 10^{-6}$ volume fraction. Figure 2 shows a scattering pattern immediately after mixing BSA and SSE [1]. Strong scattering at small Q shows the formation of µm large particles of fractal structure with an exponent of (3.38 ± 0.06). This scattering is formed within a few minutes of mixing and remains stable for several hours. At large Q scattering from BSA monomers is visible, showing that only 20 % of the protein is involved in mineralization. Those experiments performed with varying content of SSE-H_2O and SSE-D_2O (thereby changing the scattering contrast) identified the µm large particles as protein-mineral-particles (PMP) of about 40 % organic volume fraction, which also explains the fractal exponent. A schematic representation of a PMP is shown in the inset of figure 2; protein-mineral composites (green circle) exist beside protein monomers (red dots). The volume fraction of the PMP's is determined as $2 \cdot 10^{-4}$ which is too large for calcium phosphate to be the only mineral composite. Investigating the solution product of possible mineral polymorphs in SSE, the formation of hydroxyapatite and of calcium carbonate PMP's is suggested.

The SANS data clearly show that mineralization is minimized in the absence of organic molecules. Another strategy could be to enforce calcium phosphate and carbonate mineralization in the effluent by introducing organic molecules and filtering them out by subsequent UF/NF treatment, i.e. to eliminate phosphate and carbonate by coagulation.

Acknowledgement

This work was funded by the Ministry of Science, Culture and Sport (MOST) and the Bundesministerium für Bildung und Forschung (BMBF).

[1] V. Pipich et al., Langmuir 29, 7607 (2013).
[2] http://www.water-technology.net/projects/sorek-desalination-plant/
[3] Frankfurter Allgemeine (FAZ): „Wasser für das Tote Meer" vom 10.12. (2013).
[4] Z. Steiner et al., Environ. Sci. Technol. 44, 7937 (2010).

$[Be(ND_3)_4]Cl_2$: Synthesis and crystal structure

F. Kraus[1], S. A. Baer[1], M. Hoelzel[2], A. J. Karttunen[3]

[1]Department Chemie, Technische Universität München, Garching, Germany

[2]Heinz Maier-Leibnitz Zentrum (MLZ), Technische Universität München, Garching, Germany

[3]Department of Chemistry, University of Jyväskylä, Jyväskylä, Finland

Reaction of $BeCl_2$ with dry liquid ND_3 and subsequent removal of the solvent leads to the colorless microcrystalline powder $[Be(ND_3)_4]Cl_2$. It crystallizes in the orthorhombic space group *Pna*2_1 with a = 9.395(4), b = 11.901(6), c = 6.761(3) Å, V = 755.9(6), and Z = 4 at 27 °C, and a = 9.3736(8), b = 11.8162(12), c = 6.6596(6) Å, V = 737.62(12), and Z = 4 at –269.6 °C. The structure contains the tetrahedral tetraammineberyllium(II) cation [1].

Upon condensation of liquid ammonia onto anhydrous $BeCl_2$, the solvent is absorbed and a white solid is formed. Removal of the liquid ammonia and subsequent warming to room temperature leads to the formation of tetraammineberyllium(II) chloride $[Be(NH_3)_4]Cl_2$ (compound **1-H**).

Structure solution and refinement

The X-ray powder pattern of compound **1-H** could be indexed and led to an orthorhombic unit cell with lattice parameters a = 9.3878(3), b = 11.8965(4), c = 6.7637(3) Å and cell volume V = 755.39(5) Å^3. These cell parameters can not be associated with $[Be(NH_3)_4]_2Cl_4 \cdot 17NH_3$ [2], or $BeCl_2$, or any other known compound. $[Be(NH_3)_4]Cl_2$ was reported to be isotypic to K_2BeCl_4 [3]; however, our powder patterns do not support this statement and look completely different. Extinction conditions pointed to the orthorhombic space groups *Pna*2_1 and *Pnma*. We were able to solve the structure of compound **1-H** in both space groups and perform Rietveld refinements which yielded reasonable R values. Structural models with the positions of two chloride ions and four nitrogen atoms in a tetrahedron-like arrangement were also obtained.

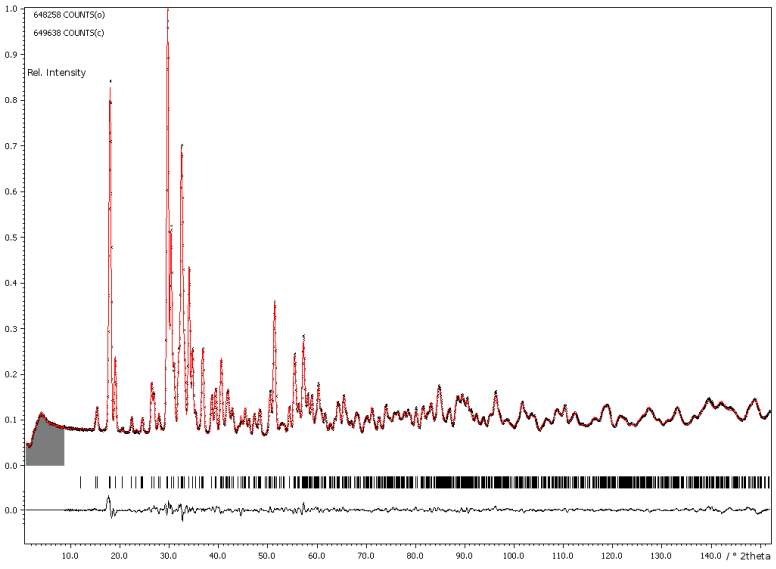

Figure 1: Neutron diffraction pattern of $[Be(ND_3)_4]Cl_2$ at –269.6 °C: experimental data (black crosses), calculated Rietveld profile (red), and difference profile (bottom, black). The reflection positions calculated are shown as black ticks.

The need for structure analysis using neutrons

Due to the X-ray data we were not able to refine atom positions and displacement parameters in a sensible manner and, evidently, we were not able to locate the H atoms at all. Thus, a structure determination on $[Be(ND_3)_4]Cl_2$ (**1-D**) using neutron diffraction at 27 and –269.6 °C was undertaken. No phase change was observed upon cooling from 27 to –269.6 °C, as cell parameters remained similar and no additional reflections were observed. The reflection conditions also pointed to the space groups *Pna*2_1 and *Pnma*. Rietveld refinements on the datasets obtained at both temperatures only led to satisfactory results for the space group *Pna*2_1. The aberration from the centrosymmetric space group *Pnma* was checked using PLATON and is quite strong [4], especially (and anticipated) for the –269.6 °C structure with a fit of only 60 % for the mirror plane in question. At 27 °C the fit of the mirror plane is 90 %. The neutron powder pattern observed at –269.6 °C. and the calculated Rietveld

profile are shown in figure 1. For crystallographic details see table 1.

The asymmetric unit contains the tetraammine-D12 beryllium(II) cation with twelve unique deuterium and four independent nitrogen atoms, which coordinate one beryllium atom in a shape similar to a tetrahedron. Additionally, two chloride anions are present with Be–Cl distances of more than 3.75 Å. The Be–N bond lengths of the $[Be(ND_3)_4]^{2+}$ cation are in the range of 1.71(2) to 1.74(2) Å. They compare well with the Be–N bond lengths found for $[Be(NH_3)_4]^{2+}$ with 1.725(1) to 1.733(3) Å [2]. N–Be–N angles are observed close to tetrahedral ones and are found between 106.9(10) and 111.3(12) °. The N–Be–N angles of the $[Be(NH_3)_4]^{2+}$cation in $[Be(NH_3)_4]_2Cl_4{\cdot}17NH_3$ are observed between 109.4(1) and 109.6(1) °[2]. The N–D distances are found in the range from 0.94(3) to 1.05(2) Å. These are in agreement with usual N–D distances [5]. The $[Be(ND_3)_4]^{2+}$ cation is shown in figure 2 (left). The unit cell of compound **1-D** at -269.6 °C is shown in figure 2 (right).

The structure of $[Be(ND_3)_4]Cl_2$ at 27 °C derived from neutron powder diffraction could only be refined

Compound	$[Be(NH_3)_4]Cl_2$	$[Be(ND_3)_4]Cl_2$	$[Be(ND_3)_4]Cl_2$
Empiric formula	$H_{12}N_4BeCl_2$	$N_4D_{12}BeCl_2$	
Color and habitus	colorless powder		
M [g/mol]	148.04	160.04	
Crystal system	orthorhombic		
Space group	*Pna2*$_1$		
a [Å]	9.3878(3)	9.395(4)	9.3736(8)
b [Å]	11.8965(4)	11.901(6)	11.8162(12)
c [Å]	6.7637(3)	6.761(3)	6.6596(6)
V [Å^3]	755.39(5)	756.0(6)	737.62(12)
Z	4		
pcalc [Mg/m^3]	1.30	1.41	1.44
λ [Å]	1.54051	1.5484	1.5484
T [C]	295	300	3.5
Rp, wRp	0.035, 0.054	0.029, 0.041	0.019, 0.023
R(F2) (all data), wR(F2) (all data)	0.084, 0.094	0.141, 0.160	0.010, 0.014
S (all data)	2.71	11.67	5.65
No. of Reflections, Parameters, Constraints, Restraints	787, 59, 49, 10	1553, 33, 212, 0	1520, 87, 1, 0
2θ range measured (min, max, increment)	5.00, 100.47, 0.005	0.95, 151.90, 0.05	
2θ range refined (min, max)	5.00, 100.47	9.6, 151.9	8.75, 151.9
(Δσ)max	0.0098	0.0182	0.0002

Table 1. Crystallographic details of the compounds **1-H** and **1-D**.

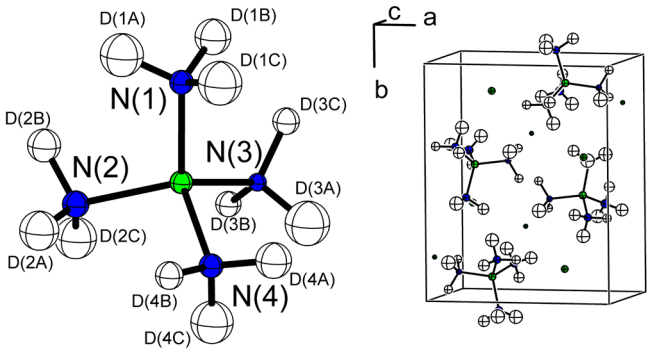

Figure 2: (Left) The tetraammine beryllium(II) cation of the title compound. Isotropic displacement parameters at 70 % at –269.6 °C. (Right) The unit cell of compound **1-D**. Isotropic thermal displacement parameters at 70 % at –269.6 °C.

using a rigid body model for the $[BeN_4]$ unit with structural parameters taken from the –269.6 °C structure. Deuterium atoms could only be refined using a riding model with a 1.2-fold isotropic displacement parameter with respect to the nitrogen atoms. The refinement results are shown in table 1. The X-ray structure of $[Be(NH_3)_4]Cl_2$ at 22 °C was refined using a riding model for the H-atoms, and distance and angle restraints/constraints for the $[Be(NH_3)_4]^{2+}$ unit. Satisfactory refinement results were achieved (table 1).

In summary, we reported on the synthesis of $[Be(ND_3)_4]Cl_2$ and its structure determination using X-ray and neutron powder diffraction techniques. Rietveld refinement on the neutron powder profiles obtained at –269.6 °C led to Be–N distances of 1.71(2) to 1.74(2) Å and N–Be–N angles from 106.9(10) to 111.3(12) ° for the tetraammine-D12 beryllium(II) cation. These structural data are in agreement with those observed for the $[Be(NH_3)_4]^{2+}$ cation in $[Be(NH_3)_4]_2Cl_4{\cdot}17NH_3$ [2]. The reflection conditions determined from the X-ray and neutron powder pattern lead to the possible space groups *Pna2*$_1$ and *Pnma*: The –269.6 °C structure is definitely *Pna2*$_1$, and the 27 °C structure is very likely to be *Pna2*$_1$.

[1] F. Kraus et al., Eur. J. Inorg. Chem. 2013, 4184 (2013).
[2] F. Kraus et al., Chem. Eur. J. 18, 2131 (2012).
[3] A. I. Grigor'ev et al., Zh. Strukt. Khim.10, 469 (1969).
[4] A. L. Spek, PLATON - A Multipurpose Crystallographic Tool, Utrecht University, Utrecht, The Netherlands (2003).
[5] T. Roßmeier, Supramolecular Chemistry with Ammonia - Structural Chemistry of New Ammonia-Proton Complexes, Universität Regensburg (2005).

Proton ordering in $(NH_4)_3H(SO_4)_2$ at low-temperature phase transitions

Y. J. Sohn[1,2], M. Meven[1,3], G. Roth[1], G. Heger[1]

[1]Institut für Kristallographie, RWTH Aachen University, Aachen, Germany

[2]Institut für Energie- und Klimaforschung (IEK-1), Forschungszentrum Jülich GmbH, Jülich, Germany

[3]Jülich Centre for Neutron Science (JCNS) at MLZ, Forschungszentrum Jülich GmbH, Garching, Germany

Single-crystal neutron diffraction was used to investigate the H-atom disorder in $(NH_4)_3H(SO_4)_2$ (triammonium hydrogen disulfate, TAHS), below room temperature. An increase in proton ordering with decreasing temperature is observed in the monoclinic TAHS-III phase, in the $(SO_4)H(SO_4)$ dimer as well as in the NH_4^+ groups. The monoclinic unit cell doubles in the **b** direction in the TAHS-IV phase and indicates a slight distortion of SO_4^{2-} and NH_4^+ tetrahedra. The decisive role of the dynamical disorder of different ammonium groups on successive phase transitions is discussed.

TAHS undergoes five different phase transitions and has superprotonic conductivity in its high-temperature phase above 413 K [1-4]. The strong hydrogen bonds in the $(SO_4)H(SO_4)$ dimers are characteristic of the crystal structure of TAHS and are best described by a double minimum potential with equal site occupancy in the high- and room-temperature phases [5, 6]. As the temperature decreases, the symmetric hydrogen bonds in the dimers become asymmetric, and the dynamically disordered ammonium groups begin ordering successively [7]. A more detailed crystal structure analysis of TAHS was carried out with respect to the precise position as well as the thermal behaviour of the protons owing to the strength of neutron diffraction.

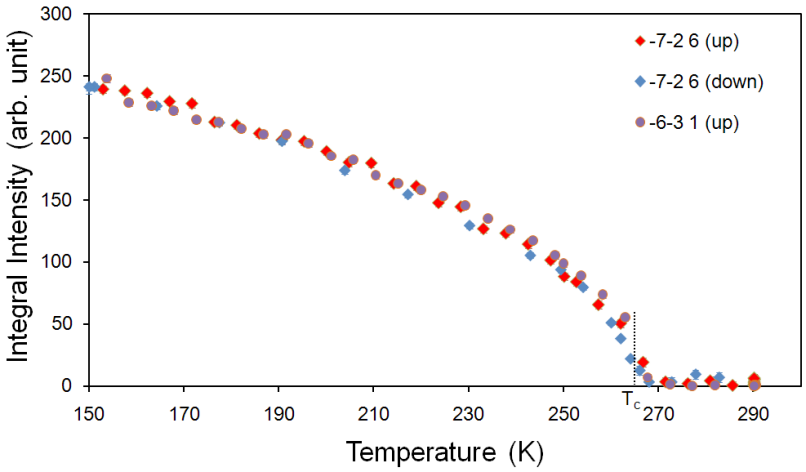

Figure 1: Continuous change of integral intensities for the chosen superstructure reflections from single-crystal neutron diffraction on heating and cooling in TAHS-III.

Single-crystal neutron diffraction at HEiDi

Large TAHS single crystals of several cm in size were grown from an aqueous solution by the temperature-cooling method. Samples of 3 x 3 x 3 mm^3 were used for single-crystal neutron diffraction experiments. A complete data set of Bragg reflection intensities was collected up to $(\sin\theta/\lambda)_{max}$ = 0.7 $Å^{-1}$ on the neutron four-circle diffractometer HEiDi with a wavelength of 0.87 Å. A Sumitomo RDK 101 cryostat was used for low-temperature measurements.

Crystal structure analysis of TAHS-III and TAHS-IV

The II/III phase transition of TAHS at 265 K has a second-order character. A continuous increase in Bragg reflection intensities of some selected superstructure reflections was observed on heating and cooling (fig. 1). For the analysis of the continuous proton ordering in TAHS-III, single-crystal neutron diffraction data were collected at 250 and 150 K. Due to the symmetry reduction, the inversion centre in the middle of the $(SO_4)H(SO_4)$ dimer disappears, and an asymmetric O-H···O hydrogen bond is formed. Assuming the II/III phase transition to be of an order-disorder type, the site occupancy of the split H-atom positions in the dimer was refined. As shown in figure 2, the H-ordering increases with decreasing temperature. The ammonium groups

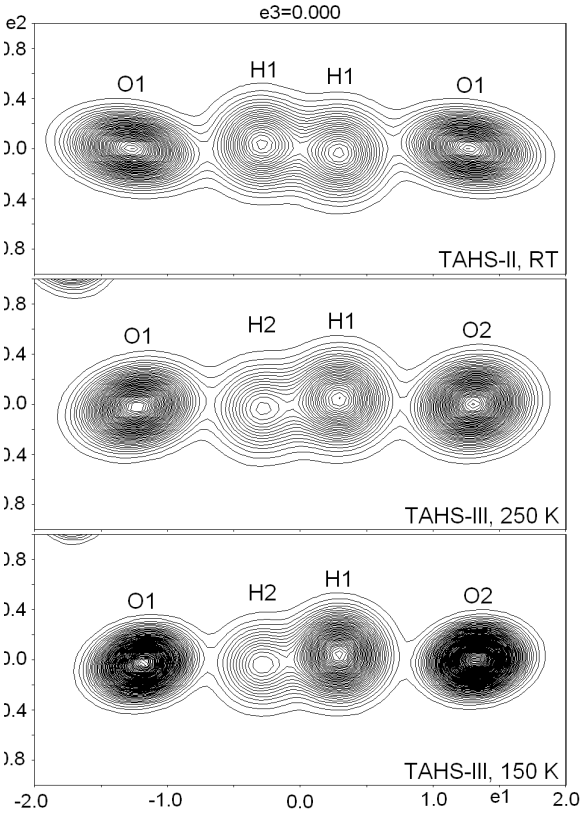

Figure 2: Increase of the H-ordering with decreasing temperature in TAHS-III.

in general positions also begin ordering, hence a distinct shrinkage of their atomic displacement parameters (ADPs) is found in TAHS-III.

The III/IV phase transition at 141 K is also of second-order. The monoclinic unit cell doubles in the **b** direction in TAHS-IV. When projected along the [010] direction, the slight shifts of SO_4^{2-} and the NH_4^+ groups are recognizable (fig. 3). This reorientation of tetrahedral groups occurs due to the presence of stronger and weaker hydrogen bonds in the system.

Phase transition mechanism of TAHS in low-temperature phases

The successive ordering of ammonium groups is very closely related to the structural phase transition of TAHS at low temperatures. Using the single-crystal neutron diffraction data, the ADPs of protons around the nitrogen could be refined. The system of TAHS deals mainly with the rotational disorder of NH_4^+ groups at low temperatures. An ordering of the ammonium groups in general positions occurs at the II/III phase transition. One of the ammonium groups in a special position begins ordering at the next phase transition III/IV. The decrease in ADPs of the other ammonium group in another special position was observed at the IV/V phase transition. From the observation of the ADPs' development for the protons, as well as from the structural information regarding the bond distances and angles of each ammonium group, the successive freezing of the individual groups was identified, which plays a key role in the low-temperature phase transitions in TAHS.

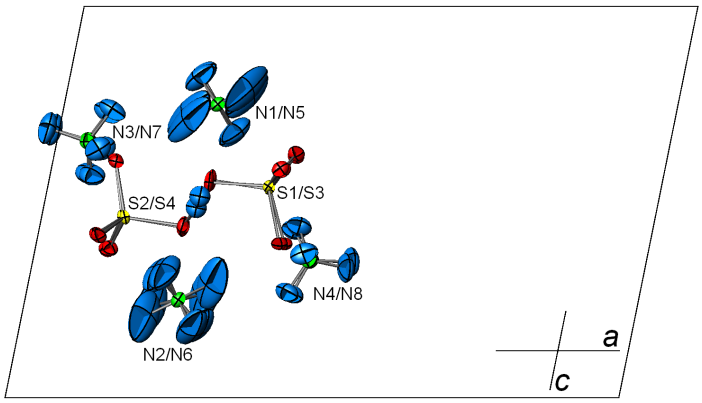

Figure 3: Asymmetric unit of the monoclinic unit cell in TAHS-IV (P2/n) at 138.5 K, projected along [010].

[1] K. Gesi, Phys. Status Solidi 33, 479 (1976).
[2] K. Gesi, Jpn. J. Appl. Phys. 19, 1051 (1980).
[3] L. Schwalowsky et al., J. Phys. Condens. Matter 10, 3019 (1998).
[4] R. H. Chen et al., J. Phys. Chem. Solids 61, 1399 (2000).
[5] Y. J. Sohn et al., Acta Crystallogr., Sect. B 65, 36 (2009).
[6] Y. J. Sohn et al., Acta Crystallogr., Sect. B 67, 116 (2011).
[7] Y. J. Sohn et al., Acta Crystallogr., Sect. B 69, 336 (2013).

Revision of the lithium intercalation into graphitic carbons

O. Dolotko[1,2], A. Senyshyn[1], M.J. Mühlbauer[1,3], H. Ehrenberg[1,3,4]

[1]Materials Science, Technische Universität Darmstadt, Darmstadt, Germany

[2]Heinz Maier-Leibnitz Zentrum (MLZ), Technische Universität München, Garching, Germany

[3]Institute for Applied Materials-Energy Storage Systems, Karlsruhe Institute of Technology, Eggenstein-Leopoldshafen, Germany

[4]Helmholtz-Institute Ulm for Electrochemical Energy Storage, Karlsruhe, Germany

Despite the common use of graphite as the anode in lithium-ion cells, the mechanism of lithium intercalation into graphite is still not completely understood. The evolution of the graphite structure in commercial Li ion cells has been studied *in situ* by using a combination of electrochemistry and high-resolution neutron powder diffraction. The phase diagram for lithiated carbons has been reconsidered and alternative ordering models for the $Li_{x<0.5}C_6$ have been proposed. Up to seven new phases of $Li_{x<0.5}C_6$ type have been detected during cell charge/discharge.

Graphite anode

Nowadays, graphite is the most commonly employed anode material in Li-ion batteries, its general intercalation feature being the formation of Li_xC_6 compounds, called stages. Of the different stages, crystal structure models are known for LiC_6 (stage I) and LiC_{12} (stage II) only. There have been long standing debates regarding the lattice metrics and atomic arrangement in LiC_{18} (IIL stage), while there have been no reports on higher-ordered lithium intercalated carbons such as stages III, IV, VIII, or I'. One reason for this lack of knowledge is the limited ability of X-ray to localize light elements for a precise structure determination. "*In-operando*" neutron scattering characterization of the entire cell during electrochemical cycling is a promising approach, providing unique information about processes occurring inside the cell, including localization of Li atoms. *In situ* investigation also eliminates any risks of material oxidation, electrolyte evaporation or cell charge changes.

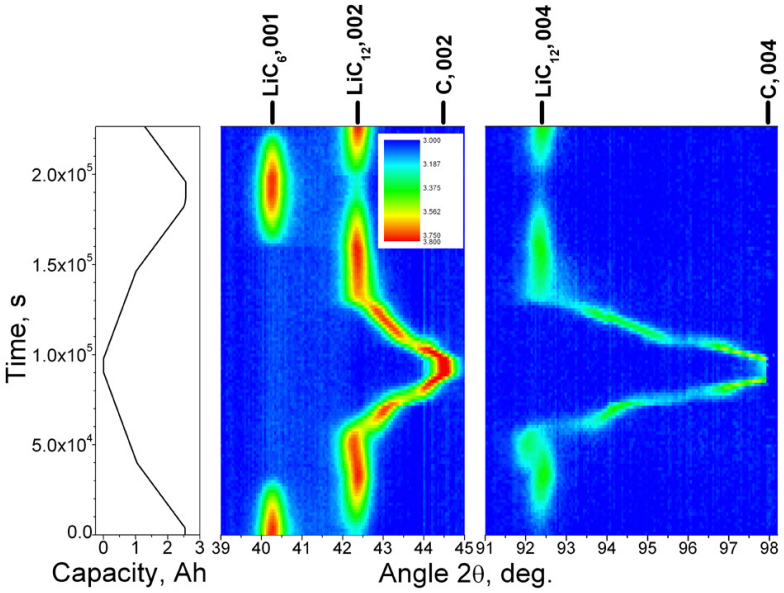

Figure 1: The time evolution of the diffraction patterns obtained in two selected 2 Theta regions.

Lithiation into graphite

A cylindrical $LiCoO_2|C|$ based Li-ion cell of 18650-type was studied "*in-operando*" at the high-resolution neutron powder diffractometer SPODI (λ = 2.53633(1) Å). In contrast to the $LiCoO_2$, which remains isostructural during the cell cycling [1, 2], a sequence of phase transformations is observed for the lithium intercalation into graphite. Stage I (LiC_6) forms when the cell is charged above 1400 mAh, ~$0.5Q_{max}$. This is the lithium intercalated carbon hosting the maximum amount of lithium (at ambient pressures). Its crystal structure resembles the structure of graphite consisting of hexagonal graphene sheets with A-A-stacking in *c* [3]. The structure of the stage II (LiC_{12}) is very similar but only every second lithium layer is occupied, resulting in a doubling of the lattice parameter *c* and a slight reduction of the (002) interatomic spacing compared to the (001) of LiC_6 due to A-A-B-B-A-A-… stacking.

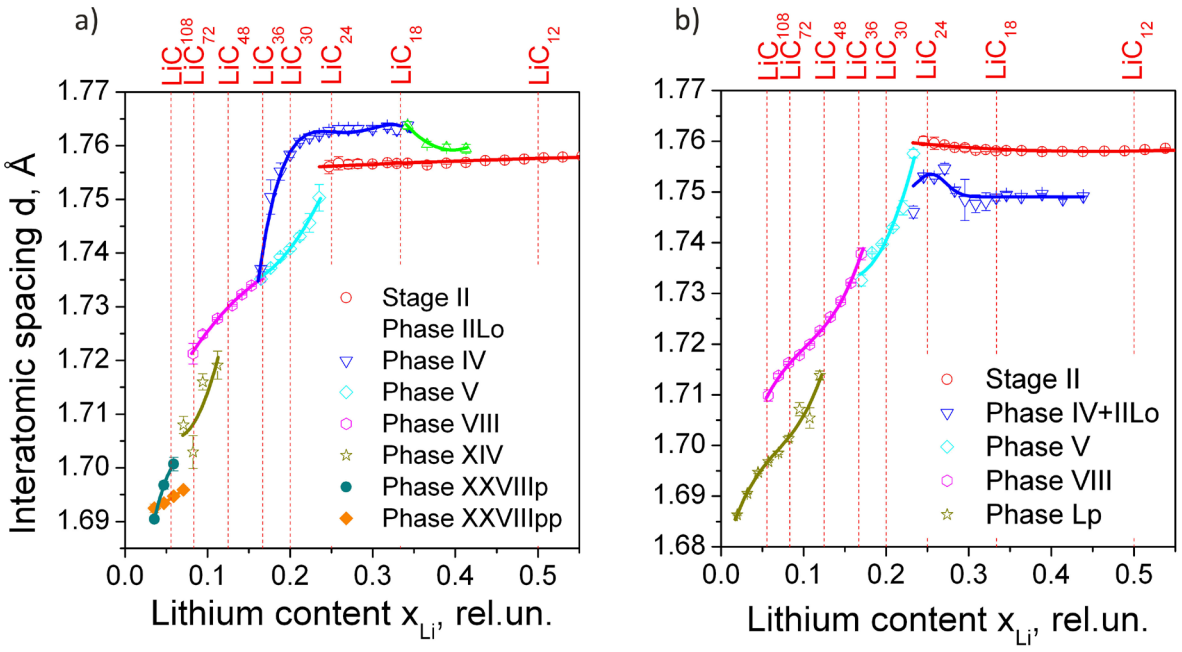

Figure 2: Interatomic spacing of different lithium intercalated carbons depending on the Li content during discharge (a) and charge (b).

The complicated non-continuous transformation of LiC_{12} into graphite consists of different stages and shows a clear asymmetry between discharge and charge (fig. 1). The structural similarity of the higher ordered stages makes their identification non-trivial. In order to reveal subtle changes, a single profile decomposition technique has been applied to the second order diffraction signals from (004) LiC_{12} to (004) C. Assuming the LiC_6-to-LiC_{12} transformation occurring at x_{Li} = 0.5, the lithium content in other phases can be quantified from the cell capacity.

The analysis of interatomic spacings and intensities revealed the presence of lithiathed carbons with well-defined separation. This is shown in terms of a lithium-carbon phase diagram (fig. 2a and 2b). While the evolution of stages I and II indicates stability of their interatomic spacings with minor deviations, the higher-ordered lithiated carbons, termed as “phases”, display a Vegard behaviour instead of forming well-defined “stages”. Phases LiC_{6N}, with integer N close to IV, V, VIII have clearly been observed, whereas no traces of phase III corresponding to LiC_{18} have been noticed. Instead of LiC_{18}, a diffuse and broad signal has been observed as a tail on the LiC_{12} peak. It is more pronounced during discharge with a maximum at x_{Li} = 0.379 and corresponds to a LiC_{16} composition (stage IIL). In total, two stages and four phases were identified during charging, while for the discharge two stages and seven phases were observed.

Lithium-graphite twisted bilayer behaviour

The observation of peaks having non-zero *h* and *k* indices revealed a formation of superstructure in a narrow capacity range. After checking different superspace index/modulation vector configurations, the best agreement was found to be with the modulation vector **k** = (α,α,0), on reducing the α upon lithium extraction. Such superstructural modulation may indicate that the mechanism of lithium intercalation into graphite is different from the commonly-accepted stage formation. An alternative structural model has been proposed where the observed modulations can be associated with a certain twist of graphene layers producing regions with A-A and A-B (B-A) type of graphene stacking, with the A-A arrangement of graphene layers being the obvious requirement for lithium intercalation [3].

[1] A. Senyshyn et al., J. Power Sources 203, 126 (2012).
[2] O. Dolotko et al., J. Electrochem. Soc. 159, A2082 (2012).
[3] A. Senyshyn et al., J. Electrochem. Soc. 160, A3198 (2013).

$H_2Ti_6O_{13}$: Synthesis, crystal structure and electrochemical Li insertion properties

J. C. Pérez-Flores[1], C. Baehtz[2], M. Hoelzel[3], A. Kuhn[1], F. García-Alvarado[1]

[1]Fac. Farmacia, Dep. Química, Universidad CEU San Pablo, Madrid, Spain

[2]Institute of Ion Beam Physics and Materials Research, Helmholtz-Zentrum Dresden Rossendorf, Dresden, Germany

[3]Heinz Maier-Leibnitz Zentrum (MLZ), Technische Universität München, Garching, Germany

Neutron diffraction studies have been carried out on $H_2Ti_6O_{13}$ which is a promising cathode material for Li-ion batteries. The structural data obtained are related to the electrochemical properties. $H_2Ti_6O_{13}$ is obtained by successive $Na^+/Li^+/H^+$ ion exchange of $Na_2Ti_6O_{13}$. Its crystal structure, solved from both synchrotron and neutron powder diffraction, shows a C2/m monoclinic symmetry. The H^+ sites in the structure close to the O3 atomic position to form a covalent O-H bond, while exhibiting a classic asymmetric hydrogen bond with O5. $H_2Ti_6O_{13}$ performance in Li/-ion batteries leads one to propose it as an innovative negative electrode, yielding ca. 170 mAh g^{-1} of reversible capacity at 1.5 V.

$H_2Ti_6O_{13}$ can be used as negative electrode material for advanced Li-ion rechargeable batteries because it affords very low toxicity properties and an easy synthesis procedure, as well as requiring inexpensive and abundant raw materials. Its electrochemical performance is quite competitive and appealing when compared with the present state-of-art, the spinel $Li_4Ti_5O_{12}$ [1-3].

Neutron powder diffraction at SPODI

$H_2Ti_6O_{13}$ is synthesized by proton exchange on $Li_2Ti_6O_{13}$ using C_6H_5COOH at 125ºC in air for 72 hours [2,3]. Neutron powder diffraction (NPD) patterns were collected at SPODI (FRM II, λ = 1.5481 Å). Synchrotron diffraction (SXRD) experiments were carried out at BM20 (HZDR at ESRF, λ = 0.495937 Å). Diffraction patterns were analyzed and crystal structures determined by the Rietveld [4] method using FullProf [5]. H atoms were sited within the $[Ti_6O_{13}]^{2-}$ skeleton framework by Fourier synthesis maps.

Lithium insertion/de-insertion properties were analyzed using coin cells (CR2032) assembled according to: (–)Li//LP30//$H_2Ti_6O_{13}$(60%)(+).

Structural characterization

Preliminary $H_2Ti_6O_{13}$ XRD confirms the monoclinic symmetry, C2/m, in agreement with the parent $Li_2Ti_6O_{13}$. Basically, diffraction patterns suggest that the initial skeleton structure is retained upon acidic exchange reaction. More powerful techniques, such as SXRD and NPD, reveal subtle structural details.

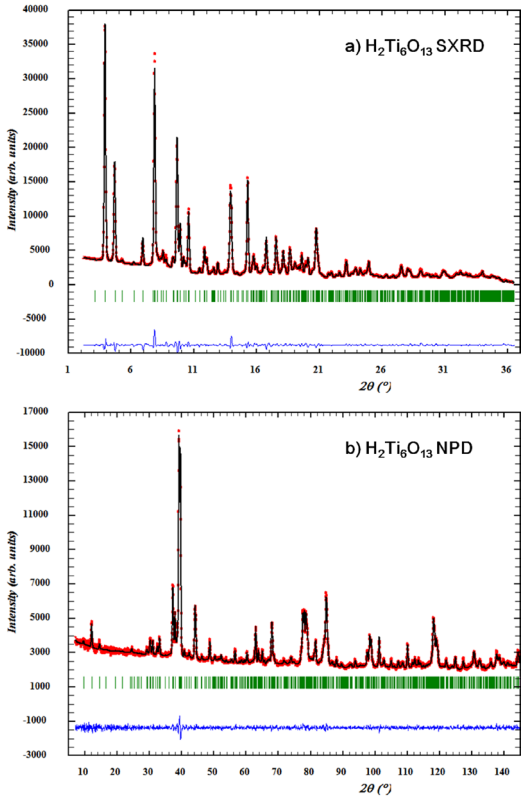

Figure 1: Rietveld refinement of a) SXRD and b) NPD patterns of $H_2Ti_6O_{13}$.

For refinement of the $H_2Ti_6O_{13}$ structure, only Ti and O have been considered. No attempts have been made to place the H atom due to its negligible contribution to the pattern relative to the other heavier atoms. Figure 1 shows the graphical result of the Rietveld refinement of $H_2Ti_6O_{13}$. The $H_2Ti_6O_{13}$ SXRD pattern (fig. 1a) reveals that (200) and (020) peaks are shifted to higher angles when compared to those of the original $Li_2Ti_6O_{13}$. This observation is consistent with the shrinking of the *a* axis and *b* axis in $H_2Ti_6O_{13}$. Moreover, the shift of the (003) peak towards lower angles agrees with the c axis increase upon ion exchange. Both trends lead to a small decrease of the unit cell volume (~3%).

NPD (fig. 1b) allows one to identify and locate the H (and Li) atoms in the structure using two dimensional Fourier difference maps to detect H (or Li) using their negative scattering length densities [6]. The H atoms were found to occupy the *4i* (*x*,0,*z*) crystallographic site, (0.0017, 0, 0.3121). Interestingly, Li atoms of $Li_2Ti_6O_{13}$ occupy the same *4i* site but different coordinates; Li exhibits a strongly distorted square planar Li-O_4 coordination.

When comparing A atoms of $A_2Ti_6O_{13}$ (A = Li, H) structures (fig. 2), H is shifted mainly along the *z* axis towards a more central position within the tunnel. This position yields a O3-H covalent bond and a hydrogen bond with O5.

Electrochemical characterization

$H_2Ti_6O_{13}$ reacts with ≈6 Li atoms per formula unit in the 3 - 1 V range, yielding a specific first discharge capacity of 315 mAh g^{-1}, close to its theoretical discharge capacity involving full reduction of Ti^{4+} to Ti^{3+}. The main electrochemical process occurs at ≈1.5 V and a shorter earlier one at ≈1.87 V. Subsequently, an irreversible transformation to an unidentified compound is related to significant capacity loss. The compound exhibits good cycling properties with a reversible capacity of 170 mAh g^{-1} (similar to $Li_2Ti_6O_{13}$). The structural and electrochemical similarities of $H_2Ti_6O_{13}$ and $Li_2Ti_6O_{13}$ can be satisfactorily explained by a

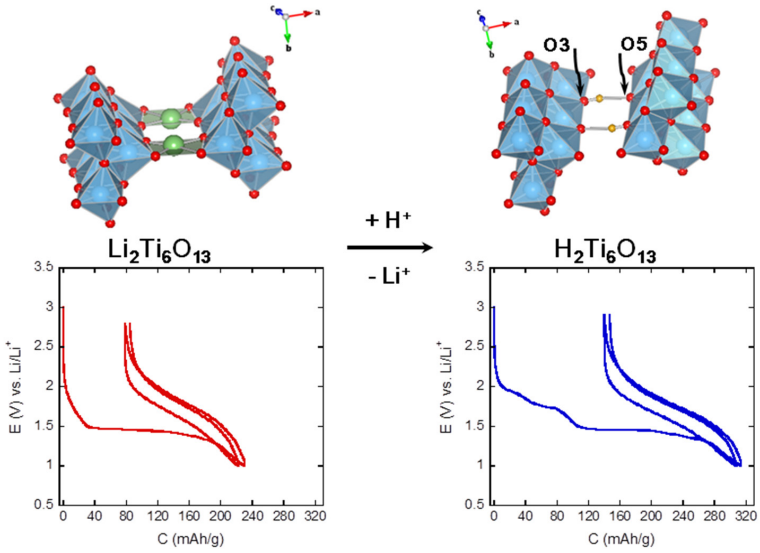

Figure 2: Schematic representations of crystal structures (up) and two first discharge-charge curves (down) of $A_2Ti_6O_{13}$ (A = Li, H).

two-stage process.

$$H_2(Ti^{4+})_6O_{13} + 2\,e^- + 2\,Li^+ \longrightarrow Li_2(Ti^{+4})_6O_{13} + H_2 \quad (1a)$$

$$Li_2(Ti^{4+})_6O_{13} + 4\,e^- + 4\,Li^+ \longrightarrow Li_6(Ti^{3+})_4(Ti^{+4})_2O_{13} \quad (1b)$$

Conclusions

$H_2Ti_6O_{13}$ was obtained by Li^+/H^+ ion exchange on $Li_2Ti_6O_{13}$ using benzoic acid. The structural characterization showed that the $[Ti_6O_{13}]^{2-}$skeleton framework remains after exchange reaction. Main lattice parameter changes affect the distortion in the ac plane. Its electrochemical behaviour leads one to propose that two Li atoms react with $H_2Ti_6O_{13}$ in the first stage of the discharge to yield H_2 and $Li_2Ti_6O_{13}$. The reversible capacity reaches 170 mAh g^{-1} at 1.7 V, which is well maintained upon cycling.

[1] R. Dominko et al., Electrochem. Commun. 8, 673 (2006).
[2] J. C. Pérez-Flores et al., J. Power Sources 196, 1378 (2011).
[3] J. C. Pérez-Flores et al., RSC Advances 2, 3530 (2012).
[4] H. Rietveld, Acta Crystallogr. 20, 508 (1996).
[5] J. Rodríguez-Carvajal, Physica B 192, 55 (1993).
[6] J. C. Pérez-Flores et al., Dalton Trans. 41, 14633 (2012).

Anisotropy of water dynamics in clays: Insights from molecular simulations for QENS analysis

V. Marry[1,2], E. Dubois[1,2], N. Malikova[3], J. Breu[4], W. Häussler[5]

[1]Physicochimie des Electrolytes, Colloïdes et Sciences Analytiques, Université Pierre et Marie Curie (UPMC), Paris, France

[2]Centre National de la Recherche Scientifique, Paris, France

[3]Laboratoire Léon Brillouin (CEA - CNRS), CEA Saclay, Gif-sur-Yvette, France

[4]Lehrstuhl für Anorganische Chemie I, Universität Bayreuth, Bayreuth, Germany

[5]Heinz Maier-Leibnitz Zentrum (MLZ) and Physik-Department E21, Technische Universität München, Garching, Germany

NRSE measurements on a synthetic hectorite clay/water system were analyzed in the light of MD simulations. The simulations containing two layers of confined water between the clay layers demonstrate that water diffusion perpendicular to the clay layers has to be taken into account in the experimental data analysis. A diffusive model having only two fit parameters $D_{\perp}$ and $D_{\parallel}$ containing clear physical significance is well adapted to the NRSE data analysis at moderate scattering vector values.

How does water diffuse in clays?

In the work highlighted here, we report on the dynamics of water confined in a quasi-planar geometry of low-hydrated charged clays [1]. We perform a combined neutron scattering and molecular dynamics simulation study which is motivated by the fact that both methods give direct access to the intermediate scattering function in the time-domain and the comparison of the results is more direct than with time-of-flight methods, for example. Water dynamics in confining media is of great importance in chemistry (heterogeneous catalysis), biotechnology (encapsulation) and soil science (permeability and transport in clays). Clays are used for many technological applications, one of which is the underground storage of radioactive waste. The dynamics of water and ions in clays has, in the past, been studied both experimentally [2-7] and via simulation techniques [8,9]. The synthetic fluorohectorite clay studied here is a well-characterized [10] homogeneous model system, in which confined water is structured as two layers between the adjacent planar clay surfaces. We compare the observed H_2O motion to the reference of bulk water in a range of temperatures, which allows us to determine the related activation energies. As an extension to previous studies, where we considered a pure two-dimensional (2D) motion in the interlayer [10,11,12], here

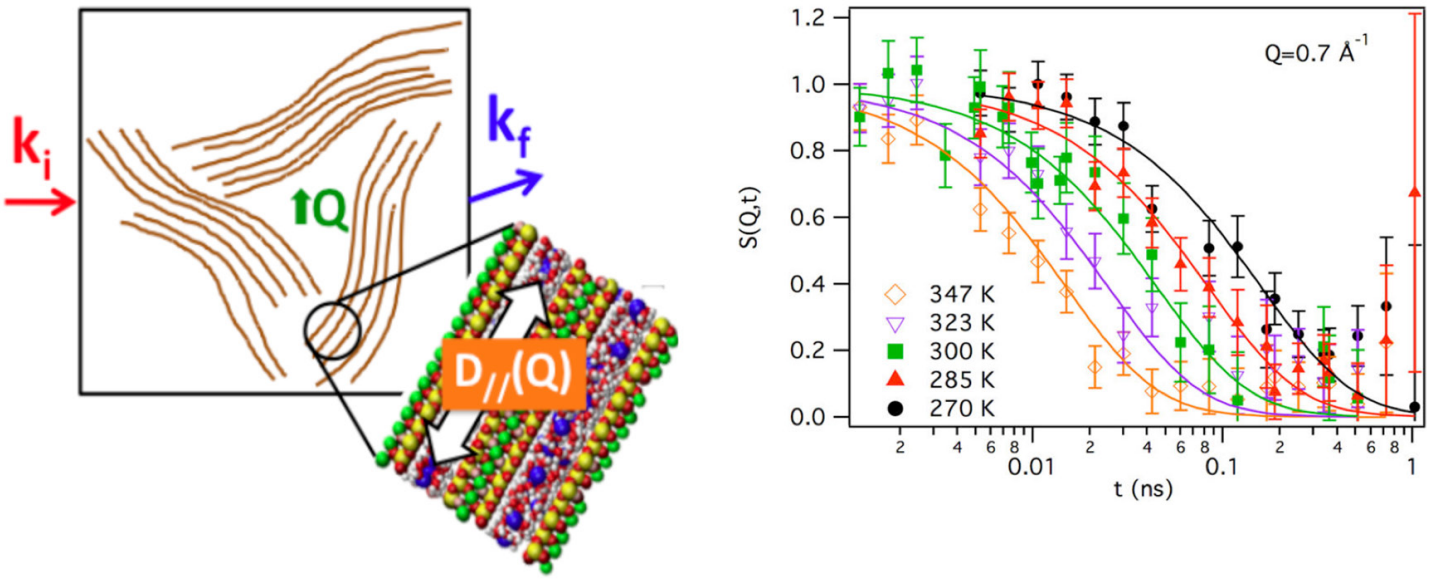

Figure 1: Sketch of the water-clay system under study (left), $S_{inc}(Q,t)$ measured on the hectorite clay system (right), both from reference 1.

we investigate H_2O translational dynamics both parallel and perpendicular to the clay surfaces. The presence of two H_2O layers allows some mobility in this direction as already suggested in reference 13. Our approach is based on a close combination of experiments and simulations, as we associate quasi-elastic neutron scattering experiments with molecular dynamics (MD) simulations, both of which give access to molecular motions on the picosecond to nanosecond time scale.

The methods of choice: molecular dynamic simulations and dynamic neutron scattering

In molecular simulations, all mobile species are described at the atomic level and moved according to Newton's equations of motion. The interactions between the atoms are taken as the sum of an electrostatic interaction, a van der Waals attraction, and an interatomic repulsion. In the present study, we choose the flexible clayFF force field [14] and the TIP4P/2005 [15] for clay and water respectively, which are the best models when it comes to reproducing experiments. Neutron resonance spin echo [16] (NRSE) experiments are performed at RESEDA [17] for six temperatures between 240 and 347 K at spin echo times 1 ps - 1 ns. The scattering vector values are chosen in the range 0.3 $Å^{-1} < Q < 0.9$ $Å^{-1}$, to avoid Bragg peaks. The signal of the sample is corrected for the empty cell signal and for the instrumental resolution measured on a graphite sample. The incoherent intermediate scattering function $S_{inc}(Q, t)$ obtained is shown in figure 1 (symbols). These are compared to the results of the MD simulations (solid lines).

The results from a combination of simulations and neutron spin echo

The comparison of NSE with MD data is direct, as both techniques give access to $S_{inc}(Q, t)$ in the time-domain. The combination of MD simulations and experimental data allows the separation of several parameters that cannot be determined from the experiments alone, for example the parallel and perpendicular diffusion coefficient. As in most studies on dynamics in confinement, we use unoriented powder clay samples in our experiments. The NSE signal being averaged along all the directions with respect to the confinement is difficult to analyze in detail unless some parameters are determined independently, such as the ratio between perpendicular and parallel diffusion coefficients. Thanks to the detailed analysis of the simulated data, separate diffusion mechanisms that contribute to the total dynamic picture can be separated and a clear physical significance for the two fitting parameters exists, given the geometry of the system. Considering this model and its limits, diffusion coefficients slowed down by a factor of 5 compared to bulk water are extracted. The activation energy of the diffusion processes is higher than in bulk water, especially when low temperatures are involved. The simulations suggest that the high activation energy is more probably linked to the presence of the cations than to the formation of hydrogen bonds between H_2O molecules and surface oxygen atoms. To give more weight to these conclusions, however, an improvement in the force field used in the simulations is necessary and is in progress.

[1] V. Marry et al., J. Phys. Chem. C 117, 15106 (2013).
[2] L. Michot et al., J. Phys. Chem. C 116, 16619 (2012).
[3] W. Gates et al., J. Phys. Chem. C 116, 5558 (2012).
[4] G. Bowers et al., J. Phys. Chem. C 115, 23395 (2011).
[5] J. Manjanna et al., Appl. Clay Sci. 43, 208 (2009).
[6] S. Savoye et al., J. Contam. Hydrol. 125, 102 (2011).
[7] M. Glaus et al., Geochim. Cosmochim. Acta 74, 1999 (2010).
[8] C. P. Morrow et al., J. Phys. Chem. C 117, 5172 (2013).
[9] I. Bourg et al., Environ. Sci. Technol. 44, 2085 (2010).
[10] N. Malikova et al., J. Phys. Chem. C 111, 17603 (2007).
[11] N. Malikova et al., Phys. Rev. Lett. 101, 265901 (2008).
[12] V. Marry et al., Environ. Sci. Technol. 45, 2850 (2011).
[13] V. Marry et al., J. Phys.: Condens. Matter 20, 104205 (2008).
[14] R. T. Cygan et al., J. Phys. Chem. B 108, 1255 (2004).
[15] J. L. F. Abascal et al., J. Chem. Phys. 123, 234505 (2005).
[16] R. Gähler et al., J. Phys. 49, 1195 (1988).
[17] W. Häussler et al., Meas. Sci. Technol. 19, 034015 (2008).

Development of Co-Re-based alloys for ultra-high temperature applications in gas turbines

D. Mukherji[1], R. Gilles[2], L. Karge[2], P. Strunz[3], and J. Rösler[1]

[1]Institut für Werkstoffe, Technische Universität Braunschweig, Braunschweig, Germany

[2]Heinz Maier-Leibnitz Zentrum (MLZ), Technische Universität München, Garching, Germany

[3]Nuclear Physics Institute ASCR, Prague, Czech Republic

Co-Re alloy development is prompted by the search for new materials for future gas turbines. Understanding transformation and microstructural stability in the Co-Re-Cr system at high temperatures is essential for successful alloy development. In-situ neutron and synchrotron measurements are being used extensively for this purpose. A joint DFG project with TU-Braunschweig (alloy developer) and MLZ (providing neutron methods) was recently started to study the strengthening TaC precipitates (10 – 60 nm size). In particular, the influence of the C to Ta ratio in the Co-Re alloy is being investigated to optimize the alloy strength and long-term stability at high temperatures.

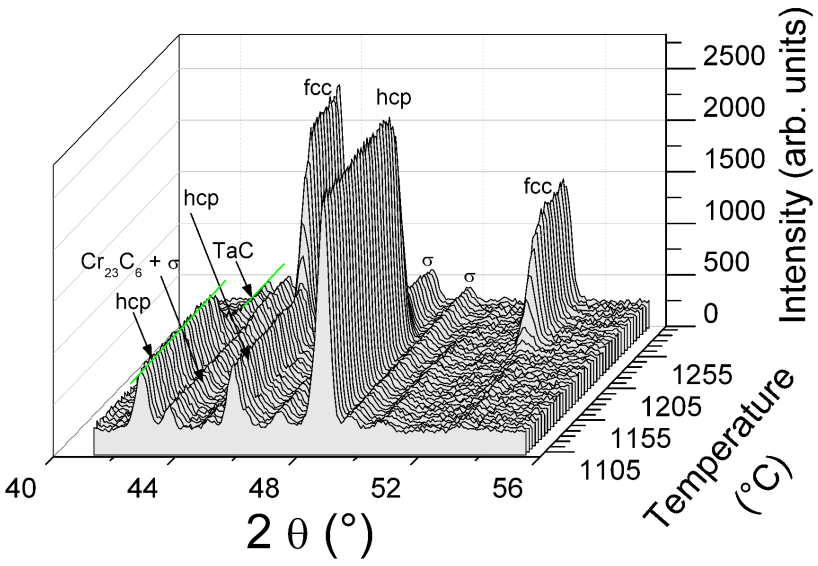

Figure 1: 3D plot showing change in diffraction peaks in Co-17Re-23Cr-1.2Ta-2.6C alloy with increasing temperature (from 1100 to 1300 °C). Major diffraction peaks from two Co matrix phases, two carbides and the σ phase are visible. It clearly shows the allotropic phase transformation of the Co-matrix from the low temperature ε-Co (hcp) to the high temperature γ-Co (fcc).

Future gas turbines need new high temperature alloys

The Co-Re based alloys are a new class of high temperature alloy designed and developed at the Technische Universität Braunschweig [1] for applications in future gas turbines as the current workhorse Ni-superalloys are reaching their limits. In order to increase application temperatures, the melting point of Co-based alloys was enhanced by adding the refractory element Rhenium and the first Co-Re-based alloy with a melting range of more than 200 °C greater than that of the single crystal Ni-superalloys was introduced in 2007 [2]. The Re addition stabilizes the ε-Co (hcp) phase as matrix, in contrast to the commercial co-alloys currently used where the matrix is γ-Co (fcc).The alloys are mainly strengthened via carbides, particularly the MC carbides of type TaC. Neutron facilities at FRM II, BER II, PSI and BNC were widely used to study the composition and phase structures in Co-Re alloys [3, 4]. Complementary diffraction and small angle scattering measurements, especially in-situ at high temperatures, were performed at the FRM II, where the hysteresis in the hcp ⇄ fcc phase transformation in the Co matrix phase was observed for the first time in a Co-Re-Cr-Ta-C alloy at temperatures above 1200 °C [5]. Figure 1 shows the diffraction peaks of the different phases and their evolution with increasing temperature from 1100 to 1300 °C in a 3D-plot, where the Co matrix transformation is clearly seen.

In-situ SANS characterize fine dispersion of strengthening TaC precipitates

Evolution of the TaC precipitates during a heat treatment cycle was monitored and selected results from in-situ SANS measurements during

holding at temperatures of 1400, 1200 and 1100 °C are shown in figure 2. The small TaC precipitates give a strong scattering contribution and the change in their size and volume fraction is clearly visible in SANS. The alloy was first heated to 1400 °C, where all fine precipitates (< 100 nm) were dissolved. Subsequent stepwise cooling from 1400 °C and holding at different temperatures of interest in the application temperature range of the alloy shows that fine TaC re-precipitates during hold at 1100 °C and the small particles grow to a size of approximately 60 nm and their volume fraction continuously increases. The experimental set up at SANS-1 is shown in figure 3.

Further evaluation of the results as well as new measurements in future will provide information on high temperature stability and the coarsening behavior of the TaC precipitates. One important question is - how they are affected by the change in the C / Ta ratio in the Co-Re alloy compositions?

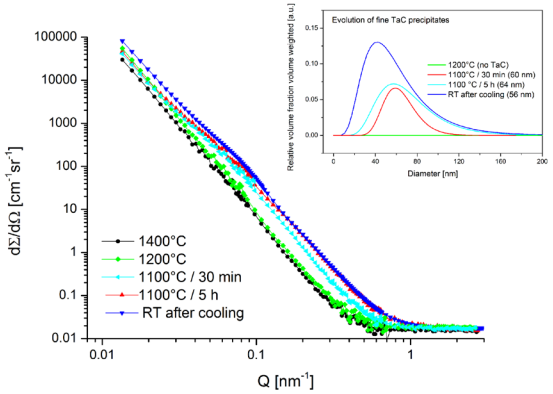

Figure 2: SANS patterns from the Co-17Re-23Cr-1.2Ta-2.6C alloy obtained at different temperatures during an in-situ heating / cooling cycle. Inset: Size distributions of TaC precipitates (volume weighted) calculated from the SANS patterns.

Figure 3: Setting up the vacuum furnace for high temperature measurements at SANS-1 instrument.

[1] D. Mukherji et al., J. Phys: Conf. Ser. 240, 012066 (2010).
[2] J. Rösler et al., Adv. Eng. Mater. 9, 876 (2007).
[3] D. Mukherji et al., Metall. Mater. Trans. A 44, 22 (2013).
[4] R. Gilles et al., J. Phys: Conf. Ser. 340, 012052 (2012).
[5] D. Mukherji et al., Mater. Lett. 64, 2608 (2010).

Chlorine determination in archaeological iron artefacts by PGAA

R. Gebhard[1], F. E. Wagner[2], U. Wagner[2], P. Albert[1], Z. Revay[3], P. Kudejova[3], K. Kleszcz[3]

[1]Archäologische Staatssammlung München, München, Germany

[2]Physik-Department E15, Technische Universität München, Garching, Germany

[3]Heinz Maier-Leibnitz Zentrum (MLZ), Technische Universität München, Garching, Germany

Over the past 3000 years, iron has become one of the most important materials in prehistoric and historic cultures. Therefore, the preservation of iron artefacts plays a predominant role in archaeological museums. After their excavation, however, archaeological iron artefacts often suffer from rapid corrosion. Chlorine is thought to play a major role in this process. For adequate conservation measures, it is therefore important to know the chlorine content of the artefacts and how effective methods of chlorine removal are [1]. Prompt Gamma Activation Analysis (PGAA) is ideally suited for determining the chlorine content of sizeable pieces without destroying the valuable objects. One can study freshly excavated objects, and asses the effectivity of chlorine removal by leaching in hydrous solutions or by heating. Measurements on some 80 samples have yielded chlorine contents between about 50 and several thousand ppm, depending on the conservation treatment, but so far show no correlation with the location and date of excavation.

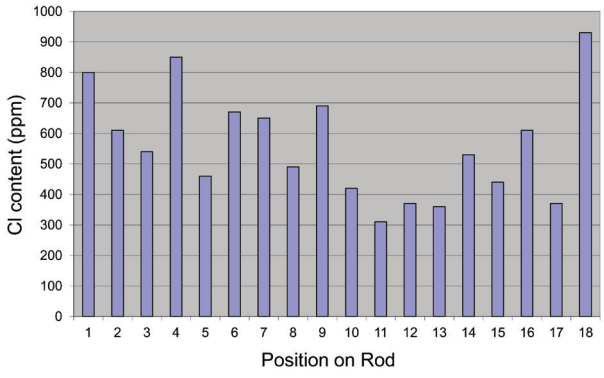

Figure 1: Chlorine contents found in 18 pieces cut out of a 40 cm long Celtic iron rod with a 8 x 15 mm^2 cross section. The data show considerable variations. The high Cl contents of the end pieces can be attributed to the higher surface-to-volume ratios at the ends.

Figure 2: Two heavily corroded iron strap ends (about 8 cm long) used to protect the ends of leather straps from the same grave excavated at Steinheim near Dillingen (Bavaria) in 1996. The upper piece is untreated, the lower one was leached in an alkaline solution of Na_2SO_3 for three months. They look very similar, but the unleached one contains 1300 ppm of Cl, while the leached one contains only 110 ppm.

We first of all had to demonstrate that Prompt Gamma Activation Analysis (PGAA) at MLZ is capable of determining the chlorine contents of iron artefacts with sufficient accuracy. By comparing the intensities of prompt gamma lines of chlorine and iron, one obtains the mass ratio of chlorine and iron in the neutron beam. With a beam size of about 20 x 20 mm^2 of the PGAA setup one can study sizeable objects. Bigger pieces can be scanned spot-by-spot. The standard sample holder can accommodate 6 flat objects about 5 x 5 cm in size. Objects for spot-by-spot scanning may be up to about 40 cm long and 5 cm wide, which means that, for instance, small swords can be studied. Since the neutrons and the high energy gamma rays can penetrate centimeters of iron, rather thick objects can be investigated. The measurements resulted in Cl contents from several tens of ppm up to several thousand ppm. A Cl-content of 50 ppm can be

determined with an accuracy of about 5 % within one hour.

Old and recent excavations

From the archaeological point of view it was of interest to study artefacts that were excavated at different times and sites. There are many objects deposited in the Archaeologische Staatssammlung München that were excavated in Bavaria as early as the end of the 19th century and are still well preserved despite, at best, rudimentary conservation treatments, while other specimens, which were excavated only recently, are heavily corroded. An explanation sometimes proposed for this is that the Cl content in the soil has increased since the introduction of large-scale fertilization with potassium chloride. We therefore studied about 40 artefacts, some excavated recently and some over a century ago. The Cl content was, indeed, found to vary widely, between 40 and 3200 ppm, but with no clear difference between old and recent excavations.

Inhomogeneous distribution of chlorine

Wide variations were also found for the distribution of chlorine within the same iron object. For instance, a forged iron rod about 40 cm long and having a cross section of 8 x 15 mm^2 excavated at the Celtic oppidum of Manching near Ingolsadt (Bavaria) in 1999 was cut into pieces, which were individually analysed. Figure 1 shows that the distribution of Cl along the rod varies considerably and stochastically. Similar results were found for other items of which several spots were analysed.

The effectivity of leaching methods

For purposes of conservation, iron artefacts are often subjected to leaching procedures to remove the chlorine, which is mainly done in alkaline hydrous solutions. In the past, the effectivity of these procedures could be assessed only by analysing the Cl content of the leaching solutions, or by destroying the artefacts for Cl analysis. Using PGAA, the Cl content of the artefacts can be determined in a non-destructive manner. First experiments confirm that leaching

Figure 3: A Celtic nail from the oppidum of Manching (ca. 9 cm long) containing only 37 ppm of Cl after thermal treatment in welding gas (N_2 + 10 % H_2) at 750 °C. The treatment took place 25 years ago and the nail survived with hardly any corrosion. PGAA shows that it contains only 37 ppm of chlorine.

is, indeed, effective, but that some residual Cl remains in the objects. For instance, two objects from the same grave (fig. 2) of which one remained untreated while the other was leached for three months, yielded Cl contents of 1300 ppm and only 110 ppm, respectively. PGAA thus opens a way towards systematic non-destructive tests of the efficiency of leaching procedures.

Chlorine removal by heating

Chlorine removal by heating is a very effective method, but it may erase the microstructure of the iron caused by the forging in antiquity. Figure 3 shows a nail from the Celtic oppidum of Manching (ca. 100 B.C.) that was heated to 750 °C in a reducing atmosphere two decades ago and is still in excellent condition. For this nail only 37 ppm of residual Cl were found. PGAA may thus help to determine the minimum temperature needed to remove the chlorine effectively, perhaps without disturbing the microstructure of the iron.

Outlook

PGAA is an accurate, non-destructive method of determining the chlorine content of archaeological iron artefacts. It can be used in the future for large scale analyses of the chlorine content of iron artefacts in museums, and will thus play an important role in the conservation of our cultural heritage.

[1] D. A. Scott et al., Iron and Steel in Art: Corrosion, Colorants, Conservation, Archetype Publications, London (2009).

NAA reveals details of the middle-age bronze door of Augsburg Cathedral

X. Li[1,2], Ch. Lierse von Gostomski[2], M. Mach[3]

[1]Forschungs-Neutronenquelle Heinz Maier-Leibnitz (FRM II), Technische Universität München, Garching, Germany

[2]Radiochemie München (RCM), Technische Universität München, Garching, Germany

[3]Bayerisches Landesamt für Denkmalpflege, München, Germany

Neutron activation analysis (NAA) was used to analyze samples from an old bronze door of Augsburg Cathedral, in order to establish a reliable screening method for a total of 35 different reliefs and more than 100 other bronze components on this object, made in the 11th century. Based on the fingerprint method, two of the samples could be identified as copies of the other two. This result provides important proof of early, local and, therefore, probably 'careful' preservation in the past.

Figure 1: Bronze heads (top: KL09 and KL10, below: KL11 and KL12) on the left door leaf.

A bronze door with a long history

The Roman bronze portal of Augsburg Cathedral dates from the first half or, at the latest, from the middle of the 11th Century. It is one of 12 major Roman bronze gates in Europe and one of the best examples of medieval casting art north of the Alps [1].

The two door wings of different size consist of a total of 35 bronze plates, 2 door pullers, 18 decorative heads and 89 borders. The relief panels depict mythological, symbolic and several biblical scenes. During restoration in the late 1990s, hundreds of samples were collected for further scientific investigation. Archaeologists hope that a number of the numerous questions that arise, e.g. where the old bronze door was produced and, above all, the context of the bronze panels, can be answered with the help of modern scientific analysis.

Neutron Activation Analysis (NAA) is a very sensitive multi-element analytical technique used for both qualitative and quantitative analysis of major and trace elements with a concentration down to the *ppt*–level (parts per trillion e.g. 1 part in 10^{12}). It is based on an extensive spectrometry of characteristic γ-rays after the sample has been irradiated in a nuclear reactor. In archaeology, NAA can give useful information about the origin of the artefacts according to the so-called "fingerprint" of the individual elemental composition in their raw materials.

Irradiation and analysis

Samples collected from four bronze heads (see fig. 1) were analyzed at the MLZ. Only several micrograms (1.5 ~4.5 mg) of samples were packed together with a neutron flux monitor (Au) in PE-

bags and loaded into a PE-irradiation capsule. The samples were irradiated within the rabbit system with a thermal neutron flux of 1.5E13 / cm²s for 30 min.

The first γ-countings were performed on a highly purity Ge-detector after a cooling period of 2 hours. Although the spectra were dominated by the activation product ^{64}Cu ($T_{1/2}$ = 12.7 h) of the major copper component in the bronze, some other minor and trace elements with short-lived isotopes, such as ^{116m}In ($T_{1/2}$ = 54 min), ^{65}Ni ($T_{1/2}$ = 2.52 h) and ^{56}Mn ($T_{1/2}$ = 2.58 h) could be detected, albeit, with large counting uncertainties.

Over the following days, the samples were measured again after the most short-lived nuclides had decayed. The long-lived nuclides could be identified without interference. In total, 24 elements were determined quantitatively or their detection limits were calculated using the computer program *MULTINAA* based on the k_0-method [2].

A new method has been developed to compare the different element compositions over several orders of magnitude from % to *ppb.* The concentration values $\rho(x)$ of the same element in different samples are normalized to unity. The values in the sample KL12 $\rho(x_0)$ are selected randomly for reference. In order to display the smaller as well as the larger values in the same plot, the sign of the comparison ratio *c* will be changed if its value is less than 1:

$$c = \frac{\rho(x)}{\rho(x_0)} - 1, \textbf{ if } \rho(x) > \rho(x_0) \textbf{ or } c = 1 - \frac{\rho(x)}{\rho(x_0)}, \textbf{ if } \rho(x) < \rho(x_0).$$

It is easy to see from figure 2 that the material of KL12 and KL10 is very similar, although both objects look quite different (see fig. 1). This discovery confirms the result of SEM/EDX measurements performed by the Bavarian State Office of Historic Monuments. As we know, the concentration of *Sn* in historical bronze made in the Middle Ages is lower than in the material made in later centuries. The samples KL10 and KL12 seem to have been produced later due to their high *Sn* concentration. This result supports the presumption that the objects KL12 and KL10 were cast as copies of the other original bronze heads KL11 and KL09 in the later period. In any case, it is an important proof of an early local and, therefore, probably 'careful' preservation in the past [3]. Since the elemental compositions in KL11 and KL09 are quite different, it seems impossible that the two older objects were produced at the same workshop at the same time.

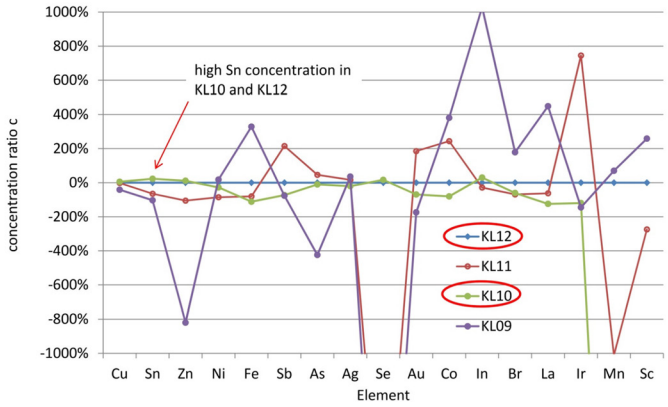

Figure 2: The concentration values $\rho(x)$ of the same element in different samples are normalized to unity. The values in the sample KL12 $\rho(x_0)$ are selected randomly for reference. The material of KL12 and KL10 seems very similar. Concentration ratios ***c*** are calculated as described in the text.

A ray of hope to answer more questions

Our positive results show that NAA is an extremely useful technique for the analysis of element composition in material. By using the finger-print method, the relation and origin of different archeological objects can be identified exactly. We hope that more mysteries associated with the historical bronze door will be solved in the near future with the help of this method.

[1] M. Weis et. al., „Denkmalpflege Information" Ausgabe B 131, 9 (2005).
[2] X. Li et. al., J. Radioanal. Nucl. Chem. Art. 215 (1996).
[3] M. Mach, Sammelband der Fachtagung "Metallkonservierung Metallrestaurierung", Universität für angewandte Kunst Wien,199 (2007).

PLEPS study of Fe-11.62 % Cr alloys for nuclear applications

S. Sojak[1], V. Slugeň[1], M. Petriska[1], M. Sahul[2], M. Skarba[2], J. Veterníková[1], M. Stacho[1]

[1]Institute of Nuclear and Physical Engineering, Slovak University of Technology, Bratislava, Slovakia

[2]Institute of Materials Science, Slovak University of Technology, Trnava, Slovakia

Radiation, heat, and mechanical resistance are crucial parameters of structural materials of Nuclear Power Plants. New structural materials of this type are reduced activation ferritic/martensitic (RAFM) steels which exhibit excellent properties such as lower activation, good resistance to volume swelling, good radiation, and heat resistance (up to 550 °C). Our work is focused on the study of radiation damage simulated by ion implantations and the evaluation of thermal annealing in RAFM steels.

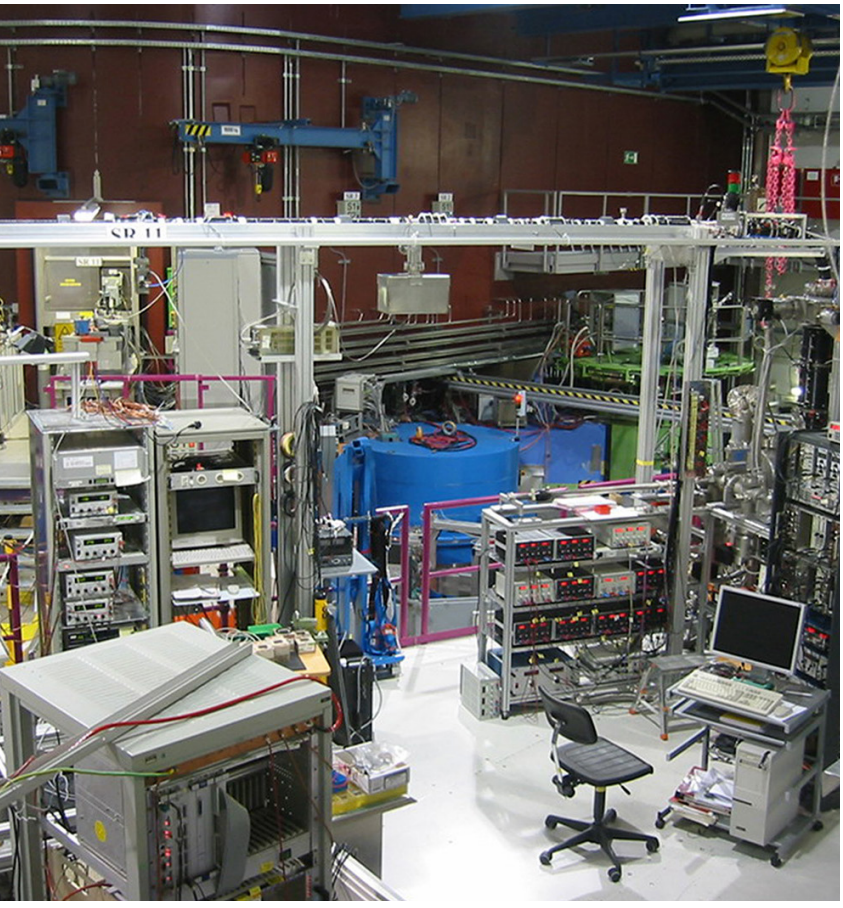

Figure 1: Experimental Hall with the PLEPS station.

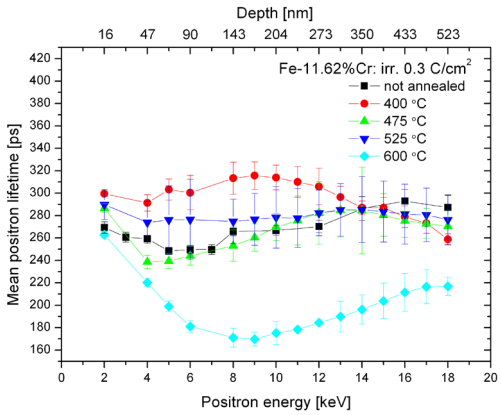

Figure 2: Mean positron lifetimes of annealed Fe-11.62 % Cr alloys.

Application of slow positron beam at PLEPS

The experimental method of choice is the Pulsed Low Energy Positron System (PLEPS) [1] at the high intensity positron source NEPOMUC [2] at the MLZ (fig. 1). This technique allows us to investigate the type and amount of the defects in the microstructure of the RAFM steels. The PLEPS study on our Fe-11.62 % Cr alloys was performed to a maximum depth of 525 nm. This investigation depth was sufficient to cover the region damaged by the ion implantations.

Specimens implanted by He ions at a dose of 0.3 C/cm^2 (~1.87 · 10^{18} ions/cm^2) showed a significant decrease in the mean positron lifetime (MLT) for a sample annealed at a temperature of 600 °C (fig. 2). Analysis based on the MLT at this temperature, over the depth of the region damaged by He ions, could be interpreted as an extensive decrease in the defect size to monovacancies or small vacancy clusters [3]. This is consistent with the literature [4], where recovery of the microstructure at this temperature has been considered. Data obtained by the PLEPS technique for samples annealed at lower tem-

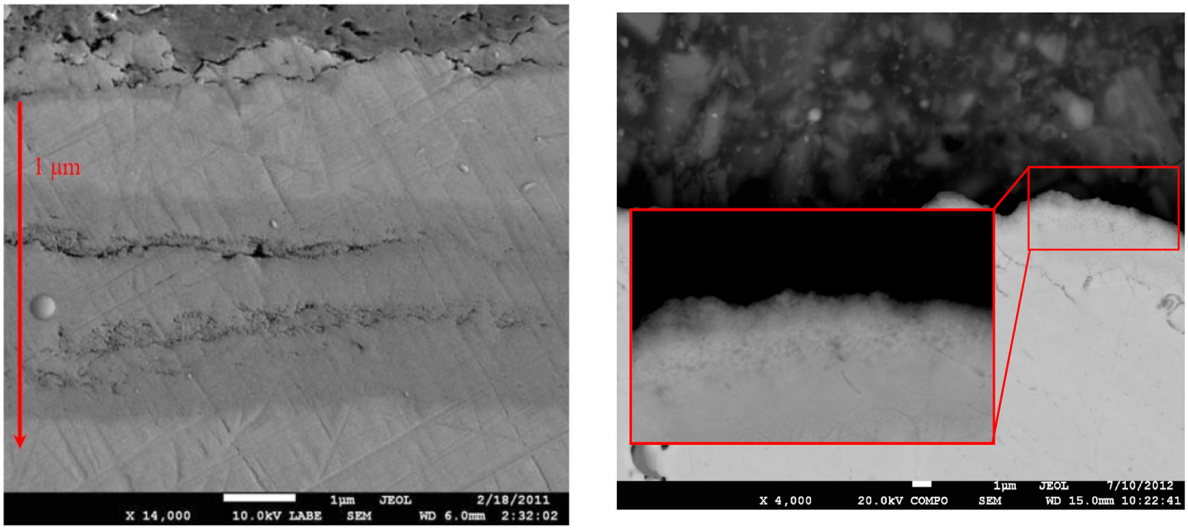

Figure 3: SEM view on a Fe-11.62 % Cr sample implanted by helium ions and annealed at 475 °C (left) and 600 °C (right). The sample was diagonally cut under a 12° angle for the SEM measurements.

peratures (400, 475, 525 °C) on the other hand did not show differences in the non-annealed state and, furthermore, no features corresponding to damages from implanted 100 keV and 250 keV He ions were observed. Therefore, additional scanning electron microscopy (SEM) studies were performed to elucidate these findings.

Scanning Electron Microscopy point of view

The SEM results (fig. 3, left) show major damage in two regions, which could be assigned to the maximum damage caused by He ions implantation at energies of 100 keV (depth of ~300 nm) and 250 keV (depth of ~550 nm). Based on this, our assumption is that MLTs measured in the samples annealed at temperatures of 400, 475, 525 °C were influenced by these two heavily damaged regions. In addition, regeneration of the microstructure after annealing at a temperature of 600 °C, as evidenced by the significant mean positron lifetime decrease, was also confirmed by the SEM measurement of this structure, where the damaged regions mostly disappeared (fig. 3, right).

Conclusions

Evaluation of the PLEPS data for annealed Fe-11.62 % Cr alloys was supported by SEM results for a specimen annealed at 475 °C. This specimen showed major damage in two regions with no annealing effect being observed (similar effects are observed at 400 and 525 °C). Only for the sample annealed at a temperature of 600 °C, the mean positron lifetime showed a major decrease. Therefore, considering the literature [4] regarding the influence of temperature on reduced activation ferritic/martensitic steels above 0.4 $T_{Melting}$, we conclude that the large voids in affected area (<1 µm) were continuously annealed out or, at least, their size decreased to monovacancies and small vacancy clusters not exceeding the size of 5 vacancies.

Acknowledgements

Grants DO-0005-12 a VEGA 1/0204/13 are acknowledged. The authors gratefully acknowledge the assistance of the staff of NEPOMUC, namely PD. Dr. Christoph Hugenschmidt and the PLEPS staff, namely Dr. Werner Egger and Luca Ravelli, at the MLZ.

[1] P. Sperr et al., Appl. Surf. Sci. 255, 35 (2008).
[2] Ch. Hugenschmidt et al., Appl. Surf. Sci. 255, 29 (2008).
[3] S. Sojak et al., J. Phys. Conf. Ser. 443, 012035 (2013) and ref. therein.
[4] K. L. Ronald et al., High-Chromium ferritic and martensitic steels for nuclear applications, USA: ASTM (2001).

Radiometric investigation of water vapour movement in wood based composites

K. Solbrig[1], K. Frühwald[1], J. B. Ressel[2], B. Schillinger[3], M. Schulz[3]

[1]Laboratory for Timber Engineering, Products and Production, Ostwestfalen-Lippe University of Applied Sciences, Lemgo, Germany

[2]Department of Wood Science, University of Hamburg, Hamburg, Germany

[3]Heinz Maier-Leibnitz Zentrum (MLZ), Technische Universität München, Garching, Germany

Many physical interrelations within the wood particle mat during the hot pressing process of wood based composites (WBC) are based on assumptions. Neutron radiography is able to distinguish between wood and moisture (X-ray lacks sufficient contrast), thereby providing specific information on dynamic processes where only models exist. Experiments at ANTARES employing a special setup evaluate the applicability of NR for in-situ investigations on vapour movement during hot pressing. The results visualise and quantify vapour movement depending on varying process parameters.

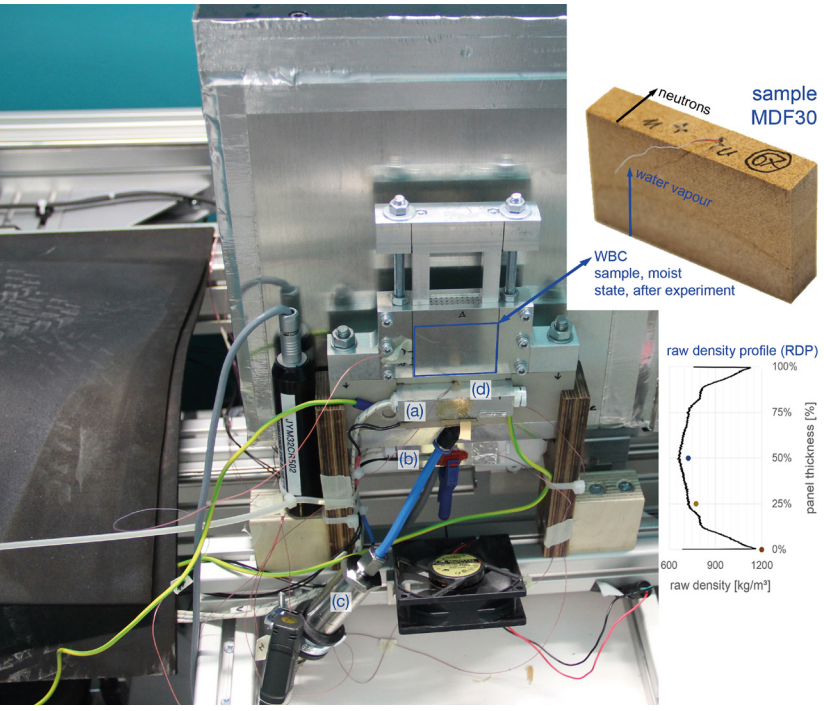

Figure 1: Experimental setup in front of ANTARES detector including heating cartridges for the sample (a) and vapour (b). Monitoring components: pressure of vapour generation cavity (c) and thermocouples at several positions (d); photograph of the exemplary sample MDF30 with its raw density profile (chart with temperature measurement positions) and directions of neutron and water vapour flow.

The hot pressing process of wood based composites

WBC are industrially produced panels made of resin-blended wood particles (e. g. wood fibres with 8 - 14 % resin content). The formed particle mats are densified and cured in hot presses. Several physical models (cf. [1]) exist for mechanisms such heat and mass transfer that occur during the hot pressing of wood particle mats. More generally, a not as yet visualised concept of a wave-front-like vapour movement exists. A continuous X-ray radiometric investigation of the hot pressing process was carried out by [2]. Standard X-ray methods lacks sufficient contrast between water vapour (H_2O) and dry wood matter (mainly H, C, N, O). On the contrary, neutron radiography (NR) is very sensitive even to small amounts of water vapour due to the considerably higher effective cross section of hydrogen compared to the other elements present. Time-resolved NR allows comprehensive measurements of the actual vapour movement over the total cross section of the WBC panel, in contrast to hitherto used estimations with single probes of temperature and vapour pressure.

Emulation of the heat and mass transfer

The experiments presented serve as preliminary tests for the in-situ investigation of the hot pressing process. To this end, an appropriate, simple setup was designed to generate heat and mass transfer (fig. 1). The predominant distinctive vapour movement inside the sample was varied within a practice-oriented range of temperature and pressure settings. NR measurements were carried out by means of a set of samples systematically covering a well-defined range of raw density profiles over the panel thickness and different initial material moisture contents. The

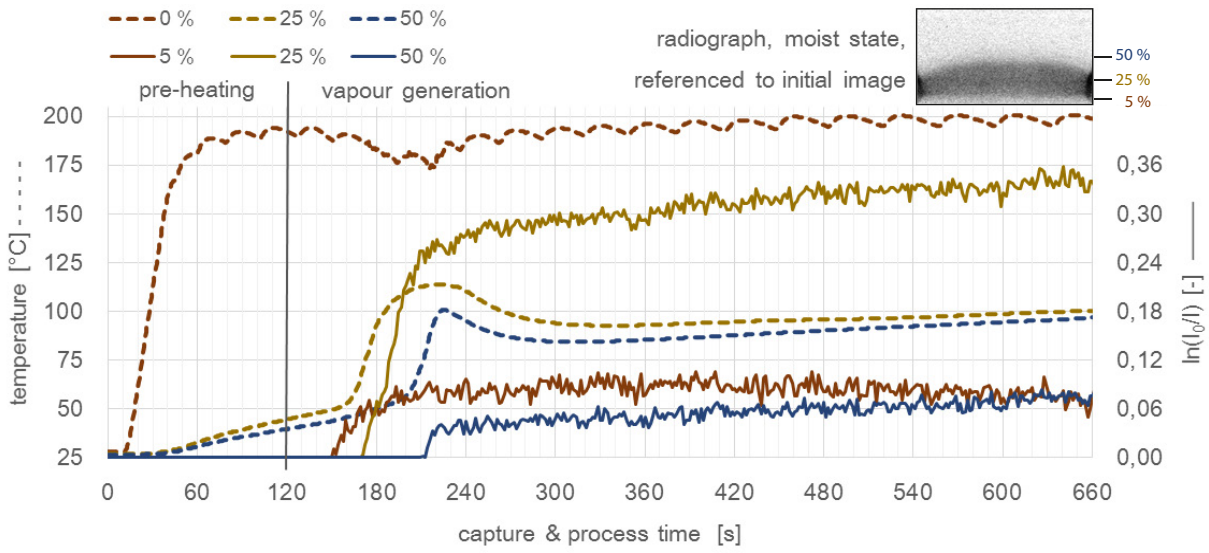

Figure 2: Process monitoring and NR measurement results of the exemplary sample MDF30 during a capture time of 660 s with temperature [°C] (dashed lines) and relative water content $\ln(I_0/I)$ [-] (solid lines) for different positions along the panel thickness [%]; insert: NR image of the moist state, representative thickness positions are marked.

amount of water for vapour generation was individually calculated per sample type to obtain reasonable specimen moisture conditions. Despite the stagnation of the emulated vapour movement after 60 - 180 s from the initial vapour generation, the process and capturing time was chosen up to 660 s (incl. 120 s of pre-heating) to obtain a desiccation within the panel surface, which typically occurs during hot pressing.

Measurements at ANTARES

The NR measurements were carried out using an L/D of 280 ($2.1 \cdot 10^8$ n cm^{-2} s^{-1}), 2 x 2 binning, an exposure time of 0.25 s at a repetition rate of 1.61 s restricted by the read out time. The pixel size was 146.5 µm. Prospectively faster and higher resolved NR imaging will be available after full completion of ANTARES.

In-situ investigation of water vapour movement

One sample was selected (fig. 1, MDF30) for exemplary presentation of the NR results in figure 2 with data of representative positions along the panel thickness [%]. To evaluate the vapour movement, i.e. the water content per time step at a certain position, the time-resolved NR images were referenced to NR images of the initial dry state (fig. 2, insert). The logarithm of this reciprocal pixel value $\ln(I_0/I)$ [-] corresponds to the relative water content (solid lines). A delayed sharp increase in the water content observed by NR proves the wave-front-like vapour movement, which is also confirmed in the correspondingly monitored temperature (dashed lines). The time delay of the increase correlates to the thickness position. A kind of vapour saturation is obvious at position 25 %. The vapour wave front does not move along the total cross section but, rather, stops at around 25 % panel thickness where the raw density decreases (fig. 1, RDP). The density decrease leads to higher permeability of the densified wood particles and a respective vapour pressure decrease resulting in a precipitation of vapour in this section. A near-surface desiccation is indicated by the falling slope of the 5 % chart (starting at 480 s).

The estimated wave-front-like vapour movement characteristic becomes clear from this brief data evaluation. Despite the preliminary nature of these experiments, the applicability of NR to quantitative in-situ investigations of the hot pressing process is shown and the results provide valuable information about mechanisms within the wood particle mat during hot pressing. This enhanced knowledge offers fundamental approaches to further improve the production of WBC and their material properties.

[1] P. E. Humphrey, In: Proc. Int. Cellucon Conf., Bangor, (1994).

[2] M. Gruchot, Diss. Uni Hamburg (2009).

Around 12 tons of Si are processed annualy at the FRM II.

Reactor & Industry

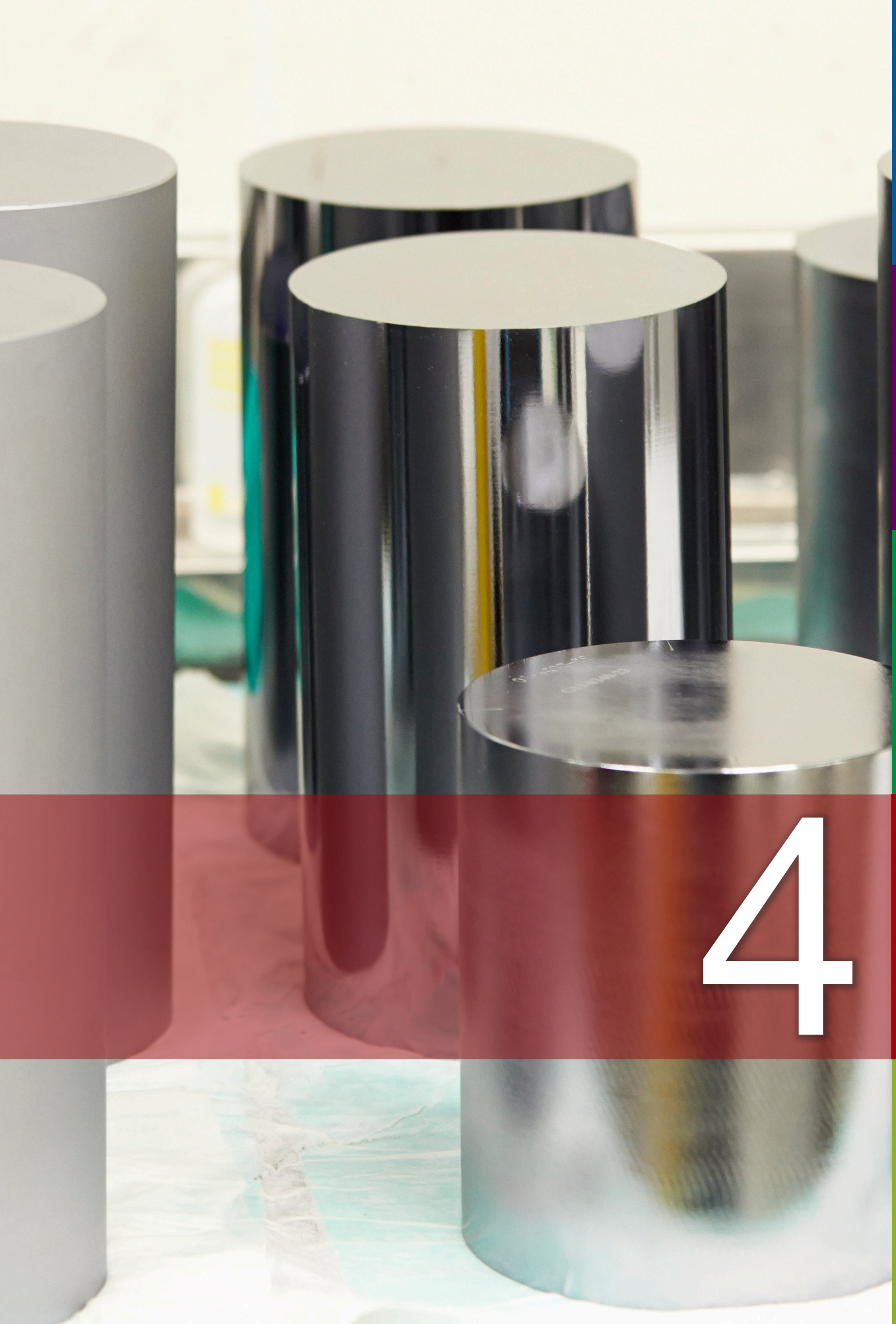

4

Reactor operation in 2013 – 100 % availability

A. Kastenmüller

Forschungs-Neutronenquelle Heinz Maier-Leibnitz (FRM II), Technische Universität München, Garching, Germany

In 2013, the FRM II was operated safely in four cycles for a total of 240 beam days. The reactor operation schedule was arranged such that a longer maintenance period of 45 days was possible in summer, allowing for the realisation of two larger longterm planned projects in addition to the usual inspections, periodic testing and maintenance. These measures included the integration of a second main check valve in the primary cooling circuit and the installation of a new freight elevator in the reactor building. There were three minor interruptions to reactor operation for the repair of mechanical components, however these days of non-operation were made up at the end of the respective cylces, thus providing an operational availability of 100 %.

240 days of reactor operation

The FRM II delivered nuclear energy totalling 4799,4 MWd in 2013. In total, 240 days of beam time were available for use in research, industry and medicine. Over the year, 1783 periodic tests, operability checks, inspections by independent experts from the regulatory body covering different subject areas, as well as maintenance work and 43 modifications to the facility that had to be referred to the regulatory body, guaranteed that the high safety standard of the neutron source FRM II was sustained, and even enhanced. There was no reportable incident in 2013.

Figure 1: The main check valve to which a second, new one has been added.

Additional main check valve

The company Kraftanlagen München, with the support of the operating crew of the FRM II, inserted an additional second main check valve into the primary cooling circuit. In 2009, the main check valve did not fully close and this failure lead to a reportable incident. Therefore, the installation of an additional second check valve was already planned back then. The installation of this valve, weighing in excess of 500 kg and requiring extensive preparations, significant modifications to the primary cooling circuit and various examinations was able to be completed during the maintenance break.

In view of the desired diversity of redundant components, the new check valve was supplied by an alternative manufacturer and uses a slightly different mechanical design compared to the original valve. The new valve was specially designed and produced for application in the FRM II and had already undergone extensive testing during the manufacturing process. In addition, the necessary modifications to the pipes of the primary circuit and the welding in of the valve itself was continuously monitored by authorised experts, in accordance with the safety significance of the primary circuit. On conclusion of the work, the pressure test of the pipes, including the valves, was successfully undertaken and the primary circuit resumed normal operation. With two main

Figure 2: The two main check valves: the new one on the left, the original one on the right.

check valves in series, together with the check valves at the primary pumps, the FRM II now has three redundant and diverse safety systems in order to prevent reverse coolant flow in the event of emergency cooling.

Installation of a new freight elevator in the reactor building

The second major project of the summer maintenance break was the upgrading of the freight elevator in the reactor building from the previous load of 2 tons to a new lifting capacity of 10 tons. Therefore, the existing elevator was removed completely and a new, indirect hydraulically operated freight elevator was installed. To this end, a total of 721 special dowels for 104 steel plates were placed in the shaft walls to anchor the new guide rails and hydraulic cylinders. The new elevator caters for significantly more transport between the reactor hall, the experimental hall and the basement of the reactor building. Now, transport during reactor operation is also possible, while this was previously only feasible when the FRM II was shut down. This will be of great importance in the future when our Mo-99 production facility comes into operation, since very heavy transport casks for the Mo-99 targets will be transported from the reactor hall to the ground floor on a weekly basis.

Further work realized in the longer summer maintenance break

Another measure in preparation for the future Mo-99 production was the welding of additional fittings in the secondary cooling circuit for the connection of the cooling circuit of the Mo-99 irradiation facility. The helium compressor motor of the cold source was equipped with a frequency inverter to compensate for fluctuations and short power failures in the external grid.

Effective measures to reduce C-14 emission

The measurements of the C-14 emission for the year 2013 add up to only 23 % of the very low annual limit allowed for C-14 emission. Since during this period the ion exchanger resins of the moderator purification system were also dried, this value shows that the measures taken to reduce the C-14 emission were effective and kept it far below the annual permissible value.

Short interruptions of the reactor operation

In October 2013, the FRM II was shut down in the middle of cycle 32 to repair the fan motor of the control rod drive. The cycle 34 was briefly interrupted twice to replace a bearing on one of the two secondary pumps as well as the fan of the helium compressor motor of the cold source. These days, which delivered no neutrons for science, industry and medicine, were all added at the end of each cycle, thus providing 100 % operational availability in 2013.

Figure 3: New freight elevator with a lifting capacity of 10 tons in the reactor building.

Irradiation facilities at FRM II

H. Gerstenberg, A. Draack

Forschungs-Neutronenquelle Heinz-Maier Lebnitz (FRM II), Technische Universität München, Garching, Germany

The irradiation facilities at FRM II, which are used mainly for commercial purposes, include the gamma irradiation facility, silicon doping facility, pneumatic rabbit facility, capsule irradiation facility and the mechanical irradiation facility. The newest of the above irradiation devices is the gamma irradiation facility that came into operation at the end of 2013. The irradiation department carried out 805 irradiations in 2013. In comparison with 2012, a total increase of 23.5 % was achieved. All these irradiations were handled by a team of 9 colleagues. Most of the team members work in two shifts to cover this high demand for irradiation.

Gamma irradiation facility

The newest facility in operation at the FRM II is gamma irradiation. It uses gamma-rays from the fission products contained in the spent fuel assemblies in the storage pool. Consequently, the facility can be used independently of the reactor cycles. In order to effect an irradiation, the facility is lowered into a spent fuel assembly (fig. 1) that provides the necessary dose rate. The majority of samples being irradiated in this facility are rock salt crystals for geological investigations. Due to irradiation with gamma-rays, the salt samples change their color permanently to blue. The change in color makes the structure of the samples visible for further evaluation by the geologists. Typically, the irradiation time ranges from several days up to a few weeks. If required, it is possible to heat the samples up to 140 °C upon irradiation. In late 2013, the gamma irradiation facility was connected to the control room of FRM II. Due to this connection all technical requirements for permanent operation are met. For 2014, the first commercial orders for the gamma irradiation facility have already been received.

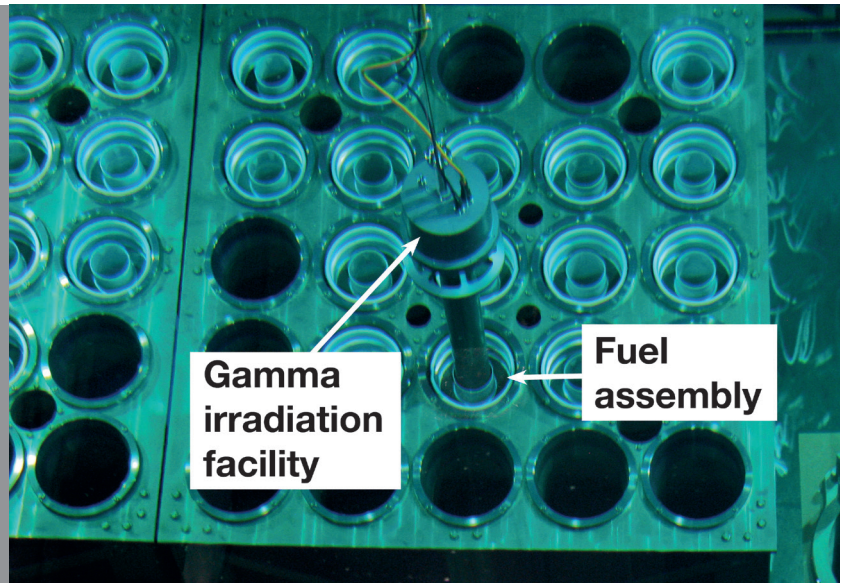

Figure 1: Gamma irradiation facility in spent fuel assemblies.

Silicon doping facility

The silicon doping facility attracted the highest demand of all at the FRM II. In 2013, 589 irradiations were processed. This number equals a total of 1258 single ingots with an accumulated weight of around 12.5 tons.

The irradiation process (neutron transmutation doping (NTD)) inside the ingot is explained by means of the following nuclear reaction:

$$^{30}Si(n,\gamma)^{31}Si \xrightarrow{\beta^-} {}^{31}P$$

The neutron capture in Si is followed by the decay of the instable ^{31}Si into ^{31}P. It increases the charge carrier density within the semiconductor and makes it possible to produce Si exhibiting a predefined target resistivity matched by the irradiation time. In order to fulfil industrial

specifications, the accuracy with respect to the target resistivity defined by the client must be met within ± 7%. Figure 2 shows the target accuracy measured by one major client. It is worth noting that all of more than 700 irradiated ingots met the specified range of acceptable resistivity and that the average accuracy was 99.25 % with respect to the target value or, in other words, extremely close to the ideal value of 100 %. The main advantage of NTD as compared to other Si doping techniques is the high achievable accuracy and homogeneity of the doping profile. Due to the rotation of the Si ingots upon irradiation and the use of a suitably shaped Ni layer acting as a gradual neutron absorber, the necessary homogeneity of the neutron flux density within the irradiation position is guaranteed.

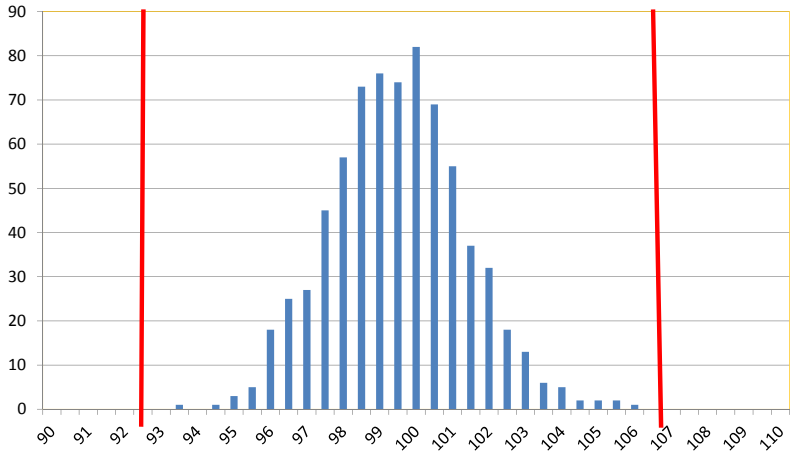

Figure 2: Target accuracy of resistivity in 2013.

Pneumatic rabbit facility

The pneumatic rabbit facility was used for 67 irradiations in 2013. It is driven by carbon dioxide, exhibits 6 independent irradiation channels and is designed for low dose irradiation from a few minutes up to $2 \cdot 10^{17}$ n/cm²s maximum. The irradiated samples may be unloaded into a lead-shielded box/container or can be transported directly to the institute for radiochemistry. Samples irradiated in the pneumatic rabbit facility are mainly used for NAA (neutron activation analysis) and as a new application for the production of ^{166}Ho, this is a possible candidate for future medical applications.

Capsule irradiation facility

In general, the water driven capsule irradiation facility offers two independent channels. Each channel can handle up to 3 capsules. In order to offer the necessary flexibility in the irradiation schedule, the KBA is designed in a way that allows the irradiation positions to be switched if required.

The demand for long-term irradiation was high in 2013. The facility was used to regularly produce ^{177}Lu up to an activity as high as 750 GBq for use as a radiopharmaceutical after refinement by the ITG company on the site of FRM II. Another important application is the activation of ^{60}Co up to 185 GBq for technical purposes. The irradiation times for these examples add up to 14 days. Due to these long irradiation times, the coverage of the most intense irradiation position KBA 1-1 was 209 days in 2013, which represents 87 % of the 240 operational days FRM II offered in this calendar year.

Mechanical irradiation facility

The mechanical irradiation facility is the only facility without any electrical components. Typical irradiation times are only a few minutes. Due to the simple setup with no shielding it is possible to irradiate only up to 4 samples per week. In total, 74 samples were irradiated in 2013. The majority of these samples were provided by geologists from all over the world. They enjoy the excellent thermalized spectrum of FRM II which allows first class preparation of minerals for geochronological purposes.

Progress in reactor conversion and fuel development

H. Breitkreutz, A. Röhrmoser, T. Zweifel, H.-Y. Chiang, T. K. Huber, R. Schenk, T. Hollmer, C. Steyer, C. Reiter, B. Baumeister, A. Egle, S. Säubert, M. Dodenhöft, R. Schauer, R. Jungwirth, R. Großmann, W. Petry

Heinz Maier-Leibnitz Zentrum (MLZ), Technische Universität München, Garching, Germany

For the conversion of FRM II to a lower enrichment , the working group „Hochdichte Brennstoffe“ performs reactor physics calculations and contributes to the necessary development of new high density reactor fuels based on Uranium-Molybdenum (UMo) alloys. Numerous international collaboration in fuel development within the HERACLES group (Europe), US DoE, Korea and others integrate the project into the worldwide aim of non-proliferation.

Uranium laboratory

In December, the AtG nuclear license for the uranium laboratory was obtained. This will permit full-sized fuel plates to be handled in order to prepare in-pile irradiation tests.

Heavy ion irradiation

Amorphous interaction layer

The UMo-Al interaction (IDL) that arises during in-pile irradiation is a major concern, as it cannot retain the gaseous fission products. Heavy ion irradiation (HII) on U-Mo/Al layer systems allows this IDL to be generated outside a reactor with comparable physical properties and the same phase composition as if created during in-pile irradiation. It is now possible to create an IDL in its amorphous form using HI and it has been demonstrated that the IDL growth mechanism is strongly dependent on the irradiation temperature and particle flux, which enhances our understanding of the IDL growth.

The major difference between HII and in-pile irradiation in the specific case of U–Mo/Al fuels remains the presence of fission gas bubbles inside in-pile irradiated fuels, which have a first order influence on the macroscopic swelling of U–Mo/Al fuel plates. Kr gas implantation into layer systems previously exposed to HII allows gas behaviour to be studied using out-of-pile

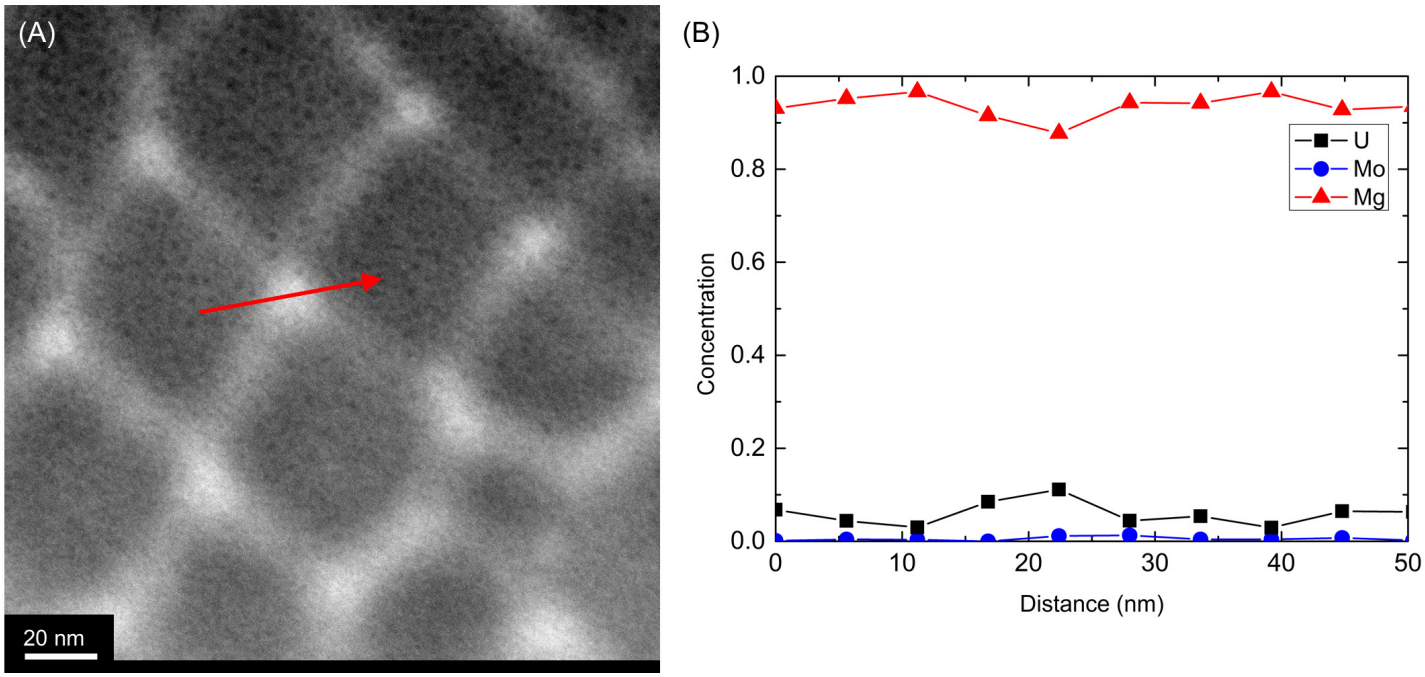

Figure 1: (A) STEM-HAADF image of the spinodal pattern of UMo/Mg bilayer irradiated at 200 °C; (B) EDX line-scan across the area between rhombi, as marked by the arrow in (A).

techniques. Indeed, first results show that the microstructural impact of Kr implantation can be very well compared to in-pile gas effects.

UMo/Mg layer systems

One means of suppressing IDL growth is a protective coating of the UMo particles with extra layers such as ZrN. Another solution would be to replace the Al matrix material by another element that does not react with UMo, e.g. Mg. HIIs at temperatures of 140 °C and 200 °C have shown that the IDL formation is in fact strongly suppressed by the use of Mg; however, if irradiated at a higher temperature, i.e ≥ 200 °C, spinodal decomposition of the IDL into an U-rich and U-poor phase favours embrittlement, i.e. a decrease in ductility.

More details of spinodal decomposition are revealed by EDX line-scans taken across the chessboard-like pattern near the irradiated UMo/Mg interface. Figure 1 indicates that the bilayer exhibits a compositional variation with a period of about 50 nm. Two phases with varying UMo/Mg content are discernable: The U-rich stripe-like pattern, and the U-poor rhombi. This pattern and its compositional variation are typical features of a spinodal decomposition: a solution decomposing into multiple phases due to limited solubility near the boundary of absolute instability.

Sample analysis

To simplify microstructural analysis, an improved metallographic preparation technique has been developed for UMo, which allows structural examinations in the low µm-range using optical microscopy.

Physical properties

Thermal properties

UMo has three main phases that differ in their Mo-content (1.5 wt.% to 6 wt.%): The orthorhombic α'-phase, the monoclinic α"-phase and the cubic γ-phase. The specific heat of the different phases is correlated to their molybdenum content. This behaviour could be confirmed by calorimetry measurements using the Differential Scanning Calorimeter in the Material Science Lab. The comparison of the α'-UMo and α"-UMo shows that this technique can even resolve a difference in the molybdenum content of only 2 wt.%.

TTT Diagram

At higher temperatures, the γ-phase of UMo increasingly decomposes into α-UMo and U2Mo. The duration of this process depends on the temperature and is normally displayed in the form of a Time-Temperature-Transition (TTT) diagram. This TTT diagram was measured at SPODI, STRESS-SPEC and DESY to update the original diagram measured in 1964.

Fuel production

In order to satisfy the demand for UMo fuel powder for future irradiation tests, FRM II and AREVA CERCA have built a powder production facility in Romans-sur-Isère, France. This includes the commissioning of a dedicated uranium laboratory as well as the construction and operation of a new atomizer. The necessary specialized electrodes as precursors are produced by means of an induction furnace. Both machines are housed in custom glove-boxes to avoid corrosion of the fuel powder.

The prototype production facility was successfully tested using inert surrogate material in mid-2013. Subsequently, tests with uraniferous material were performed, and validation of the hot production line is expected in the near future.

Molybdenum 99 - targets

A second global non-proliferation development in which the TUM is engaged is the production of highly efficient annular LEU targets for ^{99}Mo production. An experimental sputtering device for the production has been constructed, commissioned and characterized. This device allows coating of the inner side of cylindrical aluminium substrates, which has been successfully performed using surrogate material.

Reactor physics

A. Röhrmoser, H. Breitkreutz, W. Petry

Heinz Maier-Leibnitz Zentrum (MLZ), Technische Universität München, Garching, Germany

FRM II has made a commitment, unique worldwide, to convert its fuel to a lower enrichment level and has, indeed, incorporated this goal into the terms of its operational license. Since the TUM conversion programme was initiated in 2003, the primary aim of the project has been to achieve a fuel element whose enrichment is as low as reasonably feasible while, at the same time, not requiring major changes to the reactor. The main criteria for the conversion of FRM II were the inviolability of the safety margins with minimal loss of performance.

Core design calculations

Besides selection and tests for an appropriate fuel, it has been shown in the course of the last decade that the actual core requires some adjustments to the plate and element geometry in order to satisfy the safety criteria. Thanks to 3D particle transport physics (MCNP code), it was possible to predict accurately the impact of changes on users during the routine operation of the reactor.

Latest design studies for FRM II conversion

The latest design, based on monolithic UMo fuel, functions with an enrichment of only 27 %. This design uses a total of 47.5 kg Uranium and requires elongated fuel plates (75 cm instead of 70 cm), a reduced surface roughness and rounded fuel plate edges. As some of these changes to the core have not definitively been shown to be feasible, a secondary design with less aggressive changes and an enrichment of 29 % was developed to maximize the conversion feasibility. The higher density of the monolithic fuel makes it possible to have lower enrichment than with dispersed UMo fuel, for which a study with 30 % enrichment was presented in 2011. In both design studies, the flux criteria and reactor safety margins are met under steady state conditions. The expected flux loss for users of the thermal beam tubes is, in all three cases, approximately 10 %.

Code development

Even though the physics in a compact core reactor and in a large-scale power reactor are essentially identical, significant differences exist in the models that are used to describe the physics in a simplified manner in computer codes. As early as 2011, TUM discovered that the model employed in one of the most commonly used burn-up codes, MonteBurns, lacks burn-up data for about 10 strongly absorbing isotopes, mostly short-lived ones that are only relevant in high-flux research reactors, e.g. Pm148m. For FRM II,

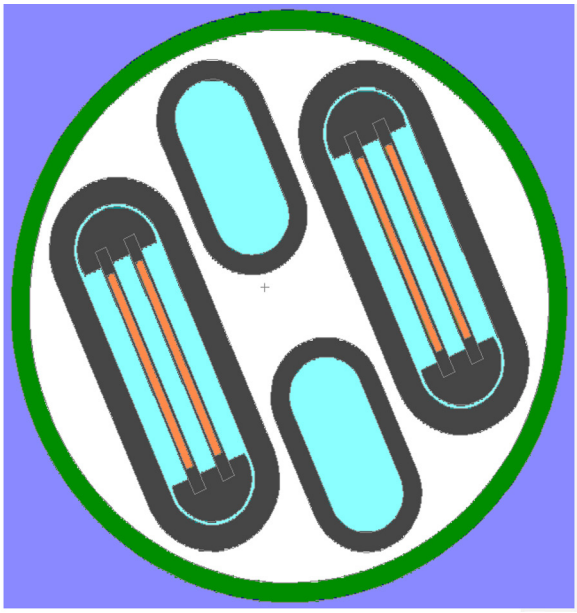

Figure 1: Detailed model of the Mo-99 irradiation tube.

this deficiency would have led to an overprediction of the actual cycle length of up to 5 days. Further investigation revealed a basic misinterpretation between data providers and code developers for the treatment of isomer pairs, which is especially relevant for the isotope pair Pm148/m in high flux reactors such as FRM II. The group developed a fix for both problems.

LEU targets for Mo-99 generation

Since 2012, the Mo-99 irradiation facility has been planned with plate type LEU targets instead of the annular HEU targets used in the first concepts. The design now comprises two identical loops that can be operated independently. Two vertical stacks are kept side by side in each loop with a maximum of four plates per stack, so that 16 plates can be irradiated at the same time.

The amount of fission products in this new design is not much less than that of the first ideas based on 15 annular targets, each with 4 g fissile material. Within the framework of the associated safety analysis, the detailed heating contributions in the channels and the possible backlash of the target-load on the reactor and its power detection were analysed using a full, combined model of the reactor core, the D_2O tank and the irradiation facility.

Heat production of converter fuel plates

The power deposition in the cooling channels and the Uranium plates of the fast converter facility (SKA) as well as the associated n-flux and the resulting heat load at the plates are comparably sensitive to the model input. This is especially true for the detailing of the converter cooling shaft as well as for the structures in the heavy water that lie between the core and the SKA, e.g. some irradiation channels. Hence, the MCNP model of the SKA facility was detailed further with exact light water supply channels left and right of the SKA box, in which the slide with the plates moves. Using this model, the heating contributions for normal reactor operation were evaluated with 1.8 kW for fully withdrawn and 73 kW for inserted plates. The calculated difference

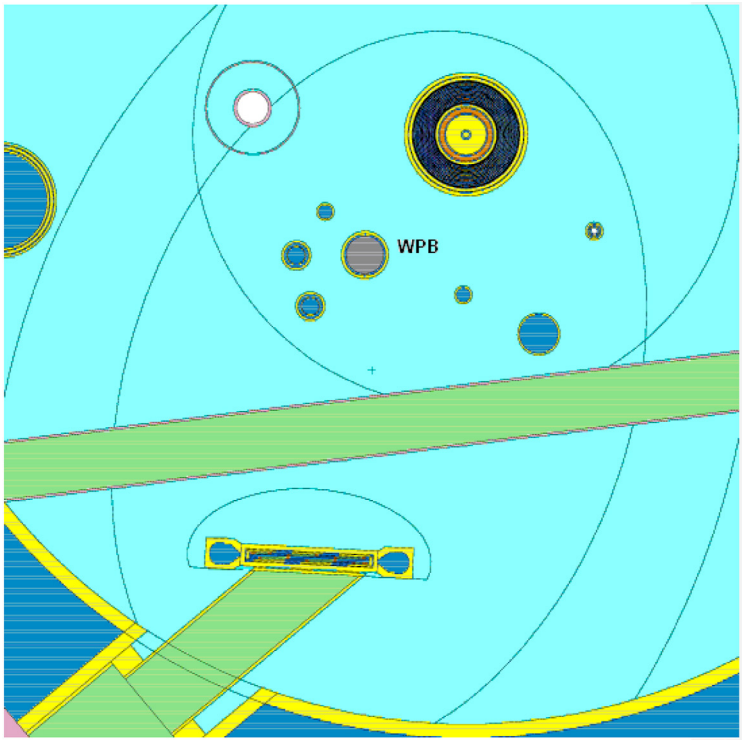

Figure 2: Model of the D_2O tank including reactor core, SKA and all components relevant in this regard.

of 71.2 kW agrees very well with the measured value of 71.5 kW. The absolute measured values are higher because an additional 13 kW are introduced via heat conduction from the hotter heavy water tank (HW) into the steadily operating SKA cooling channel. Vice versa, the HW receives an additional γ-heating of about 8 kW from the inserted SKA plates.

Data acquisition electronics of the JNSE instrument.

Facts & Figures


—CHANNEL A— —CHANNEL B—
TRG LEVEL
TRG LEVEL
DISPL LEVEL
DC DC
AC AC
EXT
REF
REM
OVFL
GATE
ns MHz
µs kHz
ms Hz
s mHz
RESET DISPL
LOCAL HOLD
FUNCTION
FREQ A
PERIOD A
RPM A
TI A–B AV
TI A–B SI
TOTAL A
TOTAL A by B
CHECK
RESOLUTION
ADRS
PARAM
LINE
GATE HOLD
FUNCTION
ATTN SLOPE FILTER MODE SLOPE ATTN
INPUT A
DC–160MHz
INPUT B
DC–100MHz
TOE 6722
UNIVERSAL CO ER
TOELLNER
BASE MODULE MPA-3

5

Events 2013: Conferences, workshops, meetings and open day

R. Bruchhaus[1], I. Crespo[2], H. Frielinghaus[1], W.M. Gan[3], R. Georgii[2], W. Van Herck[1], M. Hölzel[2], Ch. Hugenschmidt[2], Ch. Kortenbruck[2], P. Kudejova[2], I. Lommatzsch[2], B. Schillinger[2], A. Schneidewind[1], G. Simeoni[2], A. Voit[2], R. Zorn[1]

[1]Jülich Centre for Neutron Science (JCNS) at MLZ, Forschungszentrum Jülich GmbH, Garching, Germany

[2]Heinz Maier-Leibnitz Zentrum (MLZ), Technische Universität München, Garching, Germany

[3]German Engineering Materials Science Centre (GEMS) at MLZ, Helmholtz-Zentrum Geesthacht GmbH, Garching, Germany

SAAGAS Seminar Aktivierungsanalyse und Gammaspektroskopie

30 talks and 13 posters were presented at the Seminar Aktivierungsanalyse und Gammaspektroskopie (SAAGAS) held in Garching from 26th to 28th February. The main focus of the workshop, organized by Dr. Petra Kudejova (FRM II), was laid on gamma spectroscopy, which represents an important part of the activation analysis. 60 participants enjoyed the talks and the industrial exhibition by Isotope Technologies Garching GmbH, Canberra GmbH, Ortec/Ametek und Dr. Westmaier GmbH.

Sessions were held on the applications of instrumental neutron activation analysis in the in environmental sciences and methods. The second day brought talks on prompt gamma activation analysis (PGAA) and its applications in archeometry. An excursion to the Neue Pinakothek in Munich and a conference dinner at the Löwenbräukeller made for a perfect day. Medical applications were presented on the third day and, thanks to very interesting topics such as the Sr-90 samples from Fukushima, were fully attended until the end.

Most of the presentations can be found on the SAAGAS 24 website: www.frm2.tum.de/saagas24/.

MAUD – Materials Analysis using Diffraction

The workshop on March 6th and 7th aimed to make MLZ scientists and users better acquainted with the possibilities of the software MAUD and to exchange applications and expert knowledge with the author, Luca Lutterotti from the University of Trento, Italy. It was jointly organised by Dr. Markus Hölzel (FRM II) and Prof. Dr. Wolfgang Schmahl (Ludwig-Maximilians-Universität

Figure 1: Participants at the Seminar Aktivierungsanalyse und Gammaspektroskopie (SAAGAS) organized by FRM II.

Figure 2: The software for materials analysis MAUD was the topic of the workshop held at the MLZ in early March.

München). A particular aim of the workshop was to support materials science projects related to the diffractometers SPODI, STRESS-SPEC, POWTEX, and BIODIFF which benefit from the particular capabilities of MAUD.

MAUD stands for Material Analysis Using Diffraction and is a general diffraction/ reflectivity analysis program. MAUD's philosophy is to provide a kind of framework to help scientists to analyse most of the diffraction data files relevant to the Rietveld analysis method. Currently, Luca Lutterotti wants MAUD to be extended to work with new instruments with a strong focus on materials science analysis rather than on classical crystallographic structure analysis.

Further information on the software package can be found at www.ing.unitn.it/~maud/.

Grazing Incidence Scattering Software

Bringing together experts in the field of grazing incidence scattering software was the goal of the workshop held at the MLZ on 9th and 10th April. The difficulty of interpreting and analyzing Grazing Incidence Small Angle Scattering (GISAS) data formed a recurring theme during a number of the presentations and the lively discussions that followed. The organizers, the Scientific Computing Group of MLZ, took the opportunity to announce publicly their own software project for GISAS, known as BornAgain.

The discussions made it clear that a gap still exists between the current scientific work and the tools to process the resulting data. However, the different backgrounds of the participants increased understanding of the current and future need for software tools.

Figure 3: The MLZ welcomed around thirty scientists for the workshop on grazing incidence scattering software.

Figure 4: A new location for a larger internal science meeting: Grainau was the place where the scientists of MLZ exchanged ideas.

New location for a larger group: Internal Science Meeting

After five meetings at Burg Rothenfels, it was decided to enlarge our biannual internal meeting and change the venue due to the newly founded MLZ having many more colleagues than before. The decision was finally made in favour of the Jungbauernschule Grainau from June 10th to 13th. More than 90 participants were counted when the majority arrived by bus direct from the gates of FRM II. The new venue provided a high standard of accommodation, and only a few people had to be put up in nearby hotels. In particular, the scenery of the Zugspitze ensured a really congenial atmosphere.

The scientific part of the meeting comprised eight plenary overview lectures covering the five topics of the newly founded scientific groups: Soft Matter, Material Science, Quantum Phenomena, Structure, and Neutron Methods. The science groups separated for three parallel sessions where scientific contributions were discussed in more detail. An interesting evening talk was given by Prof. Dr. Peter Fierlinger on the connection between high energy physics and astronomy. Some students who could not be included in the lecture programme were given the opportunity to contribute to the poster session. The feedback afterwards was entirely positive and we look forward to our next meeting!

17th JCNS Laboratory Course on Neutron Scattering

As in previous years, this annual lab course was held at two locations from September 2nd to 13th: Forschungszentrum Jülich was the venue for the lectures and the FRM II in Garching for the experiments.

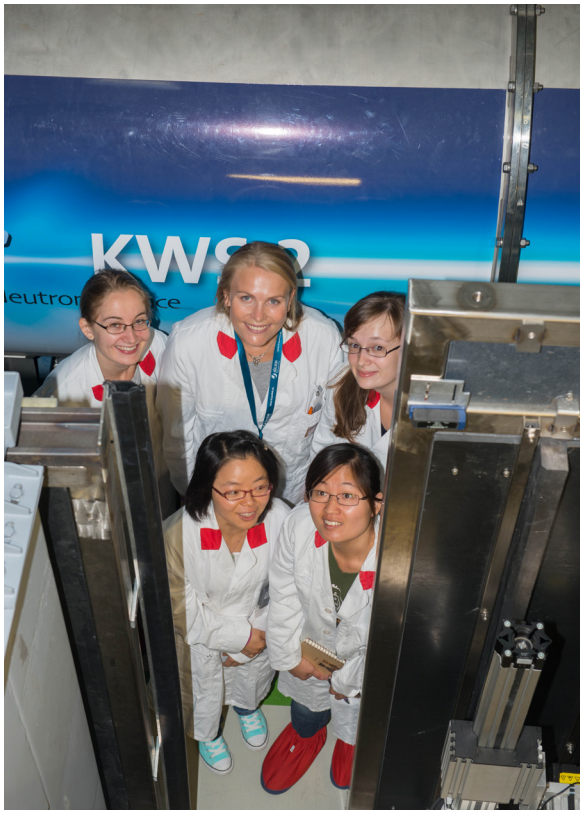

Figure 5: More and more female participants in the JCNS Laboratory Course.

The lab course is open to students of physics, chemistry, and other natural sciences worldwide. The course is part of the curricula of the Universities of Aachen and Münster. Financing came from Forschungszentrum Jülich with support from the Integrated Infrastructure Initiative for Neutron Scattering and Muon Spectroscopy (NMI3), the European Soft Matter Infrastructure project (ESMI), and the European Network of Excellence Soft Comp.

The first week of the neutron scattering course is always dedicated to lectures and assignments. In the second week, eleven instruments at the FRM II are made available for student training. These world-class instruments were provided by JCNS, RWTH Aachen, Universität Darmstadt, Universität Göttingen, LMU, and TUM.

57 students were selected from 147 applicants. 20 foreign students came from a total of 11 countries. The number of female students (42%) had increased slightly compared to the previous years.The programme was completed by a welcome party in Jülich and a farewell party in Garching.

The next JCNS laboratory course will take place from September 1st to 12th, 2014.

NINMACH

With NINMACH 2013 - Neutron Imaging and Neutron Methods in Archaeology and Cultural Heritage Research - the first conference worldwide explicitly dealing with the use of neutron methods in archaeology and cultural heritage was held at the FRM II.

From 9th to 12th September around a hundred archaeologists, conservators and physicists from all over the world were informed about still little-known methods which allow for new investigations in their fields of work.

Special emphasis was placed on neutron activation analysis (NAA), prompt gamma activation analysis, autoradiography, and neutron computed tomography.

For autoradiography, paintings can be activated for a couple of days. Some activated atoms of the paint pigments emit gamma radiation during their decay, which can be detected using X-ray films or imaging plates. This also reveals layers

Figure 6: Prof. Dr. Winfried Petry welcomes participants to the poster session at the conference on Neutron Imaging and Neutron Methods in Archaeology and Cultural Heritage Research.

of the painting that had been painted over, as well as sketchings underneath.

Neutrons can also be used in radiography and computer tomography where X-rays fail – plant seeds can be visualized in sealed ancient pottery, bronze statues can be penetrated to visualize hollow spaces and casting cores, and fossils entirely embedded in limestone can be examined, all of which deliver hardly any contrast for X-rays due to their similar composition.

In adddition to the scientific talks, the poster session with a Bavarian “Brotzeit”, and the possibility of touring either the FRM II or the Neue Pinakothek, or take part in a workshop at the Bavarian National Museum Restoration Department, the participants were especially delighted with the welcome hike to the Herzogstand, a famous Bavarian mountain with a really breathtaking view.

The next NINMACH again be held in Garching in spring 2015, and will be followed by a conference at the Budapest Neutron Centre in Hungary in 2017.

SLOPOS13

123 delegates from 21 countries accepted the NEPOMUC research group’s invitation to the 13th International Workshop on Slow Positron Beam Techniques and Applications (SLOPOS13) and gathered at the Technische Universität München from 15th to 20th September. This event is part of a series of triennial SLOPOS-conferences. It was a great honour when the international research community chose the TUM as the organiser despite keen competition from countries such as the USA, China and India.

The excellent scientific programme comprised 50 talks and 58 posters presented during two poster sessions. It was very impressive to learn about novel technical developments on positron beam facilities and the wide range of its applications all over the world.

Figure 7: More than 120 delegates at the positron workshop SLOPOS following the invitation of the Technische Universität München.

Figure 8: Established location and highly motivated participants at the JCNS Workhop on Magnetism and Correlated Electron Systems.

The workshop offered an unique opportunity to meet friends, get acquainted with new colleagues, and discuss exciting scientific topics in an informal atmosphere during a Bavarian Brotzeit at the poster sessions. Socializing had already started at the Welcome Reception in the Munich Town Hall on Sunday evening and was continued during the conference excursion when the delegates enjoyed the scenic surroundings of Lake Starnberg by boat.

The international advisory committee of SLOPOS assigned a subcommittee to award student prizes for the best presented scientific contributions. To our great delight, the prizes were given to a team of students from Finland, a French student, and the NEPOMUC team.

At the end of the conference, a guided tour of the FRM II's Experimental Hall was offered. The main focus was, of course, the positron beam facility at the high-intensity positron source NEPOMUC.

The conference was overshadowed by the sudden death of Prof. Dr. Klaus Schreckenbach immediately before the workshop. In commemoration of him as a spiritual father of the neutron induced positron source, a minute's silence was held.

JCNS Workshop on Magnetism and Correlated Electron Systems

Seventy key experts and specialists from Europe, the USA, Canada and Japan took part in this year's JCNS workshop from October 7th to 10th, which involved a total of forty invited and contributed presentations and twenty posters as part of the workshop's programme.

The charming location of the Evangelische Akademie in Tutzing, together with the enthusiasm of the highly-motivated attendees, created a stimulating atmosphere which resulted in numerous discussions throughout. The topical sessions were chosen to span an extremely wide area covering Magnetic Nanoparticles and Nanocrystals, Molecular Magnets, Unconventional Superconductors, Magnetoelectrics and Multiferroics, Frustrated and Complex Spin Systems, Interface Effects in Heterostructures, and Materials for Energy Conversion and Storage.

Thermoelectric materials for harvesting energy in waste recovery systems have found applications in niche markets. More efficient materials are urgently needed to widen the application of these devices. Inelastic scattering turns out to be an efficient tool for understanding the mechanism of the low thermal conductivity in these materials.

Figure 9: The three axes spectrometer workshop group in wintery Murnau.

JCNS contributed in total twelve oral presentations and 13 posters, underlining the key role of JCNS in neutron scattering based research in magnetism, superconductors, thin film heterostructures, and advanced instrumentation.

The next JCNS workshop will again be held in Tutzing from October 6th to 9th, 2014.

TAS Workshop with winter's onset

Thirty-two scientists from Europe and Japan attended the scientific workshop on "Single Crystal Spectroscopy: Multi-TAS or ToF?" which the Jülich Centre for Neutron Science (JCNS) of Forschungszentrum Jülich held in Murnau, Germany, from 10 - 11 October, 2013. During the night, winter's silent arrival brought with it heavy snowfall, resulting in streets and railway lines being blocked with snow. However, this unexpected event did not inhibit the lively discussions centred on the workshop's fourteen oral presentations.

Three axes spectrometers (TAS) are recognized by scientists as the instruments of choice for single crystal spectroscopy, a non-destructive analytical technique which provides detailed information on atomic motions within crystal lattices. With recent upgrades, optional multiplexing secondary spectrometers have also been developed or installed at several of the three axes spectrometers. These allow the acquisition of more information in a single scan; as a result, measurements are expected to be made faster and more efficiently. In addition, the time-of-flight (TOF) technique is a significant improvement on single crystal spectroscopy and has become a powerful complement - or alternative - to TAS spectroscopy.

During the workshop, presentations from three axes instrument scientists on multiplexing options and from TOF spectrometer scientists from reactor as well as spallation sources gave an overview of all options, both existing and planned. Attendees had the opportunity to explain their wishes and needs, and shared their experiences from the user's point of view.

From this, it became clear that the multiplexing option can turn into a rather complex set-up compared to standard TAS or TOF techniques.

TUC-MLZ Texture School@ FRM II

Following the long tradition of the Clausthal University of Technology (TUC) organizing texture schools from the early '70s, the 2013 event was held at the MLZ from October 15th to 17th. The topic of the texture school "From Area Detector to Pole Figures", organized by Prof. Dr. Heinz-

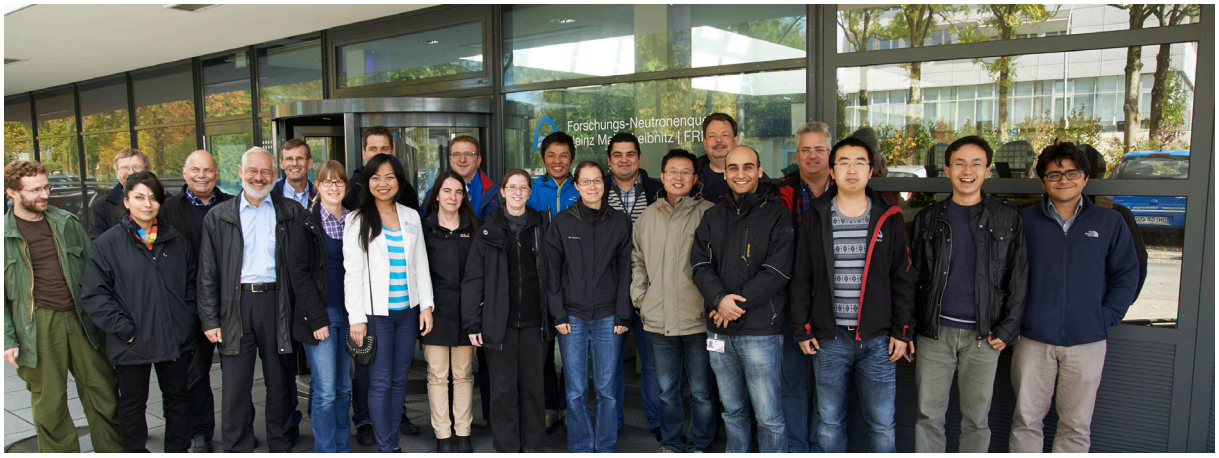

Figure 10: Practicing data treatment from area detector images to pole figures: The 22 participants of the TU Clausthal / MLZ Texture School.

Günter Brokmeier (TUC), was directly connected to modern instrumentation for neutron, synchrotron and lab-X-ray experiments. 22 participants from various universities, research institutes, and industry were welcomed by the local organisers, Dr. Michael Hofmann (FRM II) and Dr. Weimin Gan (GEMS).

The school programme comprised an introduction to crystallographic textures, pole figures and orientation distribution functions (ODFs). A key point was the practice of data treatment from area detector images to pole figures using corresponding software packages. The course was rounded off by tutorials which included the extraction and analysis of pole figures from recent measurements on STRESS-SPEC (neutrons) or HEMS (synchrotron, HZG). Finally, all the participants took the opportunity to visit the experimental halls of FRM II.

Open day at the FRM II

Bright sunshine attracted crowds of interested visitors to the research campus in Garching once again on this warm Saturday in October. And as every year, the queue to register for a tour of the FRM II in front of the desk was long and all tours were fully booked by 13:30. This year 484 visitors in total took part in the guided tours of the neutron source.

New was the strategically positioned information booth with Lego models of a three axes and a time-of-flight spectrometer in the Physics

Figure 11: Queuing in the Physics Department for a guided tour through the FRM II at the open day.

Figure 12: Work Package leaders and members of the Advisory Committee at the NMI3 Business Meeting at the MLZ.

Department of the TUM. While the visitors were queuing, the waiting time was made shorter on account of the opportunity of watching movies of the FRM II on a monitor at the booth, such as on the replacement of the fuel rod. Also new were three information boards about the MLZ and FRM II that visitors could read while queuing. The moving Lego models attracted many visitors throughout the day, who wanted to learn about neutrons, the instruments, and the research. Lectures on the MLZ and the FRM II held in the lecture hall were well attended. Topics such as hydrogen storage were enthusiastically welcomed. Even the those who were too young for the guided tour found something exciting: They were invited to target “neutrons” at the “atoms” of a crystal lattice and try to hit them. The youngsters who hit at least three “atoms” with their four “neutrons”, won a T-shirt with the logo “MLZ”.

NMI3 meeting to discuss the project’s future

On Friday, November 29th, the leaders of the NMI3 Work Packages (WP) met at the Heinz Maier-Leibnitz Zentrum (MLZ) in Garching. The scientists from LLB, ISIS, HZG, ILL, ESS, HZB, PSI, JCNS, various universities and FRM II reported on the progress of the WP’s in order to receive feedback from other members as well as from the Advisory Committee. The continuation of NMI3 throughout the European Commission Framework Programme Horizon 2020 was discussed.

F-Praktikum

In 2013 the FRM II and JCNS participated again in the “Fortgeschrittenenpraktikum” offered by the Physik-Department of TUM. A total of 50 students from the Bachelor and Master courses had registered for the practical at the MLZ facilities. Additionally, there was the “Werkstoff-Praktikum” for the international “Studiengang Ingenieurwissenschaften” of the faculty of engineering of the TU München and the Universität Salzburg with 10 participating students included in this training.

After a half-day of introduction to the neutron source FRM II and the theory of neutron scattering, each student performed two different experiments out of 14 participating instruments (HEIDI, JNSE, DNS, KWS-2, MIRA, PGAA, PANDA, PUMA, RESI, RESEDA, SPHERES, SPODI, Stress-Spec and TOFTOF). The experiments were adopted from standard user experiments typical of the physics investigated at these instruments. The experiments lasted a day each, including overnight measurements. The

Figure 13: Two students during the F-Praktikum at the instrument RESEDA.

response of the students to a short questionnaire was very enthusiastic. The main highlight for them was the possibility of working on “real” user experiments in normal operation as opposed to standard demonstration experiments.

Technical meeting on neutron scattering at high pressure

The general scope of the meeting held on December 10th and 12th was to promote the high-pressure investigations at the Heinz Maier-Leibnitz Zentrum. The characterization of the physical and chemical properties of condensed matter under extreme environmental conditions is one of the big challenges of today and of science in the near future. Despite some unique peculiarities of neutron scattering, however, high pressure investigations at large scale neutron facilities have been significantly limited so far due to the large size of the typical samples and other technical restrictions.

The participants from different facilities discussed existing equipment and expertise (complementary techniques included), basic infrastructures and the technical support required before, during and after the experiments. Great attention was also payed to the major safety aspects (laboratories, tools, testing place, etc) and the main issues for the proper handling of the HP-equipment (loading procedure, activation etc).

Figure 14: Technical meeting on neutron scattering at high pressure at the MLZ organized by Giovanna Simeoni.

The User Office on tour and further adventures

R. Bucher[1], F. Carsughi[2], U. Kurz[1], I. Lommatzsch[1], M. Neuberger[1], B. Tonin[1]

[1]Heinz Maier-Leibnitz Zentrum (MLZ), Technische Universität München, Garching, Germany
[2]Jülich Centre for Neutron Science (JCNS) at MLZ, Forschungszentrum Jülich GmbH, Garching, Germany

The User Office is happy to report on a really successful year full of user visits, experiments, reports, and travel cost forms! Neutrons and positrons were delivered smoothly to the instruments, only a few minor problems affecting our users. We were even able to use some spare time to spread our wings and leave Garching.

Presenting at Regensburg

We organised a booth at the *Spring Meeting of the Condensed Matter Section* of the Deutsche Physikalische Gesellschaft (DPG) at Regensburg in March. This conference takes place yearly and alternates between Regensburg and Dresden. This year, it attracted 5161 participants, who gave or listened to 2982 talks and held lively discussions in front of 1644 posters in total. It can therefore be rightly described as the biggest physicists' meeting in Europe. As expected, most of the participants came from German institutions, although more than 10% were visitors from other EU countries, USA and Canada, Asia, and countries further afield.

In addition to the scientific programme, there is always an industrial and book exhibition at the Spring Meeting. Here, the User Office was able to showcase for the first time the collaboration between the various partners of what has been known since February as MLZ. It offered a wonderful opportunity to attract new users: Many participants were really keen to learn about the advantages and applications of neutrons and positrons since they had never used them. Many of them were especially thrilled by the prospect of free beam time in the event of their proposal being accepted by our review panel. And what is more: Users working at German universities can also apply for reimbursement of travel and accommodation costs. We learned a lot from this experience and look forward to the next Spring Meeting in Dresden 2014!

Flavio Carsughi answering users' questions at the DPG Spring Meeting.

Towards Scotland!

In July, we headed to the Scottish capital, Edinburgh, for the *International Conference on Neutron Scattering* (ICNS) where a total of 800 scientists from 34 countries gathered together. Many of them also paid a visit to one of the more than 50 exhibitors: There, facilities, projects, and companies were presented. The MLZ shared the biggest booth with the Helmholtz-Zentrum Berlin (HZB) and welcomed many interested visitors.
This conference will be remembered especially for the stunning weather conditions. The umbrella, packed into the conference backpack as a precaution, was really useful against the - sun! A week of sunshine and temperatures around 30 °C enthralled everybody, including the organizers themselves.

A visitor from Australia

September of this year was fully packed for our team. On September 2nd, Joseph Bevitt of the Australian Nuclear Science and Technology Organisation (ANSTO) dropped in at the User Office. He is the scientific coordinator and head of the Bragg Institutes User Office. He is responsible for the management of the User Office, the proposal process through which researchers can access the instruments at Australia's Open Pool Australian Lightwater (OPAL) reactor, as well as for outreach and promotion activities. After taking up this post, he decided

Flavio Carsughi and Joseph Bevitt (ANSTO).

to visit other facilities such as the HZB, MLZ, and the Paul Scherrer Institute (PSI) in order to discuss the organisation of a User Office with colleagues working in the same area. His day in Garching started with a tour of the instruments, followed by an overview of workflow at the User Office. After lunch, information regarding our handling of industrial projects as well as our educational activities helped to create a complete picture. It was a pleasure to get to know a colleague from down under and some smart ideas were also generated by our chats.

Review panel meeting

On September 5th to 6th, this year's second review panel meeting was held in Ismaning. The joint MLZ review panels were established in 2012 and until now the workload had been divided between six subcommittees. They discharged their responsibilities in the last two review meetings held in September 2012 and March 2013.

For both these proposal rounds, we received about 300 proposals. Unfortunately, the distribution of the proposals to the six review panels can not be even as the six areas experience different levels of demand. At the first proposal round in 2013, the members of the review panel "Magnetism & Spectroscopy" had to deal with 102 proposals, which represents about 30% of the total number of submitted proposals. This large number is mainly due to the wide range of scientific applications which fall within the remit of the review panel. In order to improve the work of

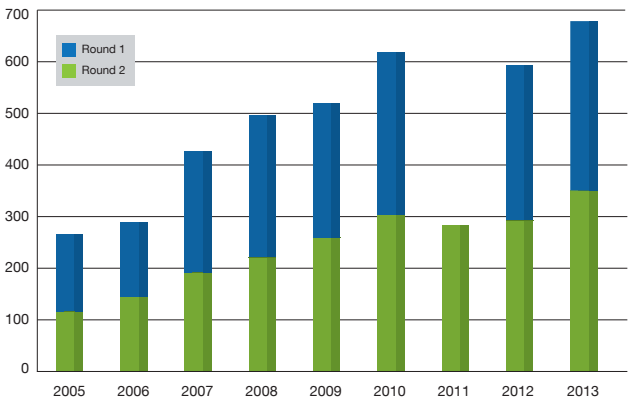

Submitted proposals since 2005.

At the ICNS, most of our colleagues came together and posed for the obligatory group photo of MLZ and HZB. This was a really serious session as you can see...

this panel, it was decided to increase the number of members from eleven to 17 and to create two subcommittees, one dealing with inelastic and the other with elastic applications. In this way we not only reduced the work load on each member of the review panel, but also gained additional experts in each field. It was a great success and the referees were really satisfied with this new situation.

Fast, faster - rapid access

Another improvement for our users was launched in July: The new Rapid Access Programme. Up to three beam days per reactor cycle are allocated to urgent short-term measurements at SPODI, KWS-2, and PGAA. The programme is devoted to those projects that do not fit into our normal proposal workflow, with two deadlines and reviews per year. First result after two rounds: The proposals submitted concerned in the main material science, magnetism and archeology, whereas the remainder was spread over biology, crystallography, chemistry, and condensed matter physics. As requests far outstrip the available beam time, this new programme appears to have hit the spot.

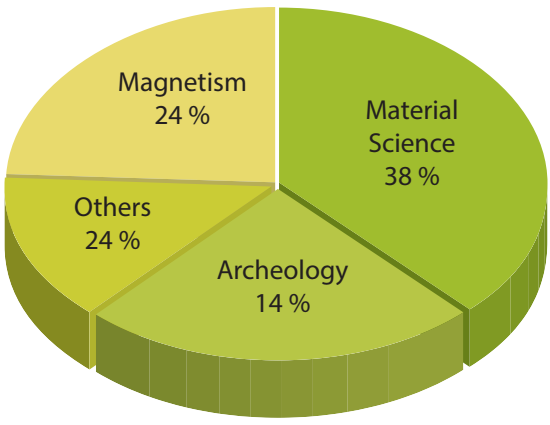

The topics of the Rapid Access Programme so far.

From science to media: the public relations office

C. Hesse[1], Ch. Kortenbruck[1], U. Kurz[1], B. Tonin[1], P. Riedel[1], A. Voit[1], A. Wenzik[2]

[1]Heinz Maier-Leibnitz Zentrum (MLZ), Technische Universität München, Garching, Germany

[2]Jülich Centre for Neutron Science (JCNS) at MLZ, Forschungszentrum Jülich GmbH, Jülich, Germany

In contrast to the past years, 2013 was period of calm, dedicated more or less to "business as usual". Media coverage was almost exclusively based on scientific news from the Heinz Maier-Leibnitz Zentrum. 2790 visitors were shown around the facilities, most of them pupils and students. About 24 science journalists were also among the visitors.

Visitors

The number of visitors has remained fairly constant for many years, at around 3000. In 2013, 2790 people visited the FRM II. Almost 60 % of them were pupils or students, with 484 taking advantage of the open day in October.

Visit of 24 science journalists

Among the visitors were 24 science journalists from the ARD group. The positive contact between the science editors of the Bayerische Rundfunk and the FRM II press office had already resulted in a visit in 2011. On this occasion, the journalists were not only treated to a very exciting tour which took in a view of the reactor pool, the Experimental and Neutron Guide Hall, but also welcoming words from the two directors, Prof. Dr. Dieter Richter and Prof. Dr. Winfried Petry, as well as the head of the TUM PR office, Ulrich Marsch.

Figure 1: The 24 TV journalists of the ARD group were given a tour of the FRM II.

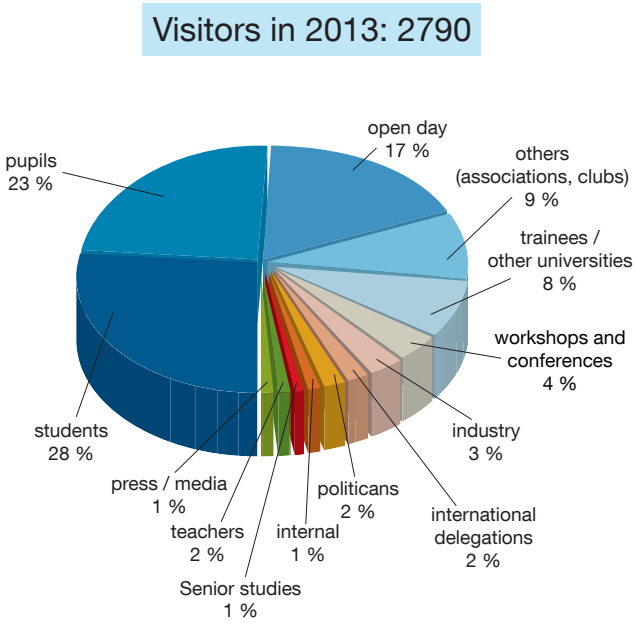

Figure 2: A total of 2790 visitors enjoyed a guided tour of the FRM II in 2013.

In September, more than 30 scholarship holders of the Bayerische Forschungsstiftung together with the management visited the neutron source. The management team was so impressed that they booked a separate visit for themselves some weeks later in order to gain a deeper insight into the possibilities afforded by neutrons.

New website

Following a supreme effort involving many hands, the new website www.mlz-garching.de

was launched in February for the inauguration of the Heinz Maier-Leibnitz Zentrum. It not only displays information about science at the MLZ and the instruments, but also its history, news about research or events and facts and figures about the MLZ and its partners. The website www.frm2.tum.de will be relaunched in 2014, displaying mainly information about the neutron source, focusing on the technical aspects.

Highlights exhibition in Wuppertal

The main event organized by the FRM II press office was the exhibition show-casing the MLZ and FRM II at the "Highlights der Physik" in Wuppertal held by the Federal Ministry of Education and Research (BMBF) and the Deutsche Physikalische Gesellschaft (DPG). The event took place right in front of the city hall in Wuppertal in the middle of the pedestrian shopping zone. In the mornings, school classes filled the tents while, in the afternoons and at the weekend, the fascinated pupils came back with their parents to show them what wonderful and interesting things they had discovered during the week.

More than 30 other institutions show-cased their experiments next to FRM II and MLZ. Two new Lego models of MLZ instruments were the great attraction of the stand. At a neutron ball toss, children were invited to throw "neutron" balls at five "atoms" and try to hit them in order to win a MLZ T-shirt. After five days, 150 T-shirts had changed hands.

Safety brochure

Every five years, government regulations require that all operators of nuclear plants supply a new safety brochure for the neighborhood. This applies equally to research reactors such as FRM II. The brochure was revised, but was withdrawn at the last moment before printing because the government was (and is) still working on new guidelines for nuclear operators. In view of this, the new brochure will be revised according to new guidelines and will therefore be printed later.

DAAD-Photoshooting

In November, the "Deutsche Akademische Austauschdienst" (DAAD) asked for a professional photo shoot at the FRM II. The DAAD wanted to enrich its archive with images from interesting research areas to promote Germany as a science leader. After intense wheeling and dealing, the DAAD allowed us make one-off use of the photos they had taken for our own brochures and web pages. The press office thanks all models, who volunteered for the pictures, which will be used in the Festschrift for the 10th anniversary of the FRM II and the new brochure on industrial and medical applications in 2014.

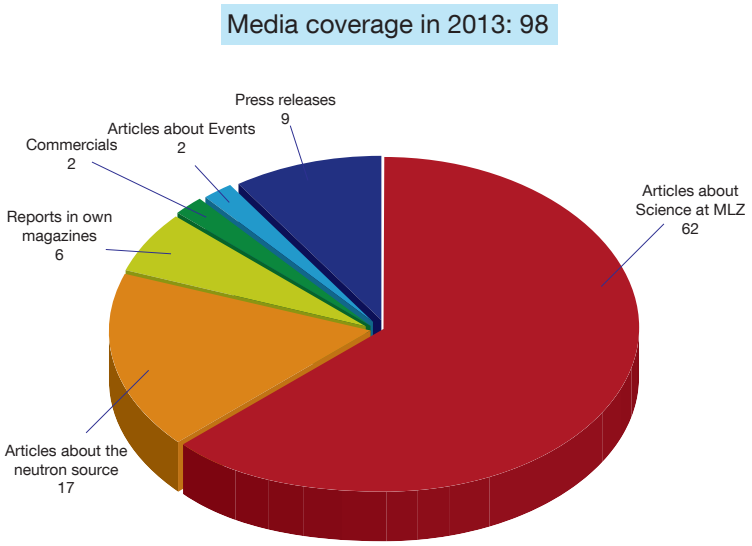

Figure 3: 62 media articles in 2013 concerned scientific topics from MLZ, for example the examination of human brains for lithium.

Media coverage

Media coverage in 2013 was focused almost exclusively on research at the Heinz Maier-Leibnitz Zentrum. Out of 87 total press clippings (excluding publications in our own media), only 17 concerned the operation of the neutron source, whereas 71 percent reported on the research carried out at the MLZ. In total, 9 press releases were sent out by the FRM II press office and their partners at JCNS. This will be intensified again in 2014. Highlights were the press release of JCNS about a brush cleaner and the TUM press release regarding lithium in the brain, found at PGAA. Even the conference NINMACH aroused interest and was reported in a podcast and an article printed in the Süddeutsche Zeitung.

Staff

Scientific Cooperation at the Heinz Maier-Leibnitz Zentrum (MLZ)

The Heinz Maier-Leibnitz Zentrum with its cooperation partners Technische Universität München (TUM), Forschungszentrum Jülich and Helmholtz-Zentrum Geesthacht (HZG) is embedded in a network of strong partners including the Max Planck Society (MPG) and numerous university groups exploiting the scientific use of the Forschungs-Neutronenquelle Heinz Maier-Leibnitz. The organizational chart is shown in the figure below.
The Administration, Reactor and Science Division, comprising the Reactor Physics and Fuel Development, belong to the Corporate Research Center FRM II (ZWE-FRM II) operated by the TUM.

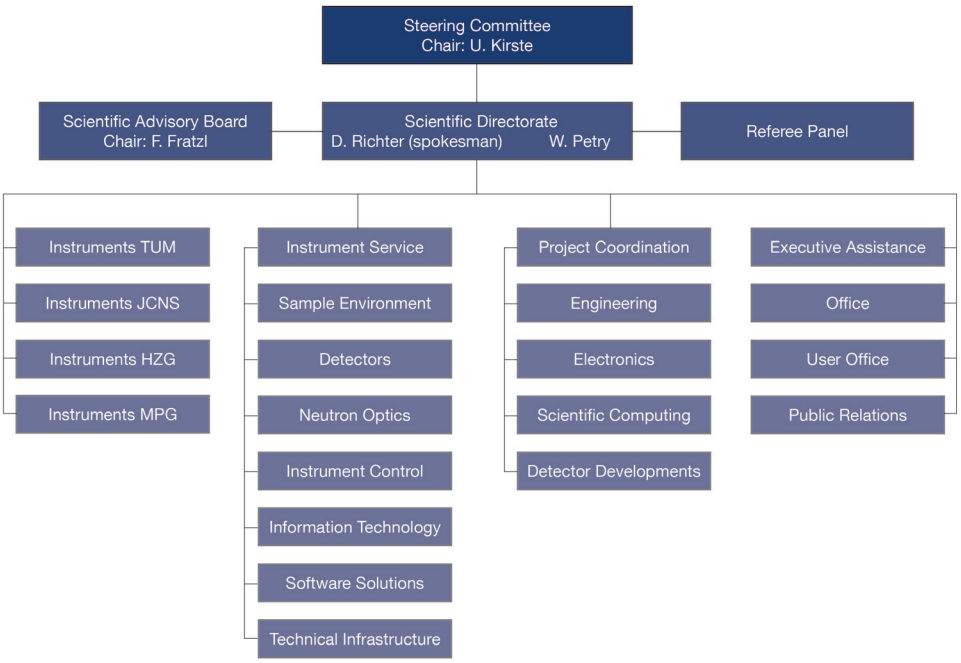

Scientific Director TUM
Prof. Dr. Winfried Petry

Deputy
Dr. Jürgen Neuhaus

Scientific Director HGF Institutions
Prof. Dr. Dieter Richter (spokesman MLZ)

Deputy
Dr. Alexander Ioffe

Executive Assistance
Dr. Rainer Bruchhaus
Dr. Connie Hesse

Office
Bettina Heilgeist
Elisabeth Jörg-Müller
Franziska Michel
Silvia Valentin-Hantschel
Karin Kleinstück (Erasmus Mundus)

User Office
Dr. Flavio Carsughi
Dr. Ina Lommatzsch
Ramona Bucher

Public Relations
Christine Kortenbruck
Petra Riedel
Silvia Valentin-Hantschel
Andrea Voit
Inês Crespo (NMI3)

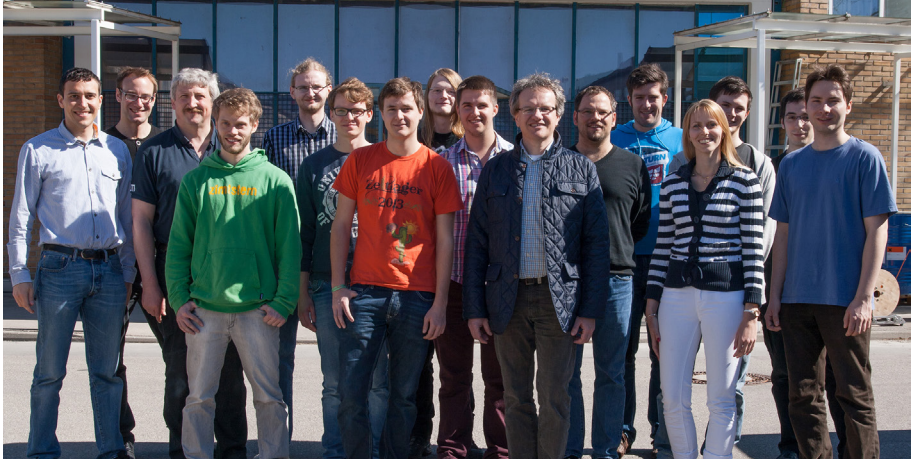

Group NEPOMUC (FRM II, TUM) with its head PD Dr. Christoph Hugenschmidt (7th from the right).

Instruments TUM

Dr. Jürgen Neuhaus

Ulrich Ackermann[1]
Dominik Bausenwein
David Behal
Christoph Berkel
Rainer Bierbaum
Dr. Christian Bocquet
Georg Brandl
Karl Braun
Dr. Thomas Bücherl[2]
Dr. Lea Canella
Hubert Ceeh[3]
Alfonso Chacón
Dr. Peng Cheng
Fernando Cristiano
Marcel Dickmann[1]
Mustafa Dogu
Dr. Oleksandr Dolotko
Dr. Werner Egger[1]
Dr. Andreas Frei
Christian Fuchs
Fabian Fuchs
Dr. Robert Georgii
Philipp Geselbracht
Stefan Giemsa[4]
Thomas Gigl[3]
Dr. Ralph Gilles
Dr. Alexander Grünwald[4]
Dr. Wolfgang Häußler
Dr. Michael Hofmann
Dr. Markus Hölzel
Dr. Christoph Hugenschmidt
Walter Hulm
Dr. Wentao Jin
Norbert Jünke
Lukas Karge
Dr. Thomas Keller[5]
Dr. Yury Khaydukov[5]
Dr. Jens Klenke
Dr. Krzysztof Kleszcz
Prof. Dr. Peter Kneschaurek
Dr. Petra Kudejova
Maximilian Kugler
Dr. Thorsten Lauer
Kathrin Lehmann
Dr. Michael Leitner
Benjamin Löwe[1]
Dr. Wiebke Lohstroh
Andreas Mantwill[3]
Markus Mayer
Leopold Meier
Mykhailo Monchak[6]
Humphrey Morhenn
Dr. Christoph Morkel
Martin Mühlbauer[6]
Nathalie Munnikes[5]
Dr. Shiababrata Nandi
Pascal Neibecker
Dr. Andreas Ostermann
Dr. Jitae Park
Dr. Neelima Paul
Dr. Bjørn Pedersen
Josef Pfanzelt
Philip Pikart[3]
Dr. Christian Piochacz
Luca Ravelli[1]
Dr. Joana Rebelo-Kornmeier
Tommy Reimann
Markus Reiner[3]
Dr. Zsolt Révay
Jandal Ringe
Heiko Saul
Johann Schilcher
Dr. Burkhard Schillinger
Philipp Schmakat
Martin Schmiele[7]
Prof. Dr. Klaus Schreckenbach†
Juri Schroffenegger
Dr. Michael Schulz
Reinhard Schwikowski
Dr. Klaus Seemann
Dr. Anatoliy Senyshyn
Günther Seidl
Dr. Stefan Seidlmayer
Svatopluk Semecky
Luca Silvi
Dr. Giovanna Simeoni
Stefan Söllradl[8]
Dr. Oleg Sobolev[9]
Dr. Olaf Soltwedel[5]
Martin Stadlbauer
Rainer Stöpler[3]
Dr. Reinhard Thamm[10]
Dr. Anke Teichert[9]
Kuo-Feng Tseng[5]
Sebastian Vohburger
Daniela Voigt-Kiely
Franz-Michael Wagner
Dr. Nicolas Walte[11]
Josef-Andreas Weber[3]
Tobias Weber
Stefan Wenisch
Rudolf Wildgruber
Andreas Wilhelm
Stephan Wlokka
Thorsten Zechlau
Samantha Zimnik
Dr. Veronika Zinth

PhD students at the MLZ.

Instruments JCNS

Prof. Dr. Dieter Richter
(Director JCNS)
Dr. Alexander Ioffe
(Head of Outstation at MLZ)

Dr. Robert Aldus
Dr. Marie-Sousai Appavou
Dr. Nikolaus Arend
Dr. Earl Babcock
Antonella Campanella
Dr. Petr Cermak
Dr. Sultan Demirdis
Dr. Zhenyu Di
Christian Felder
Erxi Feng
Dr. Artem Feoktystov
Dr. Henrich Frielinghaus
Dr. Zhendong Fu
Thomas Glomann
Marco Gödel
Barbara Gold
Bernhard Großmann
Dennis Gurzi
Adrian Hamm
Dr. Olaf Holderer
Bernhard Hopfenmüller
Dr. Andreas Houben[12]
Dr. Vladimir Hutanu[12]
Joao-Paulo Innocente
Dr. Oxana Ivanova
Dr. Sebastian Jaksch
Dr. Marina Khaneft
Abdelillah Kobba[12]
Thomas Kohnke
Dr. Denis Korolkov
Dr. Alexandros Koutsioumpas
Harald Kusche
Frederik Lipfert
Wolfgang Luberstetter[12]
Dr. Simona Maccarrone
Dr. Stefan Mattauch
Shailesh Mishra
Dr. Martin Meven[12]
Dr. Matthias Muthmann
Andreas Nebel
Dr. Kirill Nemkovski
Vladimir Ossovyi
Dr. Vitaliy Pipich
Stephen Price
Dr. Sabine Pütter
Dr. Aurel Radulescu
Christian Randau[13]
Alfred Richter
Dr. Zahir Salhi
Dr. Andrew Sazonov[12]
Dr. Maria-Maddalena Schiavone
Harald Schneider
Florian Schneider
Dr. Gerald J. Schneider
Dr. Astrid Schneidewind
Dr. Tobias Schrader
Dr. Werner Schweika
Simon Staringer
Alexandra Steffen
Florin George Stoica
Dr. Yixi Su
Dr. Amir Syed Mohd
Dr. Noemi Szekely
Dr. Jörg Voigt
Daniel Vujevic
Dr. Jens Walter[13]
Rui Wang
Baou Wu[14]
Dr. Michaela Zamponi

Instruments HZG

Nowal Alhamdany[15]
Dr. Helmut Eckerlebe
Joergen Franke
Dr. Weimin Gan
Martin Haese-Seiller
Dr. André Heinemann
Armin Kriele
Dr. Jean-François Moulin
Matthias Pomm
Sven-Arne Siegfried

Sample Environment

Dr. Jürgen Peters (head)
Michael Beywl
Peter Biber
Andreas Buchner
Alexander Friedrich
Markus Göhr
Heinrich Kolb
Melanie Resag
Herbert Weiß
Jank Wenzlaff

Detectors and Electronics

Dr. Karl Zeitelhack (head)
Yasin Abdullahi
Ilario Defendi
Dr. Martin Jurkovic
Max Panradl
Peter Wind
Dr. Irina Stefanescu
Machiel Zee

Members of the ZWE-FRM II administration with Dr. Klaus Seebach, administrative director (right).

Neutron Optics
Dr. Peter Link (head)
Christian Breunig
Eberhard Kahle
Dr. Sergey Masalovich
Andreas Ofner
Senay Öztürk
Peter Stein
Josef Weber

IT Services
Jörg Pulz (head)
Andreas Erb
Josef Ertl
Jörg Stoll
Hermann Westermayer

Instrument Control
Jens Krüger (head)
Dr. Enrico Faulhaber
Alexander Lenz

Software Solutions
Harald Wenninger
Nataliya Ivanova

Apprentices at the IT Services
Christina Cindric
Stefan Huber
Simon König
Pascal Neubert
Stefan Rainow
Sebastian Schmid

Technical Infrastructure
Dr. Herbert Reithmeier (head)
Edina Aulenbacher
Alexander Beimler
Heiner Blumenthal
Elbio Calzada
Eduard Preisenberger
Uwe Reinecke

Scientific Computing
Dr. Joachim Wuttke (head)
Dr. Celine Durniak
Dr. Marina Ganeva
Dr. Gennady Pospelov
Dr. Antti Soininen
Dr. Walter Van Herck

[1]Universität der Bundeswehr München
[2]Radiochemie, TUM
[3]Physik-Department, TUM
[4]Universität zu Köln
[5]Max-Planck-Institut für Festkörperforschung, Stuttgart
[6]Karlsruher Institut für Technologie
[7]Friedrich-Alexander-Universität Erlangen-Nürnberg
[8]Universität Bern
[9]Georg-August-Universität Göttingen
[10]Klinikum rechts der Isar, TUM
[11]Universität Bayreuth
[12]RWTH Aachen University
[13]Georg-August-Universität Göttingen
[14]Universität Konstanz
[15]TU Clausthal
[†]Deceased.

Staff members of the Department Radiation Protection with its head Michael Schmidt (3rd from right).

Corporate Research Center FRM II (ZWE-FRM II)

Board of Directors
Dr. Anton Kastenmüller, Technical Director
Prof. Dr. Winfried Petry, Scientific Director
Dr. Klaus Seebach, Administrative Director

Administration

Head
Dr. Klaus Seebach

Deputy
Reinhard Obermeier

Office
Christine Zeller

Christina Auer
Karl-Heinz Drexler
Brigitte Gallenberger
Bernd Heck
Isabella Heinath
Karin Lüttig
Marita Neuberger
Sabine Osorio
Martina Pawlik
Kerstin Rickert
Sylvia Rubsch
Günter Wagner

Visitors' service
Ulrike Kurz
Dott. Bianca Tonin-Schebesta

Reactor Division

Head of Reactor Division
Dr. Anton Kastenmüller

Deputies
Dr. Heiko Gerstenberg
Roland Schätzlein

Office
Sabine Radovics
Barbara Tiepke

Security
Ralf Brosche
Johann Stephani

Department Reactor Monitoring and Radiation Protection
Michael Schmidt (head)
Johann Aigner
Dubravka Bahmet
Rita Bertsch
Wolfgang Dollrieß
Nihad Hodzic
Harry Hottmann
Florian Jeschke
Marcel Kaleve
Vanessa Kindel
Waldtraud Kluge
Daniela Lewin
Roland Maier
Petra Müller
Bernhard Neugebauer
Klemens Otto
Thomas Ramel
Adelheid Schindler
Johann Schreiner
David Schrulle
Daniela Strobl
Michaela Uhlmann
Hans-Jürgen Werth
Josef Wetzl
Susanne Wolff
Dr. Helmut Zeising

Department Reactor Enhancement
Dr. Andreas Kusterer (head)
Alen Begic
Michaela Benedikt
Wilhelm Bünten
Jean-Marie Favoli
Johann Fink
Thomas Fliegner
Bernhard Foth
Andreas Galsterer
Mira Giourges
Christian Großklaus
Christian Herzog
Andreas Huber
Philipp Jüttner
Thomas Kormann
Daniel Kreutz
Karin Lichtenstein
Ralf Lorenz
Christa Morgenstern
Manfred Offtermatt
Britta Pollom
Andreas Scharl
Robert Schlecht
Uwe Stiegel
Volker Zill

Apprentices in the Workshops
Katharina Bulla
Florian Jaumann

Staff members of the Reactor physics group with Prof. Dr. Winfried Petry (6th from the right).

Department Reactor Operation

Dr. Axel Pichlmaier (head)
Attila Bancsov
Rainer Becker
Albin Benke
Robert Binsch
Oliver Breu
Manfred Danner
Christian Feil
Martin Flieher
Horst Gampfer
Wolfgang Glashauser
Hubert Groß
Friedrich Gründer
György Guld
Lutz Herdam
Simone Herrmann
Florian Hofstetter
Konrad Höglauer
Thomas Kalk
Georg Kaltenegger
Frank Kewitz
Marc-Guido Krümpelmann
Johann Kund
Adolf Lochinger
Manfred Macher
Gerd Mauermann
Albert Meilinger
Markus Moser
Klaus Pfaff
Ludwig Rottenkolber
Florian Schäfer
Gerhard Schlittenbauer
Christiane Wickfelder
Michael Wöhner
Christian Ziller
Ismail Zöybek

Department Irradiation and Sources

Dr. Heiko Gerstenberg (head)
Jens Birko
Alexander Draack
Heiko Fischer
Michael Fuß
Georg Haas
Wolfgang Lange
Volker Loder
Jens Molch
Christian Müller
Dietmar Päthe
Heike Schulz
Benjamin Schweiger
Michael Stadler
Norbert Wiegner
Andreas Wirtz

Department Electrical and Control Systems

Roland Schätzlein (head)
Werner Buchner
Andreas Düring
Franz Götz
Robert Krammer
Karl-Heinz Mayr
Thomas Metzger
Johann Wildgruber

FRM (old)

Stefan Förg
Josef Waronitza

Conventional Infrastructure

Karola Frey
Andreas Heinath
André Wienholz

Science Division

Reactor Physics

Dr. Anton Röhrmoser (head)
Dr. Harald Breitkreutz

Fuel Development

Dr. Harald Breitkreutz (head)
Hsin-Yin Chiang
Bruno Baumeister
Alexandra Egle
Dr. Rainer Großmann
Tobias Hollmer
Tanja Huber
Dr. Rainer Jungwirth
Christian Reiter
Dr. Anton Röhrmoser
Robert Schenk
Christian Steyer
Tobias Zweifel

Committees

Koordinierungsrat (Steering Committee)

Chairman

MRin Dr. Ulrike Kirste
Bayerisches Staatsministerium für Wissenschaft, Forschung und Kunst

Members

Karsten Beneke
Vice-Chairman of the Board of Directors of Forschungszentrum Jülich GmbH

Albert Berger
Chancellor
of the Technische Universität München

Thomas Frederking
Member of the Executive Board of Helmholtz-Zentrum Berlin GmbH

Prof. Dr. Dr. h.c. mult. Wolfgang A. Herrmann
President
Technische Universität München
represented by Prof. Dr. Thomas Hofmann,
Vice-President
of the Technische Universität München

MinR Dr. Ulrich Katenkamp
Federal Ministry of Education and Research

Prof. Dr. Wolfgang Kaysser
Member of the Executive Board of Helmholtz-Zentrum Geesthacht GmbH

MinR Stefan Kern
Federal Ministry of Education and Research

Prof. Dr. Stephan Paul
Technische Universität München
Physik-Department E18

Guests

Prof. Dr. Winfried Petry, Scientific Director of the MLZ, representing TUM

Prof. Dr. Dieter Richter, Scientific Director of the MLZ, representing HGF institutions

Dr. Anton Kastenmüller
Technical Director ZWE-FRM II,
Technische Universität München

Dr. Klaus Seebach
Administrative Director ZWE-FRM II,
Technische Universität München

Dirk Schlotmann
Forschungszentrum Jülich GmbH

Wissenschaftlicher Beirat (Scientific Advisory Board)

Chairman

Prof. Dr. Peter Fratzl
Max-Planck-Institut für Kolloid- und Grenzflächenforschung, Potsdam

Members

Prof. Dr. Hartmut Abele
Atominstitut der Österreichischen Universitäten
Technische Universität Wien, Wien

Prof. Christiane Alba-Simionesco
Laboratoire Léon Brillouin,
Centre d'Energie Atomique, Saclay

Prof. Dr. Arantxa Arbe
Unidad de Fisica de Materiales
Facultad de Quimica, San Sebastian

Prof. Dr. Andrew Harrison
Institut Laue-Langevin, Grenoble

Prof. Dr. Dirk Johrendt
Ludwig-Maximilians-Universität,
Department Chemie und Biochemie, München

Prof. Dr. Bernhard Keimer
Max-Planck-Institut für Festkörperforschung, Stuttgart

Prof. Dr. Joël Mesot
Paul Scherrer Institut, Villigen

Prof. Dr. Joachim O. Rädler
Ludwig-Maximilians-Universität,
Department für Physik, München

Prof. Dr. Walter Reimers
Technische Universität Berlin, Institut für Werkstoffwissenschaften und -technologien, Berlin

Dr. Jens Rieger
Senior Vice President, Advanced Materials & Systems Research
BASF SE, Ludwigshafen

Prof. Dr. Metin Tolan
Leiter Beschleuniger- & Synchrotronlabor
Technische Universität Dortmund, Dortmund

Evaluation of Beam Time Proposals: Members of the Review Panels

Dr. Tamás Belgya
Budapest Neutron Center, Budapest

Dr. Victor Bodnarchuk
Joint Institute for Nuclear Research
Frank Laboratory of Neutron Physics, Dubna

Prof. Dr. Jan Bonarski
Polish Academy of Sciences, Institute of Metallurgy and Materials Science, Kraków

Dr. Laszlo Bottyan
Hungarian Academy of Sciences
Institute for Particle and Nuclear Physics, Budapest

Dr. Françoise Bourrée
Laboratoire Léon Brillouin,
Centre d'Energie Atomique, Saclay

Prof. Roberto Brusa
Università degli Studi di Trento,
Facoltà di Ingegneria, Dipartimento di Fisica, Trento

Prof. Dr. Roberto Caciuffo
Institute for Transuranium Elements
Joint Research Center, Karlsruhe

Dr. Monica Ceretti
Université de Montpellier2,
Institut Charles Gerhardt, Montpellier

Dr. Niels Bech Christensen
Technical University of Denmark,
Institute of Physics, Roskilde

Dr. Pascale Deen
European Spallation Source (ESS AB), Lund

Prof. Dr. Stefan Egelhaaf
Heinrich-Heine-Universität Düsseldorf,
Lehrstuhl für Physik der weichen Materie, Düsseldorf

Prof. Dr. Helmut Ehrenberg
Karlsruher Institut für Technologie (KIT),
Institut für Angewandte Materialien, Karlsruhe

Dr. Marie Thérèse Fernandez-Diaz
Institut Laue-Langevin (ILL), Grenoble

Dr. Peter Fouquet
Institut Laue-Langevin (ILL), Grenoble

Dr. Victoria Garcia-Sakai
STFC Rutherford Appleton Laboratory, Didcot

Prof. Giacomo Diego Gatta
Università degli Studi di Milano, Milano

Prof. Dr. Rupert Gebhard
Archäologische Staatssammlung München,
Abt. Vorgeschichte, München

Dr. Jens Gibmeier
Karlsruher Institut für Technologie (KIT),
Institut für Angewandte Materialien, Karlsruhe

Dr. Béatrice Gillon
Laboratoire Léon Brillouin
Centre d'Energie Atomique, Saclay

Welcome of the members of the review panels evaluating beam time at the proposal round in September 2013.

Dr. Arsène Goukassov
Laboratoire Léon Brillouin
Centre d'Energie Atomique, Saclay

Dr. Christian Grünzweig
Paul Scherrer Institute, Villigen

Prof. Dr. Ian Williams Hamley
University of Reading, Reading

Dr. Thomas Hauss
Helmholtz-Zentrum Berlin für Materialien und Energie GmbH, Berlin

Prof. Dr. Stephen Hayden
University of Bristol
HH Wills Physics Laboratory, Bristol

Dr. Arno Hiess
European Spallation Source (ESS AB), Lund

Dr. Klaudia Hradil
Technische Universität Wien,
Röntgenzentrum, Wien

Dr. Nikolay Kardjilov
Helmholtz-Zentrum Berlin für Materialien und Energie GmbH, Berlin

Prof. Dr. Michel Kenzelmann
Paul Scherrer Institute, Laboratories for Solid State Physics & Neutron Scattering, Villigen

Prof. Christian Krempaszky
Technische Universität München,
Fakultät für Maschinenwesen, München

Dr. Eberhard Lehmann
Paul Scherrer Institute, Villigen

Prof. Dr. Martin Lerch
Technische Universität Berlin,
Institut für Chemie, Berlin

Dr. Dieter Lott
Helmholtz-Zentrum Geesthacht GmbH,
Institut für Materialforschung, Geesthacht

Prof. Dr. Andreas Magerl
Universität Erlangen-Nürnberg,
Kristallographie und Strukturphysik, Erlangen

Dr. Andreas Michels
Université de Luxembourg,
Faculté des Sciences, de la Technologie et de la Communication, Luxembourg

Dr. Bert Nickel
Ludwig Maximilians-Universität München,
Department für Physik, München

Prof. Dr. Tommy Nylander
Lund University,
Physical Chemistry, Lund

Prof. Dr. Luigi Paduano
University of Naples "Federico II",
Chemistry Department, Naples

Prof. Dr. Catherine Pappas
Delft University of Technology, Delft

Meeting of the review panel „Structure“ in Ismaning, September 2013.

Prof. Dr. Tobias Unruh
Universität Erlangen-Nürnberg,
Kristallographie und Strukturphysik, Erlangen

Dr. Lambert van Eijck
Delft University of Technology,
Department of Radiation, Radionuclides and
Reactors, Delft

Prof. Dr. Regine von Klitzing
Technische Universität Berlin,
Institut für Chemie, Stranski-Laboratorium für
Physikalische und Theoretische Chemie, Berlin

Dr. Martin Weik
Institut de Biologie Structurale, Grenoble

Dr. Andrew Wildes
Institut Laue-Langevin (ILL), Grenoble

Dr. Robert Wimpory
Helmholtz-Zentrum Berlin für Materialien und
Energie GmbH, Berlin

Partner institutions

Bayerisches Geoinstitut
Universität Bayreuth
www.bgi.uni-bayreuth.de

Georg-August-Universität Göttingen

- Institut für Physikalische Chemie
  www.uni-pc.gwdg.de/eckold
- Geowissenschaftliches Zentrum
  www.uni-goettingen.de/de/125309.html

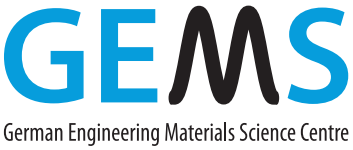

German Engineering Materials Science Centre GEMS
Helmholtz-Zentrum Geesthacht GmbH
www.hzg.de

Helmholtz-Zentrum Berlin
für Materialien und Energie GmbH *(silent partner)*
www.helmholtz-berlin.de

Jülich Centre for Neutron Science JCNS
Forschungszentrum Jülich GmbH
www.jcns.info

Karlsruher Institut für Technologie

- Institut für Angewandte Materialien –
  Energiespeichersysteme (IAM-ESS)
  www.iam.kit.edu

Ludwig-Maximilians-Universität München

- Sektion Kristallographie
  www.lmu.de/kristallographie
- Sektion Physik
  www.softmatter.physik.uni-muenchen.de

Max-Planck-Institut für Festkörperforschung, Stuttgart
www.fkf.mpg.de

Paul Scherrer Institut

- Labor für Radio- und Umweltchemie
  www.psi.ch/lch

RWTH Aachen

- Institut für Kristallographie
  www.xtal.rwth-aachen.de
- Institut für Anorganische Chemie
  www.ac.rwth-aachen.de

Technische Universität Clausthal

- Institut für Werkstoffkunde und Werkstofftechnik
  www.iww.tu-clausthal.de

Technische Universität Dresden

- Institut für Festkörperphysik
  www.physik.tu-dresden.de/ifp

Technische Universität München

- E13 – Lehrstuhl für Funktionelle Materialien
  www.e13.physik.tu-muenchen.de
- E18 – Lehrstuhl für Experimentalphysik I
  www.e18.ph.tum.de
- E21 – Lehrstuhl für Neutronenstreuung
  www.e21.ph.tum.de
- Exzellenzcluster „Origin and Structure of the Universe“
  www.universe-cluster.de
- Klinikum Rechts der Isar
  www.med.tum.de
- RCM - Radiochemie München
  www.rcm.tum.de

Universität der Bundeswehr München

- Institut für Angewandte Physik und Messtechnik
  www.unibw.de/lrt2

Universität zu Köln

- Institut für Kernphysik
  www.ikp.uni-koeln.de
- II. Physikalisches Institut
  www.ph2.uni-koeln.de

Publications

1. A. Accardo, G. Mangiapia, L. Paduano, G. Morelli and D. Tesauro, Octreotide labeled aggregates containing platinum complexes as nanovectors for drug delivery. J. Pept. Sci. 19, 190-197 (2013).

2. M. Angst, Cover Picture: Ferroelectricity from iron valence ordering in rare earth ferrites?. physica status solidi (RRL) 7 (2013).

3. L. Anovitz, D. Cole, D. Faulder, J. Sheets, H.-W. Wang, G. Rother, M. Wasbrough, R. Hjelm, M. Hartl, V. Pipich and Z. Fu, Analysis of Multiscale Porosity at the Coso Geothermal Field. Proceedings of the Thirty-Eighth Workshop on Geothermal Reservoir Engineering Stanford University (2013).

4. V. Antonelli, W. Lohstroh and H. Baier, Feasibility Study of a large chopper disk for a TOF spectrometer, Proceedings of the 19th International Conference on Composite Materials, Montreal (2013).

5. K. Arbi, M. Hoelzel, A. Kuhn, F. Garcia-Alvarado and J. Sanz, Structural Factors That Enhance Lithium Mobility in Fast-Ion $Li_{1+x}Ti_{2-x}Al_x(PO_4)_3$ ($0 \le x \le 0.4$) Conductors Investigated by Neutron Diffraction in the Temperature Range 100–500 K. Inorg. Chem. 52, 9290-9296 (2013).

6. M. V. Avdeev, V. L. Aksenov, Z. Gazová, L. Almásy, V. I. Petrenko, H. Gojzewski, A. V. Feoktystov, K. Siposova, A. Antosova, M. Timko and P. Kopcansky, On the determination of the helical structure parameters of amyloid protofilaments by small-angle neutron scattering and atomic force microscopy. J. Appl. Crystallogr. 46, 224–233 (2013).

7. E. Babcock, Z. Salhi, M.-S. Appavou, A. Feoktystov, V. Pipich, A. Radulescu, V. Ossovyi, S. Staringer and A. Ioffe, Polarization Analysis with ^{3}He Spin Filters for Separating Coherent from Incoherent Scattering in Soft Matter Studies. Physics Procedia 42, 154-162 (2013).

8. E. Babcock, Z. Salhi and A. Ioffe, Considerations on quality Factors from Super Mirrors and ^{3}He Spin Filters for Polarization Analyzers on Wide Q-Range Instrumentation. J. Phys. Soc. Jpn. 82 (2013).

9. G. Bator, L. Sobczyk, W. Sawka-Dobrowolska, J. Wuttke, A. Pawlukojc, E. Grech and J. Nowicka-Scheibe, Structural, spectroscopic and theoretical studies on 3,4,7,8-tetramethyl-1,10-phenantroline complex with picric acid. Chem. Phys. 410, 55-65 (2013).

10. M. Baum, K. Schmalzl, P. Steffens, A. Hiess, L. Regnault, M. Meven, P. Becker, L. Bohatý and M. Braden, Controlling toroidal moments by crossed electric and magnetic fields. Phys. Rev. B: Condens. Matter Mater. Phys. 88, 024414 (2013).

11. S. P. Bayrakci, D. A. Tennant, P. Leininger, T. Keller, M. Gibson, S. Wilson, R. Birgeneau and B. Keimer, Lifetimes of antiferromagnetic magnons in two and three dimensions: experiment, theory, and numerics. Phys. Rev. Lett. 111, 017204 (2013).

12. F. de Beer, F. Gruenauer, J. Radebe, T. Modise and B. Schillinger, Scientific Design of the New Neutron Radiography Facility (SANRAD) at SAFARI-1 for South Africa. Physics Procedia 43, 34-41 (2013).

13. C. J. Bennett, M. M. Attallah, M. Preuss, P. H. Shipway, T. H. Hyde and S. Bray, Finite Element Modeling of the Inertia Friction Welding of Dissimilar High-Strength Steels. Metall. Mater. Trans. A 44, 5054-5064 (2013).

14. A. K. Bera, B. Lake, A. T. M. N. Islam, B. Klemke, E. Faulhaber and J. M. Law, Field-induced magnetic ordering and single-ion anisotropy in the quasi-one-dimensional Haldane chain compound $SrNi_2V_2O_8$: A single-crystal investigation. Phys. Rev. B: Condens. Matter Mater. Phys. 87, 224423 (2013).

15. S. Bhattacharjee, A. Senyshyn, H. Fuess and D. Pandey, Morin-type spin-reorientation transition below the Néel transition in the monoclinic compositions of $(1–x)BiFeO_{3-x}PbTiO_3$ (x=0.25 and 0.27): A combined dc magnetization and x-ray and neutron powder diffraction study. Phys. Rev. B 87, 054417 (2013).

16. J.-P. Bick, D. Honecker, F. Döbrich, K. Suzuki, E. P. Gilbert, H. Frielinghaus, J. Kohlbrecher, J. Gavilano, E. M. Forgan, R. Schweins, P. Lindner, R. Birringer and A. Michels, Magnetization reversal in Nd-Fe-B based nanocomposites as seen by magnetic small-angle neutron scattering. Appl. Phys. Lett. 102, 022415 (2013).

17. D. Bock, R. Kahlau, B. Micko, B. Pötzschner, G. J. Schneider and E. A. Rössler, On the cooperative nature of the β-process in neat and binary glasses: A dielectric and nuclear magnetic resonance spectroscopy study. The Journal of Chemical Physics 139, 064508 (2013).

18. F. Bode, M. A. da Silva, P. Smith, C. D. Lorenz, S. McCullen, M. M. Stevens and C. A. Dreiss, Hybrid gelation processes in enzymatically gelled gelatin: impact on nanostructure,macroscopic properties and cellular response. Soft Matter 9, 6986-6999 (2013).

19. C. Bousige, S. Rols, J. Ollivier, H. Schober, P. Fouquet, G. G. Simeoni, V. Agafonov, V. Davydov, H. Kataura and P. Launois, From one-dimensional crystal to a one-dimensional liquid: a comprehensive dynamical study of a textbook system, C_{60} peapods. Phys. Rev. B: Condens. Matter Mater. Phys. 87, 195438 (2013).

20. M. Brasse, L. Chioncel, J. Kuneš, A. Bauer, A. Regnat, C. G. F. Blum, S. Wurmehl, C. Pfleiderer, M. A. Wilde and D. Grundler, de Haas–van Alphen effect and Fermi surface properties of single-crystal CrB_2. Phys. Rev. B: Condens. Matter Mater. Phys. 88, 155138 (2013).

21. H. Breitkreutz, R. Jungwirth, A. Röhrmoser, W. Petry, S. van den Berghe, A. Leenaers, E. Koonen, P. Lemoine, M. Ripert, H. Palancher, M.-C. Anselmet, C. Jarousse, B. Stepnik, D. Geslin, Y. Calzavara and H. Guyon, The development of dispersed UMo as a high performance research reactor fuel in Europe, Transactions RRFM 2013, 21–25 April, St. Petersburg, Russia (2013).

22. H. Breitkreutz, A. Röhrmoser and W. Petry, Monolithic UMo based fuel element designs for FRM II, Transactions RRFM 2013, 21–25 April, St. Petersburg, Russia (2013).

23. T. Bryan, J. M. González, J. P. Bacik, N. J. DeNunzio, C. J. Unkefer, T. E. Schrader, A. Ostermann, D. Dunaway-Mariano, K. N. Allen and S. Z. Fisher, Neutron diffraction studies towards deciphering the protonation state of catalytic residues in the bacterial KDN9P phosphatase. Acta Crystallogr. F-Struct. Biol. Cryst. Commun. 69, 1015-1019 (2013).

24. T. Brückel, G. Heger, D. Richter, G. Roth and E. Zorn, Laboratory Course Neutron Scattering: Lectures, Schriften des Forschungszentrum Jülich, Schlüsseltechnologien 63 (2013).

25. T. Brückel, G. Heger, D. Richter, G. Roth and E. Zorn, Laboratory Course Neutron Scattering: Experiment Manuals, Schriften des Forschungszentrum Jülich, Schlüsseltechnologien 64 (2013).

26. A. R. Brás, C. H. Hövelmann, W. Antonius, J. Teixeira, A. Radulescu, J. Allgaier, W. Pyckhout-Hintzen, A. Wischnewski and D. Richter, Molecular Approach to Supramolecular Polymer Assembly by Small Angle Neutron Scattering. Macromolecules 46, 9446-9454 (2013).

27. H. Ceeh, J. A. Weber, M. Leitner, P. Böni and C. Hugenschmidt, The source-sample stage of the new two-dimensional angular correlation of annihilation radiation spectrometer at Technische Universitat München. Rev. Sci. Instrum. 84, 043905 (2013).

28. H. Ceeh, J. Weber, C. Hugenschmidt, M. Leitner and P. Böni, First measurements with the Munich 2D-ACAR spectrometer on Cr. J. Phys.: Conf. Ser. 443, 012094 (2013).

29. H. Chang, M. Zheng, W. Gan, C. Xu and H. Brokmeier, Texture Evolution of the Mg/Al Laminated Composite by Accumulative Roll Bonding at Ambient Temperature. Rare Metal Materials and Engineering 42, 441-446 (2013).

30. T. Chatterji, O. Holderer and H. Schneider, Direct evidence for nuclear spin waves in Nd_2CuO_4 by high-resolution neutron-spin-echo spectroscopy. J. Phys.: Condens. Matter 25, 476002 (2013).

31. H. Chiang, M. Mayer, T. Zweifel, R. Jungwirth and W. Petry, RBS studies on heavy ion irradiation induced diffusion in UMo/Transition metal/Al fuel. Transactions RRFM 2013, 21–25 April, St. Petersburg, Russia (2013).

32. H.-Y. Chiang, T. Zweifel, H. Palancher, A. Bonnin, L. Beck, P. Weiser, M. Döblinger, C. Sabathier, R. Jungwirth and W. Petry, Evidence of amorphous interdiffusion layer in heavy ion irradiated U–8wt%Mo/Al interfaces. J. Nucl. Mater. 440, 117-123 (2013).

33. J. Colmenero and A. Arbe, Recent progress on polymer dynamics by neutron scattering: From simple polymers to complex materials. J. Polym. Sci. Pt. B-Polym. Phys. 51, 87–113 (2013).

34. I. Crespo and K. McEwen, The International Conference on Neutron Scattering 2013 in Edinburgh. Neutron News 24, 4-6 (2013).

35. I. Crespo and J. Neuhaus, The launch of Neutronsources.org. Neutron News 24, 37 (2013).

36. S. Disch, E. Wetterskog, R. P. Hermann, D. Korolkov, P. Busch, P. Boesecke, O. Lyon, U. Vainio, G. Salazar-Alvarez, L. Bergstrom and T. Brückel, Structural diversity in iron oxide nanoparticle assemblies as directed by particle morphology and orientation. Nanoscale 5, 3969-3975 (2013).

37. W. Doster, H. Nakagawa and M. S. Appavou, Scaling analysis of bio-molecular dynamics derived from elastic incoherent neutron scattering experiments. The Journal of Chemical Physics 139, 045105 (2013).

38. S. Ener, T. Mehaddene, B. Pedersen, M. Leitner, J. Neuhaus and W. Petry, Vibrational properties of Ni–Mn–Ga shape memory alloy in the martensite phases. New J. Phys. 15, 123016 (2013).

39. G. C. Fadda, D. Lairez, Z. Guennouni and A. Koutsioubas, Peptide Pores in Lipid Bilayers: Voltage Facilitation Pleads for a Revised Model. Phys. Rev. Lett. 111, 028102 (2013).

40. S. K. Filippov, J. M. Franklin, P. V. Konarev, P. Chytil, T. Etrych, A. Bogomolova, M. Dyakonova, C. M. Papadakis, A. Radulescu, K. Ulbrich, P. Stepanek and D. I. Svergun, Hydrolytically Degradable Polymer Micelles for Drug Delivery: A SAXS/SANS Kinetic Study. Biomacromolecules 14, 4061-4070 (2013).

41. J. Fischer, J. A. Lima, P. T. Freire, F. E. Melo, R. W. Havenith, J. Mendes Filho, R. Broer, J. Eckert and H. N. Bordallo, Molecular flexibility and structural instabilities in crystalline l-methionine. Biophys. Chem. 180-181, 76-85 (2013).

42. M. Fischer, A. Freund, S. Gsell, M. Schreck, P. Courtois, C. Stehl, G. Borchert, A. Ofner, M. Skoulatos and K. Andersen, Structural analysis of diamond mosaic crystals for neutron monochromators using synchrotron radiation. Diamond Relat. Mater. 37, 41-49 (2013).

43. P. G. Freeman, S. Giblin, K. Hradil, R. Mole and D. Prabhakaran, Development of the magnetic excitations of charge-stripe ordered $La_{2-x}Sr_xNiO_4$ on doping towards checkerboard charge order. J. Korean Phys. Soc. 62, 1453-1457 (2013).

44. H. Frielinghaus, X. Frielinghaus, N. Ruocco, J. Allgaier, W. Pyckhout-Hintzen and D. Richter, Polymers in 2-D confinement. Soft Matter 9, 10484-10492 (2013).

45. Z. Fu, Y. Zheng, Y. Xiao, S. Bedanta, A. Senyshyn, G. G. Simeoni, Y. Su, U. Rücker, P. Kögerler and T. Brückel, Coexistence of magnetic order and spin-glass-like phase in the pyrochlore antiferromagnet $Na_3Co(CO_3)_2Cl$. Phys. Rev. B: Condens. Matter Mater. Phys. 87, 214406 (2013).

46. L. G. Butler, E. H. Lehmann and B. Schillinger, Neutron Radiography, Tomography, and Diffraction of Commercial Lithium-ion Polymer Batteries. Physics Procedia 43, 331-336 (2013).

47. R. Garg, B. Narayana Rao, A. Senyshyn and R. Ranjan, Long ranged structural modulation in the pre-morphotropic phase boundary cubic-like state of the lead-free piezoelectric $Na_{1/2}Bi_{1/2}TiO_3$-$BaTiO_3$. J. Appl. Phys. 114, 234102 (2013).

48. R. Garg, B. N. Rao, A. Senyshyn, P. S. R. Krishna and R. Ranjan, Lead-free piezoelectric system $(Na_{0.5}Bi_{0.5})TiO_3$-$BaTiO_3$: Equilibrium structures and irreversible structural transformations driven by electric field and mechanical impact. Phys. Rev. B: Condens. Matter Mater. Phys. 88, 014103 (2013).

49. G. D. Gatta, P. Vignola, M. Meven and R. Rinaldi, Neutron diffraction in gemology: Single-crystal diffraction study of brazilianite, $NaAl_3(PO_4)_2(OH)_4$. Am. Mineral. 98, 1624-1630 (2013).

50. F. Ghiotto, C. Pateraki, J. Tanskanen, J. R. Severn, N. Luehmann, A. Kusmin, J. Stellbrink, M. Linnolahti and M. Bochmann, Probing the Structure of Methylalumoxane (MAO) by a Combined Chemical, Spectroscopic, Neutron Scattering, and Computational Approach. Organometallics 32, 3354-3362 (2013).

51. T. Glomann, A. Hamm, J. Allgaier, E. G. Hubner, A. Radulescu, B. Farago and G. J. Schneider, A microscopic view on the large scale chain dynamics in nanocomposites with attractive interactions. Soft Matter 9, 10559-10571 (2013).

52. T. Glomann, G. J. Schneider, J. Allgaier, A. Radulescu, W. Lohstroh, B. Farago and D. Richter, Microscopic Dynamics of Polyethylene Glycol Chains Interacting with Silica Nanoparticles. Phys. Rev. Lett. 110, 178001 (2013).

53. V. Gogonea, G. S. Gerstenecker, Z. Wu, X. Lee, C. Topbas, M. A. Wagner, T. C. Tallant, J. D. Smith, P. Callow, V. Pipich, H. Malet, G. Schoehn, J. A. DiDonato and S. L. Hazen, The low-resolution structure of nHDL reconstituted with DMPC with and without cholesterol reveals a mechanism for particle expansion. J. Lipid Res. 54, 966-983 (2013).

54. T. Gutberlet, H. Hilbig, R. Beddoe and W. Lohstroh, New insights into water bonding during early tricalcium silicate hydration with quasielastic neutron scattering. Cem. Concr. Res. 51, 104-108 (2013).

55. A. Hamann, O. Stockert, V. Fritsch, K. Grube, A. Schneidewind and H. v. Löhneysen, Evolution of the Magnetic Structure in $CeCu_{5.5}Au_{0.5}$ under Pressure towards Quantum Criticality. Phys. Rev. Lett. 110, 096404 (2013).

56. M. Hoelzel, W. M. Gan, M. Hofmann, C. Randau, G. Seidl, P. Jüttner and W. W. Schmahl, Rotatable multifunctional load frames for neutron diffractometers at FRM II—design, specifications and applications. Nucl. Instr. Meth. A 711, 101-105 (2013).

57. V. Hoepfner, P. Jacobs, P. K. Sawinski, A. Houben, J. Reim and R. Dronskowski, $RbCN_3H_4$ and $CsCN_3H_4$: A Neutron Powder and Single-Crystal X-ray Diffraction Study. Z. anorg. und allg. Chem. 639, 1232-1236 (2013).

58. M. Hofmann, W. M. Gan, J. Rebelo Kornmeier and M. Schöbel, Materials science at the diffractometer STRESS-SPEC at FRM II. Neutron News 24, 14-17 (2013).

59. O. Holderer, H. Frielinghaus, M. Monkenbusch, M. Klostermann, T. Sottmann and D. Richter, Experimental determination of bending rigidity and saddle splay modulus in bicontinuous microemulsions. Soft Matter 9, 2308-2313 (2013).

60. E. T. Hoppe, A. Sepe, M. Haese-Seiller, J.-F. Moulin and C. M. Papadakis, Density Profile in Thin Films of Polybutadiene on Silicon Oxide Substrates: A TOF-NR Study. Langmuir 29, 10759-10768 (2013).

61. T. Huber, H. Breitkreutz, F. Charlollais, S. Elegeti, C. Jarousse, R. Jungwirth, P. Lemoine, A. Röhrmoser, W. Petry, D. Staicu, C. Reiter and D. Wachs, Thermal conductivity of IRIS-TUM and IRIS-4 UMo dispersion fuel. Transactions RRFM 2013, 21–25 April, St. Petersburg, Russia (2013).

62. C. Hugenschmidt, H. Ceeh, T. Gigl, F. Lippert, C. Piochacz, P. Pikart, M. Reiner, J. Weber and S. Zimnik, The Upgrade of the Neutron Induced Positron Source NEPOMUC. J. Phys.: Conf. Ser. 443, 012079 (2013).

63. F. Hummel, Y. Su, A. Senyshyn and D. Johrendt, Weak magnetism and the Mott state of vanadium in superconducting Sr_2VO_3FeAs. Phys. Rev. B: Condens. Matter Mater. Phys. 88, 144517 (2013).

64. D. S. Inosov, G. Friemel, J. T. Park, A. C. Walters, Y. Texier, Y. Laplace, J. Bobroff, V. Hinkov, D. L. Sun, Y. Liu, R. Khasanov, K. Sedlak, P. Bourges, Y. Sidis, A. Ivanov, C. T. Lin, T. Keller and B. Keimer, Possible realization of an antiferromagnetic Griffiths phase in $Ba(Fe_{1-x}Mn_x)_2As_2$. Phys. Rev. B: Condens. Matter Mater. Phys. 87, 224425 (2013).

65. A. Ioffe, A. Feoktystov, S. Staringer, A. Radulescu, E. Babcock and Z. Salhi, Polarized Neutron Beam at the SANS Diffractometer KWS2 of the JCNS. Physics Procedia 42, 142-149 (2013).

66. O. Ivanova, O. Holderer, B. Hopfenmüller, M. Zamponi, W. Maier, W. Lehnert, M. Monkenbusch and R. Zorn, Observing Proton Motion on the Nanoscale in Polymeric Electrolyte Membranes with Quasielastic Neutron Scattering, Proceedings of EFC2013, ENEA, 281-282 (2013).

67. P. Jacobs, A. Houben, A. Senyshyn, P. Müller and R. Dronskowski, The magnetic structure of $Co(NCNH)_2$ as determined by (spin-polarized) neutron diffraction. J. Solid State Chem. 202, 149-153 (2013).

68. P. Jacobs, A. Houben, A. L. Tchougréeff and R. Dronskowski, High-resolution neutron diffraction study of CuNCN: New evidence of structure anomalies at low temperature. J. Chem. Phys. 139, 224707 (2013).

69. M. Janoschek, M. Garst, A. Bauer, P. Krautschneid, R. Georgii, P. Böni and C. Pfeiderer, Fluctuation-induced first-order phase transition in Dzyaloshinskii-Moriya helimagnets. Phys. Rev. B: Condens. Matter Mater. Phys. 87, 134407 (2013).

70. Y. Jeong, J. Park, H. Ryu, Y. Lee, W. Kim, R. Jungwirth, H. Chiang, T. Zweifel and W. Petry, Heavy ion irradiation of nitride and silicon coated UMo/Al and UMoTi/Al fuel. Transactions RRFM 2013, 21–25 April, St. Petersburg, Russia (2013).

71. W. T. Jin, S. Nandi, Y. Xiao, Y. Su, O. Zaharko, Z. Guguchia, Z. Bukowski, S. Price, W. H. Jiao, G. H. Cao and T. Brückel, Magnetic structure of superconducting $Eu(Fe_{0.82}Co_{0.18})_2As_2$ as revealed by single-crystal neutron diffraction. Phys. Rev. B: Condens. Matter Mater. Phys. 88, 214516 (2013).

72. R. Joksimovic, S. Prevost, R. Schweins, M.-S. Appavou and M. Gradzielski, Interactions of silica nanoparticles with poly(ethylene oxide) and poly(acrylic acid): Effect of the polymer molecular weight and of the surface charge. J. Colloid Interface Sci. 394, 85-93 (2013).

73. G. Jordan, C. Eulenkamp, E. Calzada, B. Schillinger, M. Hoelzel, A. Gigler, H. Stanjek and W. W. Schmahl, Quantitative In Situ Study of the Dehydration of Bentonite-Bonded Molding Sands. Clays Clay Miner. 61, 133-140 (2013).

74. E. Josef, K. Barat, I. Barsht, M. Zilberman and H. Bianco-Peled, Composite hydrogels as a vehicle for releasing drugs with a wide range of hydrophobicities. Acta Biomater. 9, 8815-8822 (2013).

75. R. Jungwirth, H. Palancher, A. Bonnin, C. Bertrand-Drira, C. Borca, V. Honkimäki, C. Jarousse, B. Stepnik, S.-H. Park, X. Iltis, W. Schmahl and W. Petry, Microstructure of as-fabricated UMo/Al(Si) plates prepared with ground and atomized powder. J. Nucl. Mater. 438, 246-260 (2013).

76. R. Jungwirth, T. Zweifel, H.-Y. Chiang, W. Petry, S. van den Berghe and A. Leenaers, Heavy ion irradiation of UMo/Al samples PVD coated with Si and ZrN layers. J. Nucl. Mater. 434, 296-302 (2013).

77. A. K. Kalyani, A. Senyshyn and R. Ranjan, Polymorphic phase boundaries and enhanced piezoelectric response in extended composition range in the lead free ferroelectric $BaTi_{1-x}Zr_xO_3$. J. Appl. Phys. 114, 014102 (2013).

78. T. Kandemir, M. Schuster, A. Senyshyn, M. Behrens and R. Schlögl, The Haber–Bosch Process Revisited: On the Real Structure and Stability of “Ammonia Iron” under Working Conditions. Angew. Chem., Int. Ed. 52, 12723-12726 (2013).

79. F. Kaneko, A. Radulescu and K. Ute, Time-resolved SANS studies on guest exchange processes in co-crystals of syndiotactic polystyrene. Polymer 54, 3145-3149 (2013).

80. Y. Khaydukov, B. Nagy, J.-H. Kim, T. Keller, A. Rühm, Y. Nikitenko, K. Zhernenkov, J. Stahn, L. Kiss, A. Csik, L. Bottyan and V. Aksenov, On the feasibility to study inverse proximity effect in a single S/F bilayer by Polarized Neutron Reflectometry. JETP Lett. 98, 107-110 (2013).

81. C. J. Kim, K. Sondergeld, M. Mazurowski, M. Gallei, M. Rehahn, T. Spehr, H. Frielinghaus and B. Stühn, Synthesis and characterization of polystyrene chains on the surface of silica nanoparticles: comparison of SANS, SAXS, and DLS results. Colloid Polym. Sci. 291, 2087-2099 (2013).

82. M. Kofu, T. Kajiwara, J. S. Gardner, G. G. Simeoni, M. Tyagi, A. Faraone, K. Nakajima, S. Ohira-Kawamura, M. Nakano and O. Yamamuro, Magnetic relaxations in a Tb-based single molecule magnet studied by quasielastic neutron scattering. Chem. Phys. 427, 147-152 (2013).

83. V. Kothai, A. Senyshyn and R. Ranjan, Competing structural phase transition scenarios in the giant tetragonality ferroelectric $BiFeO_3$-$PbTiO_3$: Isostructural vs multiphase transition. J. Appl. Phys. 113, 084102 (2013).

84. A. Koutsioubas, A. Berthaud, S. Mangenot and J. Pérez, Ab Initio and All-Atom Modeling of Detergent Organization around Aquaporin-0 Based on SAXS Data. J. Phys. Chem. B 117, 13588-13594 (2013).

85. A. Koutsioubas and J. Pérez, Incorporation of a hydration layer in the `dummy atom' ab initio structural modelling of biological macromolecules. J. Appl. Crystallogr. 46, 1884-1888 (2013).

86. S. Kozhevnikov, V. Ignatovich, F. Ott, A. Rühm and J. Major, Experimental determination of the neutron channeling length in a planar waveguide. J. Exp. Theor. Phys. 117, 636-640 (2013).

87. S. Kozhevnikov, T. Keller, Y. Khaydukov, F. Ott, A. Rühm and J. Major, Polarizing Fe-Co-Fe Planar Waveguides for the Production of Neutron Microbeams. Physics Procedia 42, 80-88 (2013).

88. F. Kraus, S. A. Baer, M. Hoelzel and A. J. Karttunen, $[Be(ND_3)_4]Cl_2$: Synthesis, Characterisation and Space-Group Determination Guided by Solid-State Quantum Chemical Calculations. Eur. J. Inorg. Chem. 2013, 4184-4190 (2013).

89. L. Kredler, W. Häußler, N. Martin and P. Böni, Development of a NRSE Spectrometer with the Help of McStas – Application to the Design of Present and Future Instruments. Physics Procedia 42, 116-120 (2013).

90. T. Krist, F. Rucker, G. Brandl and R. Georgii, High performance, large cross-section S-bender for neutron polarization. Nucl. Instr. Meth. A 698, 94-97 (2013).

91. T. A. Krol, C. Seidel, J. Schilp, M. Hofmann, W. Gan and M. F. Zaeh, Verification of structural simulation results of metal-based additive manufacturing by means of neutron diffraction. Physics Procedia 41, 842-850 (2013).

92. M. Krutyeva, A. Wischnewski, M. Monkenbusch, L. Willner, J. Maiz, C. Mijangos, A. Arbe, J. Colmenero, A. Radulescu, O. Holderer, M. Ohl and D. Richter, Effect of Nanoconfinement on Polymer Dynamics: Surface Layers and Interphases. Phys. Rev. Lett. 110, 108303 (2013).

93. R. S. Kumar, A. Svane, G. Vaitheeswaran, Y. Zhang, V. Kanchana, M. Hofmann, S. J. Campbell, Y. Xiao, P. Chow, C. Chen, Y. Zhao and A. L. Cornelius, Pressure-Induced Valence and Structural Changes in $YbMn_2Ge_2$—Inelastic X-ray Spectroscopy and Theoretical Investigations. Inorg. Chem. 52, 832-839 (2013).

94. S. Kundu, S. Gupta, J. Stellbrink, L. Willner and D. Richter, Relating structure and flow of soft colloids. Eur. Phys. J. Special Topics 222, 2757-2772 (2013).

95. A. Laschewsky, P. Müller-Buschbaum and C. M. Papadakis Thermo-responsive Amphiphilic Di- and Triblock Copolymers Based on Poly(N-isopropylacrylamide) and Poly(methoxy diethylene glycol acrylate): Aggregation and Hydrogel Formation in Bulk Solution and in Thin Films, in: Intelligent Hydrogels. G. Sadowski and W. Richtering (eds.), Springer International Publishing, 15-34. (2013).

96. A. Laso-Garcia, A. Akindinov, J. Hutsch, B. Kampfer, M. Kaspar, R. Kotte, D. Mal'kevich, L. Naumann, A. Nedosekin, V. Plotnikov, M. Sobiella, D. Stach, K. Voloshin, F. M. Wagner, C. Wendisch and J. Wustenfeld, Aging effects on low-resistive high-rate ceramics RPCs, CBM Progress Report 2012, 74 (2013).

97. J. Lichtinger, R. Gernhäuser, A. Bauer, M. Bendel, L. Canella, M. Graw, R. Krücken, P. Kudejova, E. Mützel, S. Ring, D. Seiler, S. Winkler, K. Zeitelhack and J. Schöpfer, Position sensitive measurement of lithium traces in brain tissue with neutrons. Med. Phys. 40, 023501 (2013).

98. C. Linsmeier, C.-C. Fu, A. Kaprolat, S. Nielsen, K. Mergia, R. Schäublin, R. Lindau, H. Bolt, J.-Y. Buffière, M. Caturla, B. Décamps, C. Ferrero, H. Greuner, C. Hébert, T. Höschen, M. Hofmann, C. Hugenschmidt, T. Jourdan, M. Köppen, T. Płociński, J. Riesch, M. Scheel, B. Schillinger, A. Vollmer, T. Weitkamp, W. Yao, J.-H. You and A. Zivelonghi, Advanced materials characterization and modeling using synchrotron, neutron, TEM, and novel micro-mechanical techniques—A European effort to accelerate fusion materials development. J. Nucl. Mater. 442, S834 - S845 (2013).

99. W. Lohstroh, Materials for Energy Storage, in: Nanotechnology and Energy: Science, Promises and Limits. J. Lambauer, U. Fahl, A. Voss (eds.), Pan Stanford Publishing Pte. Ltd,, Singapore (2013).

100. R. Lund, F. Barroso-Bujans, M. Z. Slimani, A. J. Moreno, L. Willner, D. Richter, A. Alegría and J. Colmenero, End-to-End Vector Dynamics of Nonentangled Polymers in Lamellar Block Copolymer Melts: The Role of Junction Point Motion. Macromolecules 46, 7477-7487 (2013).

101. B. Löwe, M. Reiner, W. Egger, C. Hugenschmidt and G. Dollinger, A position sensitive germanium detector for the measurement of angular deviation of annihilation radiation. J. Phys.: Conf. Ser. 443, 012098 (2013).

102. S. Maccarrone, D. V. Byelov, T. Auth, J. Allgaier, H. Frielinghaus, G. Gompper and D. Richter, Confinement Effects in Block Copolymer Modified Bicontinuous Microemulsions. J. Phys. Chem. B 117, 5623-5632 (2013).

103. G. Mangiapia, G. Vitiello, C. Irace, R. Santamaria, A. Colonna, R. Angelico, A. Radulescu, G. D'Errico, D. Montesarchio and L. Paduano, Anticancer Cationic Ruthenium Nanovectors: From Rational Molecular Design to Cellular Uptake and Bioactivity. Biomacromolecules 14, 2549-2560 (2013).

104. M. J. Marques, A. Castanhola Batista, J. P. Nobre, A. Loureiro and J. Rebelo Kornmeier, A utilizac ao da difrac ao de neutr oes na determinac ao do perfil de tens oes residuais em revestimentos por soldadura. Soldagem Insp. 18, 149-157 (2013).

105. V. Marry, E. Dubois, N. Malikova, J. Breu and W. Haussler, Anisotropy of Water Dynamics in Clays: Insights from Molecular Simulations for Experimental QENS Analysis. J. Phys. Chem. C 117, 15106-15115 (2013).

106. S. Masalovich, Analysis and design of multilayer structures for neutron monochromators and supermirrors. Nuclear Instruments and Methods in Physics Research A 722, 71-81 (2013).

107. M. Mazurowski, K. Sondergeld, J. Elbert, C. J. Kim, J. Li, H. Frielinghaus, M. Gallei, B. Stühn and M. Rehahn, Polystyrene Brushes on Fully Deuterated Organic Nanoparticles by Surface-Initiated Nitroxide-Mediated Radical Polymerization. Macromol. Chem. Phys. 214, 1094–1106 (2013).

108. L. Meier, M. Hofmann, P. Saal, W. Volk and H. Hoffmann, In-situ measurement of phase transformation kinetics in austempered ductile iron. Mater. Charact. 85, 124-133 (2013).

109. D. Mikhailova, A. Thomas, S. Oswald, W. Gruner, N. N. Bramnik, A. A. Tsirlin, D. M. Trots, A. Senyshyn, J. Eckert and H. Ehrenberg, Structural Changes in the $LiCrMnO_4$ Cathode Material during Electrochemical Li Extraction and Insertion. J. Electrochem. Soc. 160, A3082-A3089 (2013).

110. P. Milde, D. Köhler, J. Seidel, L. M. Eng, A. Bauer, A. Chacon, J. Kindervater, S. Mühlbauer, C. Pfleiderer, S. Buhrandt, C. Schütte and A. Rosch, Unwinding of a Skyrmion Lattice by Magnetic Monopoles. Science 340, 1076-1080 (2013).

111. R. Mittal, M. K. Gupta, S. L. Chaplot, M. Zbiri, S. Rols, H. Schober, Y. Su, T. Brueckel and T. Wolf, Spin-phonon coupling in $K_{0.8}Fe_{1.6}Se_2$ and KFe_2Se_2: Inelastic neutron scattering and ab initio phonon calculations. Phys. Rev. B: Condens. Matter Mater. Phys. 87, 184502 (2013).

112. D. Montesarchio, G. Mangiapia, G. Vitiello, D. Musumeci, C. Irace, R. Santamaria, G. D'Errico and L. Paduano, A new design for nucleolipid-based Ru(III) complexes as anticancer agents. Dalton Trans. 42, 16697-16708 (2013).

113. H. Morhenn, S. Busch, H. Meyer, D. Richter, W. Petry and T. Unruh, Collective Intermolecular Motions Dominate the Picosecond Dynamics of Short Polymer Chains. Phys. Rev. Lett. 111, 173003 (2013).

114. A. Morozov, I. Defendi, R. Engels, F. A. F. Fraga, M. M. F. R. Fraga, A. Gongadze, B. Guerard, M. Jurkovic, G. Kemmerling, G. Manzin, L. M. S. Margato, H. Niko, L. Pereira, C. Petrillo, A. Peyaud, F. Piscitelli, D. Raspino, N. J. Rhodes, F. Sacchetti, E. M. Schooneveld, V. Solovov, P. Van Esch and K. Zeitelhack, Adaptive algorithms of position and energy reconstruction in Anger-camera type detectors: experimental data processing in ANTS. J. Instrum. 8, P05002 (2013).

115. C. Mugemana, A. Joset, P. Guillet, M.-S. Appavou, N. De Souza, C.-A. Fustin, B. Leyh and J.-F. Gohy, Structure of Metallo-Supramolecular Micellar Gels. Macromol. Chem. Phys. 214, 1699–1709 (2013).

116. D. Mukherji, J. Rösler, J. Wehrs, P. Strunz, P. Beran, R. Gilles, M. Hofmann, M.

Hoelzel, H. Eckerlebe, L. Szentmiklosi and Z. Macsik, Application of In Situ Neutron and X-Ray Measurements at High Temperatures in the Development of Co-Re-Based Alloys for Gas Turbines. Metall. Mater. Trans. A 44, 22-30 (2013).

117. P. Müller-Buschbaum, Grazing incidence small-angle neutron scattering: challenges and possibilities. Polymer Journal 45, 34-42 (2013).

118. B. Nafradi, T. Keller, H. Manaka, U. Stuhr, A. Zheludev and B. Keimer, Bond randomness induced magnon decoherence in a spin-1/2 ladder compound. Phys. Rev. B: Condens. Matter Mater. Phys. 87, 020408(R) (2013).

119. B. Nagy, Y. Khaydukov, L. Kiss, S. Sajti, D. Merkel, F. Tancziko, A. Vasenko, R. Tsaregorodsev, A. Rühm, T. Keller and L. Bottyan, Controlling Exchange Coupling Strength in Ni_xCu_{1-x} Thin Films. J. Supercond. Nov. Magn. 26, 1957-1961 (2013).

120. S. Nandi, Y. Xiao, Y. Su, L. C. Chapon, T. Chatterji, W. T. Jin, S. Price, T. Wolf, P. J. Brown and T. Brückel, Magnetization distribution and orbital moment in the nonsuperconducting chalcogenide compound $K_{0.8}Fe_{1.6}Se_2$. Phys. Rev. B: Condens. Matter Mater. Phys. 88, 184413 (2013).

121. P. Naumann, N. Becker, S. Datta, T. Sottmann and S. Wiegand, Soret Coefficient in Nonionic Microemulsions: Concentration and Structure Dependence. J. Phys. Chem. B 117, 5614-5622 (2013).

122. P. Negrier, J. L. Tamarit, M. Barrio and D. Mondieig, Polymorphism in Halogen-Ethane Derivatives: CCl_3-CCl_3 and ClF_2C-CF_2Cl. Cryst. Growth Des. 13, 782-791 (2013).

123. K. Nemkovski, P. Alekseev, J.-M. Mignot and A. Ivanov, Resonant Mode in Rare-earth based Strongly Correlated Semiconductors. Physics Procedia 42, 18-24 (2013).

124. K. Nusser, G. J. Schneider and D. Richter, Rheology and Anomalous Flow Properties of Poly(ethylene-alt-propylene)-Silica Nanocomposites. Macromolecules 46, 6263-6272 (2013).

125. J. Outeiro, J.-P. Costes and J. Rebelo Kornmeier, Cyclic Variation of Residual Stress Induced by Tool Vibration in Machining Operations. Procedia CIRP 8, 493-497 (2013).

126. A. Papagiannopoulos, J. Zhao, G. Zhang, S. Pispas and A. Radulescu, Thermoresponsive transition of a PEO-b-PNIPAM copolymer: From hierarchical aggregates to well defined ellipsoidal vesicles. Polymer 54, 6373-6380 (2013).

127. A. Papon, T. C. L. Guy, K. Saalwachter, J. Oberdisse, S. Merabia, D. Long, P. Sotta, H. Frielinghaus, A. Radulescu, B. Deme, L. Noirez, H. Montes and F. Lequeux, Studying Model samples to understand mechanical Properties of filled Elastomers. KGK-Kautsch. Gummi Kunstst. 66, 52-58 (2013).

128. S. Park, C. J. Chucholowski, L. G. B. Lara, M. Hoelzel and C. Paulmann, Investigation of a new willemite-type compound, $(Li, Na, H)_{0.16}Zn_{1.92}SiO_4$. J. Solid State Chem. 200, 328-340 (2013).

129. R. Pasquino, T. C. Vasilakopoulos, Y. C. Jeong, H. Lee, S. Rogers, G. Sakellariou, J. Allgaier, A. Takano, A. R. Brás, T. Chang, S. Gooßen, W. Pyckhout-Hintzen, A. Wischnewski, N. Hadjichristidis, D. Richter, M. Rubinstein and D. Vlassopoulos, Viscosity of Ring Polymer Melts. ACS Macro Letters 2, 874-878 (2013).

130. J. P. Patel, A. Senyshyn, H. Fuess and D. Pandey, Evidence for weak ferromagnetism, isostructural phase transition, and linear magnetoelectric coupling in the multiferroic $Bi_{0.8}Pb_{0.2}Fe_{0.9}Nb_{0.1}O_3$ solid solution. Phys. Rev. B: Condens. Matter Mater. Phys. 88, 104108 (2013).

131. A. Paul and S. Mattauch, Induced moment due to perpendicular field cycling in trained exchange bias system. Pramana 80, 701-711 (2013).

132. A. Paul, N. Paul, J. Jutimoosik, R. Yimnirun, S. Rujirawat, B. Höpfner, I. Lauermann, M. Lux-Steiner, S. Mattauch and P. Böni, Change in interface magnetism of an exchange-coupled system due to the presence of nonmagnetic spacers. Phys. Rev. B: Condens. Matter Mater. Phys. 87, 014431 (2013).

133. N. Paul, M. Muller, A. Paul, E. Guenther, I. Lauermann, P. Müller-Buschbaum and M. C. Lux-Steiner, Molecularly imprinted conductive polymers for controlled trafficking of neurotransmitters at solid-liquid interfaces. Soft Matter 9, 1364-1371 (2013).

134. N. Paul, A. Paul, S. Mattauch, P. Müller-Buschbaum, P. Böni and M. C. Lux-Steiner, Interfacial smoothening of polymer multilayers with molecules: a new approach in growing supramolecular layer structures. Soft Matter 9, 10117-10128 (2013).

135. B. Penc, M. Hofmann, W. Sikora and A. Szytuła, Magnetic structures of $Er_5Rh_4Ge_{10}$ compound. J. Magn. Magn. Mater. 332, 114-117 (2013).

136. W. Petry, Neutronenstrahlung, in: Handbuch der Ergonomie (HdE). H. J. Bullinger, H. W. Jürgens, W. Rohmert (eds.), Bundesamt für Wehrtechnik und Beschaffung (2013).

137. P. Pikart and C. Hugenschmidt, Determination of electron binding energies in two-dimensional Coincident Doppler Broadening spectra. J. Phys.: Conf. Ser. 443, 012089 (2013).

138. C. Piochacz and C. Hugenschmidt, A novel setup for the pulsing and energy enhancement of a positron beam. J. Phys.: Conf. Ser. 443, 012093 (2013).

139. V. Pipich, Y. Dahdal, H. Rapaport, R. Kasher, Y. Oren and D. Schwahn, Effects of Biological Molecules on Calcium Mineral Formation Associated with Wastewater Desalination as Assessed using Small-Angle Neutron Scattering. Langmuir 29, 7607-7617 (2013).

140. S. Price, Y. Su, Y. Xiao, D. T. Adroja, T. Guidi, R. Mittal, S. Nandi, S. Matsuishi, H. Hosono and T. Brückel, Evidence of Spin Resonance Signal in Oxygen Free Superconducting $CaFe_{0.88}Co_{0.12}AsF$: An Inelastic Neutron Scattering Study. J. Phys. Soc. Jpn. 82, 104716 (2013).

141. W. Pyckhout-Hintzen, S. Westermann, A. Wischnewski, M. Monkenbusch, D. Richter, E. Straube, B. Farago and P. Lindner, Direct Observation of Nonaffine Tube Deformation in Strained Polymer Networks. Phys. Rev. Lett. 110, 196002 (2013).

142. B. N. Rao, R. Datta, S. S. Chandrashekaran, D. K. Mishra, V. Sathe, A. Senyshyn and R. Ranjan, Local structural disorder and its influence on the average global structure and polar properties in $Na_{0.5}Bi_{0.5}TiO_3$. Phys. Rev. B: Condens. Matter Mater. Phys. 88, 224103 (2013).

143. M. Rawolle, K. Sarkar, M. A. Niedermeier, M. Schindler, P. Lellig, J. S. Gutmann, J.-F. Moulin, M. Haese-Seiller, A. S. Wochnik, C. Scheu and P. Müller-Buschbaum,

Infiltration of Polymer Hole-Conductor into Mesoporous Titania Structures for Solid-State Dye-Sensitized Solar Cells. ACS Appl. Mater. Interfaces 5, 719-729 (2013).

144. G. J. Redhammer, G. Roth, A. Senyshyn, G. Tippelt and C. Pietzonka, Crystal and magnetic spin structure of Germanium-Hedenbergite,$CaFeGe_2O_6$, and a comparison with other magnetic/magnetoelectric/multiferroic pyroxenes. Z. Kristallogr. 228, 140-150 (2013).

145. M. Reiner, P. Pikart and C. Hugenschmidt, In-situ (C)DBS at high temperatures at the NEPOMUC positron beam line. J. Phys.: Conf. Ser. 443, 012071 (2013).

146. R. Richter, U. E. Berger, S. Dullinger, F. Essl, M. Leitner, M. Smith and G. Vogl, Spread of invasive ragweed: climate change, management and how to reduce allergy costs. Journal of Applied Ecology 50, 1422-1430 (2013).

147. R. Richter, S. Dullinger, F. Essl, M. Leitner and G. Vogl, How to account for habitat suitability in weed management programmes?. Biological Invasions 15, 657-669 (2013).

148. E. E. Rodriguez, D. A. Sokolov, C. Stock, M. A. Green, O. Sobolev, J. A. Rodriguez-Rivera, H. Cao and A. Daoud-Aladine, Magnetic and structural properties near the Lifshitz point in $Fe_{1+x}Te$. Phys. Rev. B: Condens. Matter Mater. Phys. 88, 165110 (2013).

149. J. Rolph, N. Iqbal, M. Hofmann, A. Evans, M. C. Hardy, M. G. Glavicic and M. Preuss, The effect of d_0 reference value on a neutron diffraction study of residual stress in a γ/γ′ nickel-base superalloy. J. Strain Anal. Eng. Des. 48, 219-228 (2013).

150. N. Ruocco, L. Dahbi, P. Driva, N. Hadjichristidis, J. Allgaier, A. Radulescu, M. Sharp, P. Lindner, E. Straube, W. Pyckhout-Hintzen and D. Richter, Microscopic Relaxation Processes in Branched-Linear Polymer Blends by Rheo-SANS. Macromolecules 46, 9122-9133 (2013).

151. A. Röhrmoser, Branching treatment of n-capture to isomer states in ORIGEN activation code and corrections in the coupled MonteBurns depletion system. Transactions RRFM 2013, 21–25 April, St. Petersburg, Russia (2013).

152. A. Röhrmoser and V. Hutanu, Strahlcharakterisierung und weitere Berechnungen zur Abschirmung des neuen Experimentierplatzes POLI-HEIDI an Strahlrohr SR-9 des FRM II (2013).

153. A. T. Rømer, J. Chang, N. B. Christensen, B. M. Andersen, K. Lefmann, L. Mähler, J. Gavilano, R. Gilardi, C. Niedermayer, H. M. Rønnow, A. Schneidewind, P. Link, M. Oda, M. Ido, N. Momono and J. Mesot, Glassy low-energy spin fluctuations and anisotropy gap in $La_{1.88}Sr_{0.12}CuO_4$. Phys. Rev. B: Condens. Matter Mater. Phys. 87, 144513 (2013).

154. B. S. G. Almqvist, A. M. Hirt, M. Herwegh, A. Ebert, J. M. Walter, B. Leiss and L. Burlini, Seismic anisotropy in the Morcles nappe shear zone: Implications for seismic imaging of crustal scale shear zones. Tectonophysics 603, 162-178 (2013).

155. J. Saroun, J. Rebelo Kornmeier, M. Hofmann, P. Mikula and M. Vrána, Analytical model for neutron diffraction peak shifts due to the surface effect. J. Appl. Crystallogr. 46, 628-638 (2013).

156. P. K. Sawinski, M. Meven, U. Englert and R. Dronskowski, Single-Crystal Neutron Diffraction Study on Guanidine, CN_3H_5. Cryst. Growth Des. 13, 1730 - 1735 (2013).

157. A. P. Sazonov, A. Gukasov, H. B. Cao, P. Bonville, E. Ressouche, C. Decorse and I. Mirebeau, Magnetic structure in the spin liquid $Tb_2Ti_2O_7$ induced by a [111] magnetic field: Search for a magnetization plateau. Phys. Rev. B: Condens. Matter Mater. Phys. 88, 184428 (2013).

158. R. Schenk, W. Petry, B. Stepnik, C. Jarousse, G. Bourdat, C. Moyroud and M. Grasse, FRM II / CERCA UMo atomizer project status. Transactions RRFM 2013, 21–25 April, St. Petersburg, Russia (2013).

159. E. Schmid, F. M. Wagner, L. Canella, H. Romm and T. E. Schmid, RBE of thermal neutrons for induction of chromosome aberrations in human lymphocytes. Radiat. Environ. Biophys. 52, 113-121 (2013).

160. M. Schmiele, T. Schindler, T. Unruh, S. Busch, H. Morhenn, M. Westermann, F. Steiniger, A. Radulescu, P. Lindner, R. Schweins and P. Boesecke, Structural characterization of the phospholipid stabilizer layer at the solid-liquid interface of dispersed triglyceride nanocrystals with small-angle x-ray and neutron scattering. Phys. Rev. E: Stat., Nonlinear, Soft Matter Phys. 87, 062316 (2013).

161. G. Schneider, T. Glomann, J. Allgaier, A. Radulescu, W. Lohstroh, B. Farago and D. Richter , Rich molecular dynamics of polymer melts in nanocomposites. Proceeding of the Polymer Processing Society 29th annual meeting (2013).

162. G. J. Schneider, K. Nusser, S. Neueder, M. Brodeck, L. Willner, B. Farago, O. Holderer, W. J. Briels and D. Richter, Anomalous chain diffusion in unentangled model polymer nanocomposites. Soft Matter 9, 4336-4348 (2013).

163. M. Schneider, R. Michels, V. Pipich, G. Goerigk, V. Sauer, H.-P. Heim and K. Huber, Morphology of Blends with Cross-Linked PMMA Microgels and Linear PMMA Chains. Macromolecules 46, 9091-9103 (2013).

164. W. J. Schreier, T. Aumüller, K. Haiser, F. O. Koller, M. Löweneck, H.-J. Musiol, T. Schrader, T. Kiefhaber, L. Moroder and W. Zinth, Following the energy transfer in and out of a polyproline-peptide. Biopolymers 100, 38-50 (2013).

165. T. Schröder, S. Schwarzmüller, C. Stiewe, J. de Boor, M. Hölzel and O. Oeckler, The Solid Solution Series $(GeTe)_x(LiSbTe_2)_2$ ($1 \leq x \leq 11$) and the Thermoelectric Properties of $(GeTe)_{11}(LiSbTe_2)_2$. Inorg. Chem. 52, 11288-11294 (2013).

166. R. Schulze, L. Szentmiklosi, P. Kudejova, L. Canella, Z. Kis, T. Belgya, J. Jolie, M. Ebert, T. Materna, K. T. Biro and Z. Hajnal, The ANCIENT CHARM project at FRM II: three-dimensional elemental mapping by prompt gamma activation imaging and neutron tomography. J. Anal. At. Spectrom. 28, 1508-1512 (2013).

167. K. M. Seemann, A. Bauer, J. Kindervater, M. Meyer, C. Besson, M. Luysberg, P. Durkin, W. Pyckhout-Hintzen, N. Budisa, R. Georgii, C. M. Schneider and P. Kögerler, Polyoxometalate-stabilized, water dispersible Fe_2Pt magnetic nanoparticles. Nanoscale 5, 2511-2519 (2013).

168. A. Senyshyn, O. Dolotko, M. J. Mühlbauer, K. Nikolowski, H. Fuess and H. Ehrenberg, Lithium Intercalation into Graphitic Carbons Revisited: Experimental Evidence for Twisted Bilayer Behavior. J. Electrochem. Soc. 160, A3198-A3205 (2013).

169. A. Senyshyn and L. Vasylechko, Low Temperature Crystal Structure Behaviour of Complex Yttrium Aluminium Oxides $YAlO_3$ and $Y_3Al_5O_{12}$. Acta Phys. Pol., A 124, 329-335 (2013).

170. E. Shin, B. S. Seong and C. M. Sim, Residual stress analysis of an aircraft landing gear part using neutron diffraction. Met. Mater.-Int. 19, 691-695 (2013).

171. Y. J. Sohn, K. M. Sparta, M. Meven, G. Roth and G. Heger, Superprotonic conductivity of $(NH_4)_3H(SO_4)_2$ in the high-temperature phase. Solid State Ion. 252, 116-120 (2013).

172. Y. J. Sohn, K. M. Sparta, S. Prinz, M. Meven, G. Roth and G. Heger, Proton ordering in $(NH_4)_3H(SO_4)_2$ at low-temperature phase transitions. Acta Crystallogr., Sect. B: Struct. Sci. 69, 336-343 (2013).

173. R. S. Solanki, S. K. Mishra, A. Senyshyn, S. Yoon, S. Baik, N. Shin and D. Pandey, Confirmation of the monoclinic Cc space group for the ground state phase of $Pb(Zr_{0.525}Ti_{0.475})O_3$: A combined synchrotron X-ray and neutron powder diffraction study. Appl. Phys. Lett. 102, 052903 (2013).

174. A. Stadler, T. Unruh, K. Namba, F. Samatey and G. Zaccai, Correlation between Supercoiling and Conformational Motions of the Bacterial Flagellar Filament. Biophys. J. 105, 2157-2165 (2013).

175. M. Stana, M. Leitner, M. Ross and B. Sepiol, Studies of atomic diffusion in Ni-Pt solid solution by x-ray photon correlation spectroscopy. J. Phys.: Condens. Matter 25, 065401 (2013).

176. I. Stefanescu, Y. Abdullahi, J. Birch, I. Defendi, R. Hall-Wilton, C. Höglund, L. Hultman, D. Seiler and K. Zeitelhack, Development of a novel macrostructured cathode for large-area neutron detectors based on the ^{10}B-containing solid converter. Nucl. Instr. Meth. A 727, 109-125 (2013).

177. I. Stefanescu, Y. Abdullahi, J. Birch, I. Defendi, R. Hall-Wilton, C. Höglund, L. Hultman, M. Zee and K. Zeitelhack, A ^{10}B-based neutron detector with stacked MultiWire Proportional Counters and macrostructured cathodes. J. Instrum. 8, P12003 (2013).

178. C. Stock, S. R. Dunsiger, R. A. Mole, X. Li and H. Luo, Coupled short-range ferroelectric and magnetic order in $PbFe_{1/2}Nb_{1/2}O_3$. Phys. Rev. B: Condens. Matter Mater. Phys. 88, 094105 (2013).

179. S. Söllradl, H. Lührs, Z. Revay, P. Kudejova, L. Canella and A. Türler, Increasing the dynamic range for the analysis of boron in PGAA. J. Radioanal. Nucl. Chem. 298, 2069-2073 (2013).

180. R. Tietze, S. Dürr, S. Lyer, N. Taccardi, P. Wasserscheid, L. Canella, F. M. Wagner, W. Petry and C. Alexiou, Phantom Studies of Neutron Capture of Boron Containing Magnetic Nanoparticles. Biomed. Eng. 58 (2013).

181. S. J. Tomanicek, R. F. Standaert, K. L. Weiss, A. Ostermann, T. E. Schrader, J. D. Ng and L. Coates, Neutron and X-ray Crystal Structures of a Perdeuterated Enzyme Inhibitor Complex Reveal the Catalytic Proton Network of the Toho-1 -Lactamase for the Acylation Reaction. J. Biol. Chem. 288, 4715-4722 (2013).

182. M. A. Uribe-Laverde, D. K. Satapathy, I. Marozau, V. K. Malik, S. Das, K. Sen, J. Stahn, A. Rühm, J.-H. Kim, T. Keller, A. Devishvili, B. P. Toperverg and C. Bernhard, Depth profile of the ferromagnetic order in a $YBa_2Cu_3O_7$/$La_{2/3}Ca_{1/3}MnO_3$ superlattice on a LSAT substrate: a polarized neutron reflectometry study. Phys. Rev. B: Condens. Matter Mater. Phys. 87, 115105 (2013).

183. P. Vignola, G. Gatta and M. Meven, A Single-Crystal Neutrons Diffraction Study of Brazilianite, $NaAl_3(PO_4)_2(OH)_4$. Contributions to the 6th International Symposium On Granitic Pegmatites (PEG 2013). W. B. Simmons, K. L. Webber (eds.), Rubellite Press, New Orleans, LA (2013).

184. J. N. Walsh, A. F. Mark, H. Abdolvand, J. A. Francis, B. Pellereau, S. Bate, M. Hofmann and P. J. Withers, The Influence of Geometry on Residual Stress Around Repair Welds. ASME 2013 Pressure Vessels and Piping Conference Proceedings (2013).

185. J. L. Wang, S. J. Campbell, M. Hofmann, S. J. Kennedy, M. Avdeev, M. Md Din, R. Zeng, Z. X. Cheng and S. X. Dou, Substitution of Y for Pr in $PrMn_2Ge_2$—The magnetism of $Pr_{0.8}Y_{0.2}Mn_2Ge_2$. J. Appl. Phys. 113, 17E147 (2013).

186. J. L. Wang, L. Caron, S. J. Campbell, S. J. Kennedy, M. Hofmann, Z. X. Cheng, M. F. Md Din, A. J. Studer, E. Brück and S. X. Dou, Driving Magnetostructural Transitions in Layered Intermetallic Compounds. Phys. Rev. Lett. 110, 217211 (2013).

187. J. L. Wang, S. J. Kennedy, S. J. Campbell, M. Hofmann and S. X. Dou, Phase gap in pseudoternary $R_{1-y}R'_yMn_2X_{2-x}X'_x$ compounds. Phys. Rev. B: Condens. Matter Mater. Phys. 87, 104401 (2013).

188. J. A. A Weber, P. Böni, H. Ceeh, M. Leitner and C. Hugenschmidt, First 2D-ACAR measurements on Cu with the new spectrometer at TUM. J. Phys.: Conf. Ser. 443, 012092 (2013).

189. T. Weber, G. Brandl, R. Georgii, W. Häußler, S. Weichselbaumer and P. Böni, Monte-Carlo Simulations for the optimisation of a TOF-MIEZE Instrument. Nucl. Instr. Meth. A 713, 71-75 (2013).

190. J. Wen, S. Li, Z. Xu, C. Zhang, M. Matsuda, O. Sobolev, J. Park, A. Christianson, E. Bourret-Courchesne, Q. Li, G. Gu, D.-H. Lee, J. M. Tranquada, G. Xu and R. Birgeneau, Enhanced low-energy magnetic excitations via suppression of the itinerancy in $Fe_{0.98-z}Cu_zTe_{0.5}Se_{0.5}$. Phys. Rev. B: Condens. Matter Mater. Phys. 88, 144509 (2013).

191. J. H. Wittke, J. C. Weaver, T. E. Bunch, J. P. Kennett, D. J. Kennett, A. M. T. Moore, G. C. Hillman, K. B. Tankersley, A. C. Goodyear, C. R. Moore, I. R. Daniel, Jr., J. H. Ray, N. H. Lopinot, D. Ferraro, I. Israde-Alcantara, J. L. Bischoff, P. S. DeCarli, R. E. Hermes, J. B. Kloosterman, Z. Revay, G. A. Howard, D. R. Kimbel, G. Kletetschka, L. Nabelek, C. P. Lipo, S. Sakai, A. West and R. B. Firestone, Evidence for deposition of 10 million tonnes of impact spherules across four continents 12,800 y ago. Proc. Natl. Acad. Sci. USA 110, E2088-E2097 (2013).

192. J. Wuttke and M. Zamponi, Simulation-guided optimization of small-angle analyzer geometry in the neutron backscattering spectrometer SPHERES. Rev. Sci. Instrum. 84, 115108 (2013).

193. Y. Xiao, S. Nandi, Y. Su, S. Price, H.-F. Li, Z. Fu, W. Jin, A. Piovano, A. Ivanov, K. Schmalzl, W. Schmidt, T. Chatterji, T. Wolf and T. Brückel, Magnetic anisotropic energy gap and low-energy spin wave excitation in the antiferromagnetic block phase of $K_2Fe_4Se_5$. Phys. Rev. B: Condens. Matter Mater. Phys. 87, 140408 (2013).

194. M. Yoshida, Y. Zhao, M. Yoshizawa-Fujita, A. Ohira, Y. Takeoka, S. Koizumi and M. Rikukawa, PFG-NMR and SANS Studies in Cation Exchange Membranes Based on Sulfonated Polyphenylene Multiblock Copolymers. ECS Transactions 50, 1045-1053 (2013).

195. M. Zanatta, A. Fontana, A. Orecchini, C. Petrillo and F. Sacchetti, Inelastic Neutron Scattering Investigation in Glassy $SiSe_2$: Complex Dynamics at the Atomic Scale. J. Phys. Chem. Lett. 4, 1143-1147 (2013).

196. C. Zhang, H.-F. Li, Y. Song, Y. Su, G. Tan, T. Netherton, C. Redding, S. V. Carr, O. Sobolev, A. Schneidewind, E. Faulhaber, L. W. Harriger, S. Li, X. Lu, D.-X. Yao, T. Das, A. V. Balatsky, T. Brückel, J. W. Lynn and P. Dai, Distinguishing $s^{\pm}$ and s^{++} electron pairing symmetries by neutron spin resonance in superconducting $NaFe_{0.935}Co_{0.045}As$. Phys. Rev. B: Condens. Matter Mater. Phys. 88, 064504 (2013).

197. C. Zhang, M. Liu, Y. Su, L.-P. Regnault, M. Wang, G. Tan, T. Brückel, T. Egami and P. Dai, Magnetic anisotropy in hole-doped superconducting $Ba_{0.67}K_{0.33}Fe_2As_2$ probed by polarized inelastic neutron scattering. Phys. Rev. B: Condens. Matter Mater. Phys. 87, 081101 (2013).

198. C. Zhang, R. Yu, Y. Su, Y. Song, M. Wang, G. Tan, T. Egami, J. A. Fernandez-Baca, E. Faulhaber, Q. Si and P. Dai, Measurement of a Double Neutron-Spin Resonance and an Anisotropic Energy Gap for Underdoped Superconducting $NaFe_{0.985}Co_{0.015}As$ Using Inelastic Neutron Scattering. Phys. Rev. Lett. 111, 207002 (2013).

199. J. Zhang, P. R. Lang, M. Meyer and J. K. G. Dhont, Synthesis and Self-Assembly of Squarelike $PbCrO_4$ Nanoplatelets via Micelle-Mediated Depletion Attraction. Langmuir 29, 4679-4687 (2013).

200. J. Zhang, P. R. Lang, W. Pyckhout-Hintzen and J. K. G. Dhont, Controllable synthesis and self-assembly of $PbCO_3$ nanorods in shape-dependent nonionic w/o microemulsions. Soft Matter 9, 7576-7582 (2013).

201. K. Zhao, Z. Deng, X. C. Wang, W. Han, J. L. Zhu, X. Li, Q. Q. Liu, R. C. Yu, T. Goko, B. Frandsen, L. Liu, F. Ning, Y. J. Uemura, H. Dabkowska, G. M. Luke, H. Luetkens, E. Morenzoni, S. R. Dunsiger, A. Senyshyn, P. Böni and C. Q. Jin, New diluted ferromagnetic semiconductor with Curie temperature up to 180 K and isostructural to the '122' iron-based superconductors. Nat. Commun. 4, 1442 (2013).

202. T. Zweifel, H. Chiang, H. Palancher, A. Bonnin, L. Beck, P. Weiser, M. Döblinger, C. Sabathier, R. Jungwirth, F. Charollais, P. Lemoine and W. Petry, Heavy ion irradiation on monolithic UMo/Al layer systems: Interdiffusion layer analysis using TEM and NANO-XRD. Transactions RRFM 2013, 21–25 April, St. Petersburg, Russia (2013).

203. T. Zweifel, H. Palancher, A. Leenaers, A. Bonnin, V. Honkimäki, R. Tucoulou, S. van den Berghe, R. Jungwirth, F. Charollais and W. Petry, Crystallographic study of Si and ZrN coated U-Mo atomised particles and of their interaction with al under thermal annealing. J. Nucl. Mater. 442, 124-132 (2013).

Theses

Doctoral theses

M. M. Baum
Neutron-Scattering Studies on Chiral Multiferroics
Universität zu Köln (2013).

J. Brand
Magnetismus von unkonventionellen Supraleitern am Beispiel von Ruthenat- und Eisen-Arsenid-Verbindungen
Universität zu Köln (2013).

B. Cao
Organic Solar Cells
Technische Universität München (2013).

T. Claudio Weber
Lattice Dynamics of Nanostructured Thermoelectric Materials
Université de Liège (2013).

C. Cooper
Competitive Adsorption in Complex Mixtures of Polymers and Particles
University of Bristol (2013).

W. Fang
Elaboration de matériaux composites nanofils/polymères pour la fabrication d'aimants permanents
CEA Saclay (2013).

T. Finger
Neutronenuntersuchungen an geschichteten Kobaltaten
Universität zu Köln (2013).

T. Glomann
Microscopic View on the Polymer Dynamics in Nanocomposites with Attractive Interactions
Westfälische Wilhelms-Universität Münster (2013).

C. Gold
Über die Natur konkurrierender Wechselwirkungen in Cer-basierten 1-9-4 Verbindungen
Universität Augsburg (2013).

M. Granite
Functional Adducts of Polymers and Carbon Nanotubes
Technion-Israel Institute of Technology (2013).

F. Groitl
High Resolution Spectroscopy with the Neutron Resonance Spin Echo Method
Technische Universität Berlin (2013).

N. Haag
Experimental Determination of the Antineutrino Spectrum of the Fission Products of U238
Technische Universität München (2013).

M. Paul Hungler
Design and development of a neutron tomography instrument fort he characterization of degradation in honeycomb composites
Royal Military College of Canada (2013).

S. Jaksch
Phasenverhalten von Poly(2-Oxazolinen) in wässriger Lösung
Technische Universität München (2013).

T. Kandemir
Solid catalysts for methanol and ammonia synthesis investigated by in-situ neutron diffraction
Technische Universität Berlin (2013).

V. Kuppili
Shape memory alloys thin films
Ludwig-Maximilians-Universität München (2013).

S. Kynde
Modelling small-angle scattering data from complex protein-lipid systems
University of Copenhagen (2013).

J. Larsen
Interplay of structure, magnetism and functionality in high-temperature superconductors and $CoCl_2$ salts
Technical University of Denmark (2013).

M. Laupheimer
Gelled Bicontinuous Microemulsions - A New Type of Orthogonal Self-Assembled Systems
Universität Stuttgart (2013).

Y. Liu
Effects of defects on the properties of wide band-gap semiconductors and related materials
Chinese Academy of Sciences (2013).

H. Lührs
The Influence of Boron on The Crystal Structure and Properties of Mullite: Investigations at Ambient, High-Pressure, and High-Temperature Conditions
Universität Bremen (2013).

C. Mark
Structure and dynamics of polymer chains grafted on nanoparticles
Westfälische Wilhelms-Universität Münster (2013).

J. Martinez Gómez
Production and characterization of ODS W alloys for fusion reactor
Universidad Carlos III de Madrid (2013).

S. Materne
Tests of prototype magnets and study on a MCP based proton detector for the neutron lifetime experiment PENeLOPE
Technische Universität München (2013).

R. Michel
Liposomes in Contact and Interacting with Silica Nanoparticles: From Decorated Vesicles to Internalized Particles
Technische Universität Berlin (2013).

S. R. Midtgaard
Self-assembling peptide and protein nanodiscs for studies of membrane proteins
University of Copenhagen (2013).

M. J. Mühlbauer
Neutron μstiX - Micrometer Structure Investigation with Real Space Reciprocal Space Crossover using Neutron Imaging Detectors
Technische Universität München (2013).

N. Munnikes
High Resolution Neutron Spectroscopy of Excitations in Superconductors
Max-Planck-Institut für Festkörperforschung (2013).

M. Muthmann
Struktur und Dynamik von Polymerschmelzen unter räumlichen Einschränkungen
Westfälische Wilhelms-Universität Münster (2013).

M. Niedermeier
Structuring of titanium dioxide films for application in photovoltaics
Technische Universität München (2013).

M. Petriska
Advanced aproaches in measurement of positron lifetime in irradiated materials
Slovak University of Technology Bratislava (2013).

S. Price
Interplay between Magnetism and Superconductivity in Iron Based High Temperature Superconductors
RWTH Aachen University (2013).

M. Rawolle
Structuring and filling of titania films for applications in photovoltaics
Technische Universität München (2013).

R. Ritz
Superconductivity and non-Fermi liquid behavior on the border of itinerant ferromagnetism
Technische Universität München (2013).

F. Roosen-Runge
Salt Effects in Protein Solutions
Universität Tübingen (2013).

N. Ruocco
Microscopic relaxation processes in branched-linear polymer blends by Rheo-SANS
Westfälische Wilhelms-Universität Münster (2013).

J. Scharnweber
Mikrostruktur- und Texturentwicklung von ARB TiAl-Kompositen
Technische Universität Dresden (2013).

A. Schmidt
Synthese und Charakterisierung anionensubstituierter Mayenite
Technische Universität Berlin (2013).

F. Schneider
Untersuchungen an Mischungen aus Mikrogelen und Polymeren
Westfälische Wilhelms-Universität Münster (2013).

F. Schulz
Studies on metal-free hydrogen activation and catalytic hydrogenation by frustrated Lewis pairs
Technische Universität München (2013).

C. Sill
Dynamics of the Iron-Binding Protein Lactoferrin
Westfälische Wilhelms-Universität Münster (2013).

S. Sun
Mica Pigments
Ludwig-Maximilians-Universität München (2013).

B. Tyrel
Criteria for Evolution of a Successful Superfamily: Fold Fitness and Structural Dynamics Explored
University of New Mexico (2013).

J. Veterníková
Study of materials for advanced reactor systems
Slovak University of Technology Bratislava (2013).

D. Weber
Synthese und Strukturelle Charakterisierung metastabiler Oxide und Oxidnitride der Übergangsmetalle
Technische Universität Berlin (2013).

L. Yu
Hydrothermal synthesis of hierachial pourous material in the system FE-O-OH
Ludwig-Maximilians-Universität München (2013).

T. Zinn
Molecular Exchange Kinetics and Structure of n-Alkyl-PEO Polymeric Micelles Studied by SANS
Westfälische Wilhelms-Universität Münster (2013).

Diploma and Master theses

M. Amann
Struktur und Phasenverhalten von C28-PEO-5K Polymermizellen in verdünnter und semiverdünnter wässriger Lösung
Westfälische Wilhelms-Universität Münster (2013).

B. Baumeister
Construction, Commissioning and Characterization of a Sputtering Device for the Production of Cylindrical Target for ^{99}Mo Production
Technische Universität München (2013).

S. Charitou
Comparative Study of Ancient Metal Objects Microstructure with Non-Destructive Methods PGAA, ND and SR-XRF
Democritus University of Thrace (2013).

S. Christensen
Measuring and modelling inelastic scattering processes in thermoelectric materials
Aahrus University (2013).

S. Eichler
Kohlenstofflangfaser-Aluminiummatrix-Verbundwerkstoffe: Simulation von thermischen Spannungen und Vergleich mit experimentellen Ergebnissen
Friedrich-Alexander-Universität Erlangen-Nürnberg (2013).

W. M. Gebauer
A Scintillator based proton detector with Silicon Photomultiplier readout for the neutron lifetime experiment PENeLOPE
Technische Universität München (2013).

C. Herold
Messung von Streuquerschnitten Ultrakalter Neutronen in festem Deuterium
Technische Universität München (2013).

M. Huber
Implementation and characterization of a precision spin-tracking toolkit for slow particles in GEANT4
Technische Universität München (2013).

J. Jutimoosik
Growth of EuO layers
Technische Universität München (2013).

T. Karawani
Interactions of DNA with carbon nanotube
Technion-Israel Institute of Technology (2013).

C.-H. Lin
Co-non solvency in thermo-respensive polymeric hydrogels
Technische Universität München (2013).

F. Lippert
Winkelaufgelöste Messung des Spektrums reemittierter Positronen aus W, Pt und Ni in Abhängigkeit der kristallografischen Orientierung
Technische Universität München (2013).

S. Mukherjee
Anomalous Exchange Coupling in $Fe_{1-x}Cu_x$/Tb Multilayers
Technische Universität München (2013).

M. Rahn
Search für topological properties in multi-k magnetic structures
Technische Universität München (2013).

C. Reiter
Methodenentwicklung, Kalorimetrie und Messung der Dichte von hochdichten Kernbrennstoffen
Technische Universität München (2013).

S. Säubert
Isothermal Transformation Kinetics in Uranium Molybdenum Alloys
Technische Universität München (2013).

R. Schauer
Entwicklung und Evaluation eines Qualitätssicherungsverfahrens für kerntechnische Sputterprozesse
Technische Universität München (2013).

O. Schipper
Hindered Diffusion of green fluorescent protein in nonionic surfactant based microemulsions
Technische Universität München (2013).

C. Soultana
Comparative Study of Ancient Metal Objects Microstructure with Non-Destructive Methods ND, PGAA, SR-XRF and SR-XRD
Democritus University of Thrace (2013).

E. Spyropoulou
Non destructive compositional study of biological samples using PGAA
Democritus University of Thrace (2013).

M. Strobl
Einfluss elektrischer Felder auf Kupferselenat und dotierte Kupferselenatproben
Technische Universität München (2013).

M. Sturm
Measurements and characterization of a laser-based Cs-atomic magnetometer
Technische Universität München (2013).

X. Sun
Magnetic properties of FePt/MnO heterodimer nanoparticles
JCNS, Forschungszentrum Jülich (2013).

N. Vishnevetskaya
Polymeric nanoparticles for drug delivery
Technische Universität München (2013).

R. Wang
Hybrid Solar Cells based on ZnO Nanostructures
Technische Universität München (2013).

P. Ziegler
Herstellung und Characterisierung von Fe-Schichten
Technische Universität München (2013).

S. Zimnik
Untersuchung der Segregation in FePt mit Röntgen und Positronenannihilation induzierter AES
Technische Universität München (2013).

Bachelor theses

A. Augenstein
Inbetriebnahme einer neuen heizbaren Probenumgebung für den Scanning Positron Beam
Ludwig-Maximilians-Universität München (2013).

C. Bordihn
Cs Atommagnetometrie mit Permanentmagnetfeldern
Technische Universität München (2013).

M. Dodenhöft
Metallografische Präparation von Uran-Molybdän
Technische Universität München (2013).

M. Dogu
Entwicklung eines elektronischen stand-alone-Moduls(MD-Modul) zur Sicherheitsüberwachung eines Neutronen-Detektorsystems und Sicherheitssteuerung einer Hochspannungsquelle
Technische Universität München (2013).

M. Engl
Design and construction of a temperature-stabilized environment for the Munich Cs Magnetometer DAVLL-type laser lock
Technische Universität München (2013).

R. Fink
Konstruktion und Bau einer Zusatzabschirmung für das 3-Achsen Spektrometer MIRA
Hochschule für angewandte Wissenschaften München (2013).

D. Gaisbauer
Set up and tests of the first coils of the neutron lifetime experiment PENeLOPE
Technische Universität München (2013).

N. Grill
Implementation of positron pulsing unit
Technische Universität München (2013).

A. Grimm
Study of pure elastic neutron scattering using the single crystal diffractometer HEIDI
Technische Universität München (2013).

N. Gustschin
Data Aquisition, Reproducibility and Analysis of Rhology Experiments on Polymer Melts
Technische Universität München (2013).

F. X. Haselbeck
Simulation und Konstruktion enes MiniMuPAD
Technische Universität München (2013).

M. Hettich
Rheologie von Flüssigkeiten
Technische Universität München (2013).

S. O. Huber
Thermische Analyse von Polymernanokompositen
Technische Universität München (2013).

S. Janaschke
Steuerungstechnische Realisierung eines Fächerchoppersystems
JCNS, Forschungszentrum Jülich (2013).

M. Knölker
Optimierung der Bestrahlungsbedingungen für die Produktion von Holmium-166-Mikrokügelchen
Technische Universität München (2013).

S. Lechelmayr
Ex- and In-Situ Dynamic Light Scattering at KWS-2: An Additional Information on Sample Quality
Technische Universität München (2013).

M. Lindner
Numerische Optimierung von Multischicht-Polarisatoren mitttels Monte-Carlo-Simulationen am Instrument POLI am FRM II
Hochschule für angewandte Wissenschaften München (2013).

Martin Losekamm
Monte Carlo Simulations and High Voltage Tests for the Future UCN-Source and nEDM-Experiment at TRIUMF
Technische Universität München (2013).

Y. Nadkernychnyy
Digital Impuls NMR-Spektrometer für polarisiertes ^{3}He-Gas
Hochschule für angewandte Wissenschaften München (2013).

F. Niederreither
Characterization of the magnetic shield of the NEDM-experiment
Technische Universität München (2013).

C. Reitinger
Deposition and characterisation of heterostructures of magnetic insulators
Technische Universität München (2013).

B. Riennäcker
Effizienzsteigerung der Positronenquelle NEPOMUC
Hochschule für angewandte Wissenschaften München (2013).

J. Rothe
First Prototype of a Trap for High-Field Seeking Ultracold Neutrons
Technische Universität München (2013).

D. Ruhsdorfer
Herstellung und Charakterisierung von deuterierten Polyethylenschichten zur Speicherung von ultrakalten Neutronen
Technische Universität München (2013).

F. Schäble
Untersuchung von Analysatorkristallen für ein Multi-Detektorsystem am kalten Drei-Achsen-Spektrometer PANDA
Technische Universität München (2013).

C. Schneider
Entwicklung und Design des Steuerungs- und Analyseprogramms für das TUM Neutron EDM experiment
Technische Universität München (2013).

M. Schnitzenbaumer
Particle Size Determination using Light Scattering
Technische Universität München (2013).

A. Schreiber
Aufbau einer Temperaturstabilisierung für eine ultrastabile Stromquelle
Technische Universität München (2013).

D. Schwienbacher
Commissioning of a sputtering system for the production of UCN-guides
Technische Universität München (2013).

R. Schönberger
Simulation of the transport and storage of ultracold neutrons
Technische Universität München (2013).

M. Seifert
Simulation of a chopper system for a time-of-flight imaging beam line at the European spallation source
Technische Universität München (2013).

S. Simeth
Verteilung von Wasserstoff in ultrananokristallinen Diamantschichten - Strukturbestimmung mit Kleinwinkelneutronenstreuung
Technische Universität München (2013).

J. R. Stockhausen
A documentation about measuring the polymer melt rheology
Technische Universität München (2013).

M. Tischler
Implementation of a ^{22}Na based positron beam
Technische Universität München (2013).

M. Waldherr
Entwicklung von Komposit-Stempel-Zylinder Druckzellen für Hochdruckexperimente bei tiefen Temperaturen
Technische Universität München (2013).

S. Weichselbaumer
Core-Shell magnetic nanoparticles investigated by neutron scattering
Technische Universität München (2013).

T. Welzel
Comissioning of the Bound Beta-Decay (BoB) Test Set Up
Technische Universität München (2013).

C. Zellner
Entwicklung und Design des Magnetfeld-Messroboters für das TUM nEDM Experiment
Technische Universität München (2013).

Miscellaneous

F. Rust
Intermolekulare Bewegung von Polyethylenglykol
TUM Kolleg Seminararbeit,
Otto-von-Taube-Gymnasium (2013).

Imprint

Publisher:

Technische Universität München
Forschungs-Neutronenquelle
Heinz Maier-Leibnitz (FRM II)
Lichtenbergstr. 1
85747 Garching
Germany

Phone: +49.89.289.14966
Fax: +49.89.289.14995
Internet: www.mlz-garching.de
E-mail: mlz@mlz-garching.de

Editors:

Dr. Henrich Frielinghaus
Dr. Robert Georgii
Dr. Connie Hesse
Dr. Michael Hofmann
Dr. Olaf Holderer
Elisabeth Jörg-Müller
Christine Kortenbruck
Dr. Peter Link
Dr. Wiebke Lohstroh
Dr. Ina Lommatzsch
Dr. Jürgen Neuhaus
Dr. Andreas Ostermann
Dr. Bjørn Pedersen
Dr. Anatoliy Senyshyn
Dr. Olaf Soltwedel
Dr. Yixi Su
Andrea Voit

Photographic credits:

Wenzel Schürmann, TUM: title image, 7, 8 (large photo), 10 (top, middle), 11 (bottom), 15, 29, 35, 79, 90, 93, 97 (top), 99 (both), 107

Andreas Heddergott / Astrid Eckert, TUM: 8 (bottom: 1st, 2nd, 4th from left), 11 (middle)

Forschungszentrum Jülich:
8 (bottom: 3rd from left)

Philipp Baur, TUM: 11 (top)

Dr. Matthias Offer, Universität Duisburg-Essen: 12 (top)

Prof. Dr. Reinhard Krause-Rehberg, Martin-Luther-Universität Halle-Wittenberg: 12 (middle)

Volker Lannert, DAAD: 89

Thomas Gigl, TUM: 94, 105

Dr. Rainer Bruchhaus, JCNS: 95

Inês Crespo, FRM II: 98

Editors and authors: other images

Design and typesetting:

Ramona Bucher
Dr. Connie Hesse
Dr. Ina Lommatzsch
Benjamin Sanchez
Andrea Voit
Adrian Weis

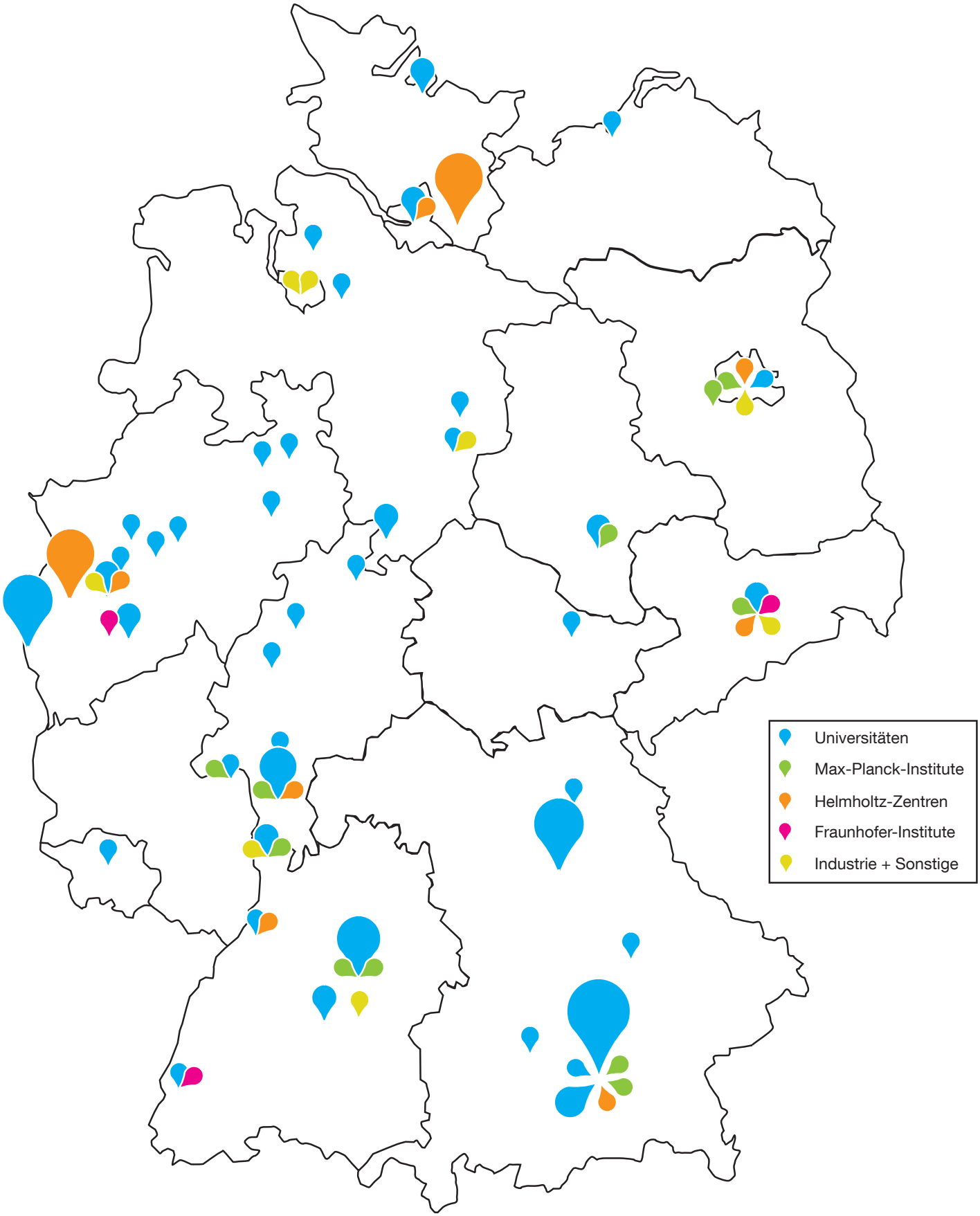

Heinz Maier-Leibnitz Zentrum (MLZ)

www.mlz-garching.de

Cover image on the back:
Location of institutes of German users of the MLZ.
The symbol size represents the number of different institutes at one university or research centre.

MLZ Instrument Suite

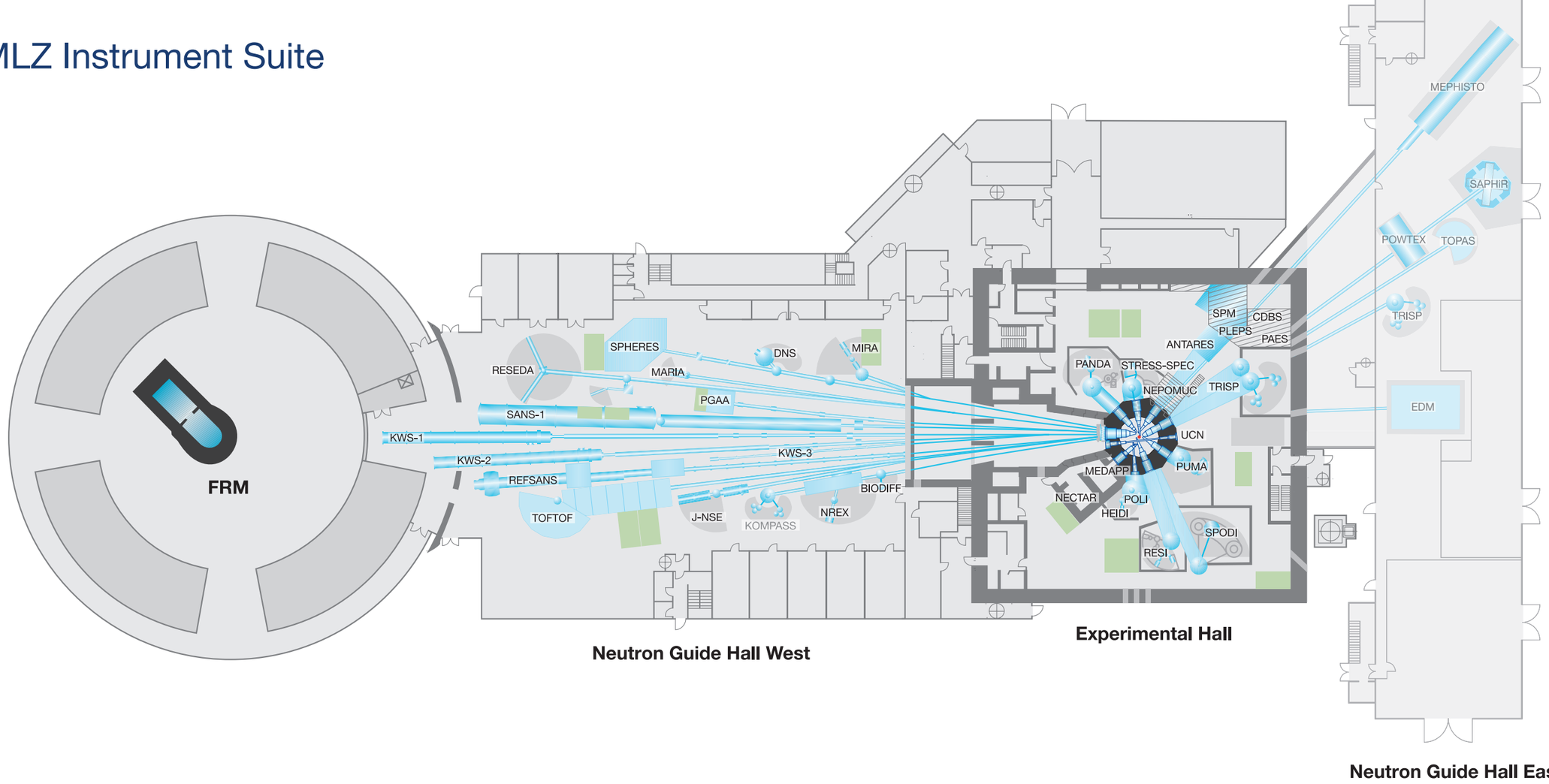

Instrument	Description	Neutrons	Status	Operated by	Funding
ANTARES	Radiography and tomography	cold	operation	TUM	TUM
BIODIFF	Diffractometer for large unit cells	cold	operation	TUM, JCNS	TUM, FZJ
DNS	Diffuse scattering spectrometer	cold	operation	JCNS	FZJ
HEIDI	Single crystal diffractometer	hot	operation	RWTH Aachen	FZJ
J-NSE	Spin-echo spectrometer	cold	operation	JCNS	FZJ
KOMPASS	Three axes spectrometer	cold	construction	Uni Köln, TUM	BMBF
KWS-1	Small angle scattering	cold	operation	JCNS	FZJ
KWS-2	Small angle scattering	cold	operation	JCNS	FZJ
KWS-3	Very small angle scattering	cold	operation	JCNS	FZJ
MARIA	Magnetic reflectometer	cold	operation	JCNS	FZJ
MEPHISTO	Facility for particle physics, PERC	cold	reconstruction	TUM	TUM, DFG
MIRA	Multipurpose instrument	cold	operation	TUM	TUM
MEDAPP	Medical irradiation treatment	fast	operation	TUM	TUM
NECTAR	Radiography and tomography	fast	operation	TUM	TUM
NEPOMUC	Positron source, CDBS, PAES, PLEPS, SPM	-	operation	TUM, UniBw München	TUM, BMBF
NREX	Reflectometer with X-ray option	cold	operation	MPI Stuttgart	MPG
PANDA	Three axes spectrometer	cold	operation	TU Dresden, JCNS	FZJ

Instrument	Description	Neutrons	Status	Operated by	Funding
PGAA	Prompt gamma activation analysis	cold	operation	Uni Köln, PSI	TUM
PUMA	Three axes spectrometer	thermal	operation	Uni Göttingen, TUM	TUM
POLI	Single-crystal diffractometer polarized neutrons	hot	operation	RWTH Aachen	BMBF, FZJ
POWTEX	Time-of-flight diffractometer	thermal	construction	RWTH Aachen, Uni Göttingen, JCNS	BMBF, FZJ
REFSANS	Reflectometer	cold	operation	GEMS	HZG
RESEDA	Resonance spin-echo spectrometer	cold	operation	TUM	TUM
RESI	Single crystal diffractometer	thermal	operation	LMU	TUM
SANS-1	Small angle scattering	cold	operation	TUM, GEMS	TUM, HZG
SAPHIR	Six anvil press for radiography and diffraction	thermal	construction	BGI	BMBF
SPHERES	Backscattering spectrometer	cold	operation	JCNS	FZJ
SPODI	Powder diffractometer	thermal	operation	KIT	TUM
STRESS-SPEC	Materials science diffractometer	thermal	operation	TUM, TU Clausthal, GEMS	TUM, HZG
TOFTOF	Time-of-flight spectrometer	cold	operation	TUM	TUM
TOPAS	Time-of-flight spectrometer	thermal	construction	JCNS	FZJ
TRISP	Three axes spin-echo spectrometer	thermal	operation	MPI Stuttgart	MPG
UCN	Ultra cold neutron source, EDM	ultra-cold	construction	TUM	TUM, DFG